DETECTION AND CHARACTERIZATION OF DEEP WATER WAVE BREAKING USING MODERATE INCIDENCE ANGLE MICROWAVE BACKSCATTER FROM THE SEA SURFACE

by

Andrew Thomas Jessup

B. S. E. University of Michigan
(1980)
S. M. Massachusetts Institute of Technology
(1988)

Submitted in Partial Fulfillment of the Requirements
of the Degree of

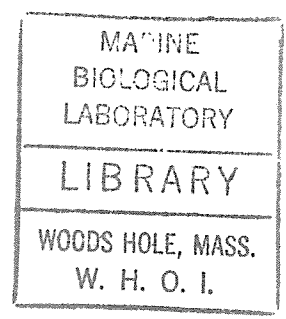DOCTOR OF PHILOSOPHY

at the

MASSACHUSETTS INSTITUTE OF TECHNOLOGY

and the

WOODS HOLE OCEANOGRAPHIC INSTITUTION

May 1990

© Massachusetts Institute of Technology and
Woods Hole Oceanographic Institution, 1990

Signature of Author —————————————————————————
Joint Program in Oceanography and Oceanographic Engineering
Massachusetts Institute of Technology
Woods Hole Oceanographic Institution

Certified by —————————————————————————
Professor W. Kendall Melville
Associate Professor, M. I. T.

Accepted by —————————————————————————
Professor W. Kendall Melville, Chairman
Joint Committee for Oceanographic Engineering

1930
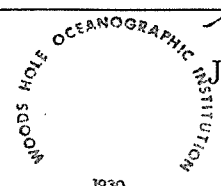
ABSTRACT

The importance of wave breaking in both microwave remote sensing and air–sea interaction has led to this investigation of the utility of a K_u–Band CW Doppler scatterometer to detect and characterize wave breaking in the open ocean. Field and laboratory measurements by previous authors of microwave backscatter from sharp–crested and breaking waves have shown that these events can exhibit characteristic signatures in moderate incidence angle measurements of the radar cross–section (RCS) and Doppler spectrum. Specifically, breaking events have been associated with polarization independent sea spikes in the RCS accompanied by increased mean frequency and bandwidth of the Doppler spectrum.

Simultaneous microwave, video, and environmental measurements were made during the SAXON experiment off Chesapeake Bay in the fall of 1988. The scatterometer was pointed upwind with an incidence angle of 45 degrees and an illumination area small compared to the wavelength of the dominant surface waves. An autocovariance estimation technique was used to produced time series of the RCS, mean Doppler frequency, and Doppler spectral bandwidth in real–time.

The joint statistics of the microwave quantities indicative of breaking are used to investigate detection schemes for breaking events identified from the video recordings. The most successful scheme is based on thresholds in both the RCS and the Doppler bandwidth determined from joint distributions for breaking and non–breaking waves. Microwave events consisting of a sea spike in the RCS accompanied by a large bandwidth are associated with the steep forward face of waves in the early stages of breaking. The location of the illumination area with respect to the phase of the breaking wave, the stage of breaking development, and the orientation of an individual crest with respect to the antenna look–direction all influence the detectability of a breaking event occurring in the vicinity of the radar spot. Since sea spikes tend to occur on the forward face of waves in the process of breaking, the whitecap associated with a given sea spike may occur after the crest of the wave responsible for the sea spike has passed the center of the illumination area. Approximately 70% of the waves which produce whitecaps within a distance of 5m of the bore sight location are successfully identified by a threshold–based detection scheme utilizing both RCS and bandwidth information.

The sea spike statistics are investigated as functions of wave field parameters and friction velocity u^*. For VV and HH polarization, the frequency of sea spike occurrence and the sea spike contribution to the mean RCS show an approximately cubic dependence on u^*, which is consistent with theoretical modelling and various measures of whitecap coverage. The data also suggest that the average RCS of an individual sea spike is not dependent on u^*. At high friction velocities ($u^* \approx 40$–50cms^{-1}), the contribution of sea spikes to the mean RCS is in the range of 5–10% for VV and 10–20% for HH. The wind speed dependence of the percentage of crests producing sea spikes is comparable to that of the fraction of breaking crests reported by previous authors. The percentage of wave crests producing sea spikes is found to vary approximately as $(Re^*)^{1.5}$, where Re^* is a Reynolds number based on u^* and the dominant surface wavelength. This result agrees with measurements of the degree of wave breaking by previous authors and is shown to be consistent with a cubic dependence on u^*. Models for the probability of wave breaking as a function of moments of the wave height spectrum are compared to our results. The Doppler frequency and bandwidth measurements are also used to inquire into the kinematics of the breaking process.

ACKNOWLEDGEMENTS

I greatly appreciate the efforts of the many individuals who have assisted me in the research summarized in this thesis.

My thesis supervisor, Ken Melville, provided much of the direction, insight, and resources which made this work possible. I am grateful that my graduate career under his guidance has been a stimulating and rewarding endeavor. I thank my committee – Jim Evans, Hans Graber, Bill Keller, Jin Kong, and Bill Plant – for their professional support and encouragement. Bill Plant's comments on the rough draft of chapter 2 were very helpful. I am especially grateful to Bill Keller of the US Naval Research Laboratory. His assistance has been truly indispensable and his unfailing enthusiasm for his work, an inspiration. He generously supplied not only his unique scatterometer but also his invaluable experience of over two decades in the field of microwave measurements.

I thank Finn Hansen of Risø National Laboratory, Roskilde, Denmark for providing friction velocity measurements for both the North Sea and the SAXON experiments. The use of video equipment in the North Sea provided by Peter Lobemier of FWG, Kiel, West Germany was appreciated. I also extend thanks to the crew of the Forschungsplattform NORDSEE.

The measurement tasks in the SAXON experiment could not have been successfully managed without the help of several people. I thank Omar Shemdin for facilitating participation in the SAXON experiment, Les McCormick for field support, and the United States Coast Guard crew of the Chesapeake Light Tower. I also thank Ted Blanc for the loan of the infrared wave gauge and the two instrument booms. I appreciate the significant time that Mark Loewen took away from his own research to provide excellent assistance in the field. Francis Felizardo wrote the environmental data acquisition software and Cheech Wang built and tested the wire wave gauge array. Jack Crocker provided superior engineering design and construction for mounting the lower instrument boom. Ying–Keung Poon and Mark Newville helped in driving the equipment between Boston and Norfolk. Mark also provided accommodations and hospitality during my numerous trips to Washington, DC over the past 5 years.

I extend a warm thanks to all the friends I have made at the Parsons Laboratory at MIT, especially to Pat Dixon for always being able to arrange anything. The informal fluid dynamics laboratory on Friday afternoons was especially enjoyable.

My father, John M. Jessup, and my family have always supported and encouraged me to pursue my aspirations. I owe the greatest thanks to my wife, Heidi Powell, for her wholehearted support and unconditional belief in me. This thesis is dedicated to the memory of my mother, Catherine C. Jessup, known affectionately to her family and friends as Kate.

TABLE OF CONTENTS

cross–section $\sigma^o(t)$ for VV and HH polarization and mean Doppler frequency for VV. The jump in $\sigma^o(t)$ coincident with a Doppler frequency maximum is typical of those associated with breaking events.

tion velocity for VV (top) and HH (bottom) polarization. For $u^* \geq 23 \text{cms}^{-1}$, there is very little scatter in the data and the slope of the least square fit over this range is 1.1 for both polarizations, indicating an approximately linear dependence.

microwave data used in this thesis. The sonic anemometer data in the top graph are for wind directions falling in the range of suspected tower interference, while those of the lower graph are judged to be unaffected by the tower.

period (horizontal line in upper graph) for RUN 05: friction veloc‐ity, u^*, and wind speed reference to 10m, U_{10}, computed using bulk formula method, wind direction, WD, and significant wave height, SWH.

same number of events are counted in VV and HH polarization near −5dB.

age of breaking crests versus U_{10}, wind speed referenced to 10m.

LIST OF TABLES

INTRODUCTION

Deep–water wave breaking plays an important role in air–sea interaction, in surface wave dissipation, and in the generation of currents. Statistics on the frequency of breaking waves and their dependence on wind and wave conditions are needed to quantify the role of wave breaking in the upper ocean. Most attempts at field measurements of breaking waves have been subjective and qualitative because of the difficulty of unambiguously detecting and quantifying individual events.

Major applications of microwave remote sensing of the ocean include the measurement of wind speed or stress using scatterometry and the imaging of surface waves by synthetic aperture radar (SAR). A detailed understanding of microwave scattering from the sea surface is essential to the application of these increasingly important remote sensing techniques. Interpretation of SAR measurements depends on knowledge of the modulation of microwave return by ocean waves, while scatterometers rely on its wind speed dependence. Although a significant measure of success has been achieved in modelling microwave backscatter from the ocean, discrepancies between theory and experiment suggest that scattering mechanisms related to breaking waves may improve the models currently in use.

Radar measurements in both the field and laboratory have indicated that sharp–crested and breaking waves can significantly enhance active microwave scattering from the ocean. Microwave detectability of breaking waves would provide a tool with which to quantify the role of wave breaking in upper ocean dynamics. This thesis presents quantitative measurements of distinctive events in microwave backscatter from the ocean surface which are caused by breaking

waves.

The major objectives of this thesis are to

1) investigate the characteristics and the source of the microwave return from breaking waves,

2) determine if the microwave signature of breaking waves can be used to unambiguously identify individual breaking events,

3) compare the dependence on wind and wave conditions of the breaking events detected by microwave measurements with other measurements of wave breaking and with analytical modelling,

4) utilize microwave Doppler velocity measurements to inquire into the kinematics of the breaking process,

5) and quantify the contribution of microwave return from breaking waves to the mean radar cross-section of the sea surface.

1.1   MEASUREMENTS AND MODELLING OF WAVE BREAKING

Ocean waves are generated by the transfer of momentum from the atmosphere to the sea surface through pressure force and the frictional drag of the wind. Wind blowing over a quiescent sea will first generate ripples of very short wavelength. The dynamics of these small-scale waves, referred to as capillary waves, are dominated by surface tension. As the wind continues to blow and more waves are generated, energy is transferred through nonlinear interactions from the short waves to longer waves with larger amplitudes. The longer waves, governed by the restoring force of gravity, continue to grow until a so-called fully-developed sea is established. At this point, the growth of the surface displacement spectrum has reached an equilibrium where the input from the wind is balanced by the mechanisms of nonlinear wave-wave interaction and wave breaking.

The ocean surface can be modelled as a two-scale or composite surface

made up of short wind–generated ripples riding on top of long gravity waves. The gravity waves include ocean swell produced by storms a long distance from the measurement site and wind waves generated by the local wind blowing over an extended distance. The long waves range in wavelength from a few meters for the wind waves to over 200 meters for long period swell, while their phase speed is in the range of 5 to 20ms^{-1}. The actual fluid particle velocity of the long waves is slow compared to the phase speed and generally lies in the range of 1 to 2ms^{-1}. The wind–generated ripples include both short gravity waves and capillary waves, the latter responding rapidly to the local wind. The short waves have wavelengths of a few millimeters to tens of centimeters. The wind–generated ripples while being advected by the long waves, also travel relative to them with a phase speed of less than 1ms^{-1}.

The turbulent process of wave breaking is inherently nonlinear and is generally not amenable to analytical description. At breaking the surface fluid particle velocity at the crest is on the order of its phase speed. This produces an unstable condition in which the fluid particles at the crest outrun the form of the underlying wave itself, causing the crest to overturn and the wave to break.

Although the breaking process defies a simple formal definition, the phenomenon has been divided by type into spilling and plunging breakers (Longuet–Higgins and Turner, 1974). Plunging breakers are more energetic and are generally described by a curling crest which lunges ahead some distance into the forward slope of the wave. Spilling breakers evolve more slowly and are characterized by a quasi–steady whitecap of turbulent water which rides down the forward face. Longuet–Higgins and Turner (1974) proposed an 'entraining plume' model of a spilling breaker in which the whitecap is described as a mixture of

water and air which travels down the surface slope under the influence of gravity. Breaking waves in the open ocean are more commonly of the spilling rather than the plunging type. The scales associated with deep–water wave breaking range from short gravity–capillary waves spilling on the steep slopes of long waves to breaking by the crests of the long waves themselves.

A 'scatterometer's eye–view' of wave breaking in the open ocean is shown in the photograph of Figure 1.1, taken during the SAXON experiment (described in Chapter 3) from 26m above the sea surface on a stationary platform located in 12m of water. The photographs in Figures 1.2 through 1.4 illustrate some of the descriptive qualities of breaking waves in the open ocean. Figure 1.2 shows a turbulent whitecap extending laterally along the crest of an actively breaking wave. The example in Figure 1.3 illustrates the steepness associated with the forward face of breaking waves in the early stages of development. Finally, the side view of a breaking crest in Figure 1.4 shows the sharp, wedge–like geometry which sometimes characterizes breaking waves in a confused sea.

1.1.1 <u>WHITECAP COVERAGE</u>

Measurements of the fraction of surface area affected by breaking, referred to as the whitecap coverage (Monahan 1969, 1971; Monahan and O'Muirchaertaigh, 1986; Toba and Chaen, 1973) make up a large portion of previous field measurements of wave breaking. Wu (1979) argued that the whitecap coverage should vary cubically with friction velocity, u_*. The friction velocity is a measure of the stress exerted by the wind on the sea surface and is a function of the stability of the air–sea boundary as well as wind speed (see Appendix B).
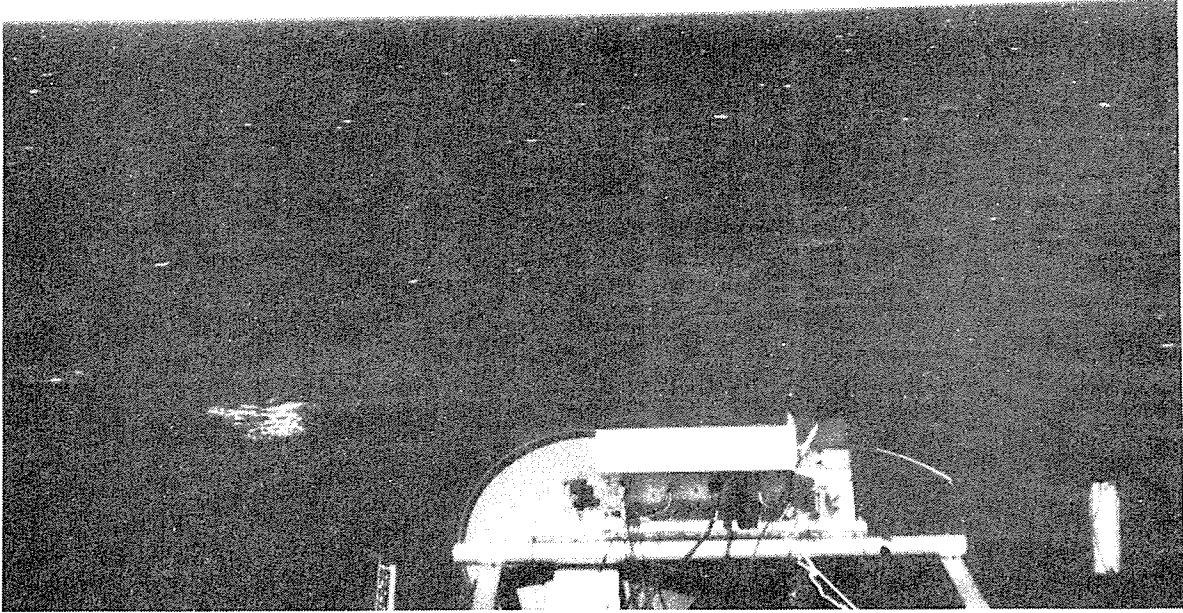
Figure 1.1: Photograph taken from the Chesapeake Light Tower during the SAXON experiment showing wave breaking in the open ocean.
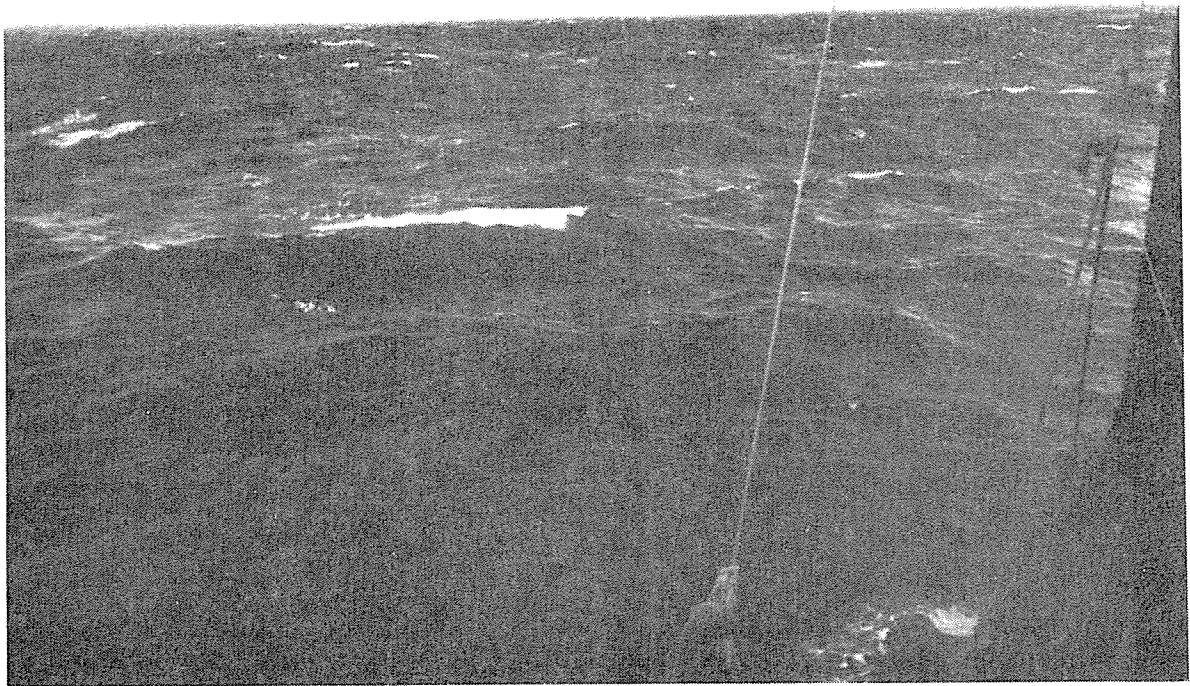
Figure 1.2: Photograph of a breaking wave with a turbulent whitecap extending laterally along the crest.
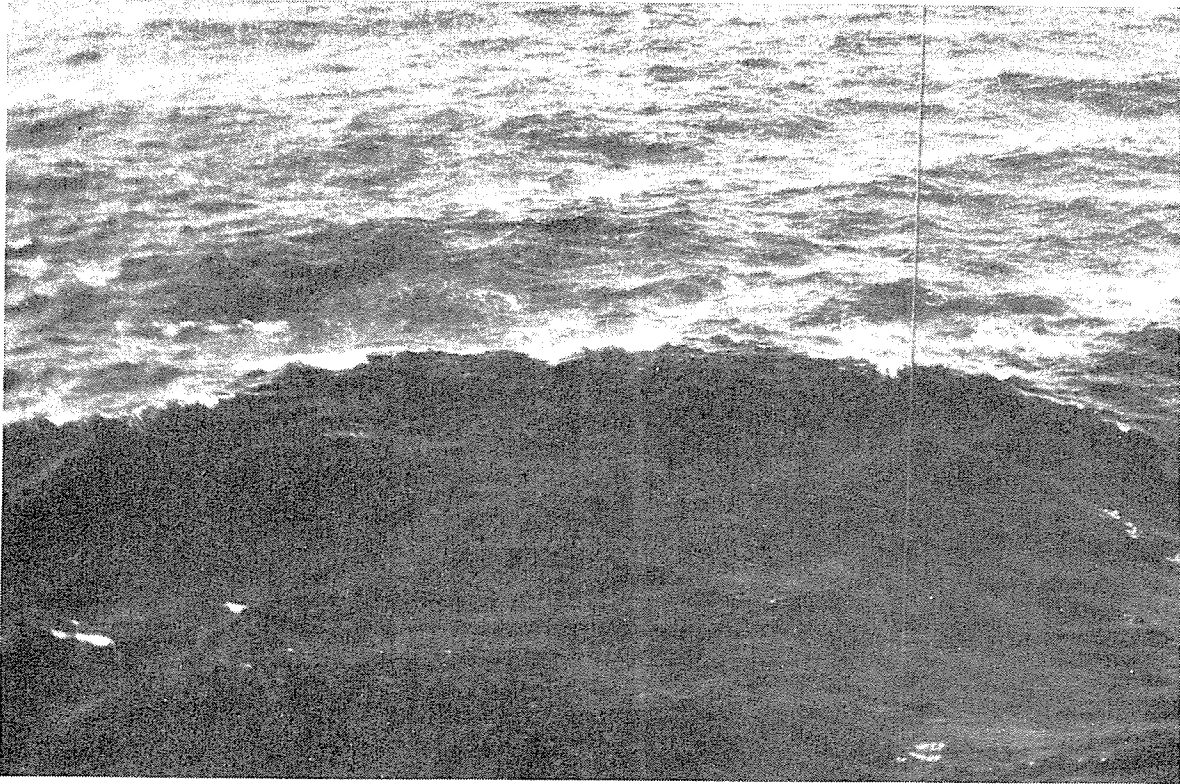
Figure 1.3: Photograph of a breaking wave in the early stages of development illustrating the extreme steepness which may occur on the forward face.
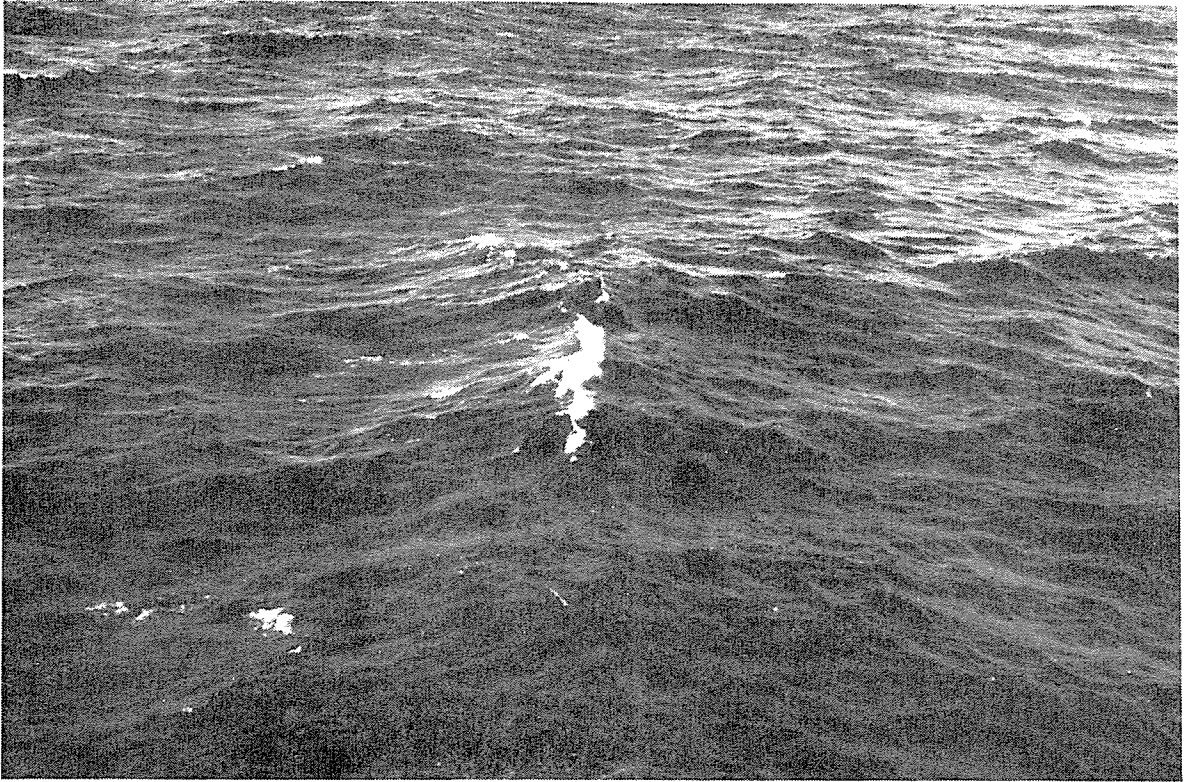
Figure 1.4: Photograph of a breaking crest showing the sharp, wedge–like geometry which sometimes characterizes breaking waves.

The expectation of a cubic dependence on u_* is based on a balance between the energy input from the wind and the energy dissipated by wave breaking. The argument assumes that the whitecap coverage, W, is proportional to the rate of energy input per unit surface area provided by the wind, $\dot{E}$. Wu (1979) states that this rate of energy input from the wind is equivalent to the rate of work done by the wind stress, τ, to produce the wind–induced surface drift current V. Since τ is proportional to u_*^2 and V has been observed to be proportional to u_* (Wu, 1975), the whitecap coverage is expected to be proportional to u_*^3:

$$W \propto \dot{E} = \tau V \propto u_*^3 \qquad (1.1)$$

Wu (1979) also gives the expected dependence on wind speed referenced to a height of 10m as

$$W \propto U_{10}^{3.75} \qquad (1.2)$$

which follows from equation (1.1) with $u_*^2 = C_D U_{10}^2$, which defines the drag coefficient, C_D, and the empirical relation $C_D \propto U_{10}^{1/2}$.

The value of a wind speed exponent for the variation of whitecap coverage has been the subject of a running debate, primarily between Monahan and Wu (most recently in Wu (1988), Monahan and Woolf (1989), and Wu(1989)). Monahan and O'Muirchaertaigh (1986) proposed the formula

$$VWC = 1.95 \times 10^{-5} \, U_{10}^{2.55} \exp\{ \, 0.0861 \, \Delta T \, \} \qquad (1.3)$$

for visual whitecap coverage, VWC, to describe the combined effect of wind speed and atmospheric stability as a function of wind speed referenced to 10m elevation, U_{10}, and the air–sea temperature difference, $\Delta T = T_s - T_a$, where T_s and T_a are the sea and air temperature, respectively.

Wu's (1988) point that stability effects should be accounted for by using u_* to characterize whitecap coverage rather U_{10} and ΔT separately is well taken. On the other hand, Monahan and O'Muirchaertaigh (1986) note that it is the rate of whitecap area formation and not the whitecap coverage which would be proportional to the energy input from the wind (due to the persistence of whitecap foam). Furthermore, Wu's assertion that the whitecap coverage exhibits a wind speed exponent of 3.75 is inconsistent with his championing of u_*^3 behavior, since the drag coefficient used to arrive at a value of 3.75 does not include stability effects.

Finally, neither author provides confidence limits nor correlation coefficients for the exponents computed using various curve fitting techniques. The scatter in whitecap coverage data, unavoidable experimental errors, and the subjective nature of visual observations suggest that differences in wind speed exponents quoted to two decimal places are not especially significant. A reasonable conclusion might be that large wind speed and friction velocity exponents computed for whitecap coverage are consistent with theoretical modelling, which indicates a cubic friction velocity dependence for the input of energy from the atmosphere to the ocean.

1.1.2 PERCENTAGE OF BREAKING CRESTS

Another measure of wave breaking is the percentage of breaking crests passing a fixed point. Figure 1.5 shows the fraction of breaking crest as a
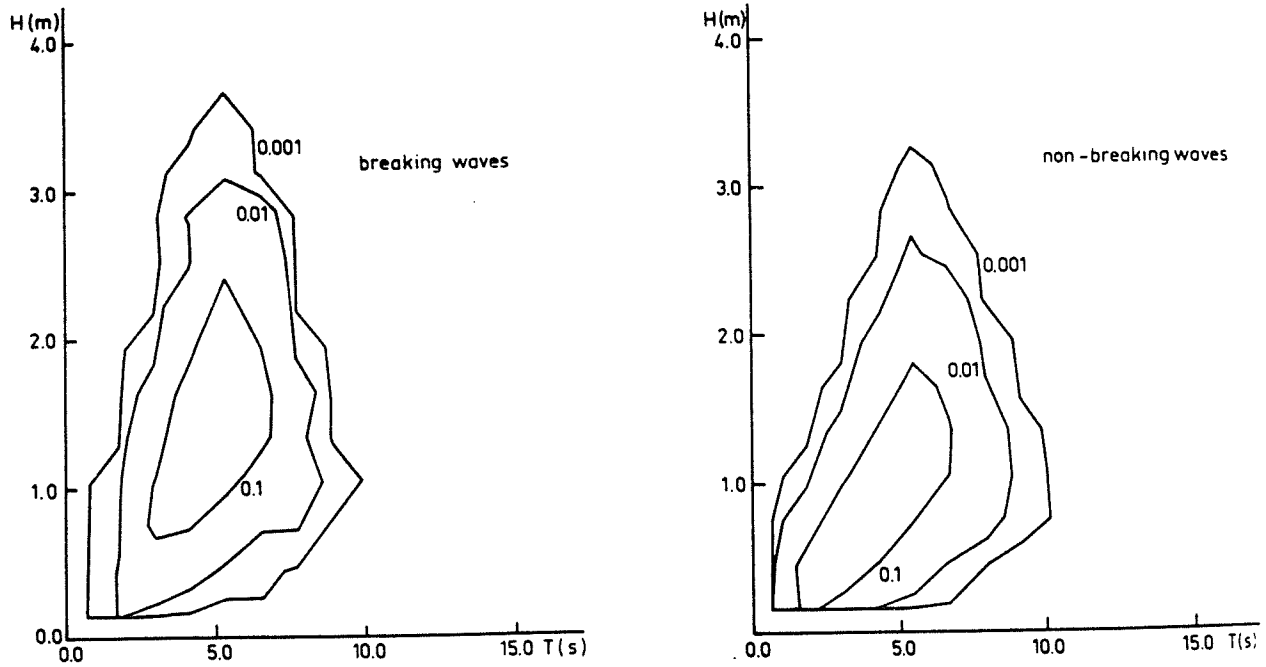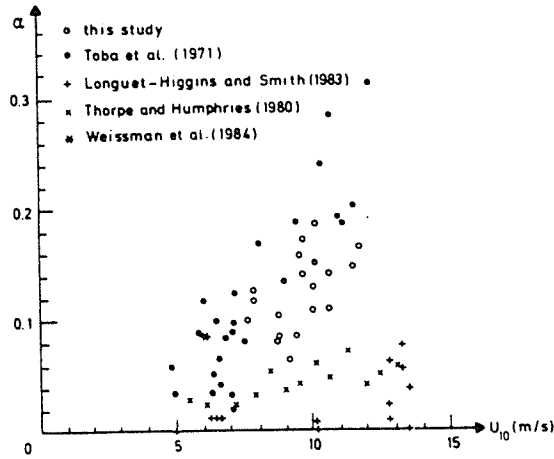
Figure 1.5: (Top) Fraction of breaking crests α vs. wind speed U_{10} for several studies based on point measurements of breaking (from Holthuijsen and Herbers, 1986).

Figure 1.6: (Bottom) Joint probability density functions of wave height H and wave period T for breaking and non—breaking waves. Note that significant overlap indicates the failure of breaking criteria based on surface displacement measurements alone (from Holthuijsen and Herbers, 1986).

function of U_{10} for studies based on point measurements of breaking. There is relatively good agreements between Holthuijsen and Herbers (1986) and Toba et al. (1971), who used similar techniques. Holthuijsen and Herbers (1986) concluded that surface displacement measurements fail to unambiguously detect individual breaking waves, as indicated in Figure 1.6 by the joint probability density functions of wave height H and period T for breaking and non–breaking waves. More limited results have been reported in studies which used direct measurements of surface displacement to detect breaking events. Longuet–Higgins and Smith (1983) and Thorpe and Humphries (1980) used wire wave gauges to detect abrupt changes in surface elevation attributed to breaking waves. Weissman, Atakturk, and Katsaros (1984) correlated increases in the energy of high frequency waves with visual observations of breaking.

1.2 DEPENDENCE OF WAVE BREAKING ON WAVE CONDITIONS

1.2.1 ROUGHNESS REYNOLDS NUMBER Re*

Casual observation of the development of wind–generated waves on previously calm water indicates that the local wind stress can dominate small– to intermediate–scale breaking. However, in addition to the action of the wind, wave breaking can result from wave interactions which are independent of the wind. The random phase of large–scale ocean waves propagating in different directions can lead to constructive interference resulting in unstable crests which ultimately break. Furthermore, these two general types of breaking can occur in concert, leading to wave breaking over a wide range of scales.

Toba and colleagues (Toba and Kunishi, 1970; Toba, 1972; Toba and Chaen,

1973) have proposed that the dependence of wave breaking on the combined effects of wind stress and wave conditions can be described by a dimensionless variable which resembles a Reynolds number:

$$Re^* = \frac{u_* \, L}{\nu},\tag{1.4}$$

where L is a length scale characteristic of the sea surface (eg., the wavelength corresponding to the peak frequency of the surface displacement spectrum) and ν is the kinematic viscosity of air. The formulation is based on a macroscopic approach to the momentum balance at the air–sea interface (Toba, 1972) and supported by field measurements of whitecap coverage (Toba and Chaen, 1973) and wind tunnel measurements of the percentage of breaking crests (Toba and Kunishi, 1970).

Addressing the combined effect of wind and wave conditions on breaking was motivated by the observed dependence of the drag coefficient, C_D, on sea state as well as wind speed (Toba and Kunishi, 1970). Figure 1.7 shows the drag coefficient (referenced to 10m height, $\gamma_{10}^2 = C_D$) plotted against $Re_2^* = u_* H/\nu$ (a Reynolds number related to Re* by Toba, 1972), where H is a characteristic wave height scale. The sharp increase of the drag coefficient at approximately $Re_2^* = 10^3$ coincides with the beginning of air entrainment by breaking. The implication is that the increased momentum transferred from the air to the water in the process of breaking is directly reflected in this increase in the drag coefficient.

The theoretical basis for the dependence of wave breaking on Re* is a local balance which determines the transfer of momentum and mechanical energy from
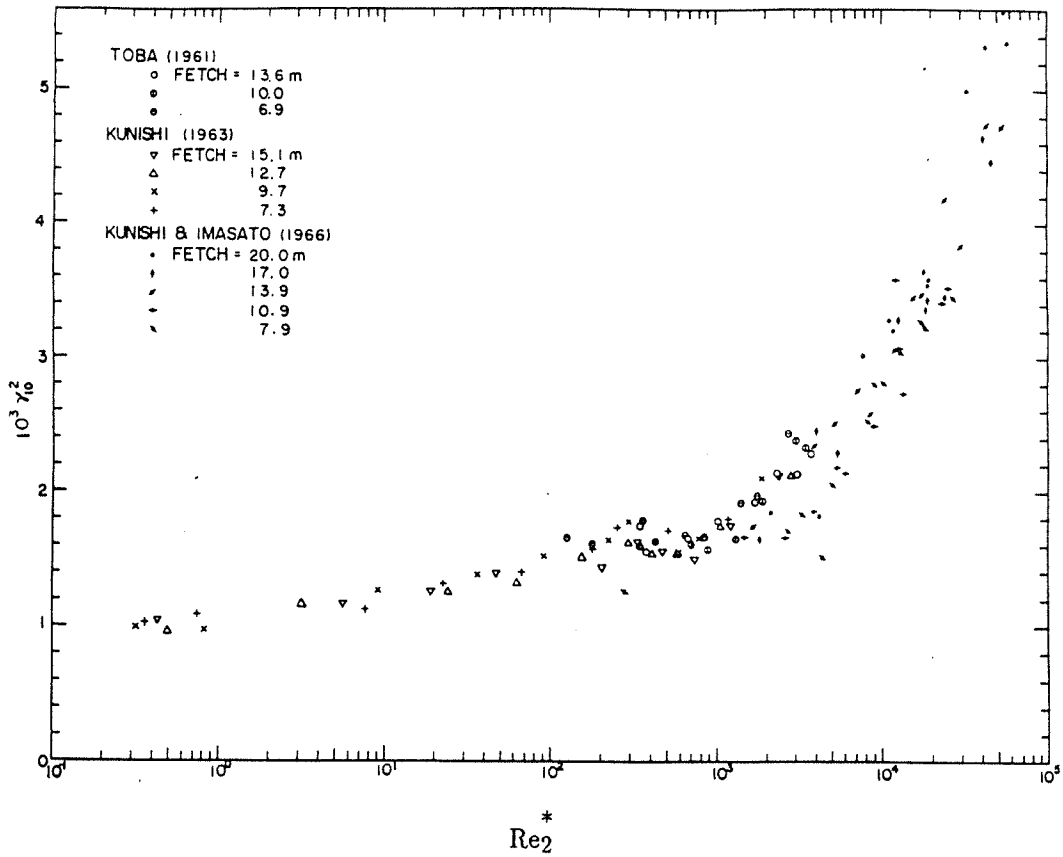
Figure 1.7: Laboratory measurements of drag coefficient $\gamma^2_{10}(=C_d)$ vs. Re^*_2 showing a sharp increase at approximately $Re^*_2 = 10^3$ coinciding with the onset of breaking (from Toba and Kunishi, 1970).

the atmosphere to the ocean. Toba (1972) asserts that, under equilibrium conditions, the dissipation of energy by breaking must equal the energy input from the wind. Furthermore, the energy dissipation process is envisioned as a cascade from the large–scale turbulence of breaking to final dissipation at small scales by molecular viscosity. Following Toba's notation, let r be the ratio of the wind stress supported by the waves to the total wind stress τ. The wind stress is related to the friction velocity, u_*, by

$$\tau = \rho u_*^2, \tag{1.5}$$

where ρ is the air density. The average horizontal surface velocity due to the orbital motion of the wind waves is referred to as the Stokes' drift. Toba (1972) argues that the rate of work done by the wind on the waves is given by the product of the wind stress supported by the waves, $r\tau$, and the Stokes' drift, u_0:

$$r\tau u_0. \tag{1.6}$$

Using dimensional analysis, Toba (1972) concludes that u_0 is proportional to u_* and thus the energy input from the wind to the waves can be expressed as

$$r'u_*^3, \tag{1.7}$$

by dividing (1.6) by ρ and combining into r' the ratio r and the proportionality constant between V and u_*. Toba represents the rate of energy dissipation by molecular viscosity as

$$\int_{0}^{Z} \mu\ \overline{D}\ dz \qquad\qquad (1.8)$$

where μ is the dynamic viscosity of water, $\overline{D}$ behaves like the squared magnitude of the velocity gradient, $(\partial u/\partial z)^2$, and Z is the depth over which the dissipation occurs. Dividing (1.8) by ρ and using the variables u_*, L, and ν for scaling, a variable which scales as the rate of energy dissipation due to molecular viscosity is $\nu u_*^2/L$. Then the overall process of energy dissipation due to wave breaking can be characterized by the dimensionless ratio of the scaling parameters for the input from the wind, equation (1.7), to that of the dissipation by viscosity, resulting in $Re^*=u_*L/\nu$.

Figure 1.8 shows field results reported by Toba and Chaen (1973) of the percentage of whitecap coverage as a function of Re^*. For values of $Re^*>4\times10^4$, a straight line fit with slope 1.5 was proposed and a value of $Re^*= 2\times10^4$ was given as the onset of breaking. Figure 1.9 shows wind tunnel results from Toba and Kunishi (1970) for the fraction of breaking crests as a function of Re^* on a linear–log plot, indicating the onset of breaking at $Re^* > 3\times10^3$ and from which an exponent of 1.4 has been estimated.

A relationship between the parameter Re_* and u_* can be found by applying the fetch dependent scaling relations suggested by Kitaigorodskii (1970). A variety of field measurements, summarized by Phillips (1980), suggest that the dimensionless frequency of the spectral peak, $\omega_0 u_*/g$, is related to the dimensionless fetch, xg/u_*^2, by:
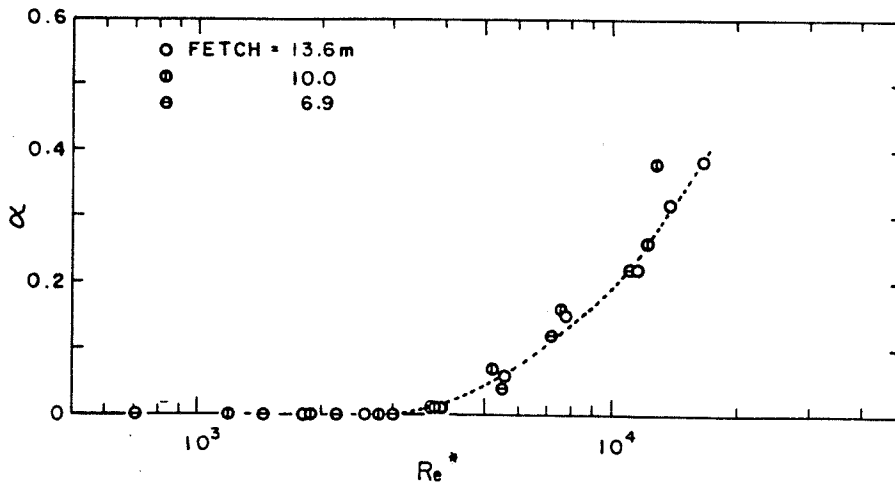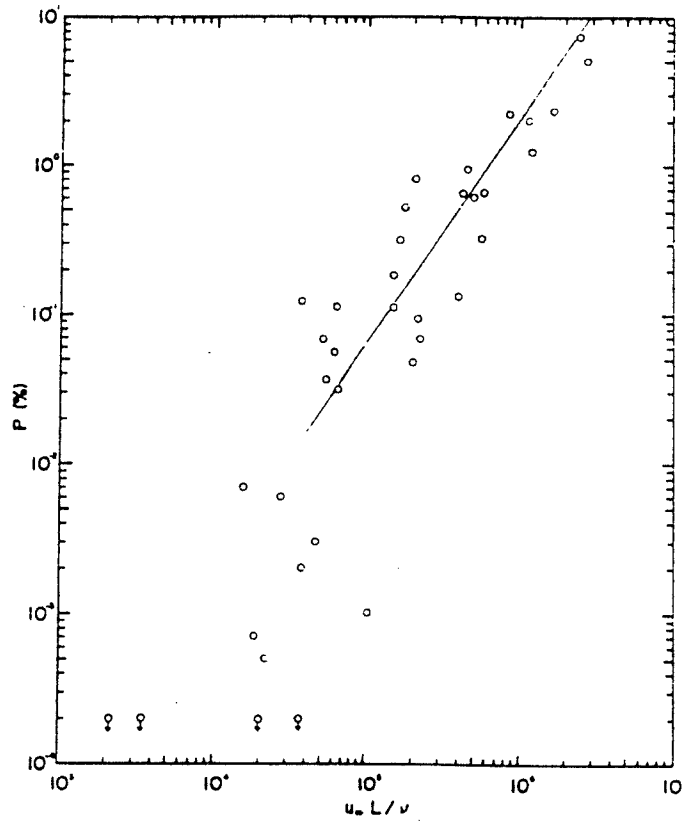
Figure 1.8: (Top) Field measurements of percentage of whitecap coverage vs Re*. Slope of straight line fit shown on log–log plot is 1.5 (from Toba and Chaen, 1973).

Figure 1.9: (Bottom) Wind tunnel measurements of fraction of breaking crests vs Re*. Data exhibit approximately $Re^{*1.4}$ dependence for $Re^* > 3 \times 10^3$ (from Toba and Kunishi, 1970).

$$\frac{\omega_0 u_*}{g} \approx 2.2 \quad \left(\frac{x\,g}{u_*^2}\right)^{-\frac{1}{4}}. \tag{1.9}$$

The deep–water dispersion relation is

$$\omega^2 = gk, \tag{1.10}$$

where $k = 2\pi\lambda$ is the surface wavenumber for the wavelength λ. If the wavelength λ_0 corresponding to the peak frequency of the surface displacement spectrum is given through the dispersion relation as

$$\lambda_0 = \frac{2\,\pi\,g}{\omega_0^2} \tag{1.11}$$

then, as noted by Phillips (1980), the expression (1.9) becomes

$$\frac{x}{\lambda_0} \approx 0.8 \quad \left(\frac{x\,g}{u_*^2}\right)^{\frac{1}{2}}. \tag{1.12}$$

Rearranging (1.12) indicates that the characteristic wavelength λ_0 is proportional to the friction velocity u_*:

$$\lambda_0 \approx 0.8 \quad \left(\frac{x}{g}\right)^{\frac{1}{2}} u_*. \tag{1.13}$$

If the characteristic wavelength λ_0 is used for the length scale L in expression

(1.4), the Reynolds number Re* is proportional to u_*^2. Thus the Re*-exponent

of 1.5 for the fraction of breaking crests estimated from Figure 1.5 is consistent

with the cubic friction velocity dependence of other measures of wave breaking

such as whitecap coverage. Note that a Re* based on λ_0 in equation (1.13)

incorporates the friction velocity and fetch dependence into a single parameter.

1.2.2 STATISTICAL MODELS FOR THE PROBABILITY OF WAVE BREAKING

Several authors have recently developed quantitative expressions for the

probability of wave breaking in terms of integral properties of the surface

displacement spectrum (Ochi and Tsai, 1983; Snyder and Kennedy, 1983;

Glazman, 1986; Srokoz, 1986, Glazman and Weichman, 1989). These formulations

have a common statistical basis in the results of Cartwright and Longuet–Higgins

(1956) concerning the distribution of maxima of a random function, which were an

application to ocean waves of the works by Rice (1944, 1945) on the analysis of

random electrical noise. The physical basis of these models is the idea that a

wave crest will break when it exceeds a threshold criterion based on its local

slope or (equivalently for deep–water waves) its downward vertical acceleration.

The models have several drawbacks, not least among them is that the threshold

criterion for breaking results from the application of linear wave theory to

describe the breaking process. Furthermore, they all consider the sea surface as a

stationary and homogeneous Gaussian process. These assumptions can be

tolerated if the models provide relatively good agreement with observation. A

more serious concern is the difficulty introduced by the theoretically indeterminate

nature of the variance of the vertical acceleration of the sea surface, on which

each formulation relies. Nonetheless, the models do address the wave spectral

dependence of breaking and their simple analytical formulas are easily tested.

The idea that a wave will break when its downward acceleration exceeds a specific threshold is based on the theoretical result that the acceleration near the crest of a Stokes' wave of maximum height is $-g/2$ (Stokes, 1880; Longuet–Higgins, 1962), where g is the gravitational acceleration. The alternative formulation in terms of a steepness threshold has its basis in Michell's (1893) result that waves will break when their height exceeds a specific percentage of the Stokes' limiting wavelength. The equivalence of a criterion on the slope and on the vertical acceleration for deep–water waves is shown by considering the surface displacement $\eta(x,t)$ for a linear, one–dimensional, progressive wave with wavenumber k and radian frequency ω:

$$\eta(x,t) \; = \; A \; \exp\{j(kx-\omega t)\}. \tag{1.14}$$

The squared magnitude of the local slope is,

$$\left|\frac{\partial \eta}{\partial x}\right|^2 \; = \; (kA)^2 \tag{1.15}$$

while that of the non–dimensional vertical acceleration is given by

$$\frac{1}{g^2} \left|\frac{\partial^2 \eta}{\partial t^2}\right|^2 \; = \; \left[\frac{\omega^2 A}{g}\right]^2 . \tag{1.16}$$

Applying the deep–water dispersion relation, equation (1.10), shows that the slope and non–dimensional vertical acceleration are equivalent:

$$\left|\frac{\partial \eta}{\partial x}\right|^2 = \frac{1}{g^2} \left|\frac{\partial^2 \eta}{\partial t^2}\right|^2 \tag{1.17}$$

The criterion based on the Stokes limiting wave is derived for a sea of regular waves, though laboratory experiments indicate that steep regular waves break before this limit (Van Dorn and Pazan, 1975). A lower threshold than that implied by the Stokes' limit has also been indicated for irregular waves generated in the laboratory (Ochi and Tsai (1983)).

For a random sea, an integrated measure of steepness based on the surface displacement spectrum $S(\omega)$ is given by the mean square slope

$$s^2 = \int k^2 \, S(\omega) \, d\omega \tag{1.18}$$

and that of the vertical acceleration is given by the fourth moment of $S(\omega)$,

$$m_4 = \frac{1}{g^2} \int \omega^4 \, S(\omega) \, d\omega. \tag{1.19}$$

This high order moment provides the spectral dependence used by the statistical models for the probability for breaking. A principal difficulty with the evaluation of (1.19) is that both the theoretical and observed dependence of $S(\omega)$ at higher frequency is such that the integral does not converge. Phillips' (1977) development of the theory of the equilibrium range of wind waves predicts that $S(\omega)$ varies as ω^{-5} for higher frequencies away from the spectral peak. Although this behavior was supported by observation, more recent modelling and evidence

suggest that an ω^{-4} dependence may be more appropriate (Phillips, 1985).

In either case, the behavior of the displacement spectrum $S(\omega)$ at higher frequencies requires some artifice which permits evaluation of the integral defining the fourth moment m_4. Some authors have chosen to introduce a cutoff frequency ω_c (Snyder and Kennedy, 1983; Srokosz, 1986), while Glazman(1986) suggests 'partial averaging' (essentially forcing convergence by filtering out higher frequencies) and Ochi and Tsai (1983) do not indicate how they address this problem. Ironically, the models acknowledge the importance of higher frequencies in the breaking process, but must limit their inclusion in order to obtain a useful result.

A cutoff frequency, ω_c, implies a minimum length scale of $L_s = g/(2\pi \omega_c^2)$ through the dispersion relation (1.10). In the context of measurements, the cutoff frequency may be the highest resolvable frequency determined by the limiting wavelength which a measuring device can resolve. However, this minimum length scale may not correspond to that which is relevant to the breaking process itself. The practical requirement of specifying a cutoff frequency combined with the uncertainty in the threshold values on slope or acceleration introduce an unpleasant ambiguity in comparing the models with actual measurements. Nonetheless, by recognizing the artificial nature of a given combination of threshold and cutoff frequency, the functional dependence of the probability of breaking on the fourth moment of the surface displacement spectrum can still be investigated.

The formulation for the spectral dependence of the probability of wave breaking most appropriate to microwave detection is that of Srokosz (1986), which expresses the probability B that a breaking crest will occur at a given point on

the surface (or equivalently the fraction of breaking crests) as a simple function of the fourth moment of $S(\omega)$ and the downward acceleration threshold αg:

$$B = \exp\left\{-\frac{\alpha^2 \, g^2}{2 \, m_4^2}\right\}. \qquad (1.20)$$

As noted by Srokosz (1986), his model reproduces the results of Ochi and Tsai (1983) and their approaches are essentially equivalent; his criterion on the vertical acceleration can be transformed into their steepness criterion and both approaches have the same theoretical origins. Equation (1.20) is derived by integration of the expression from Cartwright and Longuet–Higgins (1956) for the probability distribution function for local maxima by restricting the limits of integration to include only those crests with a downward acceleration greater than αg. The results of both Snyder and Kennedy (1983) and Glazman (1986) are in terms of the fractional area of the sea surface covered by breaking, which is less appropriate to the microwave measurement techniques employed in this thesis. Figure 1.10 shows the probability of breaking B given by equation (1.20) as a function of the dimensionless fourth moment $m_4 g^{-2}$ for threshold values of $\alpha=0.4$ (solid line) and $\alpha=0.5$ (dashed line), indicating the sensitivity of the results to the threshold criterion.

Kennedy and Snyder (1983) estimated values of α from simultaneous measurements of directional spectra and whitecap coverage during the BOMEX experiment. They found that α ranged from 0.52 to 0.40 for a range of wind speeds from 5 to 10 ms^{-1}, suggesting a decrease with increasing wind speed. However, they do not indicate the wave spectrum cutoff frequency used in this
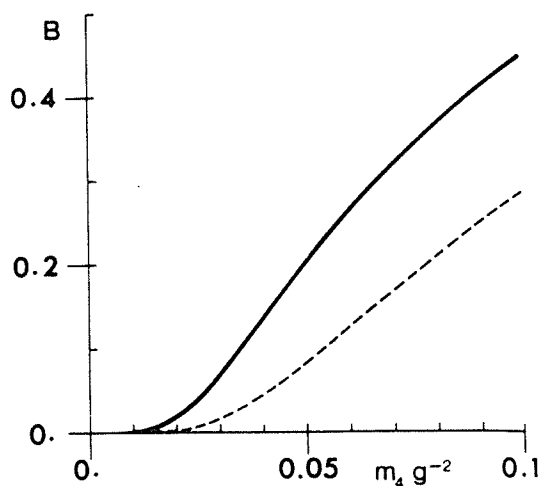
Figure 1.10: Probability B (expression 1.19) of a breaking crest occurring vs the dimensionless fourth moment of the surface displacement spectrum $m_4 g^{-2}$. The solid line is for the parameter $\alpha = 0.4$ while the dashed line is for $\alpha=0.5$ (from Srokoz, 1983).
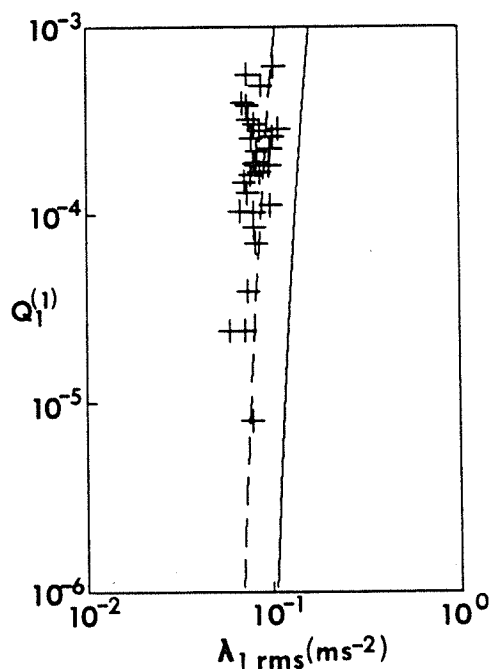
Figure 1.11: Probability of breaking $Q_1(1)$ vs rms partial acceleration λ_1^{rms}. Field measurements are indicated by crosses while solid line is model result with $\alpha=0.5$ and wave spectral cutoff frequency $\omega_c=2\omega_p$, where ω_p is the peak frequency. Dashed line is model result with $\alpha=0.5$ and wave spectrum extended to $\omega_c=5\omega_p$ (from Snyder, Smith and Kennedy, 1983).

analysis. Snyder, Smith and Kennedy (1983) concluded that a value of $\alpha=0.5$ gave good agreement with their field experiments and with the theoretical model of Snyder and Kennedy (1983). However, this conclusion appears to be ambiguous because of the manner in which the cutoff frequency was utilized in the computation of the vertical acceleration. Figure 1.11 shows their measured probability of breaking, $Q_1(1)$, as a function of what they term the rms partial acceleration, λ_1^{rms}. This acceleration is equivalent to the square root of the fourth moment m_4 with a cutoff frequency $\omega_c = N\omega_p$ with $N=2$, where ω_p is the radian frequency of the peak of the displacement spectrum $S(\omega)$. The solid line in Figure 1.11 corresponds to their model results with a threshold level of $\alpha=0.5$ and using the same cutoff frequency of twice the spectral peak frequency. The value of $N=2$ was used in computing the vertical acceleration because this was the practical limit of their surface displacement measurements. From the data listed by Kennedy and Snyder (1983) in their Table 2, the cutoff frequency with $N=2$ ranged from 4.04 to 5.30 rads^{-1} (0.64 to 0.84 Hz). The dashed line in Figure 1.11 is the basis for their assertion that a value of $\alpha=0.5$ is consistent with their measurements, but the manner in which this line was deemed appropriate is somewhat contrived. The dashed line corresponds to their model results with a cutoff frequency of $N=5$ times the spectral peak, computed by assuming that the (unmeasured) part of the frequency spectrum from $\omega_c = 2\omega_p$ to $\omega_c = 5\omega_p$ is consistent with modelling by Kennedy (1978). The choice of $N=5$ was based on a comparison of the computed probability of the partial acceleration field with experimental estimates from measurements of only two individual breaking events (see Figures 7 to 9 in Snyder et al., 1983). Thus their conclusion that $\alpha=0.5$ is an appropriate threshold for the integrated mean square acceleration is based on

very limited measurements which the authors themselves describe cautiously as 'somewhat indirect evidence.' All of these models rely on the two relatively arbitrary parameters of a threshold coefficient α and a cutoff frequency ω_c. Thus any comparison between theory and experiment should be interpreted with these limitations in mind.

1.3 PREVIOUS MICROWAVE MEASUREMENTS OF WAVE BREAKING

Evidence from over two decades of research indicates that breaking waves can significantly contribute to microwave backscatter from the sea surface. A brief review of this rich history is presented here as a guide to the literature of wave breaking and microwave remote sensing. A more detailed review is given in Jessup (1988).

Radar backscatter from the ocean surface has been analyzed in terms of electromagnetic wave theory applied to statistically rough surfaces. Useful analytical results have been obtained from models based on the methods of geometrical and physical optics combined with perturbation theory (Valenzuela, 1978). The radar return is typically characterized by the normalized radar cross–section, σ^0, which is proportional to the received power averaged over the illumination area (see Appendix A). In general it is a function of incidence angle, polarization, and frequency. The variation of the radar cross–section with incidence angle may be divided into three regimes. Near vertical incidence, or nadir, the scattering is modelled by specular reflection from facets tangent to the surface. At moderate incidence angles, the resonant mechanism known as Bragg scattering dominates the return. As grazing incidence is approached, other scattering mechanisms such as shadowing and wedge diffraction by wave crests

can become important.

1.3.1 BRAGG RESONANT SCATTERING

For angles of incidence between approximately 20 and 80 degrees, Bragg resonant scattering occurs when individual components of the surface roughness spectrum match the radar wavelength, causing coherent addition of the scattered electromagnetic waves. For slightly rough surfaces, (that is, when the surface roughness height is small compared to the radar wavelength) the backscattering cross–section is described by the small perturbation model and is proportional to the amplitude of the wave satisfying the Bragg resonant condition (Rice, 1951):

$$k = 2\kappa \sin\theta \qquad (1.21)$$

where k is the surface wavenumber, κ is the radar wavenumber and θ is the angle of incidence measured between the surface normal and the radar look–direction. In the small perturbation model, the cross–section for horizontal polarization is less than that for vertical. Thus the ratio of the vertically polarized cross–section to the horizontally polarized cross–section, known as the polarization ratio, is always greater than unity. This is in contrast to the specular point model for scattering near nadir, in which there is no polarization dependence and the polarization ratio is equal to unity. The polarization ratio is often used as a parameter for classifying the amount of specular reflection from a composite or two–scale rough surface (Barrick and Peake, 1968).

For radar wavelengths on the order of a few centimeters, the resonant scatterers are short wind ripples which ride on top of long gravity waves, and a

composite model is used to describe the two–scale nature of the sea surface (Wright, 1968). In essence, the presence of the long waves changes the local incidence angle of the slightly rough surface treated by the small perturbation model. Ocean measurements in the centimeter–range of radar wavelengths indicate that the composite model generally predicts the radar cross–section for vertical polarization. However, the composite model significantly under predicts the horizontally polarized return (Guinard et al., 1971, Donelan and Pierson, 1987). The discrepancy, which increases with incidence angle, is also indicated by the observed ocean polarization ratio being smaller than its predicted value (Wright, 1968). This behavior suggests that additional scattering mechanisms may be important for horizontal polarization at moderate to large incidence angle.

1.3.2 DOPPLER SPECTRUM CHARACTERISTICS

Information about the ocean surface is also contained in the Doppler spectrum of the radar return. Crombie's (1955) original conclusion that resonant scatter occurred in the return from ocean waves was based on the finding that the scatterers moved at the speed of gravity waves satisfying the Bragg condition. To first order, the Doppler shift produced is equal to the frequency of the surface wave responsible for the Bragg resonant scatter (Barrick, 1972). Bass et al. (1968) found that the spectrum width and centroid frequency depended on sea roughness. Pidgeon (1968) reported larger mean Doppler shifts for horizontally polarized return over that for vertical polarization. First–order models of the Doppler spectrum predict a larger mean Doppler shift for horizontal polarization, but they still under predict observations (Valenzuela and Laing, 1970; Hasselmann and Schieler, 1970).

Wright and Keller (1971) reported that the Doppler bandwidth is proportional to wind speed at fixed fetch in wave tank experiments. Duncan et al. (1974) extended these measurements and found that the Doppler bandwidth was only partly accounted for by the particle velocity of the dominant wave. A system of free and bound scatterers was proposed to explain the unexpected nature of their results. The free scatterers are the Bragg resonant wind ripples, which have a mean wave speed different from that of the dominant wave. The bound scatterers travel at or near the phase speed of the dominant waves and at high wind speeds are associated with breaking.

Grazing incidence measurements of sea spikes and Doppler spectra do not necessarily extend to moderate incidence angles. However, a number of results near grazing incidence have indicated that scattering from sharp–crested and breaking waves should be considered to account for discrepancies between models and observations at incidence angles away from grazing. The grazing incidence measurements of Pidgeon (1968) and Mel'nichuk and Chernikov (1971) were recently reconsidered by Trizna (1985), who interpreted them in terms of the mechanisms responsible for the Doppler shift. For vertical polarization measurements, his model predicted the spectral peak to within experimental error. However, an additional scatterer velocity was present for horizontal polarization. He speculated that a wedge type of scatter from near–breaking wave crests may be important for horizontally polarized scatter at grazing incidence.

The spiky nature of radar return at low grazing angles has long been associated with sharp–crested and breaking waves (Katzin, 1957; Long, 1974, 1983; Kalmykov and Pustovoytenko, 1976; Lewis and Olin, 1980; Ewell et al, 1984). Spiky–like fluctuations are more prominent for horizontal polarization and may be

due to specular reflections from facets (Long, 1983). Lewis and Olin (1980) used simultaneous video recordings to conclude that high amplitude sea spikes are associated with the development and decay of whitecaps. Ewell et al. (1984) presented measurements in which sea spikes were tracked in range and azimuth. They showed that the sea spikes moved with a speed approximately equal to the phase speed of the dominant ocean waves. Wetzel (1981) used a plume model of a breaking wave (Longuet–Higgins and Turner, 1974) to investigate the relative importance of wedges, spilling breakers, and surface roughness to radar return near grazing incidence. The model emphasizes return from the hydraulic jump–like 'toe' of a spilling breaker. The results were cautiously interpreted and the need for a morphology of an evolving breaker was emphasized.

1.3.3 <u>WAVE TANK STUDIES</u>

The wave tank studies by Duncan et al. (1974) and Lee (1978) have also found that theoretically computed polarization ratios are much larger than measured values. Duncan et al. observed scattering due to wave breaking which was independent of polarization and was a major contributor to the return at high winds. They also reported significant variability in both the magnitude and bandwidth of the Doppler spectrum in the presence of breaking.

Kwoh and Lake (1981) presented a laboratory study of the relative contributions to X–band radar return from mechanically generated water waves due to specular and nonspecular reflections. The specular reflections were attributed to either the turbulent wake of breaking or the steep capillaries generated in the process. The polarization ratio of these events was very close to unity and they speculate that such events may be responsible for the ocean

polarization ratio being smaller than predicted by perturbation theory. The nonspecular contribution to the backscattered power was attributed to wedge–like diffraction from the small radius crests of breaking or near breaking waves. More recently, Kwoh, Lake, and Rungaldier (1988) reported on field measurements of microwave return from breaking events generated by interactions between surface and internal waves. They found evidence to support the association of specular–type return with wave breaking.

Another set of laboratory measurements that is relevant to scattering from breaking waves is that of Banner and Fooks (1985). They made X–band radar measurements of stationary small–scale breaking waves generated in a flume. Like Kwoh and Lake, they found high levels of backscattered power were associated with the breaking region. However, Banner and Fooks concluded that the measured backscatter was consistent with Bragg scattering from hydrodynamic disturbances generated just ahead of the breaking crest. They also suggest that the bound scatterers associated with the phase speed of the dominant wave proposed by Duncan et al. (1974) may correspond to these hydrodynamic disturbances.

1.3.4 IMPLICATIONS FOR SYNTHETIC APERTURE RADAR (SAR)

The short gravity–capillary waves that are the Bragg scatterers for radar wavelengths in the centimeter range are modulated in amplitude and advected by the long waves upon which they ride. These hydrodynamic modulations are manifested in the backscattered power as modulations in both amplitude and frequency. The modulation transfer function (MTF) is used to quantify these and other effects such as tilt modulation which are relevant to the imaging of ocean

surface waves by Synthetic Aperture Radar (SAR). The MTF is defined by a linear or weak modulation theory in which the change in the radar cross–section is assumed to be proportional to the amplitude of the long waves (Keller and Wright, 1975; Alpers and Hasselmann, 1978). This linear modulation model predicts a modulation transfer function on the same order as that observed for low to moderate sea states (Alpers and Jones, 1978; Wright et al., 1980). However, field observations suggest that there exists another source of modulation other than that of the straining of the short waves by long waves (Plant et al., 1978, Wright et al., 1980). Banner and Fooks (1985) suggest that one source for these elevated modulation levels is the modulation of small–scale breaking events occurring near the crests of the long waves.

Extensive streaking in SAR images of ocean waves was attributed to wave breaking be Lyzenga and Shuchman (1983). The features were attributed to degraded azimuthal resolution associated with localized scatterer coherence times of order 10^{-2} s. The coherence time relevant to azimuthal image degradation in SAR corresponds to the reciprocal of the Doppler spectral bandwidth (Alpers, Rufenach, and Cross, 1981). When the coherence time is small compared to the image integration time, the image is smeared and the azimuthal resolution is approximately proportional to the inverse of the coherence time (Lyzenga and Shuchman, 1983).

1.3.5 MODELLING OF BACKSCATTER FROM BREAKING WAVES

There is mounting evidence that wave breaking can make a significant contribution to radar backscatter at moderate incidence angles. Field observations of breaking waves were reported by Keller et al. (1981) in which Doppler spectra

measurements at X–band were correlated with breaking events. They indicated that the scatterer speed during breaking can increase toward the phase speed of the dominant waves and that the bandwidth of the Doppler spectrum was greatly increased. The suggestion was made that scattering from breaking waves may include contributions such as specular surface reflections and volume scatter. They assert that a quantitative analysis of this type of measurement may yield the speed distribution and size of breaking waves and that a coherent microwave radar may be the ideal instrument to study wave breaking.

Alpers et al. (1981) have reviewed the spiky nature of the return from high sea states at moderate incidence angles. They suggest that the large returns under such conditions may be due to the spontaneous generation of Bragg resonant waves at the steep crests of breaking waves. Lyzenga et al. (1983) derived an analytical expression for the contribution of wedge scattering to the radar cross–section. Their model shows that wedges can provide an additional scattering mechanism which exhibits the correct polarization dependence to improve predictions based on the composite model.

Donelan and Pierson (1987) highlighted the importance of wave breaking in microwave remote sensing in a study of the wind speed dependence of the radar cross–section. A composite model for radar backscatter was applied to the radar cross–section measurements of Schroeder et al. (1984). A number of additional scattering mechanisms associated with sharp–crested and breaking waves were used to augment deficiencies in the model for horizontal polarization. Their simple model illustrated how a number of proposed scattering mechanisms associated with breaking events can improve the long established but partially inadequate composite surface model of microwave scattering.

Phillips (1988) has recently considered the friction velocity dependence of the frequency of occurrence of sea spikes and their contribution to the mean radar cross–section. He proposes that for moderate incidence angles, the mean normalized radar cross–section, σ^0, is the sum of separate contributions from Bragg scattering, σ_B^0, and from sea spikes, σ_{SS}^0, associated with localized breaking events:

$$\sigma^0 = \sigma_B^0 + \sigma_{SS}^0. \tag{1.22}$$

The small perturbation model for backscattering from the sea surface (Wright, 1966) was combined with an expression for the ocean gravity wave spectral density $\psi(\mathbf{k})$ under equilibrium conditions (Phillips, 1985):

$$\psi(\mathbf{k}) = \beta |\cos\varphi|^{1/2} u_* \, g^{-1/2} \, k^{-7/2}, \tag{1.23}$$

where β is a constant, k is the ocean wavenumber, φ is the angle between the wind and wave propagation direction, and g is the gravitational acceleration. The Bragg contribution σ_B^0 was then given by

$$\sigma_B^0 = \frac{\pi\beta}{2\sqrt{2}} \, |\cos\varphi|^{1/2} \, \sin^{1/2}\theta \, \cot^4\theta \, F_1(\theta) \, \left[u_*^2 \kappa/g \right]^{1/2}, \tag{1.24}$$

where θ is the incidence angle and κ is the electromagnetic wavenumber. The function $F_1(\theta)$ in general will depend on the transmitted and received polarization as well as θ. The form of $\psi(\mathbf{k})$ given by (1.23) is valid for wavenumbers in the

gravity wave range whose phase speed is large compared with u_*.

Equation (1.24) predicts that the contribution from Bragg scattering varies linearly with friction velocity u_* for a given radar frequency, incidence angle, and azimuth angle φ. Measurements of radar backscatter in the frequency range 0.4 to 9 GHz from Guinard, Ransome, and Daley (1971) were used by Phillips to support the frequency and friction velocity dependence of equation (1.24). Strictly speaking, the form of the wave spectral density (1.23) is valid only in the gravity–wave range. Thus the comparison of (1.24) with radar measurements in the centimeter range of wavelengths may be questioned.

Based on previous work concerning the energy dissipation due to wave breaking (Phillips, 1985), Phillips derived an expression for σ^0_{SS}, the contribution of sea spikes to the mean normalized radar cross–section:

$$\sigma^0_{SS} \approx F_2(\theta,\ \chi)\ \left[u_*^2 \kappa / g\right]^{3/2}, \tag{1.25}$$

where χ is the angle between the radar look direction and the wind. Equation (1.25) predicts that for a given measurement geometry and radar frequency, the contribution of sea spikes to σ^0 is proportional to the friction velocity cubed.

Finally, a cubic dependence on friction velocity was also predicted for the frequency of sea spike occurrence per unit area,

$$\nu(k_1)\ \propto\ g^{-1} k_1^4 u_*^3, \tag{1.26}$$

where k_1 is a threshold wavenumber significantly larger than that of the spectral peak. Phillips asserts that breaking events associated with larger wavelengths

may be expected to produce more intense returns and that setting a radar cross–section threshold above which a sea spike is counted corresponds to identifying breaking events associated with wavenumbers below the threshold wavenumber k_1. If sea spikes are caused by scattering from breaking waves producing whitecaps, then equation (1.26) is consistent with theoretical modeling which indicates that the whitecap coverage should vary as u_*^3 (Wu, 1979) and with correspondingly large wind speed exponents for various measurements of whitecap coverage (Ross and Cardone, 1974; Wu, 1979; Monahan and O'Muircheartaigh, 1986).

Melville, Loewen, Felizardo, Jessup, and Buckingham (1988) reported measurements of microwave scattering and sound generation by controlled breaking events in the laboratory. The results showed that the dissipation due to breaking correlated almost linearly with both the backscattered microwave power and the radiated acoustic power. Most recently, Jessup, Keller, and Melville (1990) presented the first quantitative analysis of sea spikes in moderate incidence backscatter over a range of environmental conditions. Chapter 2 of this thesis is an excerpt from Jessup et al. (1990) and reports on the friction velocity dependence of the frequency of occurrence of sea spikes and their contribution to the mean normalized radar cross–section.

Previous investigators have indicated that breaking waves may be responsible for discrepancies between modelling and measurement of the mean radar cross–section of the ocean surface. Quantifying the contribution of microwave return from breaking waves will aid in determining the importance of including them in improved models. The literature concerning microwave backscatter from breaking waves indicates that the detection of individual breaking events may be

accomplished by considering a combination of the radar parameters which are sensitive to their extreme geometry and turbulent nature. Unambiguous identification of individual breaking events based on quantitative microwave measurements would be a significant improvement over detection techniques relying on visual observations. The laboratory results of Melville et al. (1988) and modelling by Phillips (1988) suggest that information about the breaking process itself may be inferred from microwave measurements of breaking waves. If their results can be applied to the field, then microwave observations of breaking waves may yield important dynamic and acoustic information on the wave field and the upper ocean.

CHAPTER 2

PRELIMINARY EXPERIMENT: NORTH SEA PLATFORM

A preliminary investigation of the statistics of sea spikes and their contribution to the mean normalized radar cross–section was undertaken using measurements of microwave backscatter, friction velocity, and wave height made during a two week period in May 1987 from the German research platform NORDSEE. The platform is located in 30m of water approximately 40 nautical miles off the German peninsula in the North Sea (see Jessup, 1988 or Keller, Wissman, and Alpers, 1988). The measurements were performed in conjunction with the installation of a system for studying the long–term variation of the mean radar cross–section; thus, the experiment was not specifically designed to study the sea spikes associated with wave breaking and the data set is of limited duration. Nevertheless, these measurements provided the first quantitative analysis of sea spikes over a range of environmental conditions by presenting the friction velocity dependence of their frequency of occurrence and their contribution to the mean normalized radar cross–section. More detailed discussions of the microwave signature of breaking waves and alternative detection schemes are given in chapter 4. This chapter is an excerpt from Jessup, Keller, and Melville (1990).

2.1 EXPERIMENTAL PROCEDURE AND DATA ANALYSIS

The microwave backscatter measurements were made using a coherent, continuous–wave, dual–polarized scatterometer operating at 14 GHz (Ku–band, wavelength 2.14cm, Doppler conversion: 94Hz per ms^{-1}) with a transmit power of 200 mW. The instrument was designed, built, and calibrated at the US Naval Research Laboratory, Washington, DC. The instrument incorporates linear dual–polarized antennas which allow simultaneous vertical (VV) and horizontal

(HH) like–polarization measurements. In–phase and quadrature channels at baseband for both polarizations provide a complex time series output. The envelope of the signal is proportional to the received power and its rate of change of phase is the Doppler shift frequency. The complex output scheme permits discrimination of positive and negative target velocities. The instrument was mounted 31 m above the mean sea surface, aimed with an incidence angle of 45° and pointed northwest at 315° true. In this configuration, the measurement was well within the far–field of the antennas and the two–way 3–dB elliptical illumination area on the sea surface was approximately 1.8 x 2.5 m². The radar was calibrated in situ using a swinging sphere and the absolute normalized radar cross–section values quoted here are accurate to within ±1dB. The sea spike results are not dependent on the accuracy of the measurement but rather on its precision, or the relative stability of the calibration over time. Experience with systems of similar design indicates that the relative measurement error is less than 1 dB.

Direct measurements of friction velocity were provided by Risoe National Laboratory, Roskilde, Denmark, using a sonic anemometer (Kaijo–Denki, model DAT–300 with probe head type TR–61–B) mounted on a boom extending 20 m due west of the platform at a height of 33 m above the sea surface. Wave height measurements from the Baylor gauge permanently installed on the platform were used to obtain a characteristic phase speed with which to normalize the Doppler velocity measurements.

The radar output and wave height data were recorded on a Hewlett–Packard HP3968A FM analog tape recorder (Bandwidth 625 Hz), while the data acquisition system for the sonic anemometer produced 10–minute averages of the friction velocity u_* in real–time. The microwave signal was digitally sampled at

2 kHz and reduced to time series of the received power and the mean Doppler frequency with an averaging time of 0.25 s. The mean Doppler frequency was computed using the covariance estimation technique commonly used for Doppler weather radar (Doviak and Zrnic, 1984). Comparison of this technique with calculation of the first moment of the Doppler spectrum using Fourier transform methods showed excellent agreement. Details of the covariance processing technique are given in chapter 3 and Appendix C.

The normalized radar cross–section is proportional to the backscattered power averaged over the illumination area; the notation σ^0 often implies an additional time average. In an effort to avoid confusion, we will use σ^0 to denote the time–averaged normalized radar cross–section and $\sigma^0(t)$ to be the time series from which σ^0 is computed, that is

$$\sigma^0 = \frac{1}{T} \int_0^T \sigma^0(t) \ dt, \tag{2.1}$$

for a time series of length T.

In a typical open ocean environment, 10–15% or less of the wave crests passing a fixed location might be breaking (Holthuijsen and Herbers, 1986). Thus a relatively long time record must be used in order to provide enough samples to ensure the statistical significance of an analysis based on counting events. On the other hand, the time record should not be so long that the environmental conditions have drastically changed. For our analysis, a record length of one–hour was chosen over which to compute the averages of interest. Out of a total of approximately 80 hours of analog tape recordings, 48 hours of data have been

selected for this analysis.

Figure 2.1 is a example of a 64 second time series of processed data which includes a typical sea spike. The two top traces show the variation of $\sigma^0(t)$ on a linear scale for VV and HH polarization. The mean Doppler frequency shown in the bottom trace is proportional to the line–of–sight component of the surface scatter velocity averaged over the illumination area, which is dominated by the orbital velocity of the long surface waves (Plant and Keller, 1983). For both polarizations, the sea spike at approximately 23 sec is characterized by a large excursion in backscattered power and a local maximum in the Doppler frequency.

Comparison of the time series of radar cross–section for increasing values of friction velocity illustrates qualitatively how the frequency of occurrence of sea spikes increases. Figure 2.2 shows three representative time series of length 10 minutes of VV radar cross–section data for different values of u_*. The top trace is for a low value of 16 cms^{-1}, for which little or no breaking would be expected. In addition to an increase in the mean radar cross–section, the number of sea spikes is increased in the second and third traces for which the friction velocity is 33 cms^{-1} and 46 cms^{-1}, respectively.

Wave breaking is a process which occurs over a wide range of scales, from small– or micro–scale breaking (Phillips and Banner, 1974), through intermediate–sized breaking events, which may not produce discernible foam patches, to larger events which generate whitecaps. Figures 2.1 and 2.2 illustrate that the amplitude of spikes in σ^0 also occur over a wide range of scales. As noted above, previous authors have associated large sea spikes with breaking waves, that is, events which produce whitecaps. The correlation of lesser amplitude spikes with smaller scale breaking is unclear without supplementary
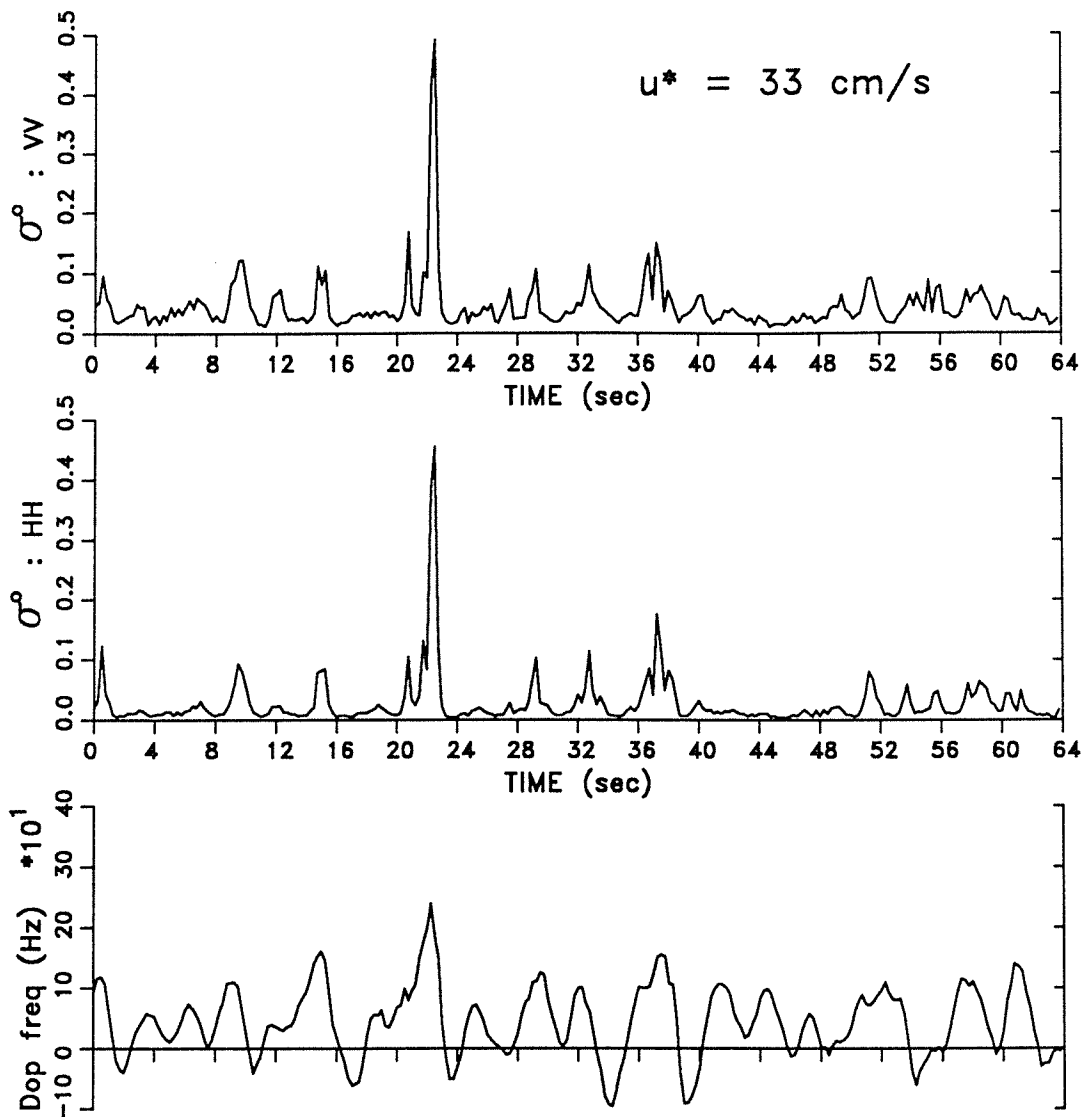
Figure 2.1: Simultaneous time series (64 s) of the normalized radar cross-section $\sigma^o(t)$ for VV and HH polarization and mean Doppler frequency for VV. The jump in $\sigma^o(t)$ coincident with a Doppler frequency maximum is typical of those associated with breaking events.
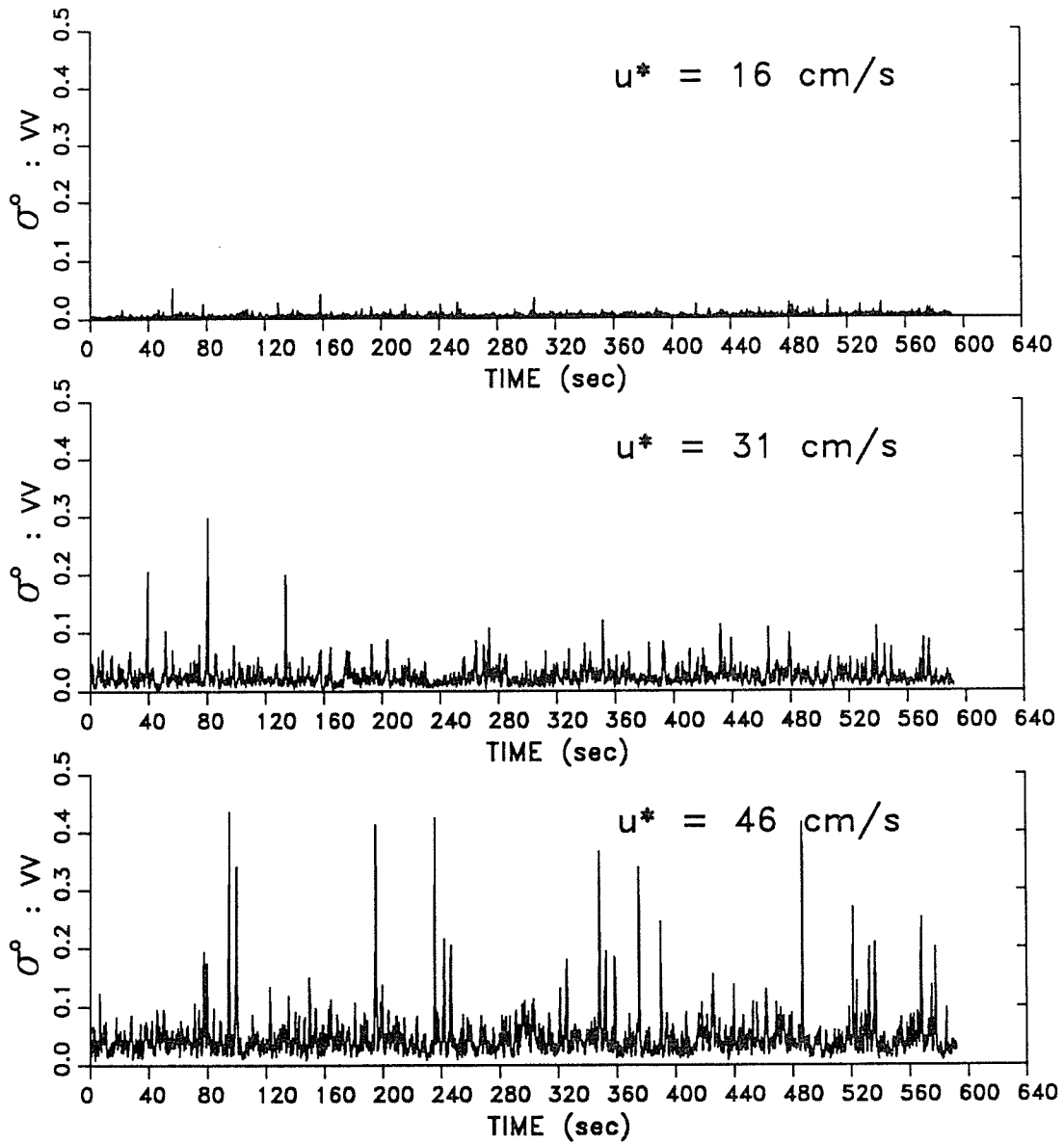
Figure 2.2: Comparison of time series (10 min) of radar cross–section, $\sigma^o(t)$, for VV polarization showing the qualitative difference in frequency of occurrence of sea spikes with increasing friction velocity u^*.

information such as a video image. We also note that Phillips' expression for the frequency of sea spike occurrence (equation 1.16), was derived for 'larger scale breakers producing the more intense return' (Phillips, 1988). To avoid the ambiguity associated with smaller sea spikes and for comparison with equation (1.16), we will concentrate on detecting sea spikes which are likely to be associated with larger scale breaking events. Furthermore, we will take larger scale breaking events to be those occurring at or near the long wave crests. Thus our detection scheme should identify large sea spikes associated with the long wave crests.

From comparison of the time series of the radar cross–section and the mean Doppler shift (see Figure 2.1), large spikes in the return power are clearly associated with large positive surface velocities, corresponding to measurements at or near the long wave crests. Scatter plots of the distribution of the measured velocity for VV polarization as a function of the peak value of $\sigma^0(t)$ for two different friction velocities are shown in Figure 3. The Doppler frequency is proportional to the areal average of the line–of–sight component of the surface scatterer velocities, which we assume to be nearly horizontal at a wave crest. The measured velocity values in Figure 2.3 have been resolved to be horizontal, which is appropriate for the larger sea spikes associated with large velocities (the lower velocity values associated with parts of the wave other than the crest are corrupted). Since the crest velocity of a breaking wave is expected to be of the order of its phase speed, the measured velocities have been normalized by the phase speed corresponding to the wave spectral density peak.

Figure 2.3a is for a friction velocity of 28 cms^{-1}, while Figure 2.3b is for a higher value of 49 cms^{-1}. In both cases, low values of $\sigma^0_{peak}(t)$ correspond to
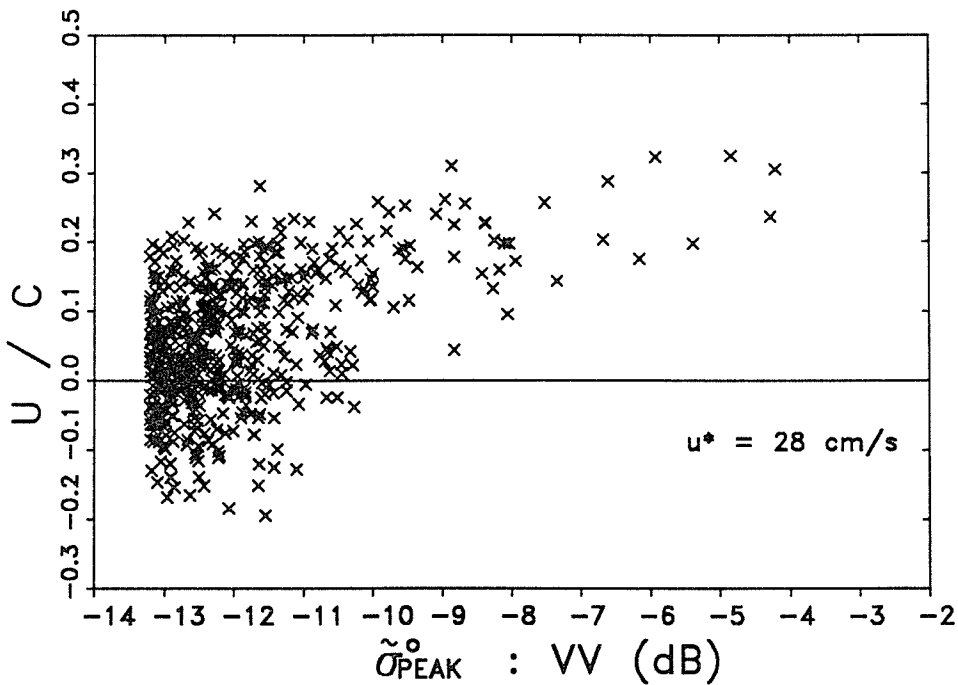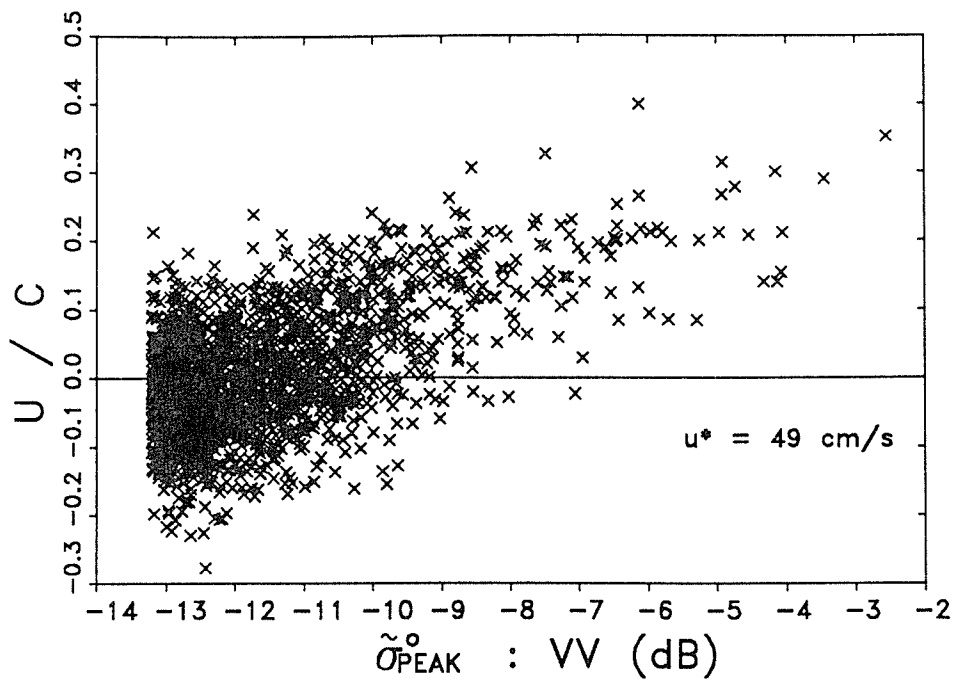
Figure 2.3: Scatter plots showing the distribution of normalized surface scatterer velocity for peak radar cross–section (VV) for two different friction velocities. The detection threshold of −7.2 dB has been chosen to detect mainly sea spikes associated with a positive velocity, corresponding to a location near a long wave crest.

negative velocities, which indicate return from a location away from a wave crest. Above some threshold, only positive velocities are found and the more intense returns are associated with larger positive velocities. Scatter plots for each hour of data processed have been analyzed and a threshold of $\sigma^0(t) = -7.2$ dB has been chosen to eliminate most large sea spikes associated with negative velocities for both VV and HH polarizations over a friction velocity range of $15 \leq u_* \leq 49 \text{cms}^{-1}$.

The use of a fixed threshold for analyzing data over a wide range of friction velocity may at first seem inappropriate, since from Figure 3 the σ^0_{peak} values at which negative velocities are eliminated appears to be a function of u_*. However, consider the implication of Phillips' assertion (noted above in chapter 1) that sea spike intensity should increase with the wavelength or scale associated with the breaking event. If we accept this assertion and assume that the sea spike intensity corresponding to a particular scale of breaker is not itself a function of u_*, then a fixed detection threshold is appropriate for detecting events in the same range of scale regardless of u_*.

The usefulness of a counting technique would be enhanced if the sea spike properties were relatively insensitive to the choice of detection threshold over some reasonable intensity range. In order to investigate this threshold dependence, we have counted the number of sea spikes in one–hour records as a function of the cross–section threshold for different friction velocities. Examples of this analysis for three different friction velocities are given in Figure 2.4, showing that for a given u_*, the number of events decreases as the threshold increases. The relatively constant slope and spacing of these curves over a threshold range of several dB indicates that the sea spike statistics may not be especially sensitive to the choice of threshold. That is, the relative change between curves of
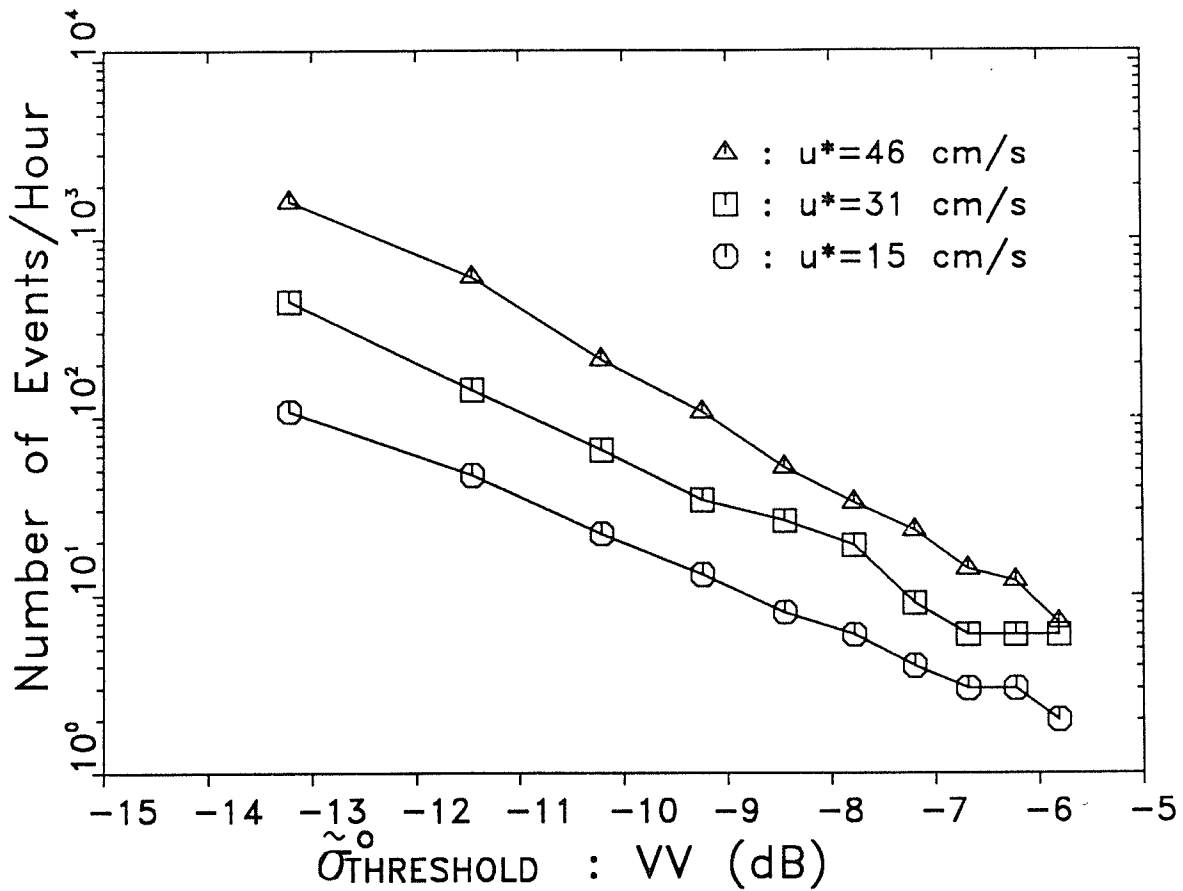
Figure 2.4: The number of sea spikes, N, in a one hour record as a function of radar cross–section detection threshold over a wide range friction velocities, u*. The relatively constant slope and spacing of curves indicates that sea spike statistics are not strongly dependent on threshold over a range of several dB.

different u_* for a given threshold is not a strong function of that threshold. To quantify the threshold dependence of the sea spike statistics presented below, the detection threshold was varied over a range of approximately 3 dB, centered at the chosen level of −7.2 dB.

The threshold of −7.2 dB is supported by previous analysis of video recordings taken during the experiment (Jessup, 1988). One hour of simultaneous radar and video measurements ($u_* = 26$ cms^{-1}) were made by visually aligning the radar antennas and video camera to be aimed at approximately the same location on the sea surface. A spectrum analyzer connected to one channel of the radar output was then used in conjunction with a video monitor to optimize the alignment as well as possible. Although there was no way to measure the accuracy of the alignment, the presence of a whitecap on the video monitor was repeatedly associated with a large jump in received power and increased Doppler frequency. Unfortunately, the quality of the video recording was seriously degraded by a mismatch in video formats between the camera and recording unit.

Despite the alignment uncertainty and the poor recording quality, the one-hour video tape was carefully reviewed in conjunction with the simultaneous microwave measurements to yield useful but limited quantitative information. The radar data was played into a spectrum analyzer to produce time histories of Doppler spectra in a waterfall or spectral map display. A total of 82 events which exhibited a microwave signature characteristic of breaking events were identified from the Doppler maps. The video tape was independently viewed and a total of 71 whitecaps were counted. Due to the poor quality of the video, no attempt was made to classify the size or scale of the whitecaps identified.

Although the number of events counted independently in the radar and

video recordings were roughly the same, only 43 breaking events were simultaneously found in both the radar and video recordings. Nonetheless, approximately 70% of the events which simultaneously appeared as whitecaps on the video monitor and were identified in the Doppler spectral maps were subsequently detected by the intensity threshold of −7.2 dB. The discrepancy between the number of independently counted and simultaneously occurring events may be due to: (1) misalignment of the radar and video spots, (2) the radar detecting breaking events which do not produce a whitecap, and (3) whitecap events which do not produce a distinctive microwave signature. A breaking event which does not produce a noticeable whitecap may correspond to the intermediate scale breaking mentioned above, while a whitecap whose propagation direction is oblique to the radar look direction may not produce a distinctive microwave signature. The uncertainty in alignment of the radar and video spots and the poor quality of the video recording have frustrated attempts to extract further meaningful results from these simultaneous measurements.

By analogy with the computational definition of σ^0 given by (2.1), the mean normalized sea spike radar cross–section σ^0_{SS} corresponding to the sea spike contribution to σ^0 is

$$\sigma^0_{SS} = \frac{1}{T} \sum_{i=1}^{N} \int_{T_i} \sigma^0_{SS}(t) \; dt \qquad (2.2)$$

where $\sigma^0_{SS}(t)$ is the contribution of an individual sea spike, N is the number of sea spikes in a record of length T, and T_i is the duration of the ith event.

The two methods we have chosen to define an individual sea spike intensity
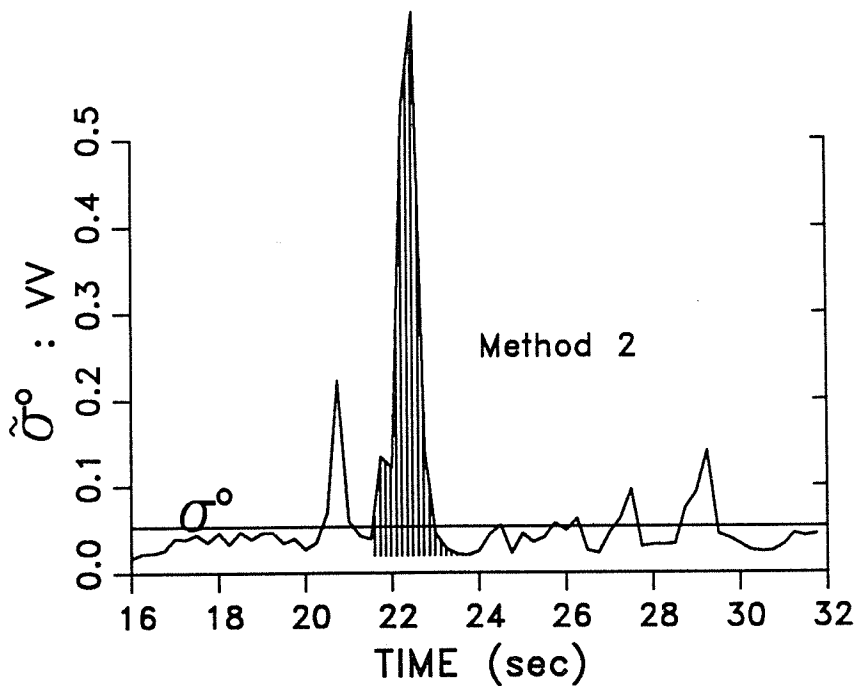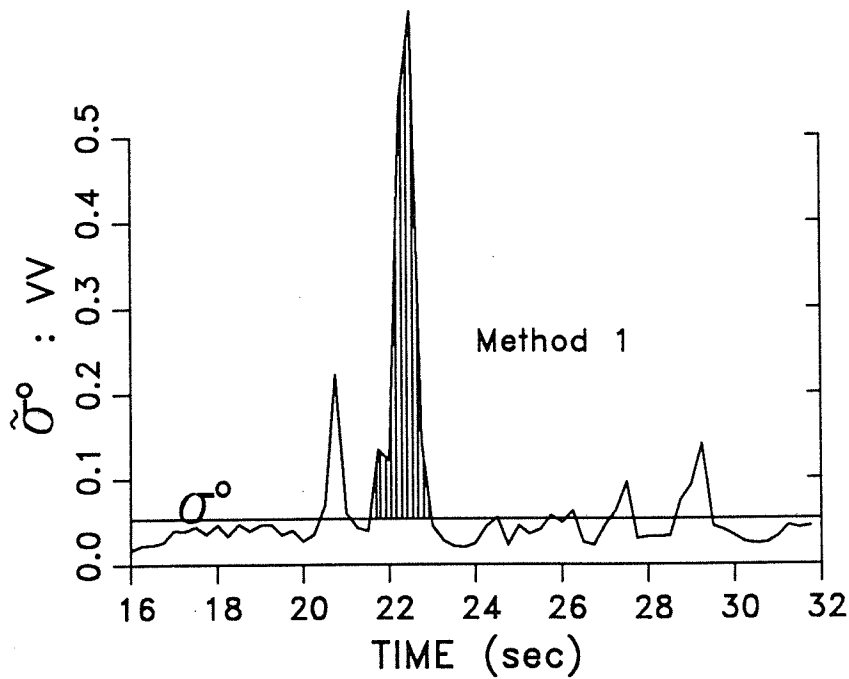
Figure 2.5: A schematic diagram showing the two methods used to compute the sea spike contribution to the normalized radar cross-section. The horizontal line labeled σ^o is the normalized radar cross-section for a one-hour record. The contribution of an individual sea spike corresponds to the shaded area. The duration of the sea spike in method 1 is taken as the time during which $\sigma^o(t)$ is elevated above the mean σ^o. In method 2, the spike duration is taken as the time between local minima on either side of the sea spike peak.

and duration are illustrated in Figure 2.5. For method 1, T_i is the time over which the radar cross–section is elevated above the mean, σ^0, and $\sigma^0_{SS}(t)$ is that portion of the total cross–section which is above the mean during T_i:

$$\sigma^0_{SS}(t) \; = \; \sigma^0(t) \; - \; \sigma^0. \tag{2.3}$$

The duration T_i for method 2 is the time between local minima on either side of the sea spike maximum and $\sigma^0_{SS}(t)$ is given by

$$\sigma^0_{SS}(t) \; = \; \sigma^0(t) \; - \; \sigma^0_{min}, \tag{2.4}$$

where σ^0_{min} is the lesser of the local minima defining T_i. While other methods are possible, these two provide reasonable upper and lower bounds on the contribution of an individual sea spike.

2.2 RESULTS

The measured mean normalized radar cross–section σ^0 is plotted versus friction velocity u_* on a log–log scale for VV and HH polarization in Figure 2.6, where each point represents the mean for a one–hour record. The radar antennas remained fixed during the experiment, pointing in the NW direction of 315° true. All data analyzed were for wind directions in the angular bands from 340–360° or 270–280°. That is, the angle φ between the radar look–direction and the wind was between 25–45° for all measurements. These data are presented together since the variation of σ^0 is expected to be symmetric about $\varphi = 0$ and the range of φ variation for the data is 20° or less. The data at higher friction velocities
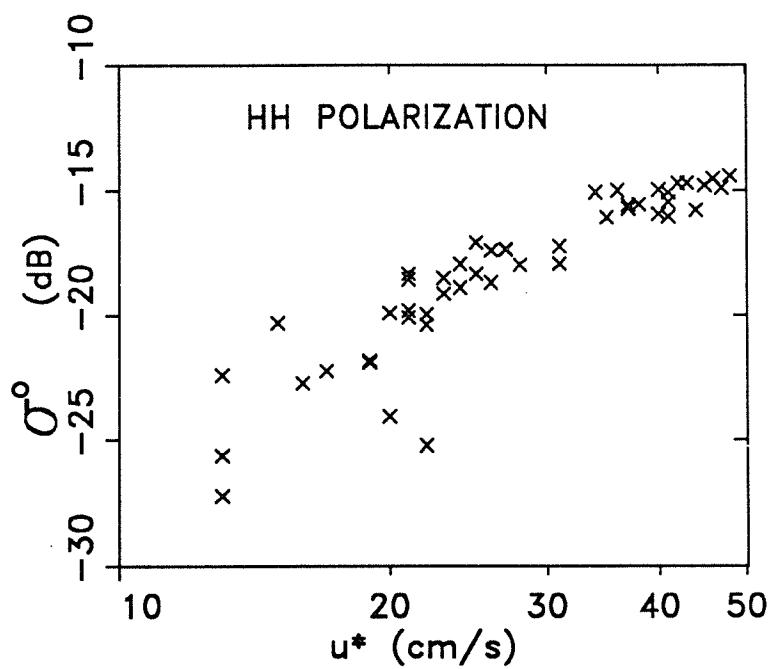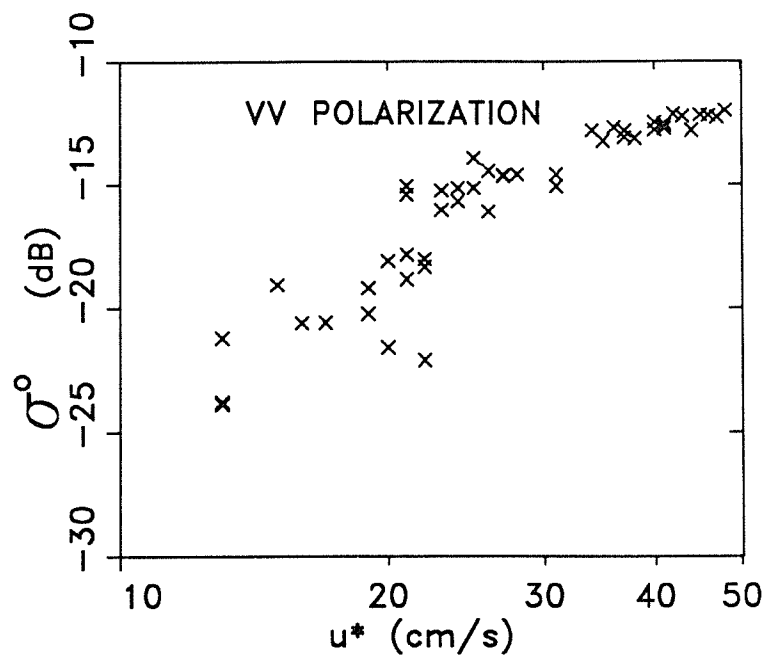
Figure 2.6: The normalized radar cross–section versus friction velocity u* for VV (top) and HH (bottom) polarization (each point represents a one–hour record). Note the relatively large amount of scatter for low u* values compared to the high degree of correlation for large u*.

in Figure 2.6 appear to be highly correlated, but the scatter at lower values of u_* suggests that a linear fit over the entire range of u_* is not appropriate.

The cross–section of an individual breaking event is expected to be a function of the orientation of its crest with respect to the radar look direction. A reasonable assumption is that the directional distribution of breaking wave crests is symmetric about the wind. Then upwind measurements made over a restricted range of the angle φ between the radar look direction and the wind should provide a valid sampling of breaking events, even if that angular range is not centered at $\varphi = 0$.

The sea spike contribution σ^0_{SS} as defined by method 1 (equations (10) and (11) and Figure 2.5a) is shown versus friction velocity u_* on a log–log plot in Figure 2.7 for the cross–section threshold of −7.2 dB. For the relation:

$$\sigma^0_{SS} = C_1 u_*^{\alpha} \tag{2.5}$$

we find the exponent α of the least squares linear fit to be 3.3 and 3.5 for VV and HH polarizations, respectively. The exponent α does not vary greatly over a threshold range of 3 dB for both methods of defining the sea spike and is listed with 95% confidence levels and correlation coefficients ρ (Bendat and Piersol, 1986) in the upper portion of Table 2.1.

The relative importance of the sea spike contribution to the mean radar cross–section is of interest for improving current models for σ^0. Figure 2.8 shows the fractional cross–section due to sea spikes, σ^0_{SS}/σ^0, versus friction velocity for the cross–section threshold of −7.2 dB. Clearly, sea spikes contribute a greater fraction of the return power for HH than for VV polarization. In general, the
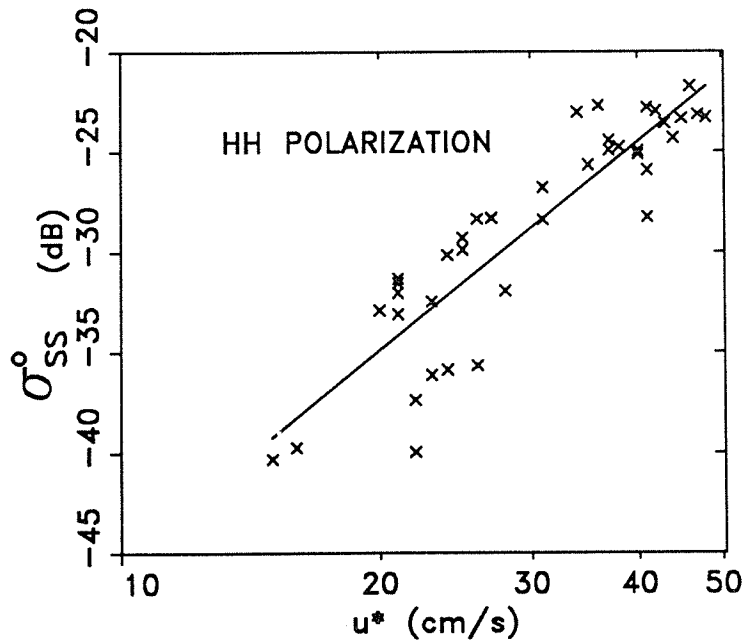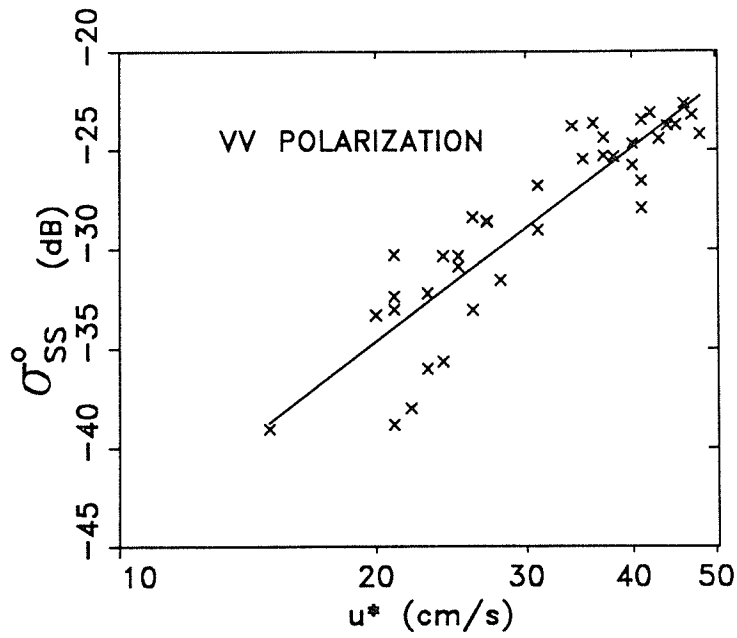
Figure 2.7: The sea spike contribution $\sigma^o{}_{ss}$ to the normalized radar cross–section versus friction velocity u^* using method 1 and a threshold of $\sigma^o(t)=-7.2$ dB. The slope of the least squares line is 3.3 for VV (top) and 3.5 for HH (bottom), indicating a roughly cubic dependence.

TABLE 2.1: FRICTION VELOCITY EXPONENTS

$$\sigma^0_{ss} = C_1 \, u_*^{\alpha}$$

Threshold (dB):		−9.0	−7.2	−6.0
Method 1:	VV	3.3±0.5 (0.91)	3.3±0.5 (0.90)	3.2±0.7 (0.85)
	HH	3.1±0.5 (0.90)	3.5±0.6 (0.89)	3.4±0.6 (0.89)
Method 2:	VV	3.8±0.5 (0.93)	3.6±0.6 (0.89)	3.6±0.7 (0.88)
	HH	3.3±0.5 (0.91)	3.5±0.6 (0.89)	3.5±0.7 (0.88)

$$N = C_2 \, u_*^{\delta}$$

Threshold (dB):	−9.0	−7.2	−6.0
VV	3.6±0.6 (0.89)	2.8±0.5 (0.89)	3.0±0.6 (0.88)
HH	3.0±0.6 (0.84)	2.8±0.4 (0.91)	2.7±0.5 (0.87)
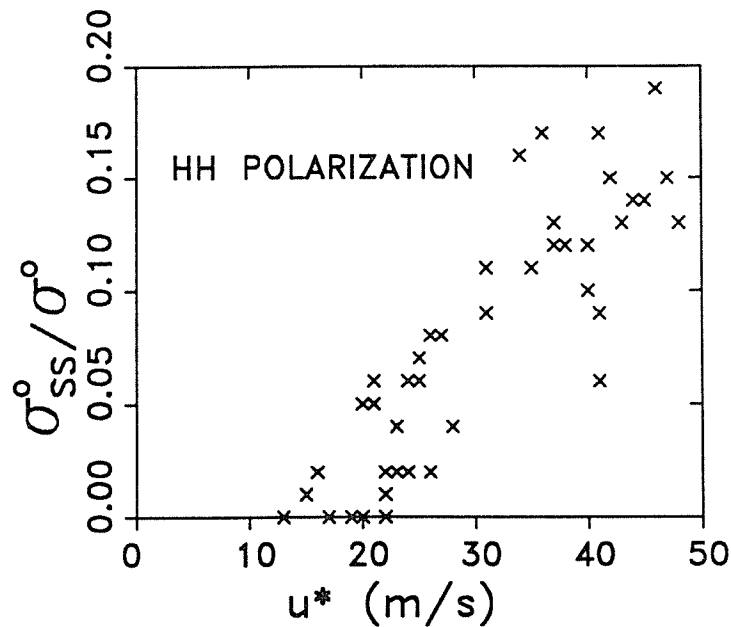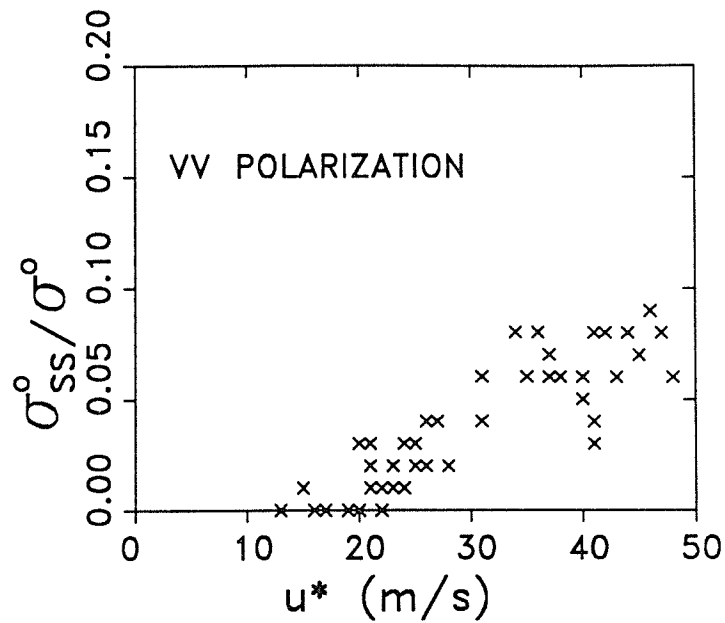
Figure 2.8: The fractional radar cross–section σ^o_{ss}/σ^o due to sea spikes versus friction velocity u* using method 1 and a threshold of −7.2 dB. At high u*, the sea spike contribution to the mean cross–section measured between 25° and 45° relative to the wind is approximately 5–10% for VV (top) and 10–20% for HH (bottom) polarization.

average polarization ratio $\sigma_{VV}^0/\sigma_{HH}^0$ is greater than unity (Wright, 1966), but during a breaking event, the instantaneous polarization ratio can approach or equal unity (Kwoh and Lake, 1981). Therefore, the larger contribution of sea spikes to σ_{HH}^0 is expected. The value of the fractional radar cross–section is of course a function of the cross–section threshold. For the threshold of −7.2 dB, the percentage of the return power due to sea spikes with $25° \leq \varphi \leq 45°$ at high friction velocity is approximately 5–10% for VV polarization and 10–20% for HH polarization.

The residual radar cross–section, σ_{res}^0, given by

$$\sigma_{res}^0 = \sigma^0 - \sigma_{SS}^0 \tag{2.6}$$

using method 1 for the threshold of −7.2 dB is plotted versus friction velocity in Figure 2.9. Since the maximum sea spike contribution for this threshold is 20% (approximately 1 dB for HH polarization at large u_*), Figure 2.9 is similar in appearance to the plot of σ^0 in Figure 2.6. As with Figure 2.6, the scatter of the data in Figure 2.9 at lower values of u_* does not suggest a least square fit over the entire range of u_*. The fit for $u_* \geq 23$ cms[-1] shown in Figure 2.9, for which a high degree of correlation is apparent, gives exponents very nearly equal to unity: 1.1±0.2 (ρ=0.93) for VV polarization and 1.1±0.2 (ρ=0.92) for HH polarization.

Figure 2.10 shows the frequency of occurrence of sea spikes for the threshold of −7.2 dB as the number of events N in each one–hour record for which at least 2 events were counted and the sea spike contribution was at least 1%, that is for $N > 1$ and $\sigma_{SS}^0/\sigma^0 \geq 0.01$. The least square fit,
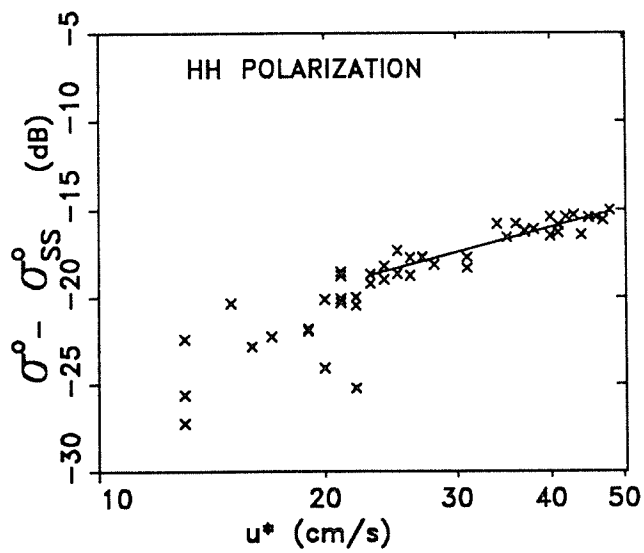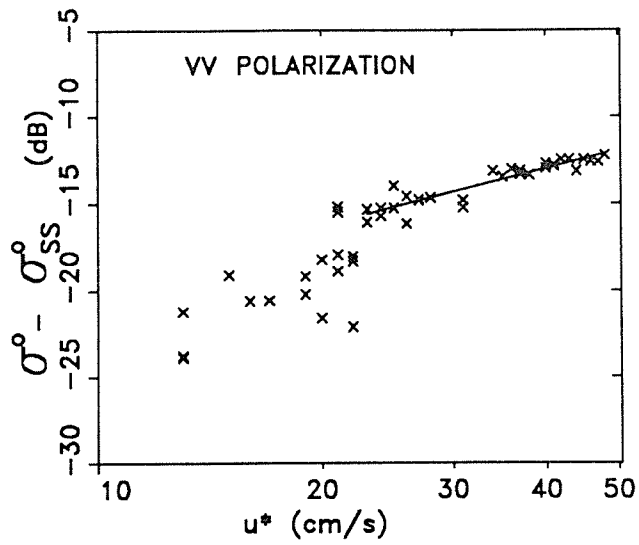
Figure 2.9: The residual radar cross–section, $\sigma^0-\sigma^0_{ss}$, versus friction velocity for VV (top) and HH (bottom) polarization. For u*$\geq$23cms^{-1}, there is very little scatter in the data and the slope of the least square fit over this range is 1.1 for both polarizations, indicating an approximately linear dependence.
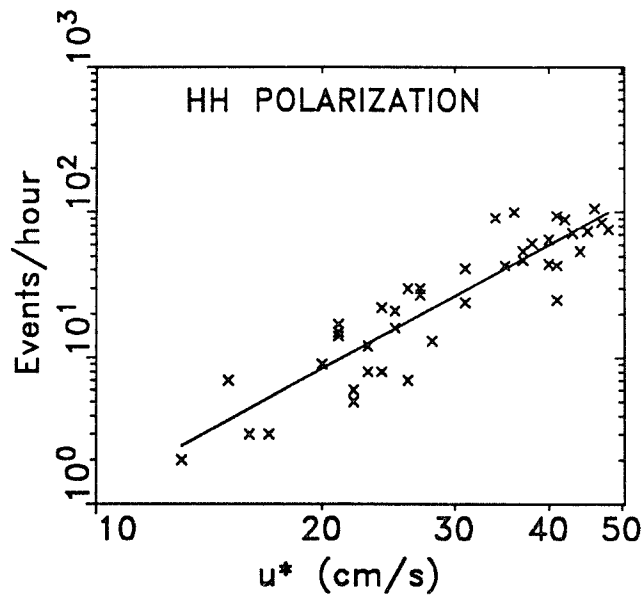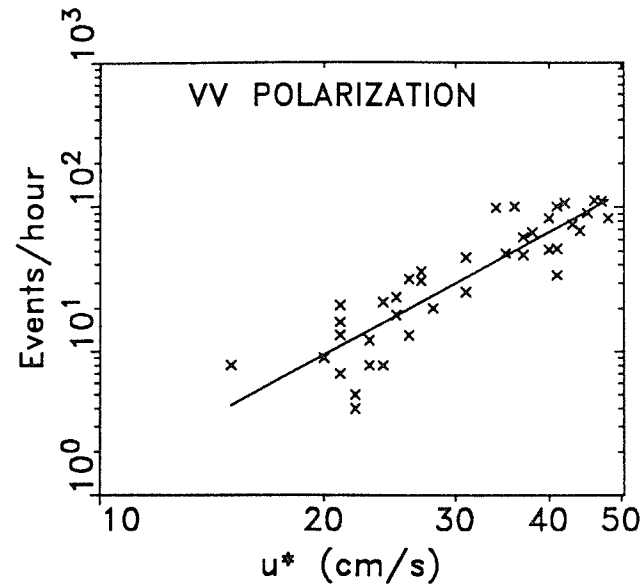
Figure 2.10: The frequency of occurrence of sea spikes in terms of number of events in a one–hour record, N, versus friction velocity u* for VV (top) and HH (bottom) polarization. The slope of the least squares fit is 3.5 for VV and 3.1 for HH, indicating an approximately cubic dependence.

$$N = C_2 \, u_*^{\delta}, \tag{2.7}$$

finds friction velocity exponents of 2.8 for both VV and HH polarization, for the threshold of −7.2 dB. The exponents δ and correlation coefficients ρ for a threshold range of 3 dB are given in the lower portion of Table 1. As with the friction velocity dependence of σ^0_{SS}, the exponent δ does not significantly change over this threshold range.

The friction velocity exponents computed for both the sea spike contribution to the mean cross–section and the frequency of occurrence are all close to 3 (see Table 2.1). This similar dependence on u_* implies that σ^0_{SS} and N may be linearly related. Therefore, in Figure 2.11 we have plotted N, the number of events in each one–hour record, against σ^0_{SS} for the threshold of −7.2 dB. The exponents η for

$$N = C_3 \, \sigma^{0\eta}_{SS} \tag{2.8}$$

are 0.82±0.06 (ρ=0.98) and 0.77±0.05 (ρ=0.98) for VV and HH polarization, respectively.

2.3 DISCUSSION

The argument may be made that sea spikes defined by a rationally chosen yet somewhat arbitrary intensity threshold may not necessarily be due to breaking events. For instance, the random nature of the distribution of scatterers on the sea surface may lead to constructive interference resulting in a sea spike having
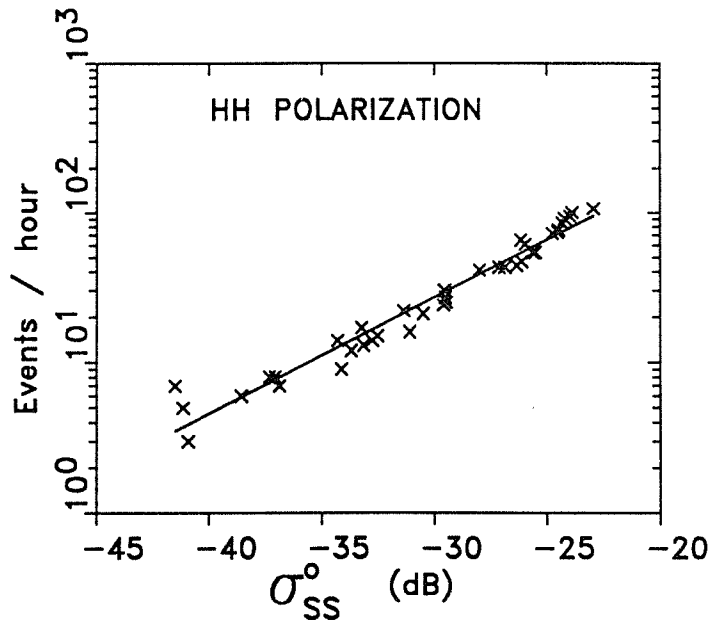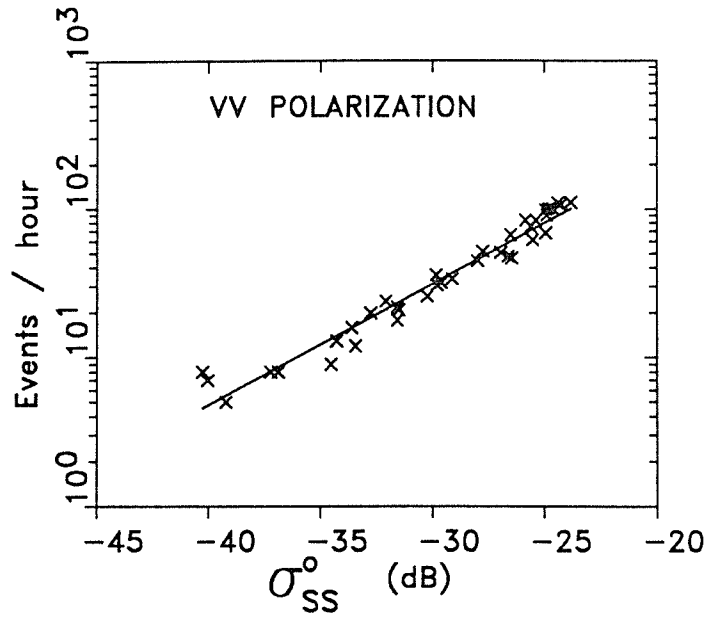
Figure 2.11 The frequency of occurrence of sea spikes, N, plotted against sea spike contribution, σ^o_{ss}, to the normalized radar cross–section. The slope of the least squares fit is 0.77 for VV (top) and 0.82 for HH (bottom). The nearly linear dependence suggest that the cross section of an average sea spike, ie., σ^o_{ss}/N, may be independent of u^*.

little to do with breaking. This argument is diminished by the distributions shown in Figure 2.4, which indicates that large peak radar cross–sections are generally associated with large surface scatter velocities. Furthermore, the choice of a relatively large threshold ensures that the sea spikes counted will be associated with positive surface scatterer velocities.

For friction velocities below 20 cms⁻¹ or so, less than 10 events per hour were counted for the chosen threshold of −7.2 dB (see Figure 2.10). Melville (1977) suggested that a minimum friction velocity for the onset of breaking may occur in the neighborhood of 23 cms⁻¹. Thus deletion of low friction velocity points from Figure 2.10 and also from Figure 2.7 might be justified on the grounds that virtually no breaking events occur. However, the minimum friction velocity for the onset of breaking is likely to depend on other factors not available in this data set. For example, long wave slope has been shown to affect σ^0 at X–band (Keller, Plant, and Weissman, 1985), especially at low wind speeds. Indeed, the increased scatter of σ^0 for low u_* in Figure 2.6 may be an indication of this effect. Removal of the low velocity data does not significantly change the computed exponents and thus we present all available data in the interest of completeness.

The residual radar cross–section given by (2.6) and plotted in Figure 2.9 (as well at the total radar cross–section in Figure 2.6) shows much less scatter for the larger values of u_*. This observation motivated the linear fit over the higher friction velocity values shown in Figure 2.9. The residual radar cross–section, σ^0_{res}, corresponds to Phillips' (1988) Bragg contribution, equation (1.5), which is based on the wave spectral density $\psi(\mathbf{k})$ given by (1.4). The derivation of the spectral density assumes that losses due to breaking are important in the

equilibrium range of validity of $\psi(\mathbf{k})$ (Phillips, 1985). Since little wave breaking is expected at low u_*, the friction velocity exponents close to unity for σ^0_{res} at higher u_* might be interpreted as supporting Phillips' predicted linear dependence. Strictly speaking, however, equation (1.5) for the Bragg contribution should not be applied to these data (Bragg wavelength of 1.51 cm) since $\psi(\mathbf{k})$ is derived only for gravity waves.

The scatter in the plot of N versus σ^0_{SS} (Figure 2.11) is significantly less than that for each quantity plotted individually against u_* (Figures 2.7 and 2.10). This observation indicates that the dependencies of N and σ^0_{SS} on other as yet unknown parameters may be similar. Futhermore, the nearly linear dependence between the sea spike contribution to the radar cross–section and the frequency of occurrence of sea spikes implies that the average radar cross–section of a sea spike, ie., σ^0_{SS}/N, may be independent of u_*. An average sea spike cross–section which is independent of u_* might be consistent with the fact that breaking occurs over a wide range of scales. If the cross–section of a breaking wave is a measure of its size, then the size distribution of breakers and the increase in the number of breaking events at all scales might be such that the average sea spike return is invariant.

2.4 CONCLUSIONS

Field and laboratory measurements of microwave backscatter at moderate incidence in the presence of wave breaking have indicated that steep and breaking waves produce events referred to as sea spikes. We have presented quantitative measurements of the relationship between the friction velocity u_* and sea spikes for the Ku–band radar cross–section. The intensity threshold for the definition of the sea spike contribution to the mean radar cross–section was chosen to count large sea spikes associated with a positive mean Doppler frequency.

The variation of the sea spike contribution σ_{SS}^0 with friction velocity was found to be consistent with Phillips' (1988) prediction of a cubic dependence, equation (1.14). The fractional power for high friction velocities ($u_* \approx 40 - 50$ cms^{-1}) measured 25° to 45° relative to the wind was found to be approximately 5–10% for VV polarization and 10–20% for HH polarization using the procedure designated method 1 (equations (2.2) and (2.3) and Figure 2.5a). These findings support the inclusion of breaking waves in scattering models for HH polarization.

The frequency of occurrence of sea spikes was computed as the number of events counted in a one–hour record for the chosen threshold. The roughly cubic dependence on friction velocity is consistent with theoretical modeling and field measurements of whitecap coverage reported by other investigators and with Phillips' (1988) result, equation (1.15). Finally, the data suggest that the contribution of an average sea spike to σ^0 may be independent of u_*.

CHAPTER 3

SAXON EXPERIMENTAL PROCEDURE

The SAXON experiment at the Cheasapeake Light Tower (CLT) off Norfolk, Virginia in the fall of 1988 provided the opportunity to further investigate the microwave scattering by breaking waves. Over a 6 week period, simultaneous microwave, video, and environmental measurements were made resulting in approximately 350 hours of data processed in real time, 200 hours of archived data on analog tapes, and 100 hours of video recordings. Figure 3.1 shows the location of the CLT, which is situated in 12m meters of water at the mouth of the Chesapeake Bay.

The photograph of the tower in Figure 3.2 was taken from the south side. Figure 3.3 is a diagram of the tower viewed from the north showing elevation levels and the location of the upper and lower instrument booms. The scatterometer and video camera assembly were mounted on the upper rail at the helicopter deck level of 26m above mean sea level (MSL). The plan view diagrams of the catwalk and helicopter deck levels in Figure 3.4a and 3.4b also show the boom locations. In order to keep the scatterometer pointed into the wind as much as possible, its location was changed as the wind direction varied. The look–direction and fetch for each mounting location are shown in the plan view of the tower in Figure 3.4b.

The boat dock consisting of vertical pilings along the perimeter of the northwest quadrant of the tower is also shown in Figures 3.2–3.4. The photograph in Figure 3.5 shows the additional bumpers made of horizontal wooden beams which were attached to the north side of the tower. Surface wave reflections from these waterline obstacles were observed by eye at various times during the experiment. However, the effect of these reflections at the
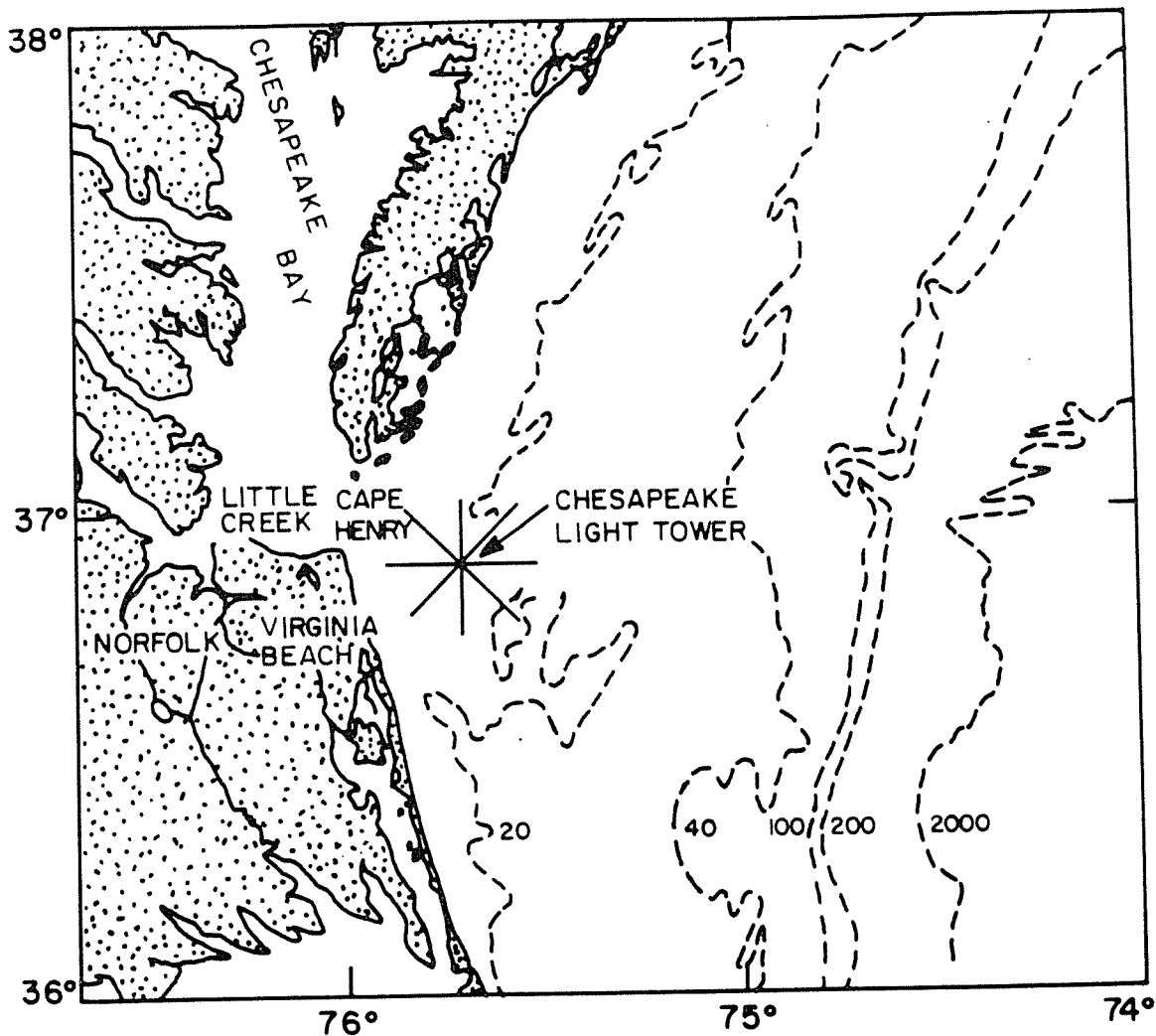
Figure 3.1: Location of USCG Chesapeake Light Tower (CLT), 15 n mi
(25km) off Cape Henry, Virginia Beach, Virginia, USA, in 12 m of water.
Latitude: 36° 55' N, Longitude: 75° 43' W, depth contours in meters.
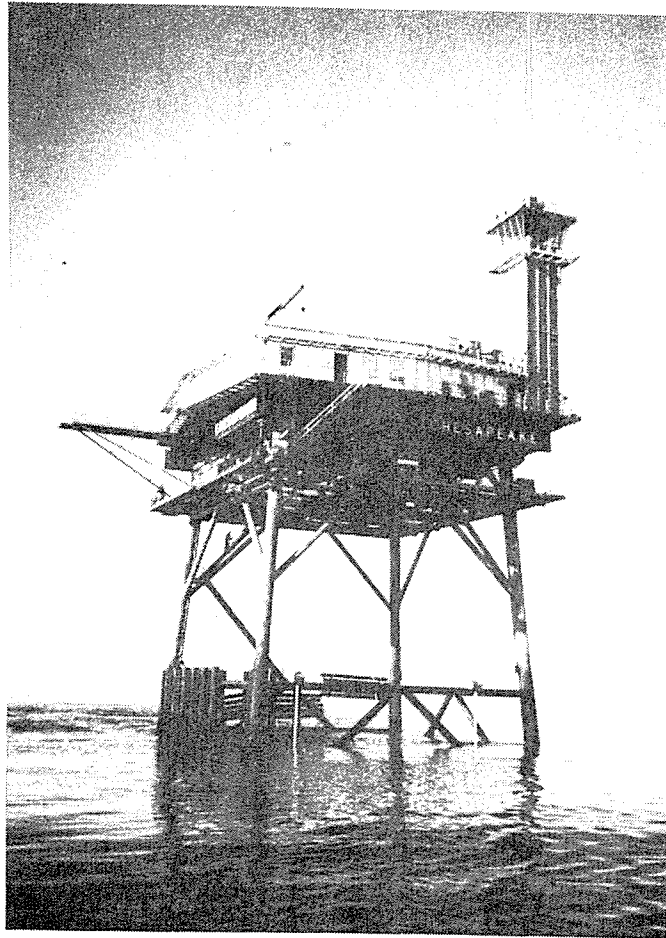
Figure 3.2: Photograph of CLT as viewed from the south side. Permanent landing consists of vertical pilings along the northwest quadrant of the tower, extending down from the catwalk level. Horizontal wooden beams along the north side of tower are temporary bumpers (see also Figures 3.3, 3.4a, and 3.5).
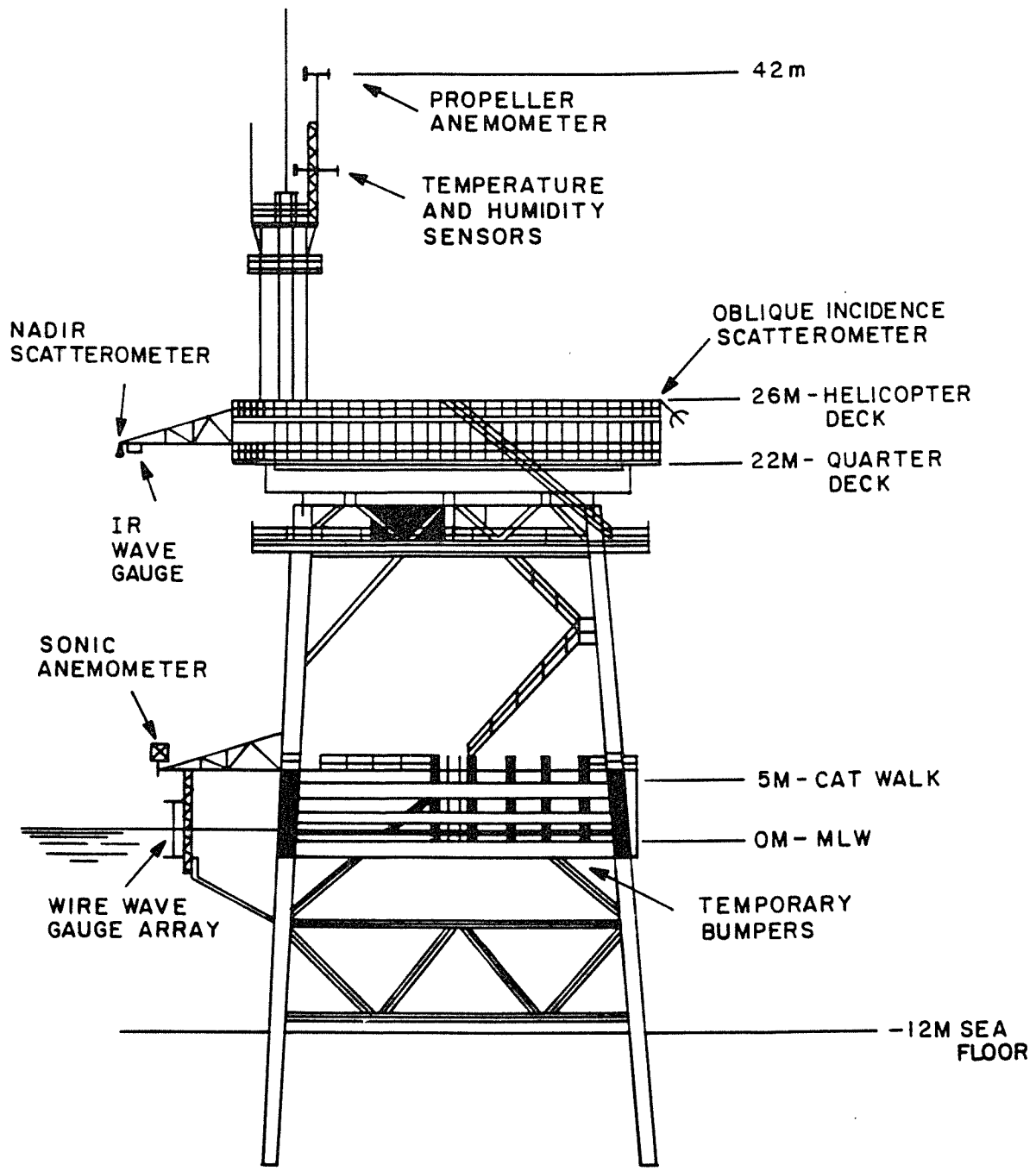
Figure 3.3: Diagram of CLT as viewed from the north side showing various elevation levels and location of instruments. The oblique incidence scatterometer used in this experiment was mounted as several locations around the tower (see Figure 3.4a). The nadir scatterometer mounted on the upper boom was not used for this experiment (see Appendix E).
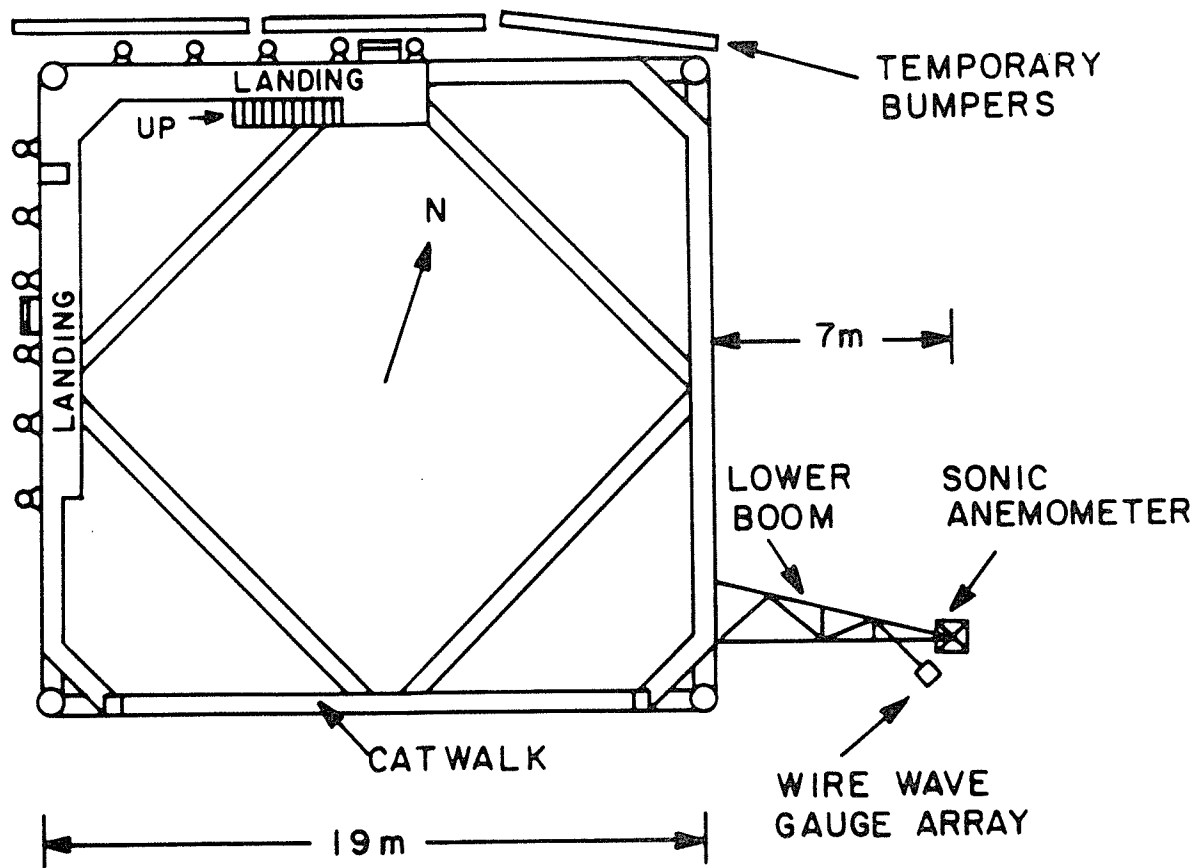
Figure 3.4a: Plan diagram of CLT catwalk elevation showing location of lower instrument boom, permanent landing along NW quadrant, and temporary bumpers along the north side.
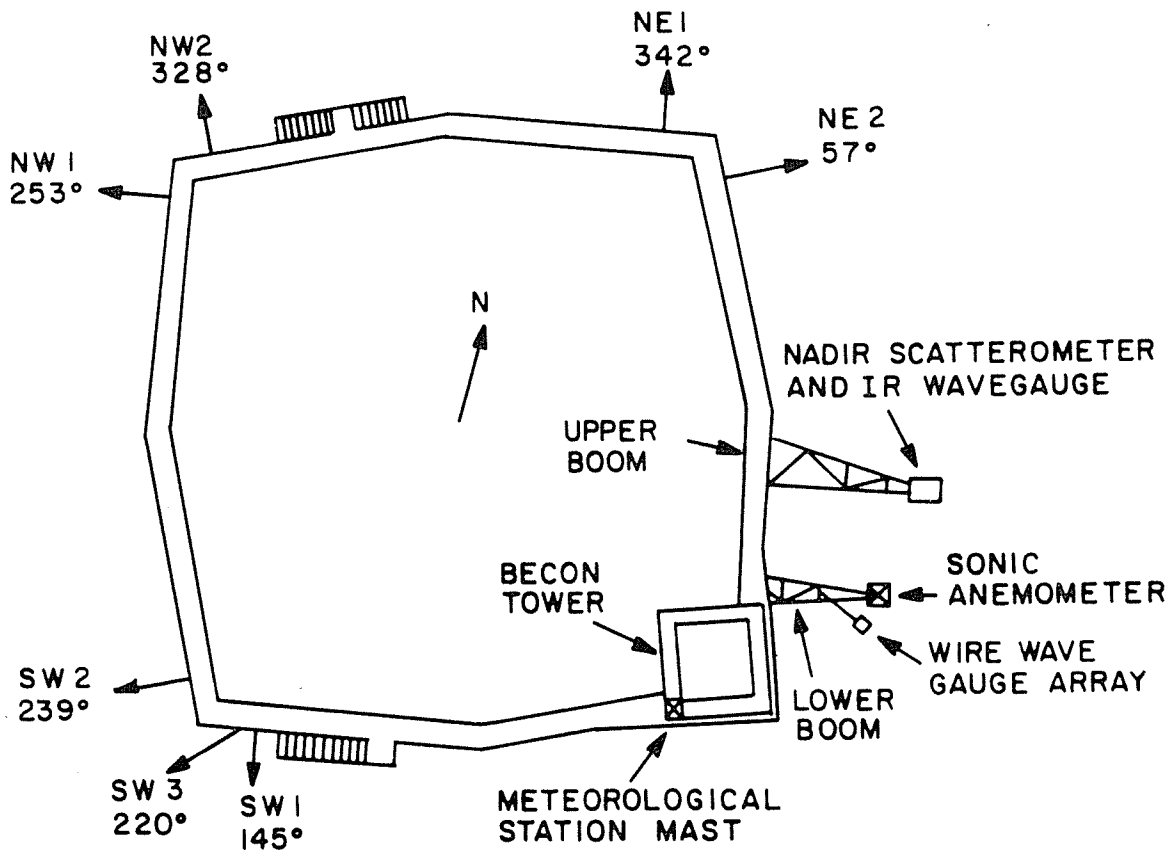
Figure 3.4b: Plan diagram of CLT helicopter elevation showing location of upper and lower booms and meteorological station mast atop the beacon tower. Also indicated are the scatterometer mounting sites and corresponding antenna look directions.
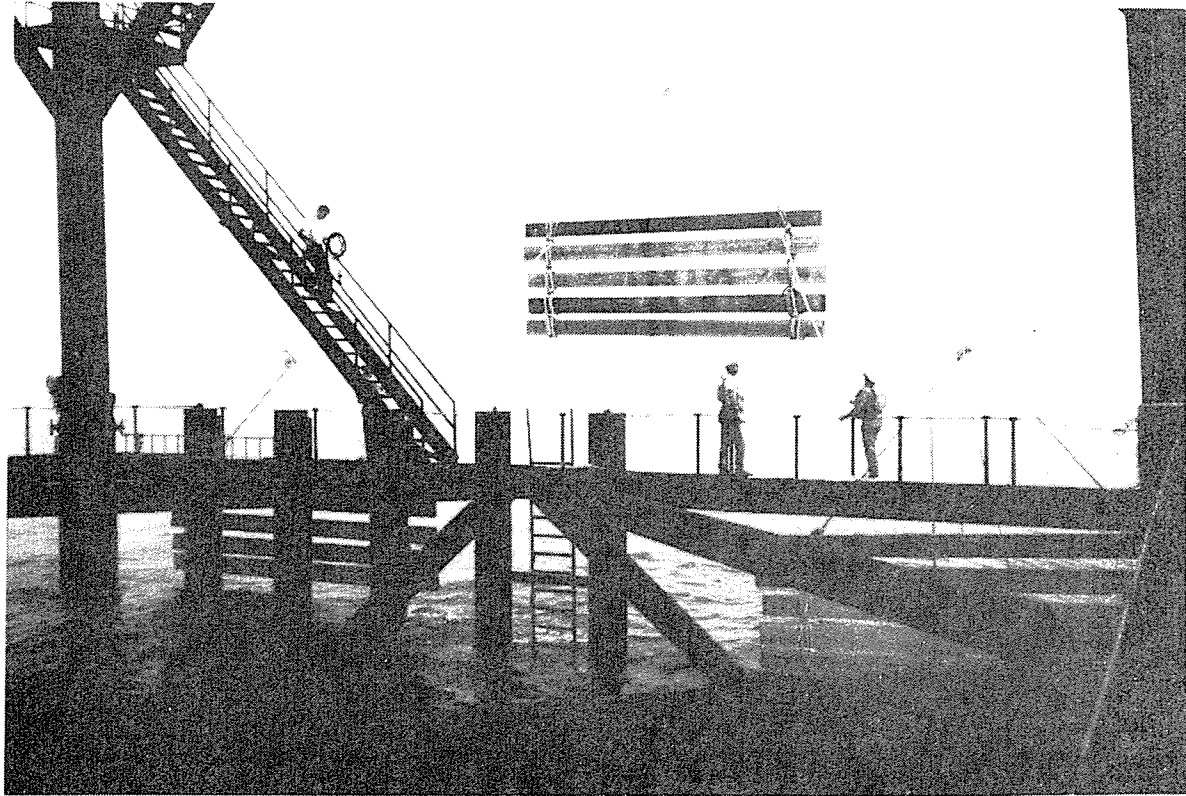
Figure 3.5: Photograph taken from CLT catwalk looking north, showing pilings along permanent landing and temporary bumpers of horizontal wooden beams being lowered into position along the north side.

scatterometer illumination area located 26m away from the tower was judged to be minimal, except during extreme sea conditions.

3.1 INSTRUMENTATION

3.1.1 SCATTEROMETER

The microwave backscatter measurements were made using a scatterometer identical in design to that used in the preliminary experiment described in chapter 2 (section 2.1). Figure 3.6 shows the two, dual–polarized, linear antennas mounted side–by–side on the upper railing of the Chesapeake Light Tower. The transmitting antenna is a 20cm–diameter horn with a one–way, 3dB beamwidth of approximately 6.7^o (Nurad Model 130DL1). The receiving antenna is a 60cm–diameter parabola with a one–way, 3dB beamwidth of approximately 2.5^o (TerraCom Model 166–0333–02). Typical beampatterns supplied by the manufacturers for the horn and parabola are shown in Figures 3.7 and 3.8. The effective two–way, 3dB beamwidth for the combination of antennas was approximately 2.4^o.

The scatterometer is a two stage device consisting of a radio frequency (RF) unit and an intermediate frequency (IF) unit. The weatherized RF unit, shown in Figure 3.9, was located directly behind the antennas. The IF unit was housed indoors with the data acquisition system. Figure 3.10 is a block diagram representing the vertically polarized channel of the receiver. The circuit for horizontal polarization is conceptually identical to that of the vertical and is not shown.

The scatterometer design uses two slightly different transmit frequencies
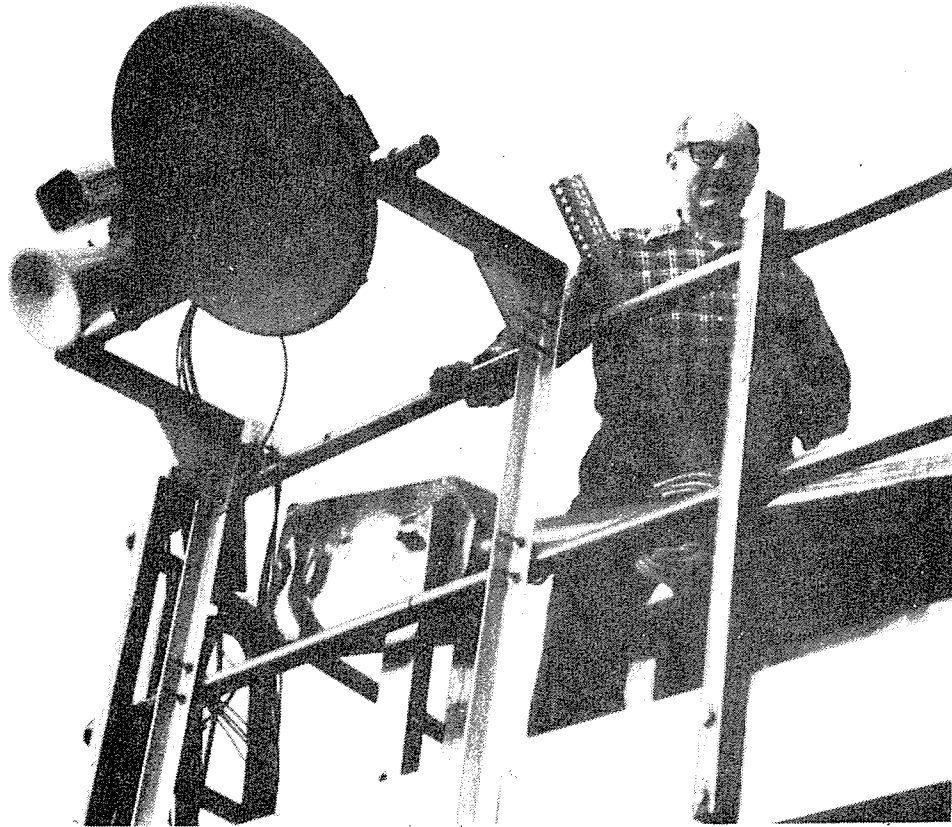
Figure 3.6 Photograph of scatterometer antennas and video camera housing mounted on railing at the helicopter deck elevation. Pictured is William C. Keller of the US Naval Research Laboratory.
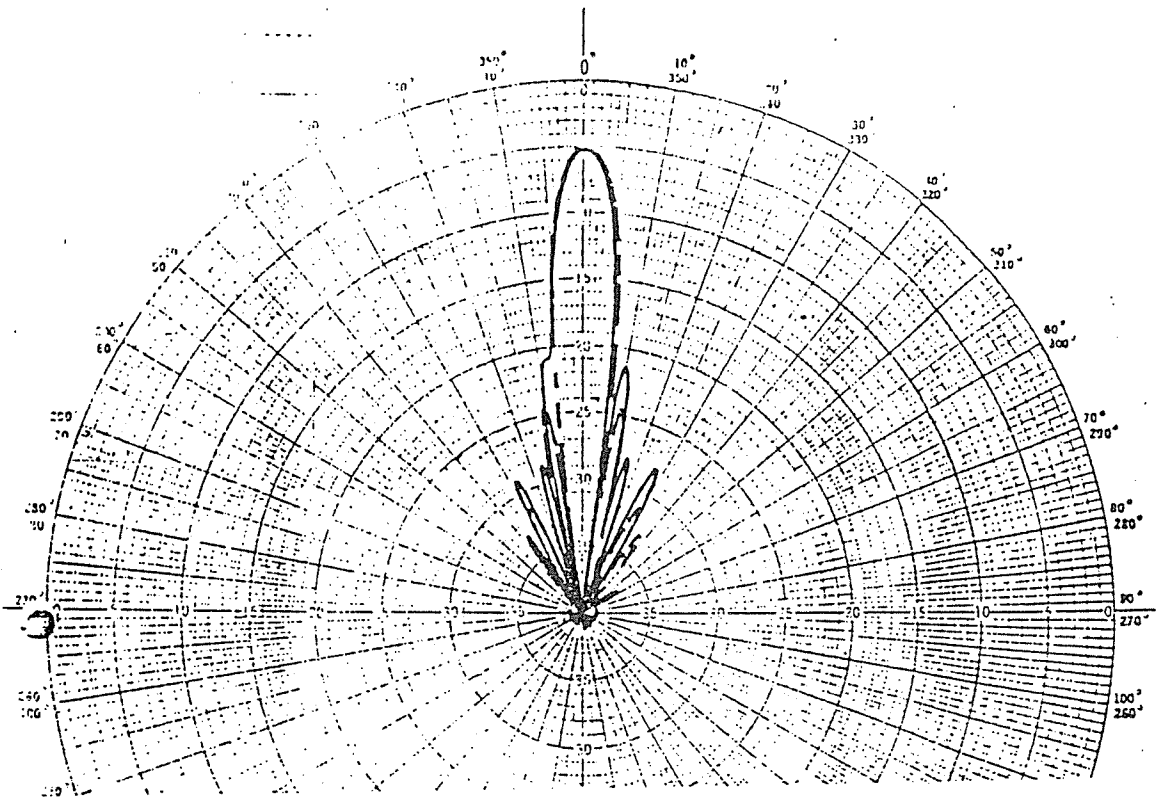
Figure 3.7 Typical antenna pattern (E–plane, horizontal polarization) of 20cm horn antenna of scatterometer. The one–way, 3dB beamwidth is 6.3° and the first side lobe is approximately 17dB down at approximately ±10° from the antenna axis.

DATE: 10/85
REFLECTOR: 2'
FEED: 166-0333-002
FREQUENCY: 14.2 GHz
POLARIZATION: VERTICAL
CALIBRATION: 0=36.2 dBil
3db BEAMWIDTH: 2.6°

RELATIVE POWER (dB)

SCALE

DATE: 10/85
REFLECTOR: 2'
FEED: 166-0333-002
FREQUENCY: 14.2 GHz
POLARIZATION: HORIZONTAL
CALIBRATION: 0=36.2 dBil
3db BEAMWIDTH: 2.4°

RELATIVE POWER (dB)

SCALE
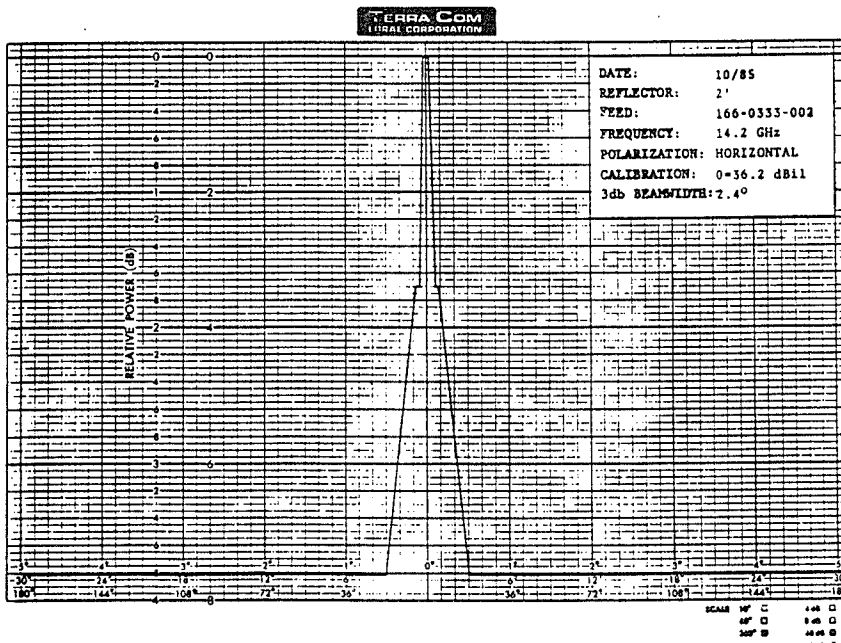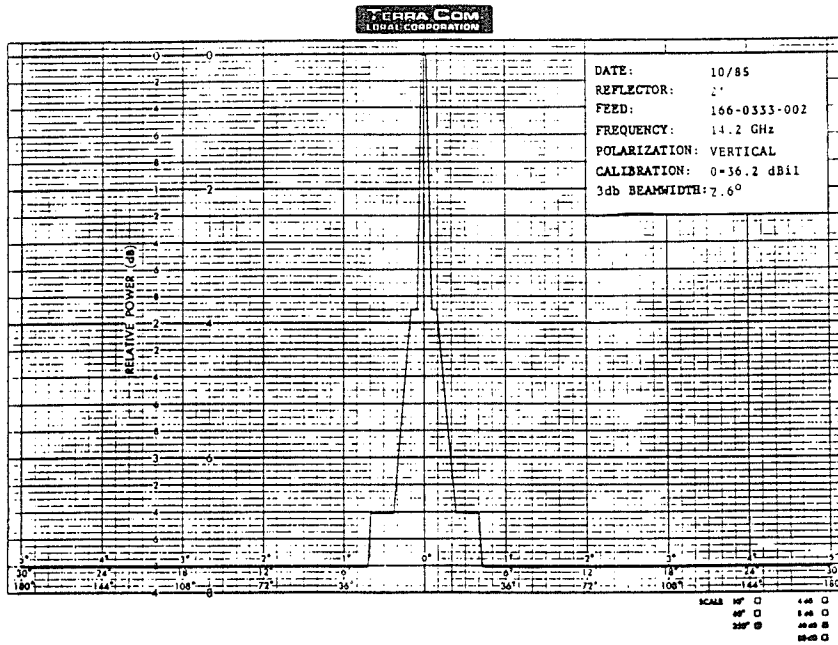
Figure 3.8: Typical antenna beam patterns for 60cm parabola (E–plane). Top: vertical polarization, one–way, 3dB beamwidth 2.6º, bottom: horizontal polarization, one–way, 3dB beamwidth 2.4º.
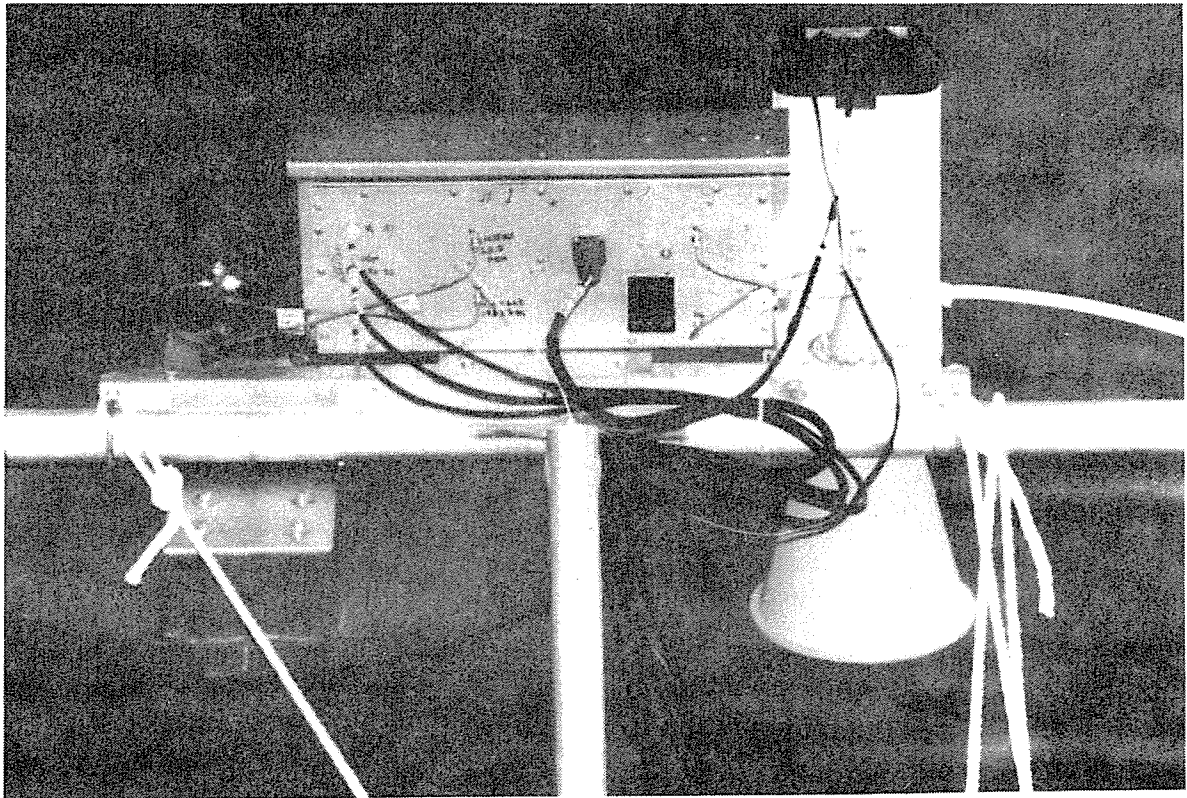
Figure 3.9: Photograph of scatterometer antenna assembly taken from the rear, showing RF unit, antennas, and video housing.

SCATTEROMETER: VV RECEIVER
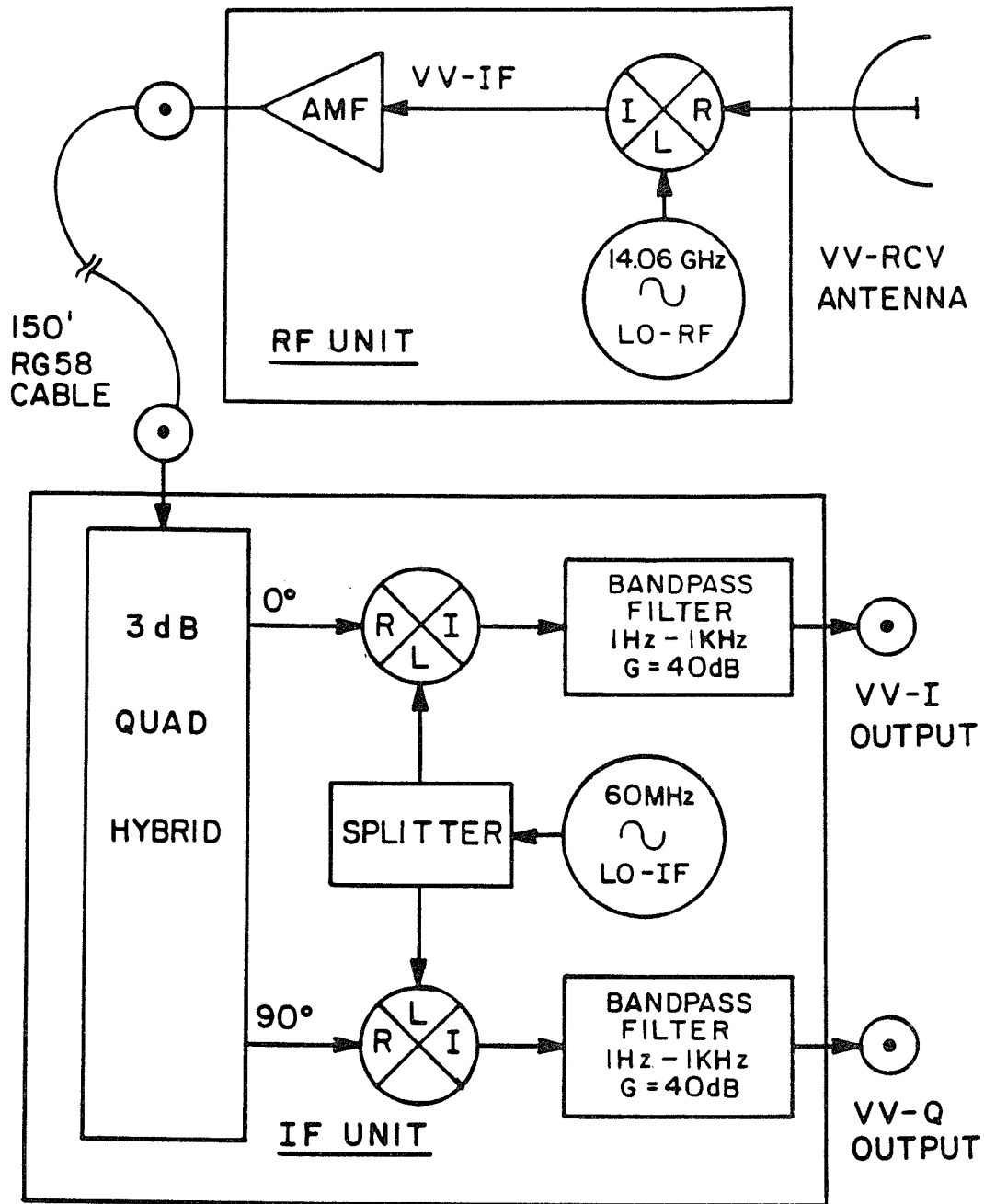
Figure 3.10: Block diagram illustrating the VV polarization channel of the receiver, consisting of the RF unit (top) and IF unit (bottom).

to provide simultaneous vertical (VV) and horizontal (HH) like–polarized measurements. The difference frequency of 60MHz between the vertically polarized transmit frequency of 14.00GHz and the horizontally polarized transmit frequency of 14.06GHz is equal to the frequency of the local oscillator used in the IF unit. For vertical polarization, the received signal frequency is 14.00GHz plus the signed Doppler shift frequency (Doppler conversion: 94Hz per ms^{-1}). In the RF unit, the VV received signal is mixed with the local oscillator, labelled LO–RF in Figure 3.10, operating at 14.06GHz. The mixer produces output at frequencies equal to the sum and difference of its two inputs. The signal corresponding to the sum frequency is eventually discarded by low pass filtering in the IF unit. In this design, the difference frequency from the RF mixer is 60MHz plus the Doppler shift frequency. This intermediate frequency signal, labelled VV–IF in Figure 3.10, is amplified in the RF unit and travels out to the IF unit along RG58 coaxial cable.

In the IF unit, the intermediate frequency signal is split and shifted in phase by a quadrature hybrid device. The phase shift for one output of this device is 0°, while that of the second is 90°. Each phase shifted signal is then separately mixed down to baseband frequency with a coherent local oscillator operating at 60MHz. These audio frequency signals are then amplified and bandpass filtered to produce the in–phase and quadrature outputs, labelled VV–I and VV–Q, respectively, in Figure 3.10. The bandpass filter has a highpass frequency of 1Hz to eliminate feed–through at the transmit frequency. The lowpass frequency limit of 1kHz eliminates the sum–frequency outputs of the mixers while providing adequate bandwidth for sea surface measurements.

As in the preliminary experiment, the scatterometer was calibrated using a swinging sphere, and the absolute radar cross–section values quoted here are accurate to within ±1dB. Experience with systems of similar design indicates that the precision, or relative stability of the calibration over time, is better than ±0.5dB. Details of the radar cross–section calibration are given in Appendix A.

An image spectrum of the actual Doppler spectrum which is symmetric about zero frequency is a consequence of amplitude and phase imbalance between the I and Q channels. The image suppression for the SAXON experiment was better than 20dB for over the frequency range of interest. The procedure used to tune the scatterometer for optimal image rejection is outlined in Appendix A.

3.1.2   SURFACE DISPLACEMENT MEASUREMENTS

Figures 3.3 and 3.4 shows the location of the two surface displacement measuring devices used in this analysis. The radio tower used to support the array of three wire wave gauges mounted vertically on the lower instrument boom can be seen in the photograph of Figure 3.11. These capacitance–type displacement gauges were constructed at MIT based on a design from the Applied Physics Laboratory, Johns Hopkins University. Figure 3.12 shows the Thorn–EMI infrared (IR) wave height sensor mounted on the upper boom at a height of 23m, approximately 5m to the north of the wire array. In this configuration, the footprint of the IR wave gauge was approximately 10m from the base of the tower. Average values of surface displacement variance from both devices were processed in real–time, while selected portions of unprocessed
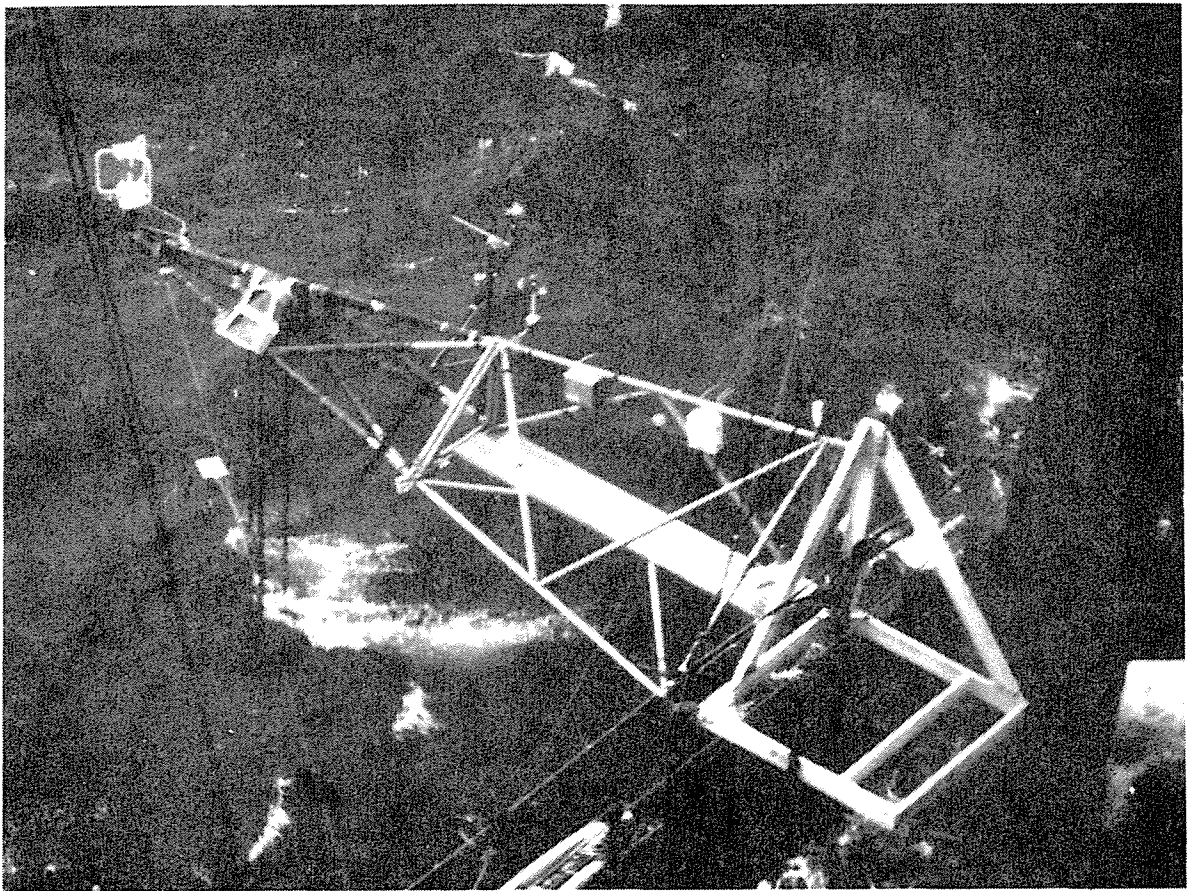
Figure 3.11 Photograph of lower instrument boom mounted on the east side of the CLT at the catwalk level. The sonic anemometer is mounted on the end of the boom. The vertical radio tower section extending below the sea surface holds the wire wave gauge array.
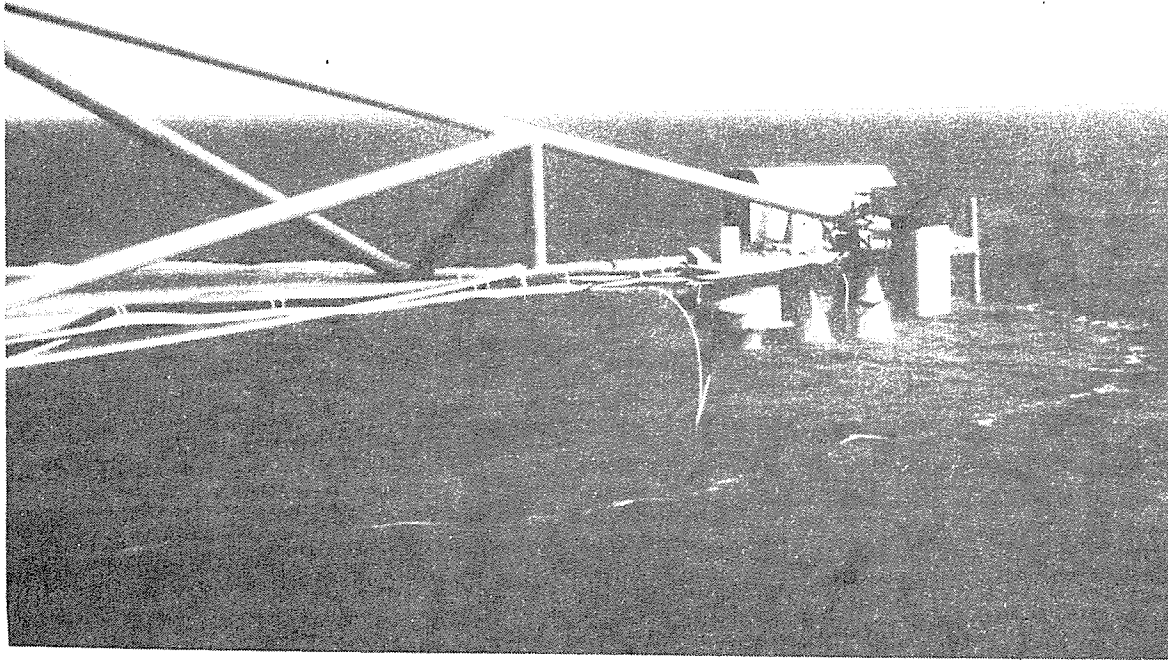
Figure 3.12: Photograph of the upper boom showing infrared wave gauge (cylindrical housing on far left). Also shown is a nadir–looking scatterometer and video camera housing not used in this thesis research (see Appendix E).

data were recorded on analog tape.

Since the scatterometer data acquisition system could be run continuously, the coverage of microwave data is significantly greater than the analog recordings of the wave gauges. Therefore, surface displacement spectra derived from the microwave measurements have been used in order to provide an adequate amount of wave data. Plant, Keller, and Cross (1983) presented a method for deriving surface displacement spectra from the time series of the mean Doppler frequency. The derivation is based on linear wave theory and the assumption that the line–of–sight velocity measured by the scatterometer is dominated by the surface wave orbital velocity. With this assumption, the measured velocity, $V(t)$, may be expressed in terms of $u(t)$, the horizontal component of orbital velocity in the propagation direction, and $w(t)$, the vertical component:

$$V(t) = u(t) \sin\theta \cos\varphi + w(t) \cos\theta \tag{3.1}$$

where θ is the incidence angle and φ is the angle between the antenna look–direction and the wave direction.

Using the shallow water horizontal and vertical orbital velocities from linear wave theory,

$$u(t) = \frac{2\pi f\ A(f)}{\tanh kh} \cos 2\pi ft, \tag{3.2}$$

$$w(t) = 2\pi f\ A(f) \sin 2\pi ft, \tag{3.3}$$

equation (3.1) for the line–of–sight velocity becomes

$$V(t) = \frac{2\pi f \; A(f)}{\tanh(kh)}\left[\sin\theta \; \cos\varphi \; \cos 2\pi ft + \cos\theta \; \tanh(kh)\sin 2\pi ft\right], \qquad (3.4)$$

where $A(f)$ is the amplitude of the wave with frequency f and wavenumber k in water depth h. By applying the Fourier transform to equation (3.4), the surface displacement spectrum $E(f)$, defined for $f \geq 0$, is found to be

$$E(f) = \frac{\tanh^2 kh \; G_{vv}(f)}{(2\pi f)^2 \; (\cos^2\theta \; \tanh(kh) + \cos\varphi \; \sin\theta)}, \qquad (3.5)$$

where $G_{vv}(f)$ is the power spectrum of $V(t)$, defined for $f \geq 0$.

Figure 3.13 shows four typical comparisons between the Doppler–derived spectra and those computed from the wire wave gauge measurements. The spectra shown are estimates of the power spectral density, computed from the complex Fourier coefficients of the finite Fourier transform. The mean Doppler frequency time series is sampled at a rate of 4Hz. Each spectrum is the average of 30 spectra computed from records zero padded to 512 points, corresponding to a total time of approximately 1 hour (3552s). A Hanning window was applied to each record prior to the use of an FFT algorithm to compute the Fourier coefficients, from which the estimate of the Doppler spectrum was computed. The spectrum was then smoothed using a weighted running average, resulting in a reduction of variance equivalent to 160 degrees of freedom.

The solid trace in each log–log graph of Figure 3.13 is the
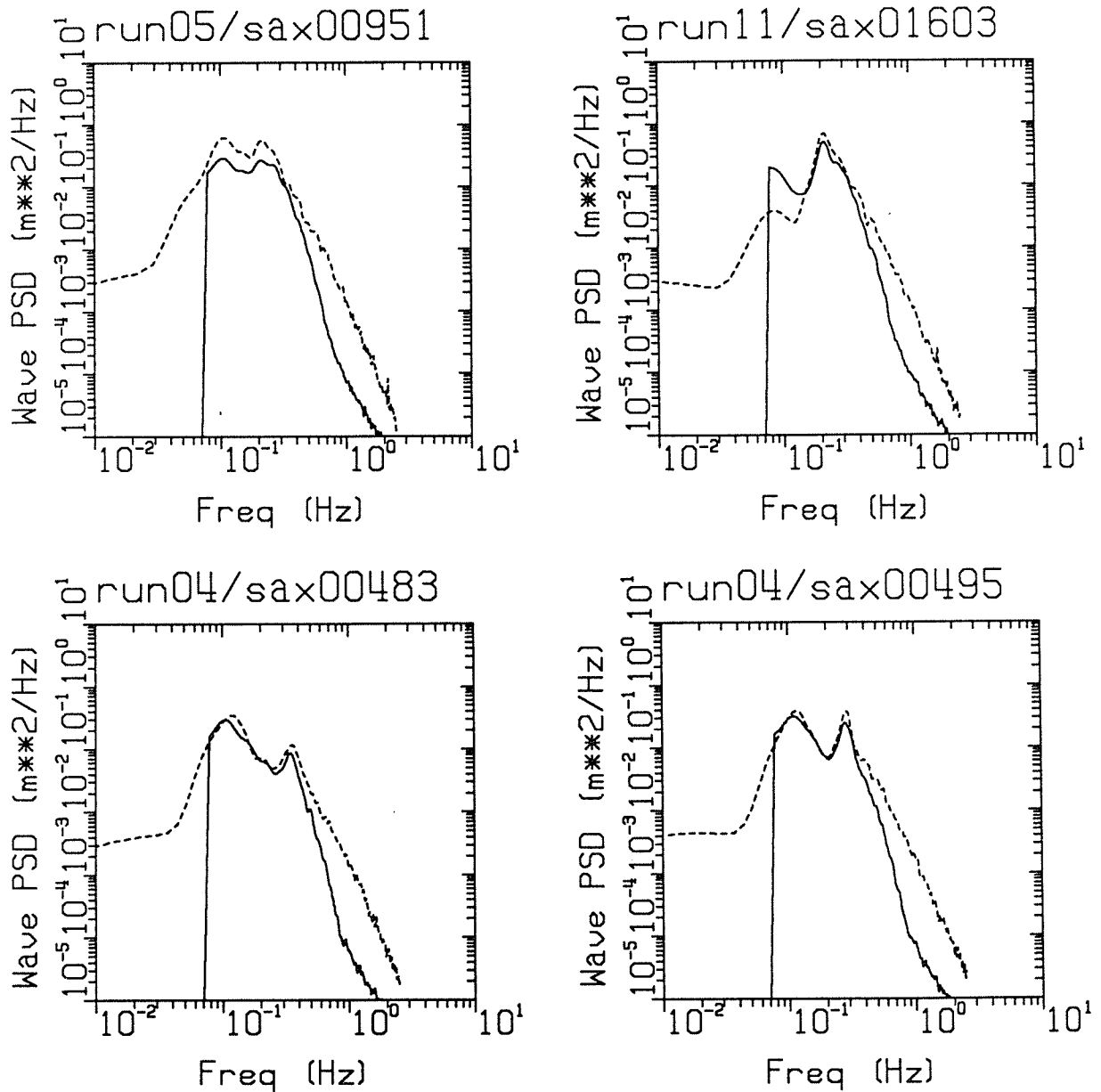
Figure 3.13: Comparison of surface displacement spectra computed from wire wave gauge measurements (dashed line) and derived from the time series of the mean Doppler frequency of the microwave measurements, equation (3.5), (solid line). Each spectrum corresponds to a one–hour time record.

Doppler–derived spectrum, equation (3.5), which begins to fall off for frequencies greater than approximately f=0.5 Hz due to the finite dimensions of the illumination area. The low frequency part of the spectrum, from $0 \leq f \leq 0.05$ Hz, is not shown or used because of the behavior of E(f) in expression (3.5) as f approaches zero requires a noise cutoff. Spectra from the wire wave gauge measurements are plotted as dashed lines in Figure 3.13. Comparison of the Doppler–derived spectra with the wire measurements indicates good agreement in frequency distribution up to roughly f=0.5Hz. In some cases, the magnitude of the Doppler–derived spectra is lower than that of the wire measurements, which may be due to the assumption of a unidirectional wave field in the derivation of equation (3.5).

3.1.3 METEOROLOGICAL MEASUREMENTS

Measurements of wind speed and direction, air and sea temperature, and relative humidity were processed in real–time to produce average values at 10–minute intervals. The anemometer, air temperature sensor, and relative humidity probe were mounted at the top of the light tower as shown in Figure 3.14, at a height of approximately 42m above the sea surface. The sea temperature sensor was tethered from a float to remain approximately 1m below the sea surface. Model numbers and specifications for the the meteorological instruments, manufactured by R.M. Young Co., are given in Appendix E.

The logarithmic wind profile at height z is given by
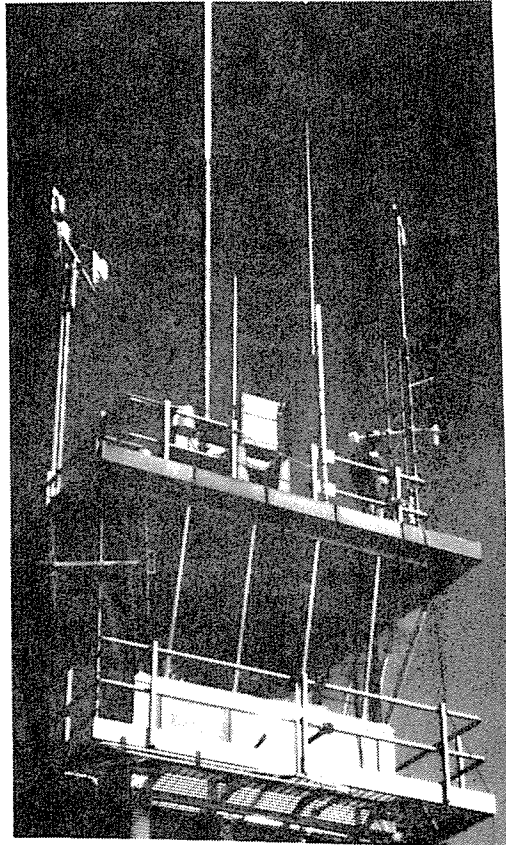
Figure 3.14: Photograph showing radio tower installed atop the beacon tower (far right corner) holding the propeller anemometer, air temperature probe, and humidity sensor.

$$U_z = \frac{u_*}{\kappa} \{ \ln(z/z_0) - \Psi(z/L) \}, \tag{3.6}$$

where $\kappa = 0.40$ is von Karman's constant, z_0 is the roughness height of the surface, and L is the Monin–Obukov stability length. Values of friction velocity, u_*, and wind speed referenced to a height of 10m, U_{10}, were iteratively computed using the 10 minute averages of wind speed, air–sea temperature difference, and relative humidity. In the computation, the roughness height z_0 was taken to be composed of a smooth surface contribution z_s and an aerodynamic roughness contribution z_c as outlined in Smith (1988):

$$
\begin{aligned}
z_0 &= z_s + z_c, \\
z_s &= 0.11\nu / u_*, \\
z_c &= a\, u_*^2 / g,
\end{aligned}
\tag{3.7}
$$

where ν is the dynamic viscosity of air and g the gravitational acceleration. The value of a=0.0185 suggested by Wu(1980) was chosen as being consistent with the limited fetch and shallow water depth at the Chesapeake Light Tower. The bulk stability parameter z/L was estimated using the formula proposed by Large and Pond (1981). The computational scheme and formulas used to estimate the friction velocity, u_*, using bulk aerodynamic measurements are given in detail in Appendix B. The computed results were further averaged to produce values of u_* and U_{10} corresponding to the 1–hour

measurement periods of interest.

Direct measurements of friction velocity were made during the SAXON experiment by RISO National Laboratory, Roskilde, Denmark, with a sonic anemometer identical to that used in the preliminary experiment described in Chapter 2. The sonic anemometer can be seen in Figure 3.11 mounted on the end of lower instrument boom. The boom extended 7m to the east of the tower in the direction 65° true at an elevation of 5m above MSL. Averages of the direct measurements of friction velocity over 10-minute intervals were computed in real-time. Unfortunately, the sonic anemometer measurements of friction velocity were found to be susceptible to tower interference. The data have been judged to be free of tower interference for a 90° window of azimuth centered about the direction in which the lower boom was pointed (Geernaert, 1989, personal communication). Since the scatterometer measurements of interest covered a much wider range of wind directions than the window covered by the sonic anemometer, the direct measurements of u_* were used only for comparison with the friction velocity values computed using the bulk formulation outlined above.

Figures 3.15 and 3.16 show two comparisons of time series of the sonic anemometer measurements and bulk method estimates of friction velocity, u_*, wind speed referenced to 10m, U_{10} (labelled WS on the plots), and wind direction, WD. The bulk method values are plotted as (+)'s and the sonic measurements as (x)'s. The shaded region in the graph of wind direction is the range of wind directions for which the sonic anemometer measurements are suspected of being influenced by the tower. The wind direction in the first comparison (Figure 3.15) falls mostly in the range of unaffected sonic
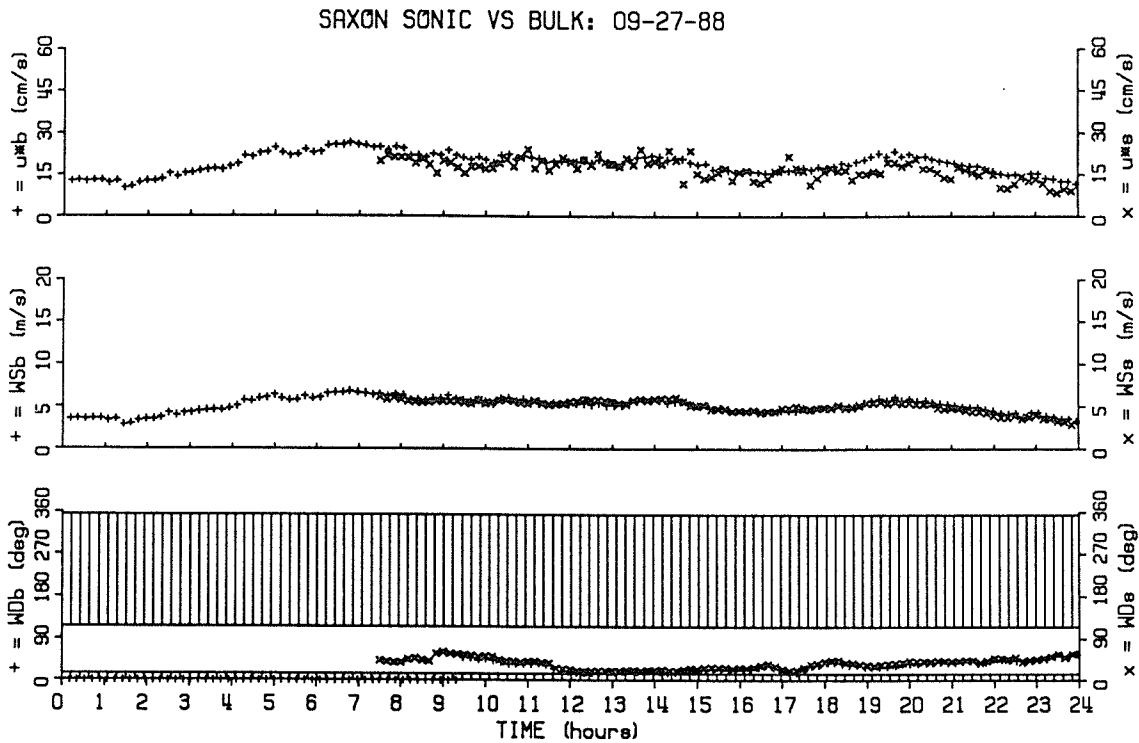
Figure 3.15: Time series comparing 10–min averages of sonic anemometer measurements (X) and bulk formula estimates (+) of friction velocity, u* (top) and wind speed reference to 10m (middle, labelled WS) for 9–27–88. The shaded region in the graph of wind direction, WD, (bottom) shows the range of values over which the sonic anemometer measurements were suspected to be influence by the tower.
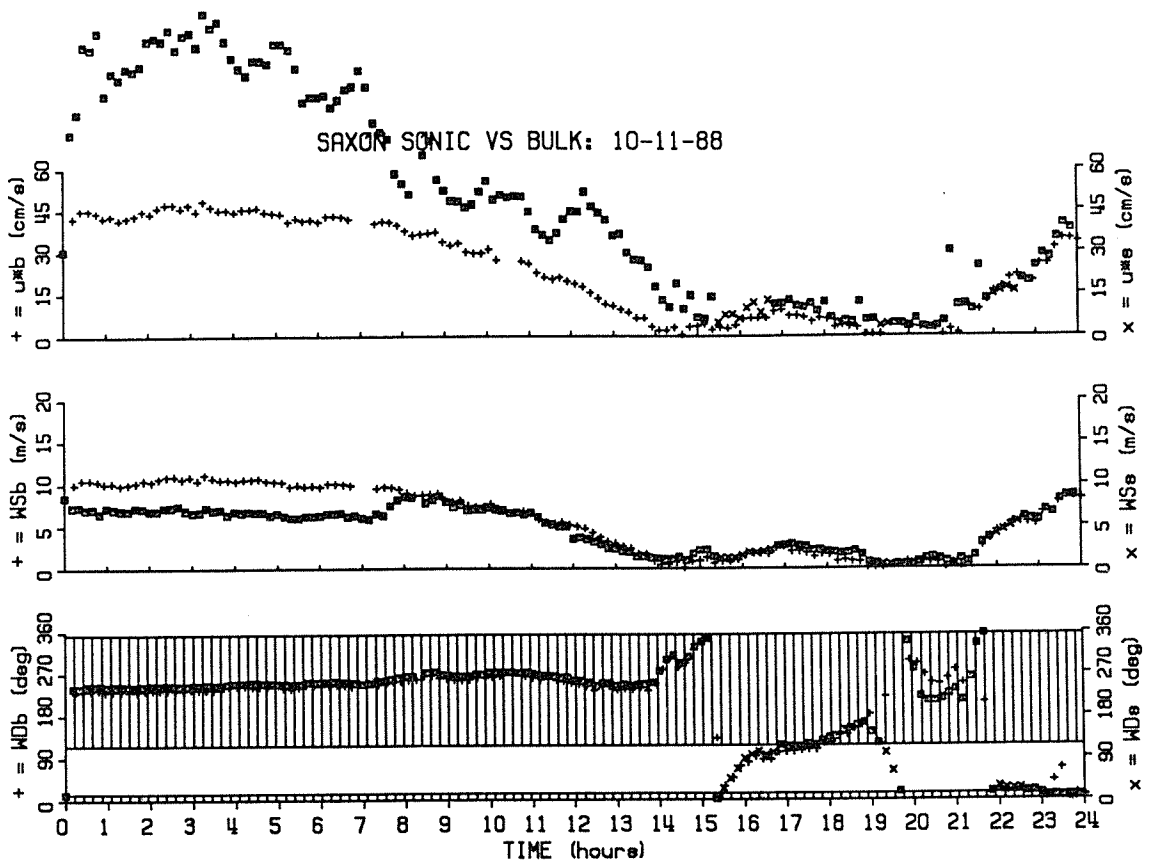
Figure 3.16: Same as Figure 3.15 except for 10–11–88. Sonic data for wind directions falling in the range of suspected tower interference are plotted as square symbols.

anemometer measurements. Comparison of the time series of u_* for this example shows that the bulk method and sonic anemometer values agree reasonably well. In general, the sonic anemometer data exhibit a greater amount variance than the bulk–method values. The second comparison (Figure 3.16) is a case where the sonic anemometer measurements were clearly affected by the tower. Figure 3.17 shows scatter plots of the bulk measurements versus the sonic anemometer measurements for all periods of microwave data used in this thesis. The sonic measurements considered to be influenced by the tower are shown in the upper plot. The lower plot of Figure 3.17 shows the sonic data judged to be free of tower interference, for which the wind direction, WD, was in the range $20^{\circ} \leq WD \leq 110^{\circ}$. In general, the agreement between the bulk method values and the unaffected sonic anemometer data is consistent with the expected performance of the bulk formulation (Blanc, 1985).

3.1.4 VIDEO RECORDINGS

Simultaneous video recordings colocated with the scatterometer illumination area were made with a black and white NEC model TI–23A $\frac{1}{2}$–inch format CCD camera with a 1/1000th sec shutter. Two different lenses were used at 45° incidence: a 12.5 mm lens with a resulting field of view of approximately 18x18m^2 and a 25 mm lens with a field of view of approximately 9x9m^2. The recordings were made with a Panasonic model AG–6300 VHS video cassette recorder. The video camera was mounted on the antenna assembly and aligned with the geometric axis of the antennas (see Figures 3.6 and 3.9). A calibration of this alignment was made in the field with the scatterometer aimed vertically downward and a corner reflector
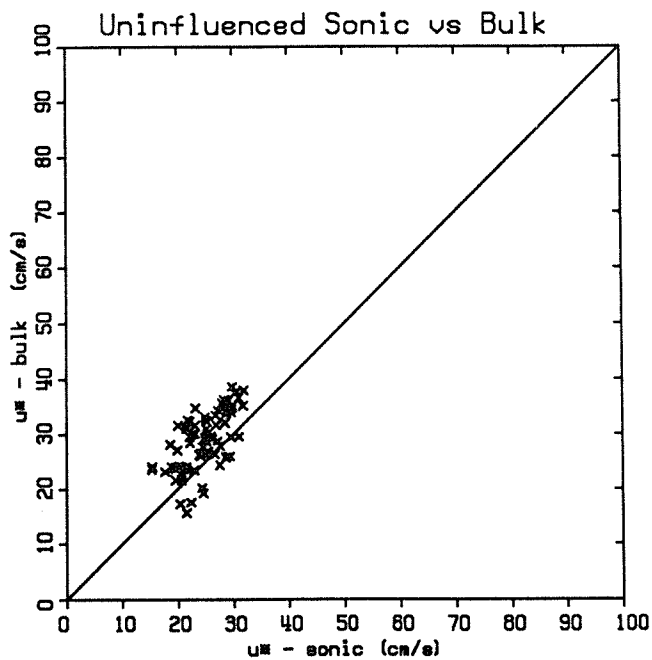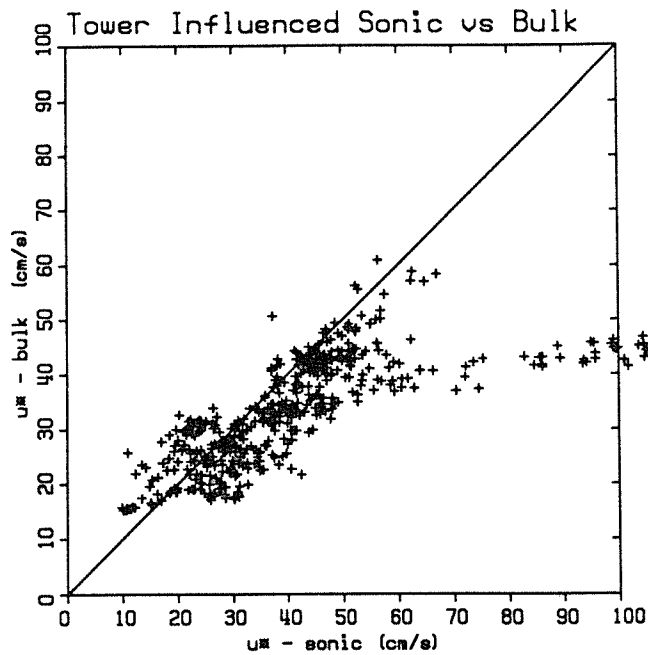
Figure 3.17: Scatter plots of 10–min averages of bulk formula estimates vs sonic anemometer measurements of u* for the 41 hours of microwave data used in this thesis. The sonic anemometer data in the top graph are for wind directions falling in the range of suspected tower interference, while those of the lower graph are judged to be unaffected by the tower.

hanging from the axis of the antennas. The alignment is estimated to be accurate to within 0.5m.

3.2 DATA ACQUISITION AND PROCESSING PROCEDURES

Figure 3.18 is a photograph of the equipment racks which housed the data acquisition and processing hardware. A block diagram of the scatterometer and video recording system is shown in Figure 3.19. Table 3.1 summarizes the sampling rates and processing procedure for each data channel.

Table 3.1: DATA SAMPLING RATES

CHANNEL	SAMPLING RATE (Hz)	COMMENTS
VV–I	2000	Time series of σ^0, 1st and
VV–Q	2000	2nd spectral moments,
HH–I	2000	record length 10 minutes,
HH–Q	2000	time step 0.25s
WIRE WAVE GAUGES	60	Sampled continuously at given
IR WAVE GAUGE	60	rate and processed
WIND SPEED	60	in real–time to produce
WIND DIRECTION	60	10–minute averages
AIR TEMPERATURE	10	Sampled once in 10 minutes
SEA TEMPERATURE	10	at the given rate, averaged
HUMIDITY	10	over a period of 10 seconds

In order to provide continuous data acquisition and rapid access to experimental results, a real–time system was designed to acquire and process the microwave data in the field. This system was based on an NEC Powermate 386 personal computer equipped with a Metrabyte DAS–16 Analog–to–Digital converter board and an N/Hance optical disk drive for data
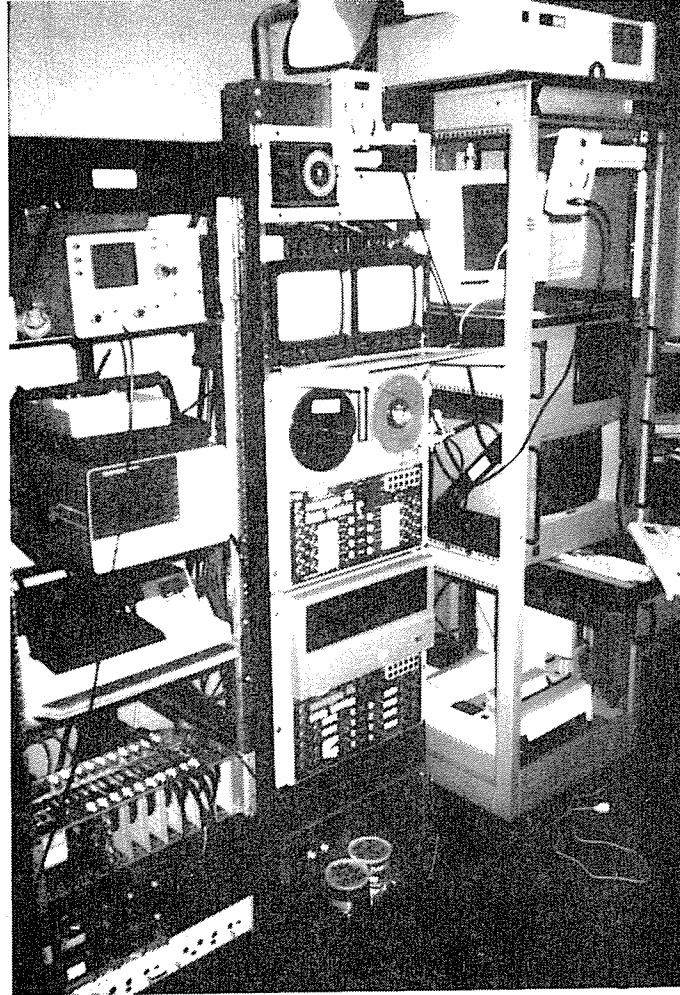
Figure 3.18: Photograph of instrument racks containing data acquisition and processing system.

SCATTEROMETER DATA ACQUISITION SYSTEM
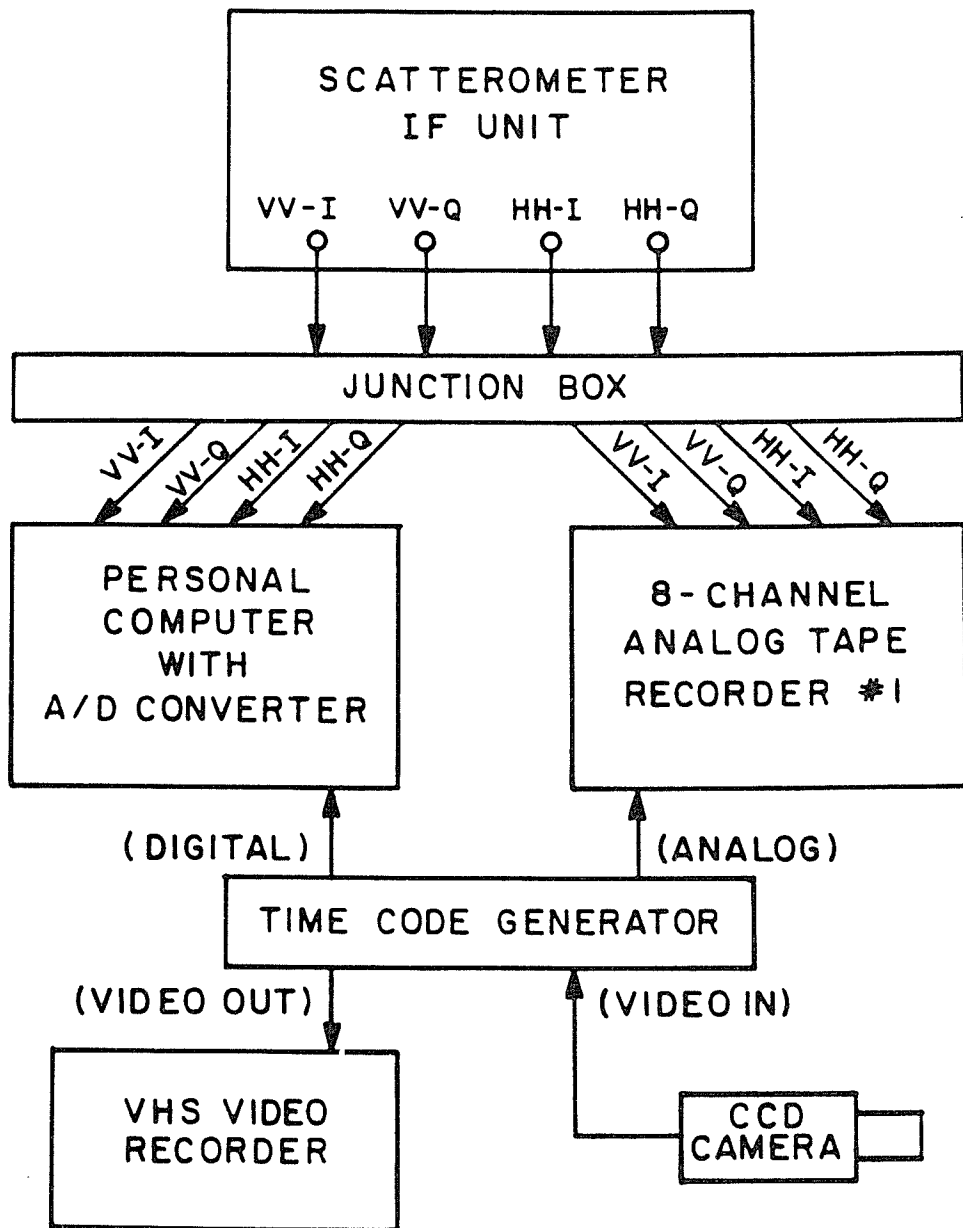
Figure 3.19: Block diagram of scatterometer and video data acquisition and processing system. The timing of all recording systems was synchronized by using an IRIG–B time code generator with a serial output and video time insertion.

storage. Selected periods of the scatterometer and wave gauge data were also recorded on a Hewlett–Packard HP3968A FM 8–channel analog tape recorder (bandwidth 625 Hz) as a backup to the PC–based system and in order to have an archive of unprocessed data. The time base for the experiment was provided by a DATUM model 9300 IRIG–B time code generator/translator configured with an serial output port and video time insertion. All times used in the SAXON experiment are local time, which was Eastern Daylight Savings Time. The latter option adds the time to the video image, while the serial port provides computer access to the time code. The analog IRIG–B time code signal was recorded directly on the analog tape recorder used for archival purposes. The data acquisition system for the meteorological and wave gauge data is represented in Figure 3.20. An IBM–AT personal computer was used to produce the 10–minute averages outlined above, while a second analog tape recorder was used for archival purposes.

3.2.1 SAMPLING RATE AND INTEGRATION TIME

The instantaneous backscattered power is a power–weighted sum of contributions from scatterers distributed over the illumination area. The relative motion of the individual scatterers causes fluctuations in the receive power, introducing uncertainty between the measured power and its true mean. Electrical noise also adds to this uncertainty in the received power as an estimator. In order to obtain a meaningful estimate of the mean backscattered power, the received power is averaged in time in order to reduce the uncertainty.

Let the true mean output power be $\overline{P}$, the estimated mean $\hat{P}$, and the

ENVIRONMENTAL DATA ACQUISITION SYSTEM
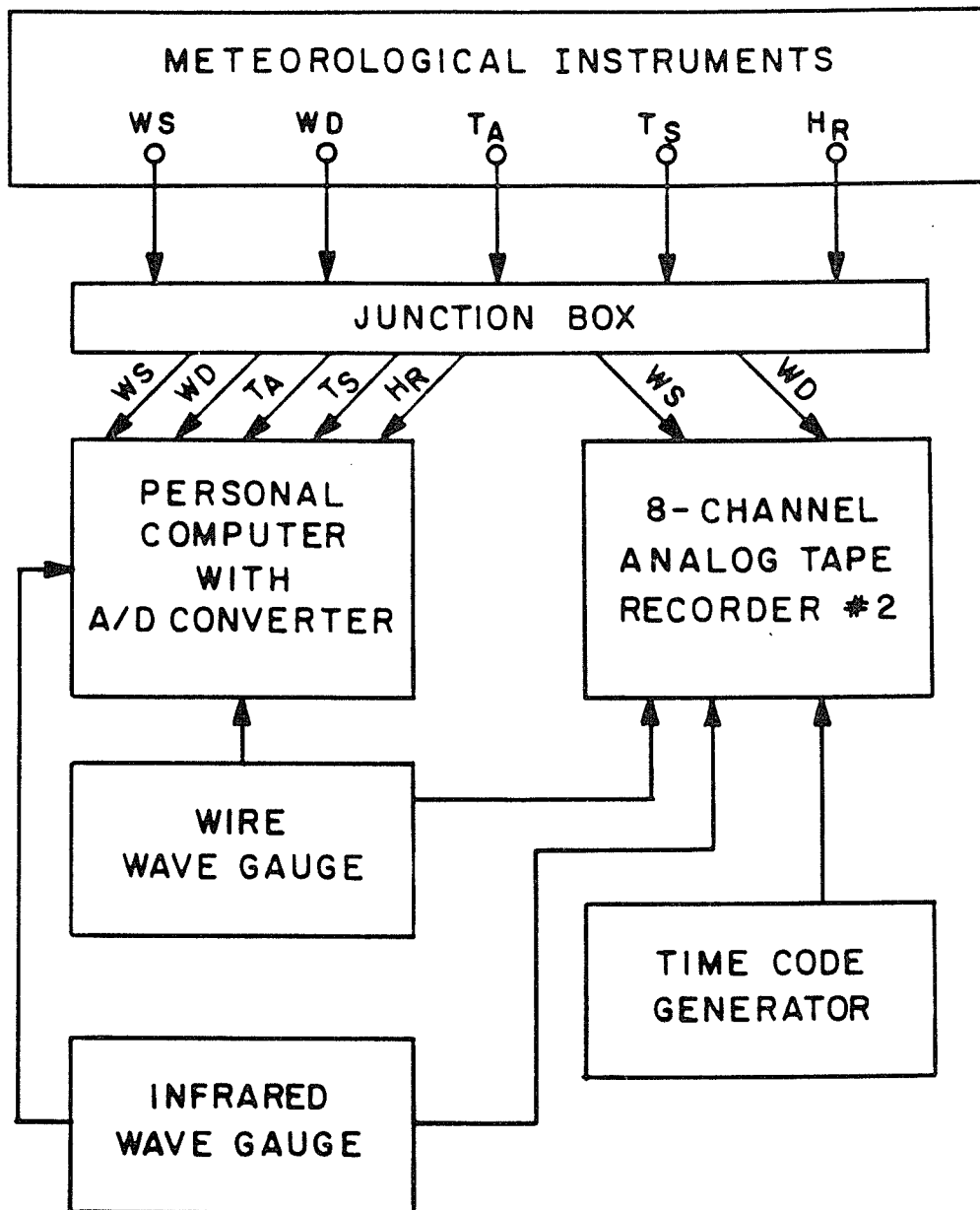
Figure 3.20: Block diagram of environmental data acquisition and processing system.

m–th individual sample of the power be P_m. For M independent samples, the estimate formed by a uniform average

$$\hat{P} = \frac{1}{M} \sum P_m \qquad (3.8)$$

will result in a reduction in the variance of $\hat{P}$ over that of a single sample estimate by a factor of 1/M. The range of the summation in equation (3.8) and all other summations in this chapter is from m=1 to m=M−1.

However, if the samples are correlated, the variance reduction is given by the equivalent number of independent samples, which can be formulated in terms of the normalized covariance of the received power. The equivalent number of independent samples M_I for a stationary process with M equally–spaced but correlated samples is given by

$$\frac{1}{M_I} = \sum \frac{M - |m|}{M^2} \rho_P(m\Delta t) \qquad (3.9)$$

where $\rho_P(m\Delta t)$ is the normalized covariance or correlation coefficient at lag $\tau = m\Delta t$ and Δt is the time sampling interval (Doviak and Zrnic, 1984; Papoulis, 1965). Note that the correlation coefficient in equation (3.9) is that of the received power which is proportional to the square of the receiver output voltage. The time series of the received power can be thought of as the output of a square law detector with the received Doppler signal as input. In this case the output correlation coefficient is equal to the square of the input correlation coefficient (Papoulis, 1965).

In order to estimate the reduction of variance, consider a signal with Gaussian power spectrum as input to a square law detector. The Gaussian power spectrum P(f) with bandwidth B and mean frequency $\bar{f}$, is given by

$$P(f) = \frac{P_o}{\sqrt{2\pi}\ B} \exp\{\ -(f-\bar{f})^2/\ 2B^2\ \}, \qquad (3.10)$$

and corresponding autocorrelation function at lag τ is given by

$$R(\tau) = P_o \exp\{\ -2(\pi B\tau)^2\}\ e^{j2\pi\bar{f}\tau}. \qquad (3.11)$$

The magnitude of the normalized covariance for the received power is

$$\rho_P(m\ \Delta t) = \exp\{\ -(2\pi m B\Delta t)^2\}, \qquad (3.12)$$

where B is the bandwidth of the input power spectrum. Substituting (3.12) into (3.9), the number of independent samples for Gaussian distributed backscatter becomes

$$\frac{1}{M_I} = \sum \frac{M - |m|}{M^2} \exp\{\ -(2\pi m B\Delta t)^2\} \qquad (3.13)$$

The number of independent samples M_I given by (3.13) is plotted in Figure 3.21 as a function of the normalized bandwidth $B_N = B\Delta t$ for different

number of total samples M. Notice that B_N and M are <u>not</u> independent, since $M=T_I/\Delta t$, where T_I is the averaging or integration time. Therefore, for a given bandwidth B, horizontal lines in Figure 3.21 are lines of constant integration time T_I, while vertical lines correspond to lines of constant sampling rate. The reduction in variance is effectively determined by the integration time, as long as the time series is not under sampled.

Thus the choice of averaging or integration time involves a compromise between a time long enough to provide adequate reduction of the variance of the estimator and yet short enough to resolve the dynamics of the breaking process. An integration time of 0.25s was judged as a suitable compromise. For a nominal bandwidth of 25Hz and a sampling rate of 2 KHz, the number of independent samples with $T_I=0.25s$ is approximately 20, implying that the variance of the power estimate would be 5% of its mean.

From a dynamical point of view, an integration time of $T_I=0.25s$ may be somewhat long. For example, the crest of a wave with phase speed 10ms^{-1} would transit a 2m–diameter illumination area in 0.20s. In order to resolve the features of such an event, an integration time of 0.10s or less may be desirable. However, the number of independent samples is reduced in direct proportion to the reduction in integration time. An investigation of the effect of a shorter integration time T_I was performed on the archived data and is discussed in chapter 5.

3.2.2 COVARIANCE PROCESSING TECHNIQUE

Characterization of the backscattered signal is provided by estimating the moments of its power spectrum. The ith moment of the frequency power
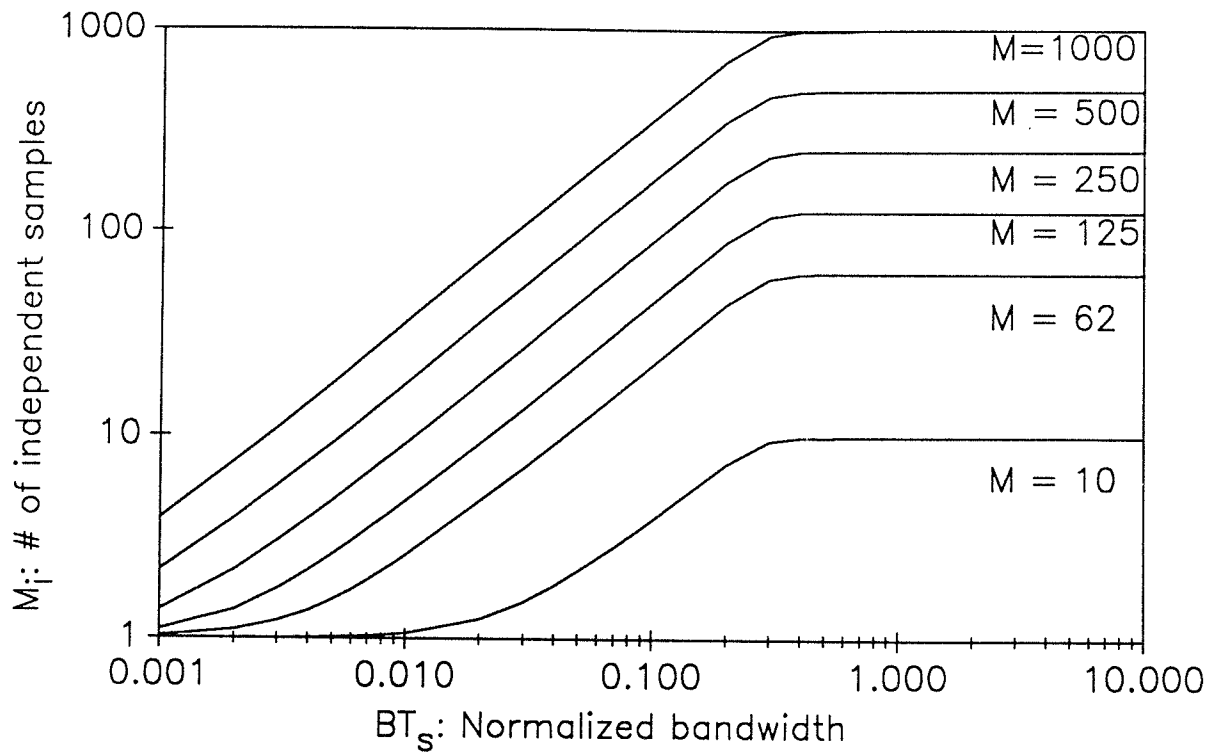
Figure 3.21: Equivalent number of independent samples as a function of normalize bandwidth, BT_s, where T_s is the sampling interval (Δt in the text), for a Gaussian input to a square law detector (equation (3.13)).

spectrum P(f) is given by

$$\int f^i \, P(f) \, df, \quad i = 0, 1, 2, \ldots \tag{3.14}$$

The first three moments are the most important for interpreting the physical processes responsible for the backscattered signal.

The zeroth moment of the spectrum is the return power and provides a measure of target strength. In general, it is a function of the transmitted signal (frequency and polarization), measurement geometry (incidence angle and azimuth relative to surface wave direction), and surface characteristics (roughness and local slope). The first moment of the spectrum normalized by the zeroth moment corresponds to the mean Doppler frequency shift. It is proportional to the power–weighted line–of–sight velocity of the scatterers within the illumination area. The square–root of the second moment of the power–normalized spectrum provides a measure of the Doppler bandwidth and as such indicates the range of scatterer velocities responsible for the return signal. The reciprocal of the bandwidth is interpreted as a measure of the coherence time of the process.

The microwave signal was digitally sampled at 2 kHz and reduced to time series of the received power, mean Doppler frequency, and Doppler bandwidth with an integration time of 0.25s. The mean Doppler frequency and bandwidth were computed using the covariance moment estimation technique commonly used in weather radar (Doviak and Zrnic, 1984). Traditional methods for moment estimation involve direct computation from

estimates of the power spectrum P(f). In practical terms, this procedure dictates the use of a Fast Fourier Transform algorithm to estimate P(f) followed by the moment computations. Computer hardware exists which permits this processing to be performed in real–time for the integration times of interest here. However, the expense of implementing a spectral–based computation scheme was judged to be prohibitive, and the covariance processing technique for spectral moment estimation was chosen as a practical alternative.

Covariance processing was developed by Rummler (1968) and is extensively used in Doppler weather radar applications. A general outline of the technique follows and the computational formulas are given in Appendix C. The technique is widely applied to pulsed Doppler systems but is readily adapted to continuous wave measurements. Oceanographic applications include Doppler velocity measurements using sonar (Pinkel 1979, 1983; Plueddemann, 1987) and measurements of the frequency dispersion of acoustic tones (Dahl, Baggeroer, and Dyer, 1988).

The covariance processing technique is based on the fact that the autocovariance function and the power spectral density form a Fourier transform pair. The autocovariance function $R(\tau)$ is defined for lag τ as

$$R(\tau) = z^*(t) \; z(t+\tau) \qquad (3.15)$$

where $z(t)$ is a complex time series given by

$$z(t) = I(t) \; + \; j \; Q(t) \qquad (3.16)$$

where the real part of z(t), Re(z)=I(t), and the imaginary part of z(t), Im(z)=Q(t) are referred to as the in-phase and quadrature demodulates, respectively.

Since the power spectrum P(f) is defined as the magnitude of the Fourier transform of the autocorrelation R(τ), the latter may be expressed in terms of the former as

$$R(\tau) = \int P(f) \exp\{j2\pi\tau \, f\} \, df. \tag{3.17}$$

This expression may be rewritten in terms of the power-weighted mean Doppler frequency, $\bar{f}$, as

$$R(\tau) = \exp\{j2\pi\tau \, \bar{f}\} \int P(f) \exp\{j2\pi\tau \, (f-\bar{f}) \} \, df. \tag{3.18}$$

Note that if the integral in (3.18) is real, then the mean Doppler frequency $\bar{f}$ is given simply as

$$\bar{f} = \frac{\arg(R(\tau))}{2\pi\tau}. \tag{3.19}$$

In order for the integral in (3.18) to be real, the spectrum P(f) must be symmetric with respect to $\bar{f}$. Otherwise, there is a bias introduced which depends on the imaginary part of the integral in (3.18). However, this bias is

small for asymmetric spectra with bandwidth small compared to the Nyquist interval (Doviak and Zrnic, 1984). This narrow–band assumption is the main limitation on the performance of the first moment estimator for signals with large signal–to–noise ratios and large signal–to–noise–bandwidth ratios.

The constraint on the performance of the second–moment estimator is more severe. Rigorously, the bandwidth estimator is unbiased only for Gaussian shaped spectra. For a time series with Gaussian power spectrum (3.10) and corresponding autocorrelation function (3.11), the bandwidth B may be obtained from the the magnitude of the normalized covariance

$$\rho(\tau) = \exp\{ -2(\pi B \tau)^2 \} \tag{3.20}$$

for a given lag τ_0 as

$$B^2 = \frac{\ln\{\rho(\tau_0)\}^{-1}}{2 \ \pi^2 \ \tau_0^2} \ . \tag{3.21}$$

Figures 3.22 is an example of the performance of the first and second moment estimators compared to direct computation from periodogram estimates of the power spectrum. The mean Doppler frequency estimator shows excellent agreement, while the bandwidth estimator tends to underestimate spectrally computed value. Note however that the agreement is better at higher rather than at lower bandwidths. Since our main interest is in characterizing breaking events (which tend to have large bandwidths), the performance of the second–moment estimator was judged to provide a good compromise between
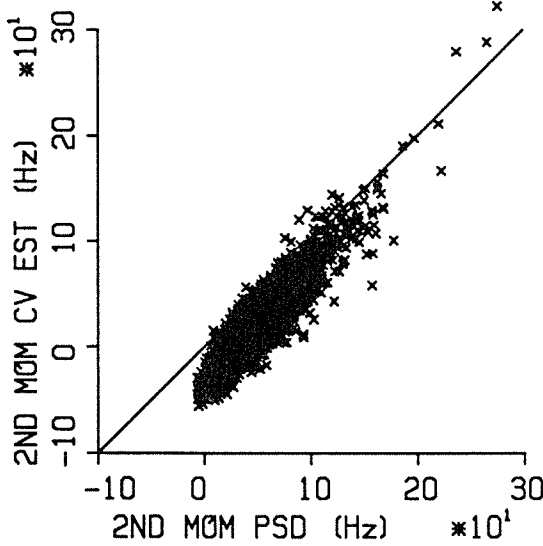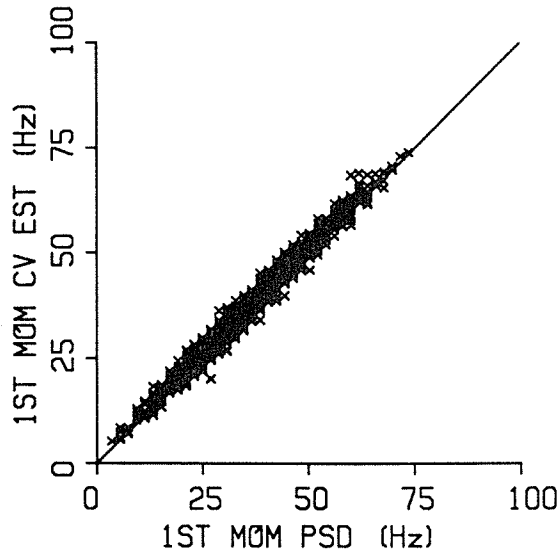
Figure 3.22: Scatter plots comparing first and second Doppler spectral moments computed using the covariance processing technique (y–axes, labelled CV EST) and direct computation from the power spectrum (x–axes, labelled PSD).

accuracy and cost.

3.2.3 DATA EDITING

The wide variety of environmental conditions encountered during the SAXON experiment required careful editing of the data. Constraints on the wind direction relative to antenna look–direction, variability of wind speed, and wave conditions were set in order to isolate their effect on the results. As outlined in chapter 2 (section 2.2), the radar cross–section of an individual breaking event may depend on its orientation with respect to the antenna look–direction. In order to minimize the effect of this dependence, the angle φ between the wind and look–direction was restricted to the range $0° \leq \varphi \leq 25°$ for all data processed.

As outlined in chapter 2 (section 2.1), a record length of one–hour was chosen over which to compute averages of the microwave statistics related to individual breaking events. With an anticipated cubic friction velocity dependence of the frequency of occurrence of breaking events (equation 1.19), a constraint on the variability of u_* and/or the wind speed is appropriate to eliminate scatter due to uncertainty in the wind stress. To this end, the standard deviation of u_* and U_{10} for each 1–hour record was limited such that the range of u_* values during any 1–hr period was less than 2.5 cms^{-1} and similarly the range for U_{10} was less than 0.5 ms^{-1}. In addition to a constraint on the variability of the friction velocity, a lower limit was imposed. For $u_* \leq 25$ cms^{-1}, the number of large sea spikes was too small to permit meaningful statistics over the 1–hour measurement period and thus data below this value were not included.

A total of 44 one–hour records of data processed in situ have been selected for analysis using the constraints on wind speed variability and antenna look direction outlined above. This data set is composed of seven numbered subsets of several hours each, which are summarized in Table 3.1. The duration of each run is indicated in the daily time series of environmental conditions shown in Figures 3.23 through 3.29, which also include plots of the corresponding surface displacement spectra. The time series are the 10–minute averages of friction velocity, u_*, wind speed referenced to 10m, U_{10}, wind direction, WD, and significant wave height, SWH (defined as 4 times the standard deviation of the surface displacement). The mid–time of the 1–hour measurement periods within a given run is shown for each surface displacement spectrum in Figures 3.23–3.29. Each spectrum has been extended in frequency from f=0.6 Hz to f=2.5 by a dashed line of f^{-4}. This extension will be used in chapter 5 in using models based on moments of the surface displacement spectrum.

The edited data set, summarized in Table 3.2, covers a wide range of wind and wave conditions. The summary table lists the number of 1–hour records used in each run and the range of parameters characterizing the wind and wave conditions. The frequencies F_{LO} and F_{HI} correspond to the peak frequencies of the surface displacement spectra which are generally associated with swell and wind waves, respectively. The variability of wind and wave conditions apparent in the time series and in the surface displacement spectra indicates that equilibrium conditions did not exist. Runs designated 4, 5, and 9 exhibit mixed sea conditions, as indicated by the two distinct peaks in the surface displacement spectra. For Runs 1 and 6, the spectra have single, low

frequency peaks characteristic of long wavelength swell. Runs 11 and 12 also exhibit unimodal surface displacement spectra, but with peak frequencies in the range of locally generated wind waves. Fetch lengths for runs 1 and 4 were essentially unlimited, whereas the remainder of the runs had fetch lengths in the range of 28–32km.

Table 3.2: <u>DATA RUN CHARACTERISTICS</u>

RUN ID	HRS	FLO (Hz)	FHI (Hz)	SWH (m)	u* (cm/s)	U_{10} (m/s)	FETCH(km) look—dir
1	8	.13–.16	N/A	1.4–1.8	23–32	6.3–9.6	unlimited NE2/57°
4	4	.11	.27–.35	0.7–1.0	26–30	7.1–8.5	unlimited SW1/164°
5	6	.11	.25	1.0–1.1	26–31	6.3–7.9	32 NE1/342°
6	3	.09–.11	N/A	1.5–1.8	38–43	9.6–10.5	32 NE1/342°
9	5	0.10	.24–.27	1.1–1.3	42–46	10.4–11.5	28 SW3/220°
11	6	N/A	.22–.24	0.7–1.0	25–33	6.2–8.3	32 NE1/342°
12	12	N/A	.20–.25	1.0–1.2	38–48	8.4–11.7	32 NE1/342°

<u>Key to Table 3.2</u>

Run ID: Identification number

HRS: Number of hours in the run

FLO: Peak frequency of the surface displacement spectrum in the range associated with long wavelength, low frequency swell

FHI: Peak frequency of surface displacement spectrum in higher frequency range of shorter wavelength, higher frequency wind waves

SWH: Significant wave height, defined as $4 \, (\text{var} \; \eta(t))^{\frac{1}{2}}$, where $\eta(t)$ is the surface displacement measured in meters

u*:   Friction velocity (see equations (1.5), (3.6), and Appendix B)

U_{10}:   Wind speed referenced to an elevation of 10m above the sea surface (see equation (3.6) and Appendix B)

Fetch: Distance from measurement site to nearest land in upwind direction

Location/   location of scatterometer on tower (see Figure 3.4b)
Direction   look direction of antennas corresponding to location
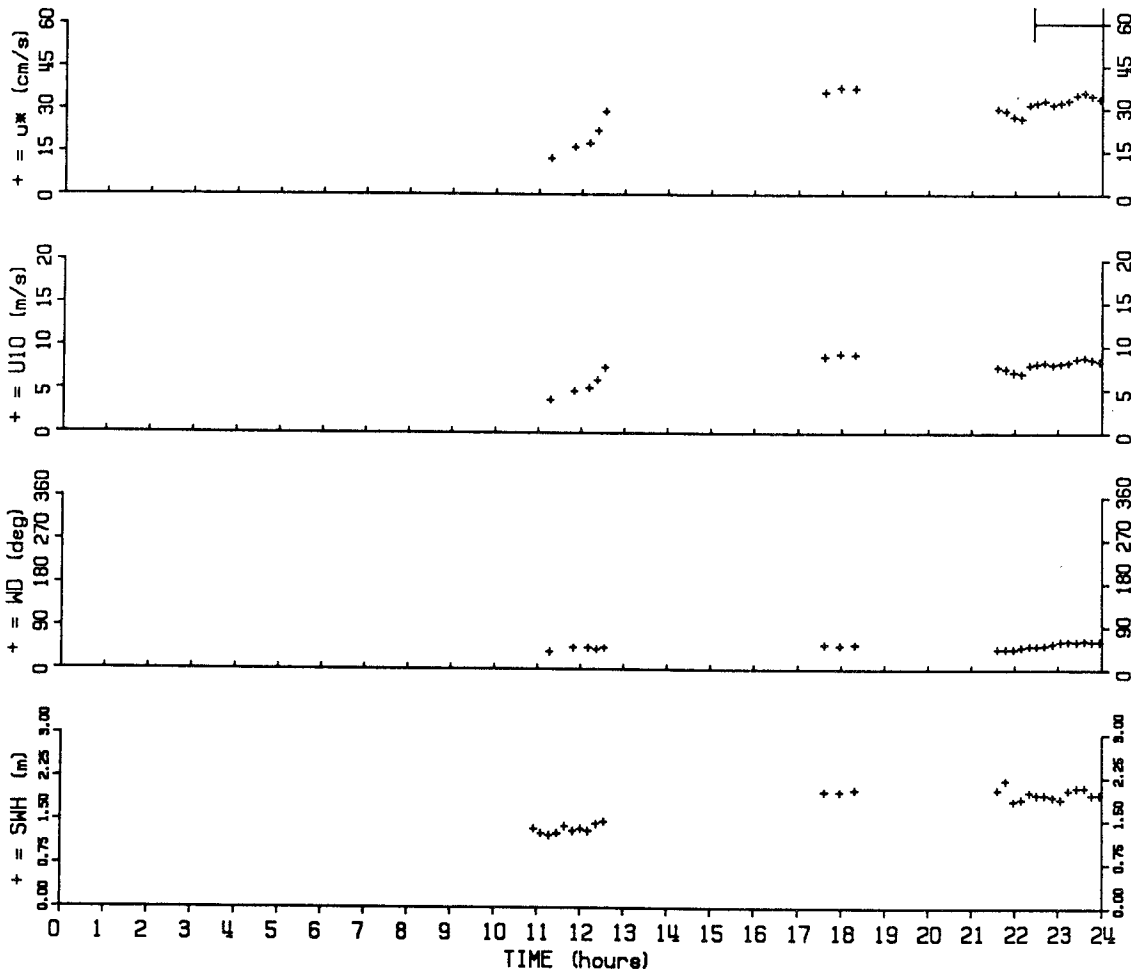
Figure 3.23a: Time series of environmental measurements showing time period (horizontal line in upper graph) for RUN 01: friction velocity, u^*, and wind speed reference to 10m, U_{10}, computed using bulk formula method, wind direction, WD, and significant wave height, SWH.

SAXON RUN DURATION 09-30-88: RUN 01
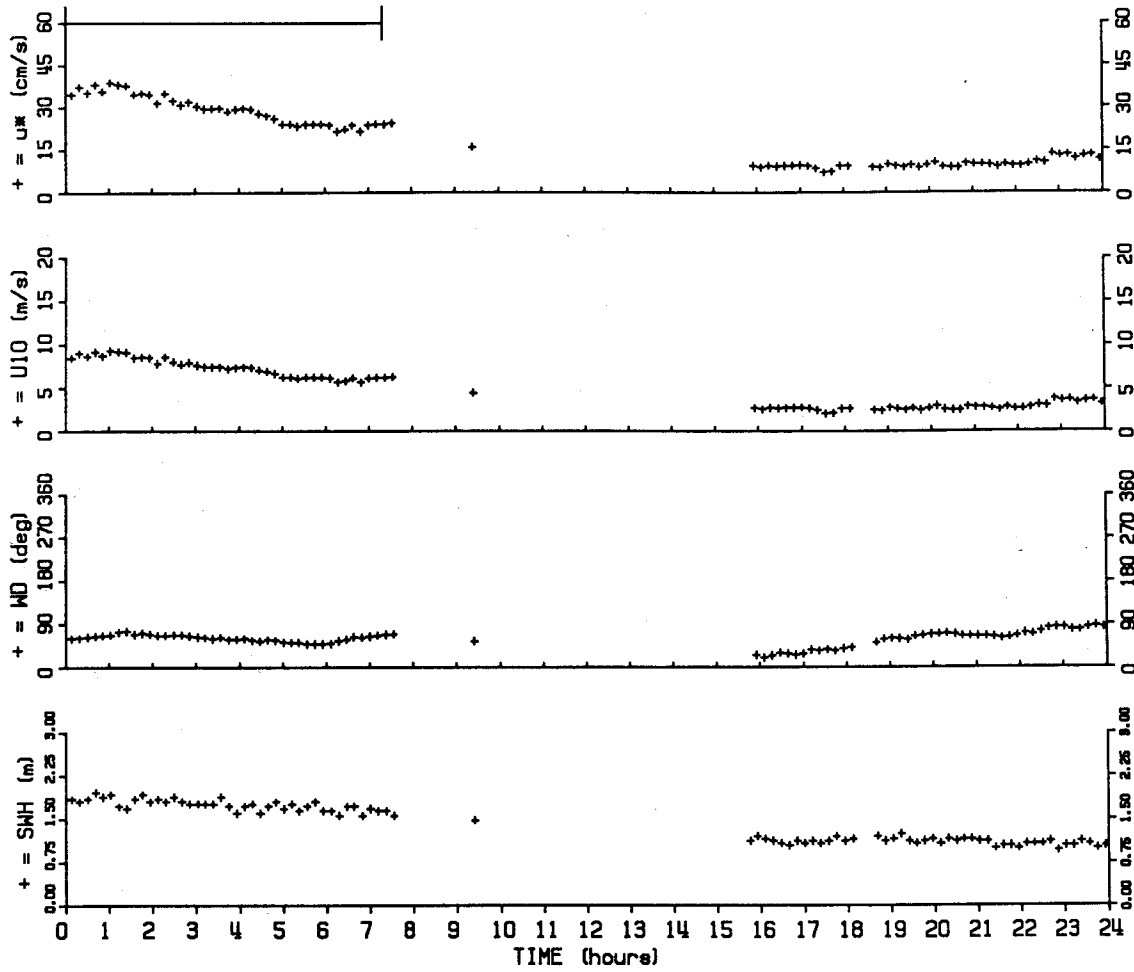
Figure 3.23a (continued): See caption, previous page.
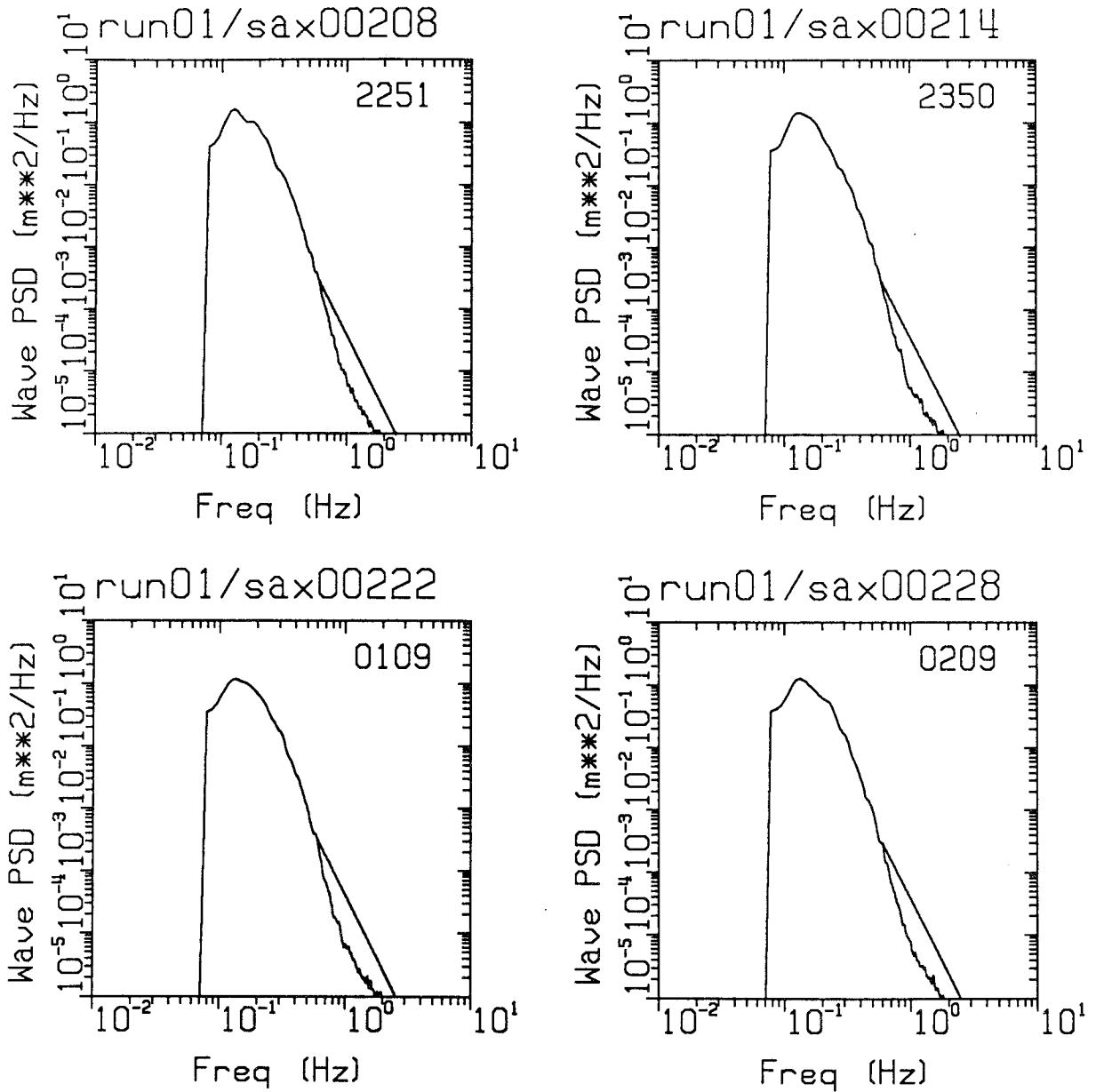
Figure 3.23b: Hourly surface displacement spectra derived from microwave measurements (equation 3.5) for RUN 01. Mid–time of measurement is indicated in upper right hand corner of each plot. Spectra have been extended from f=0.6Hz with an f^{-4} power law.
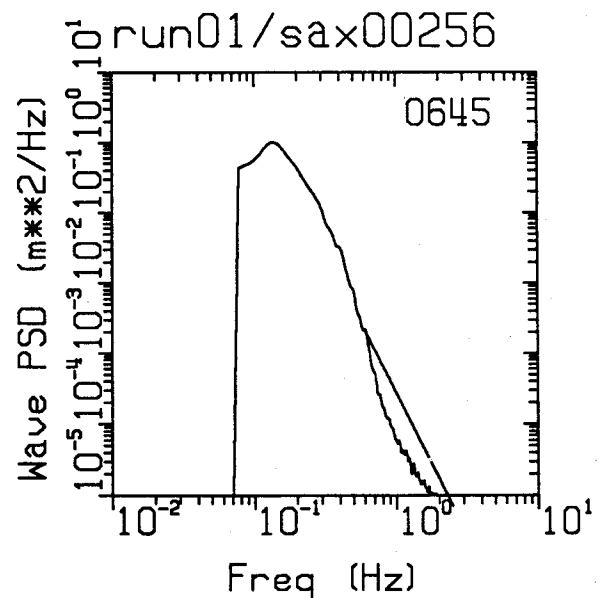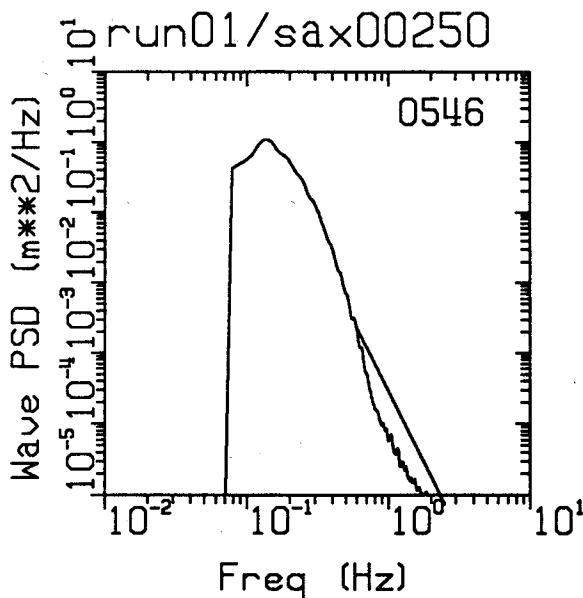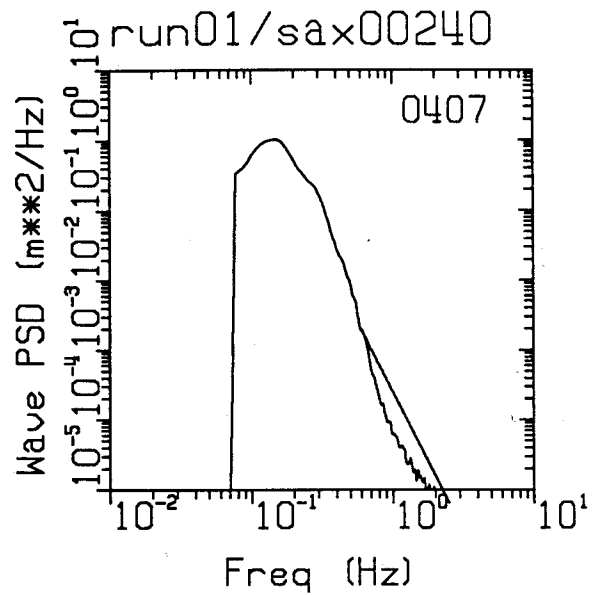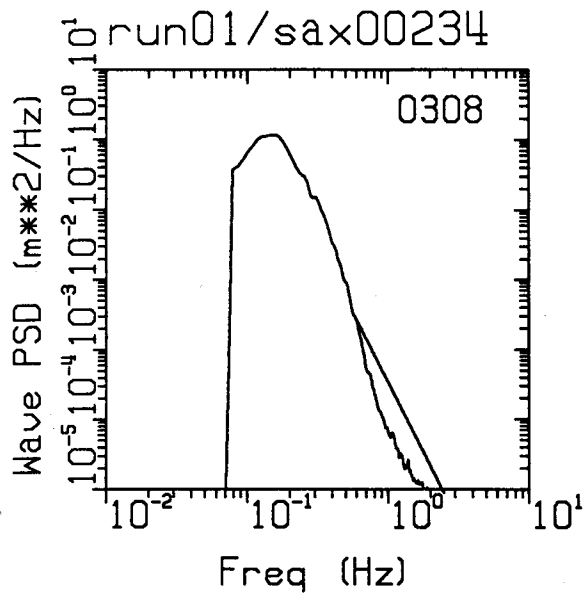
Figure 3.23b (continued): See caption, previous page.

SAXON RUN DURATION 10-02-88: RUN 04
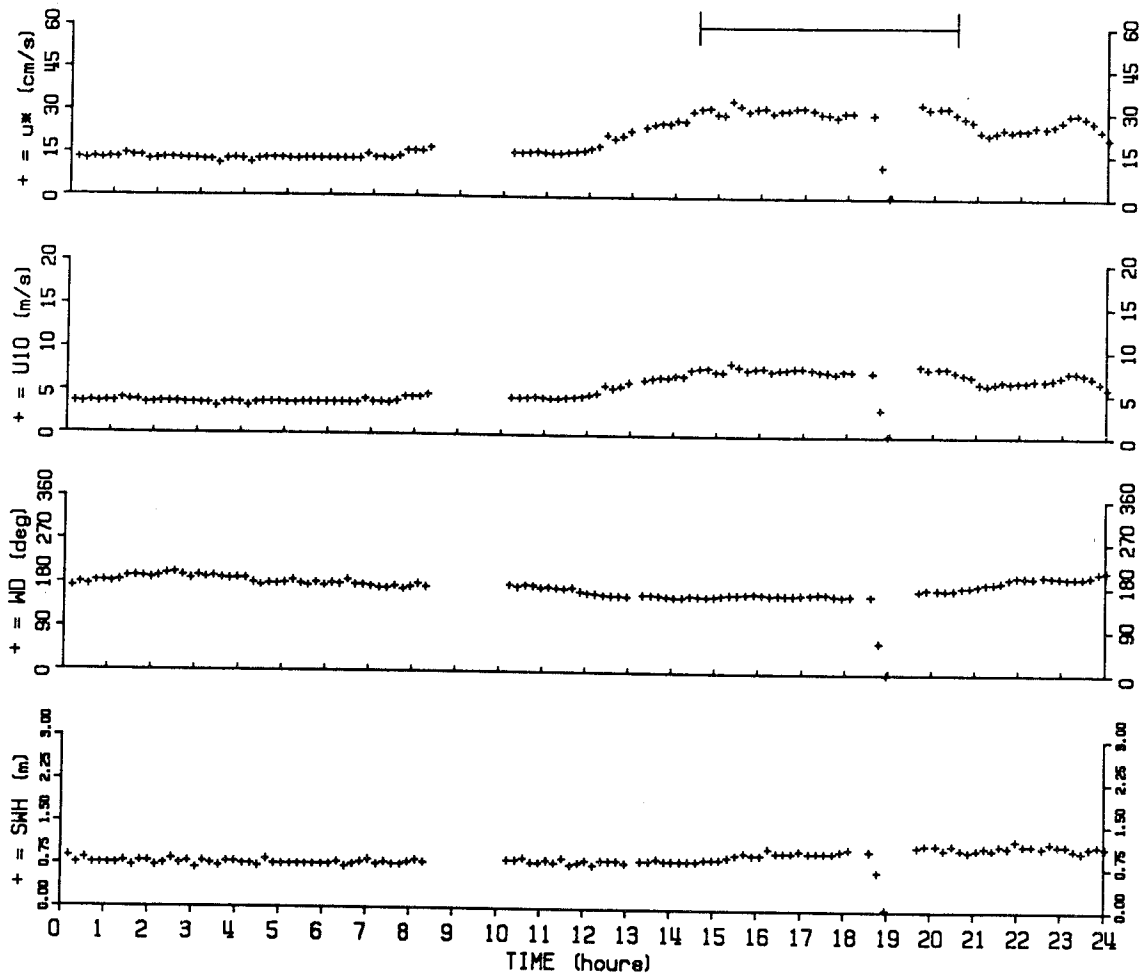
Figure 3.24a: Time series of environmental measurements showing time period (horizontal line in upper graph) for RUN 04: friction velocity, u^*, and wind speed reference to 10m, U_{10}, computed using bulk formula method, wind direction, WD, and significant wave height, SWH.
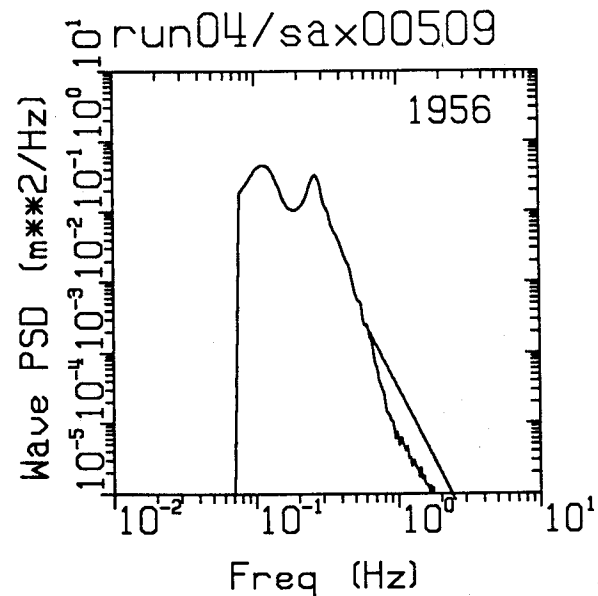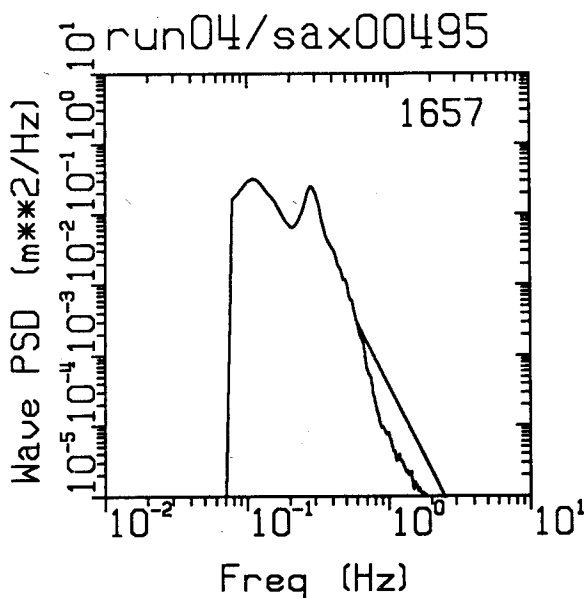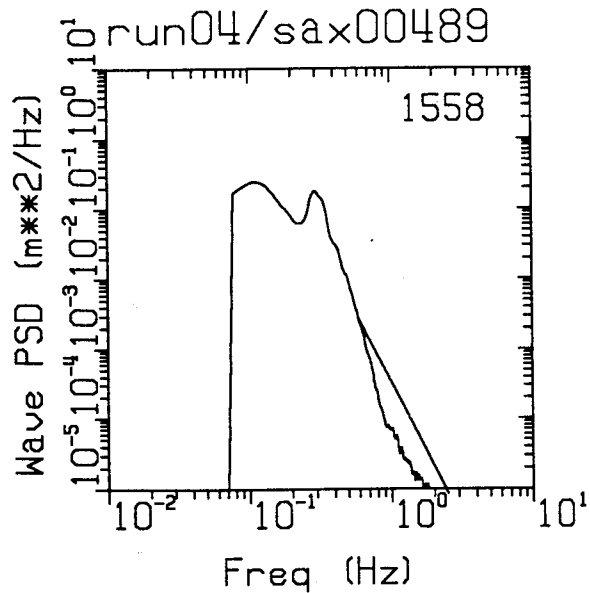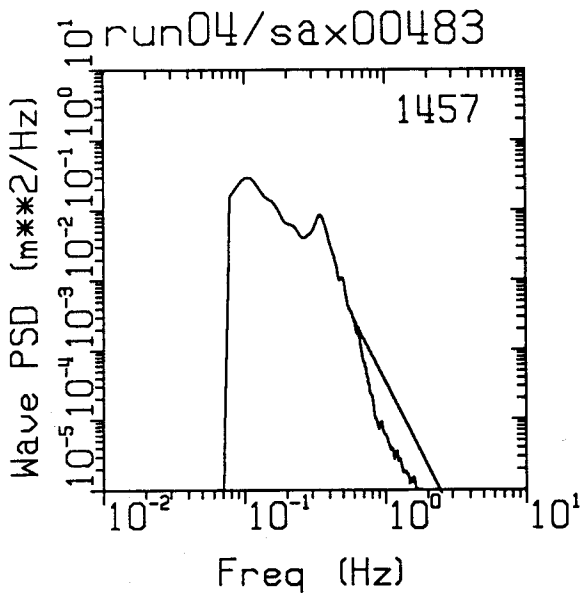
Figure 3.24b: Hourly surface displacement spectra derived from microwave measurements (equation 3.5) for RUN 04. Mid–time of measurement is indicated in upper right hand corner of each plot. Spectra have been extended from f=0.6Hz with an f⁻⁴ power law.

SAXON RUN DURATION 10-06-88: RUN 05
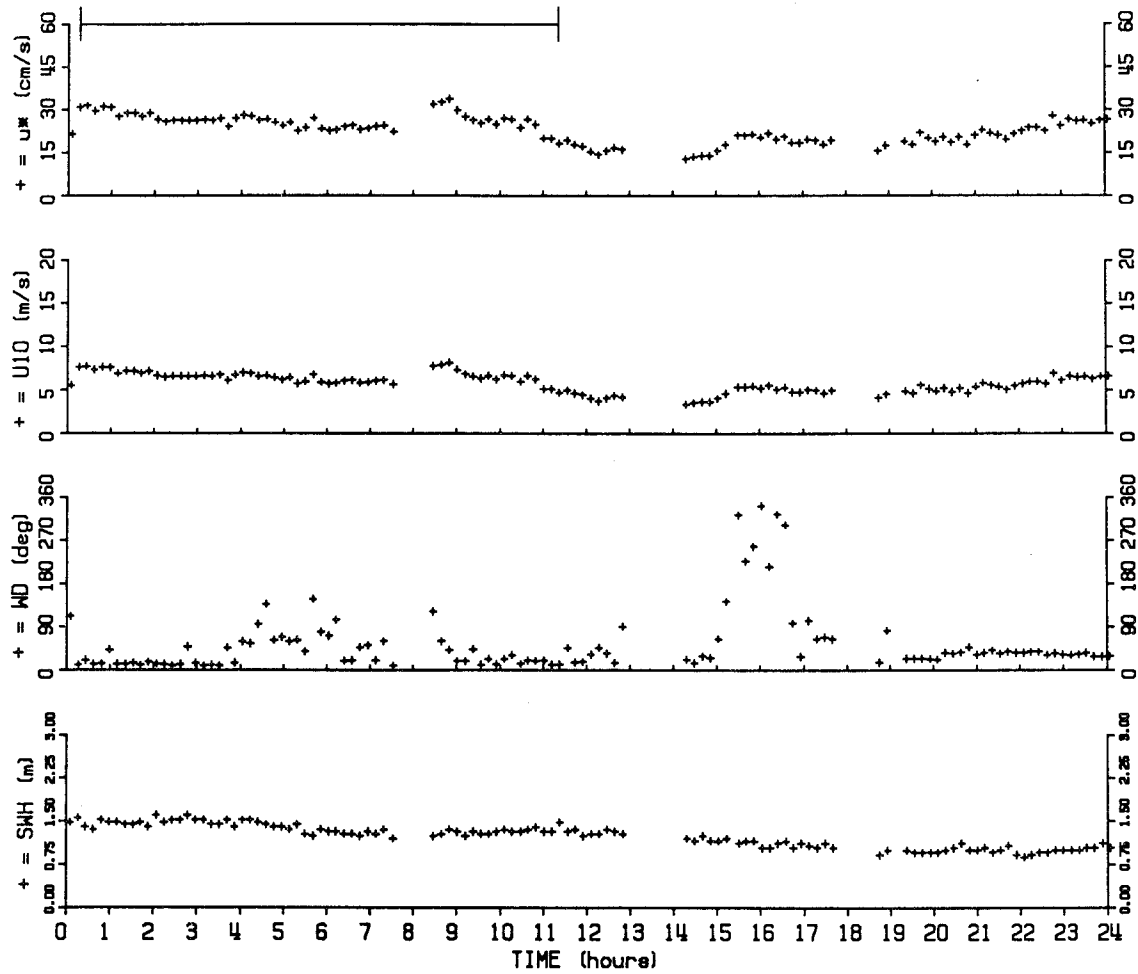
Figure 3.25a: Time series of environmental measurements showing time period (horizontal line in upper graph) for RUN 05: friction velocity, u^*, and wind speed reference to 10m, U_{10}, computed using bulk formula method, wind direction, WD, and significant wave height, SWH.
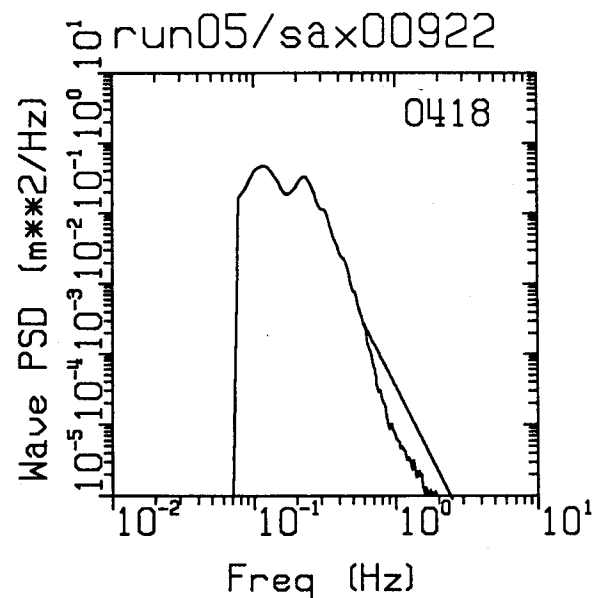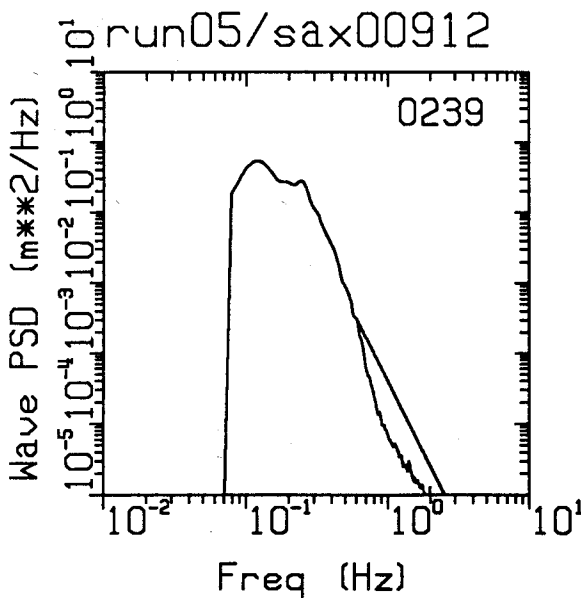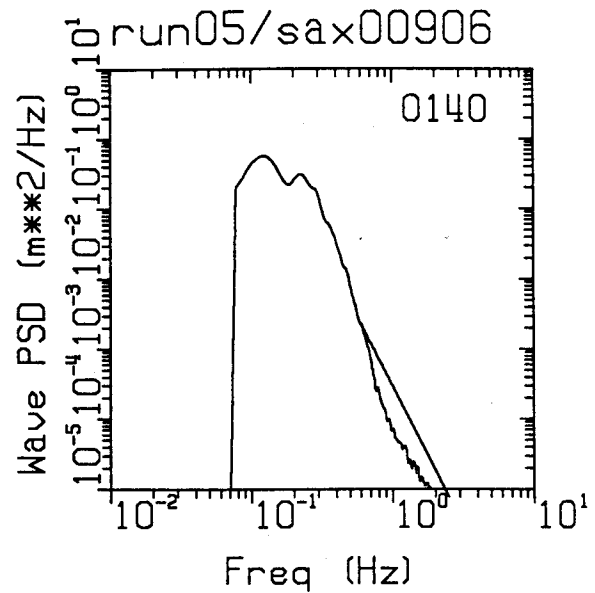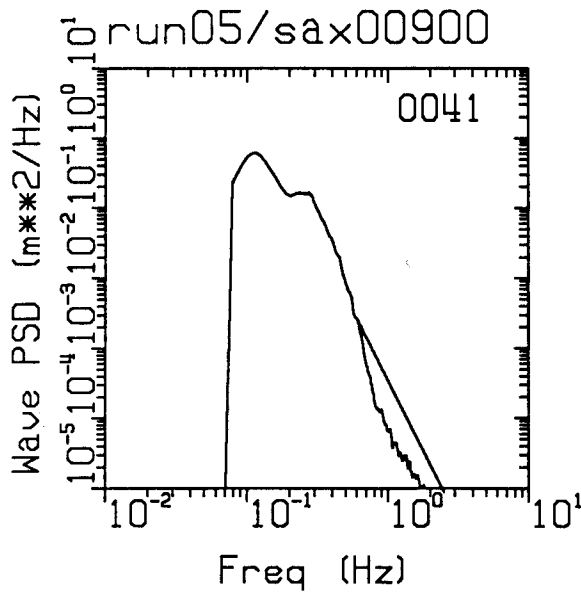
Figure 3.25b: Hourly surface displacement spectra derived from microwave measurements (equation 3.5) for RUN 05. Mid–time of measurement is indicated in upper right hand corner of each plot. Spectra have been extended from f=0.6Hz with an f^{-4} power law.
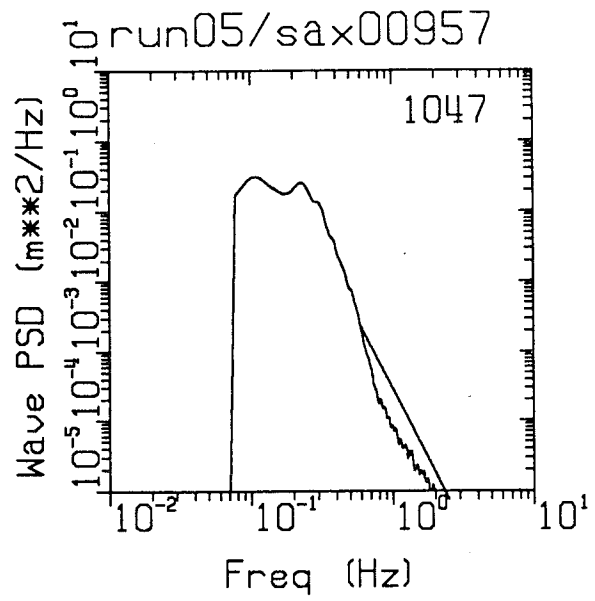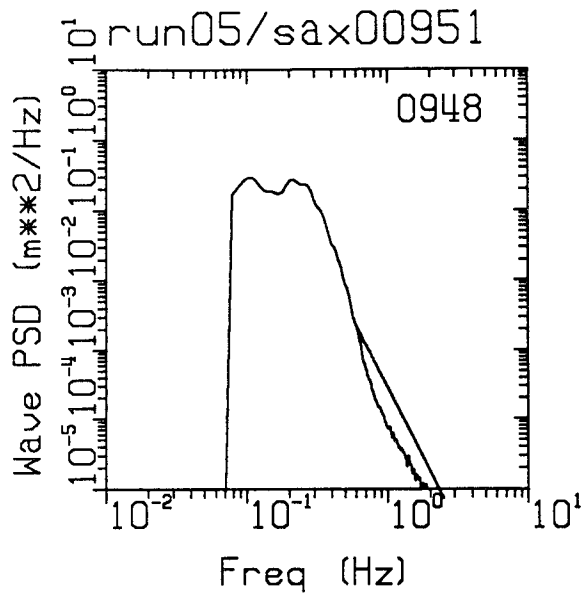
Figure 3.25b (continued): See caption, previous page.

SAXON RUN DURATION 10-08-88: RUN 06
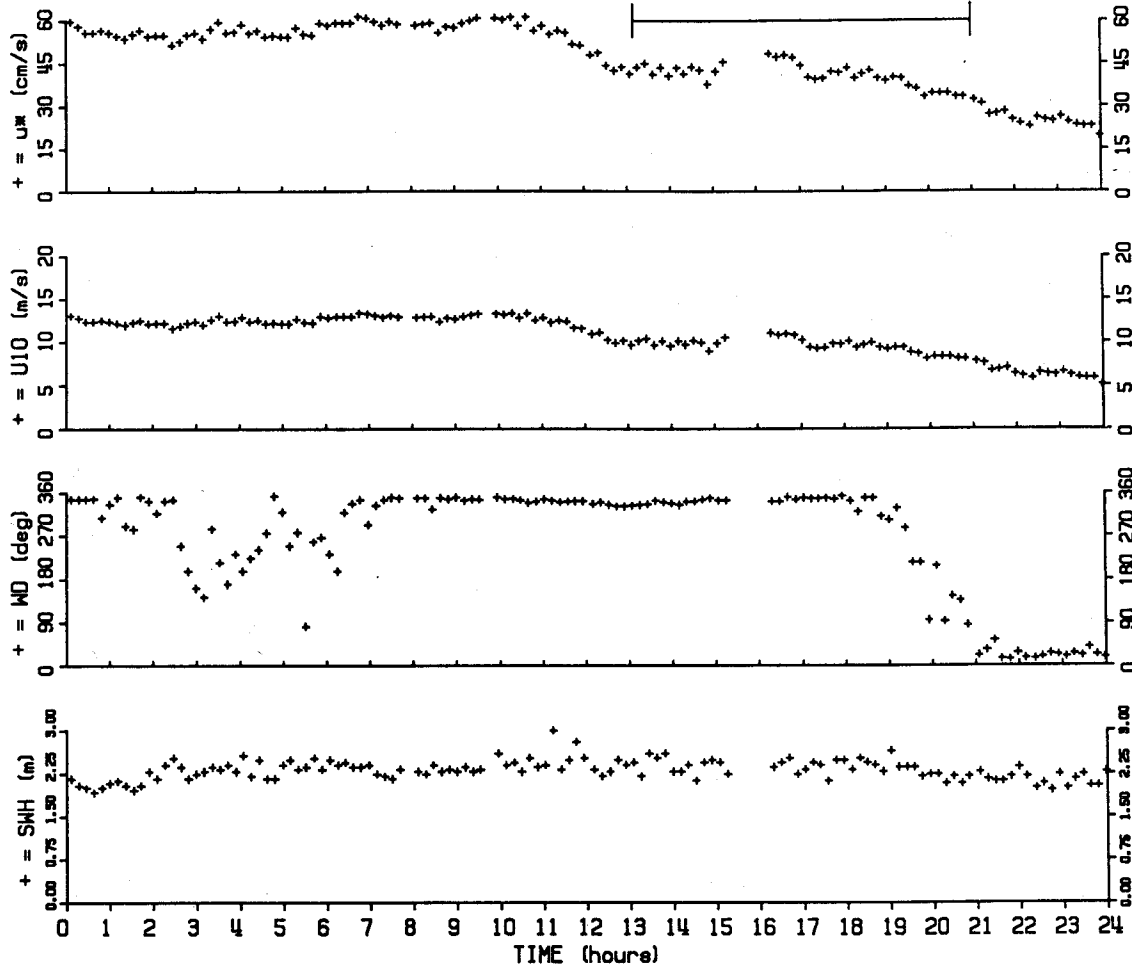
Figure 3.26a: Time series of environmental measurements showing time period (horizontal line in upper graph) for RUN 06: friction velocity, u^*, and wind speed reference to 10m, U_{10}, computed using bulk formula method, wind direction, WD, and significant wave height, SWH.
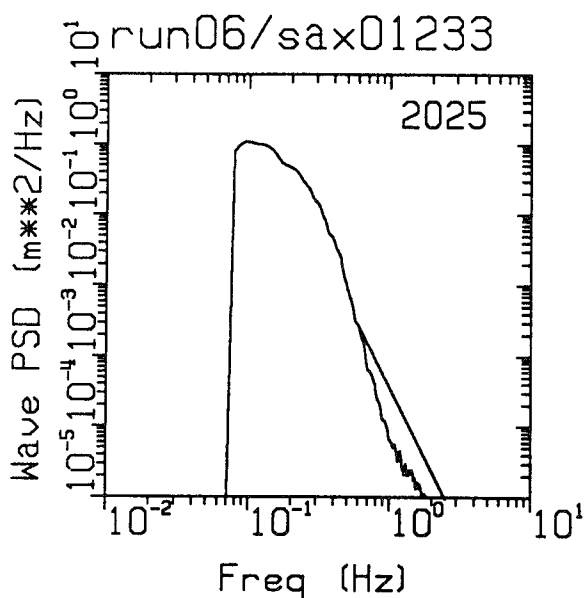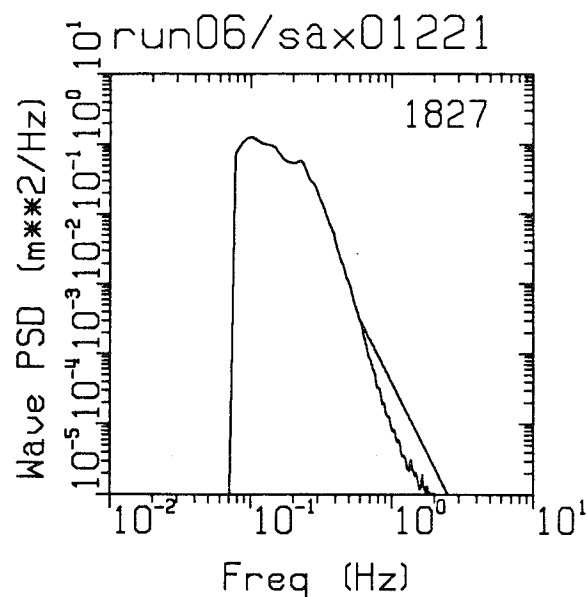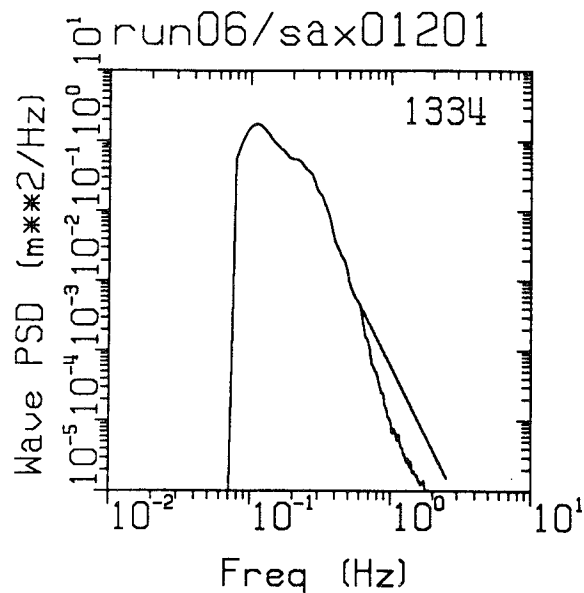
Figure 3.26b: Hourly surface displacement spectra derived from microwave measurements (equation 3.5) for RUN 06. Mid–time of measurement is indicated in upper right hand corner of each plot. Spectra have been extended from f=0.6Hz with an f^{-4} power law.

SAXON RUN DURATION 10-11-88: RUN 09
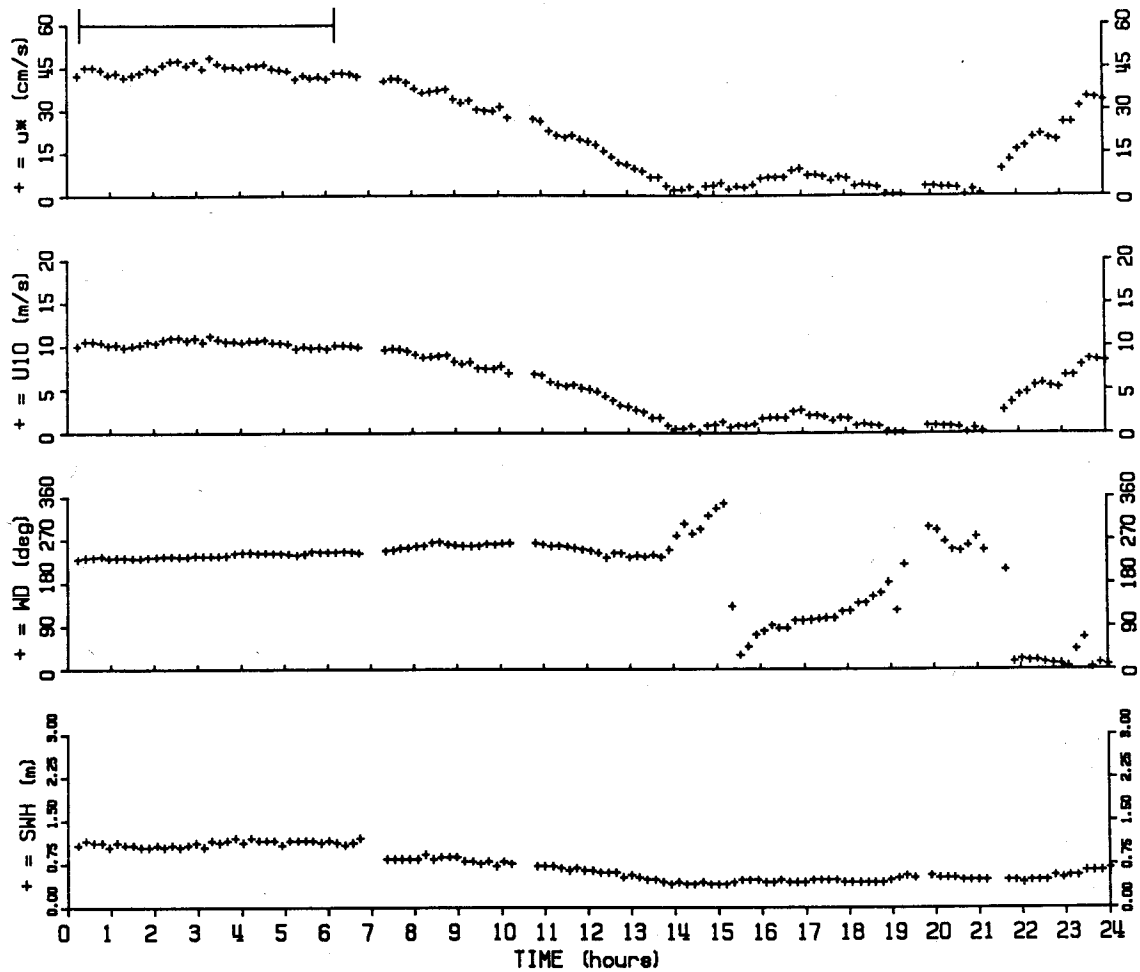
Figure 3.27a: Time series of environmental measurements showing time period (horizontal line in upper graph) for RUN 09: friction velocity, u^*, and wind speed reference to 10m, U_{10}, computed using bulk formula method, wind direction, WD, and significant wave height, SWH.
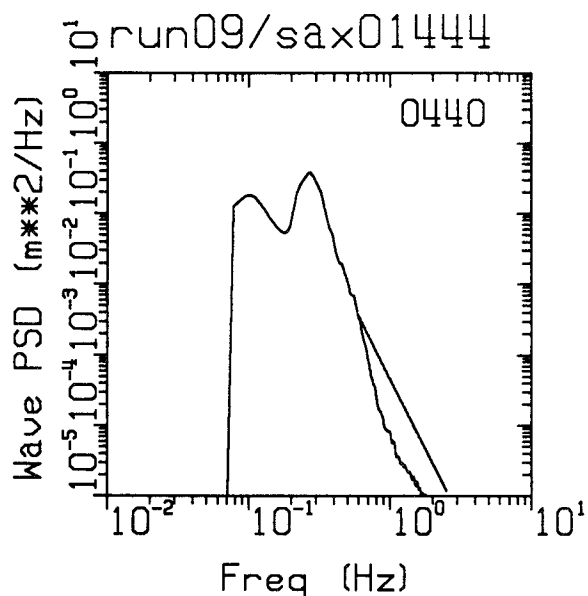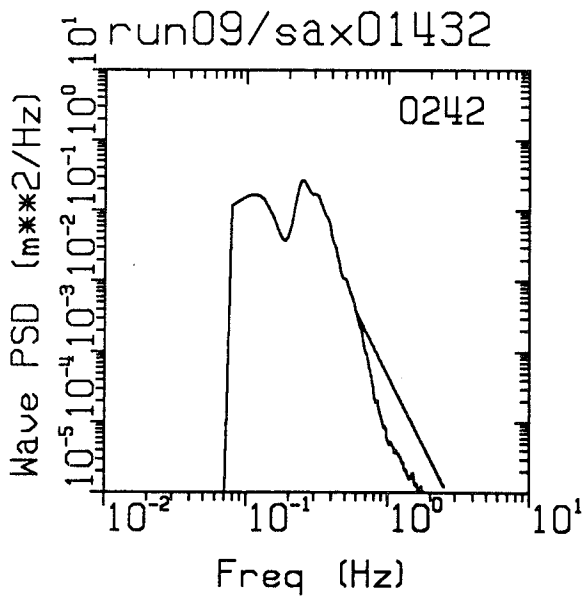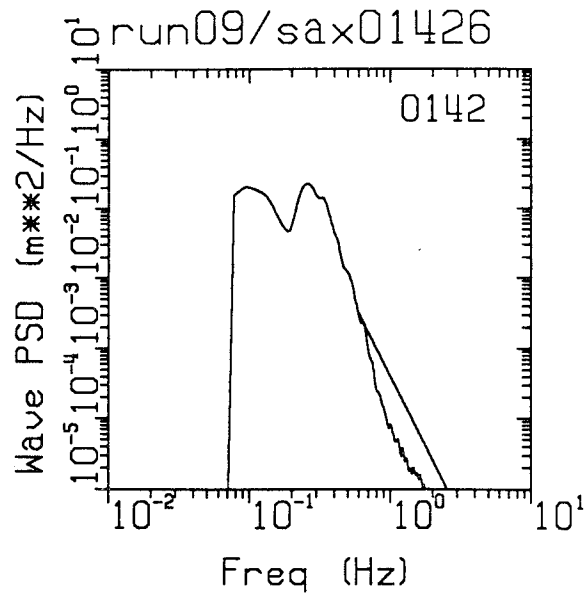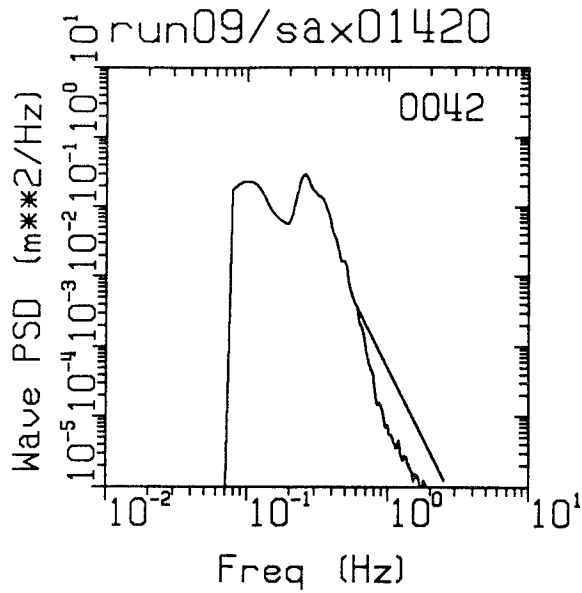
Figure 3.27b: Hourly surface displacement spectra derived from microwave measurements (equation 3.5) for RUN 09. Mid–time of measurement is indicated in upper right hand corner of each plot. Spectra have been extended from f=0.6Hz with an f^{-4} power law.
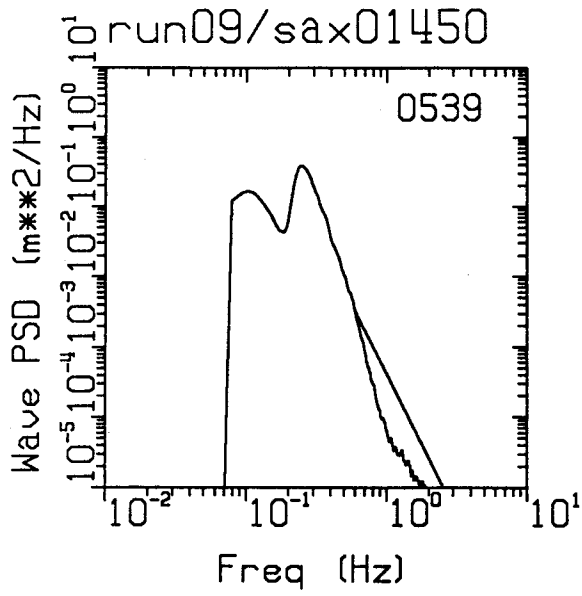
Figure 3.27b (continued): See caption, previous page.

SAXON RUN DURATION 10-12-88: RUN 11
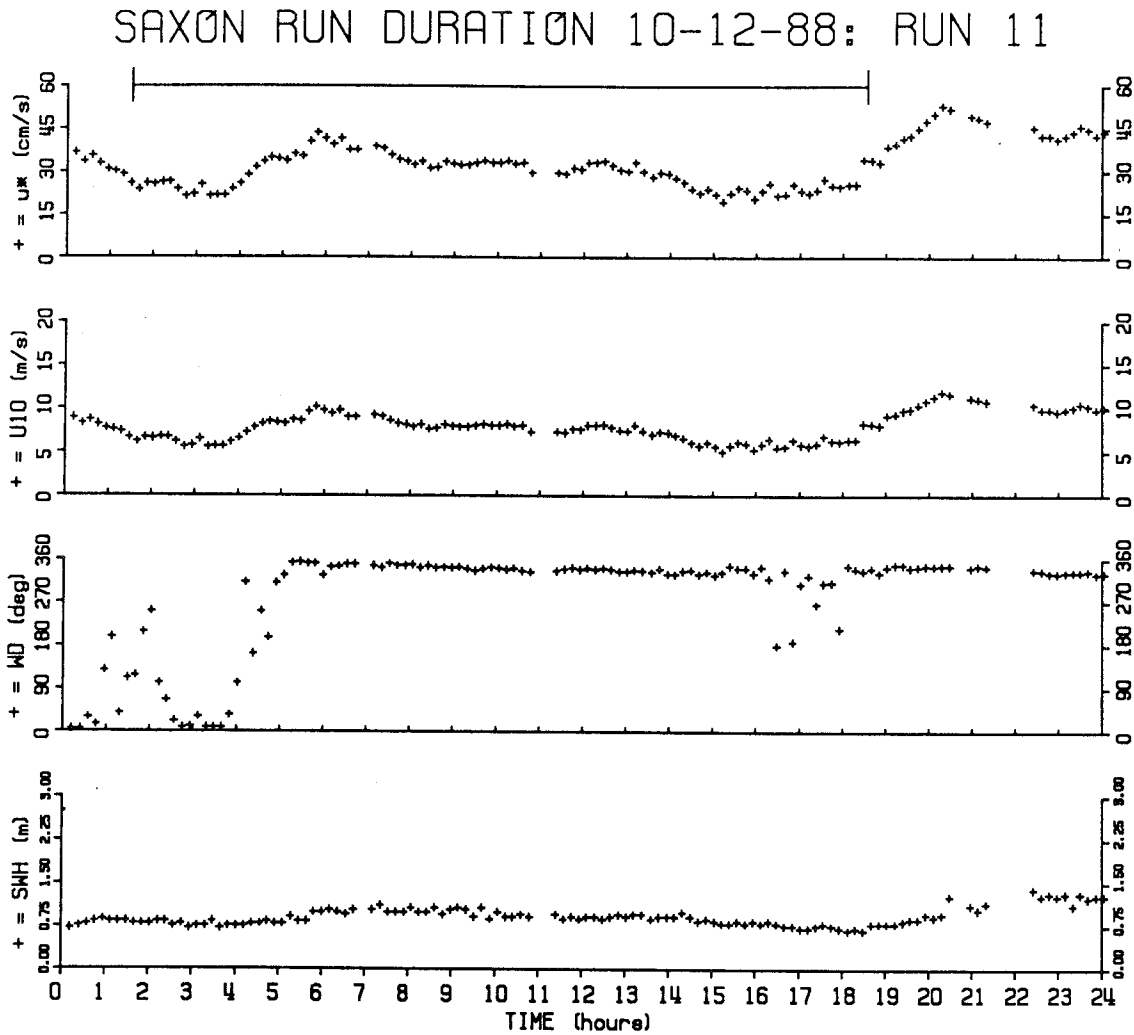
Figure 3.28a: Time series of environmental measurements showing time period (horizontal line in upper graph) for RUN 11: friction velocity, u^*, and wind speed reference to 10m, U_{10}, computed using bulk formula method, wind direction, WD, and significant wave height, SWH.
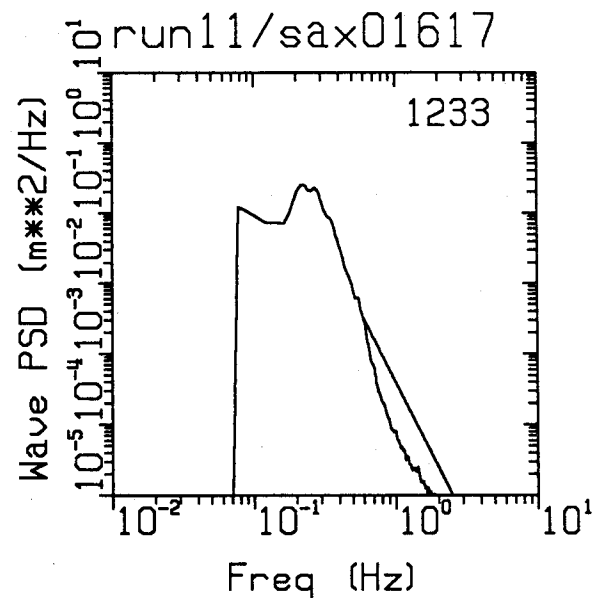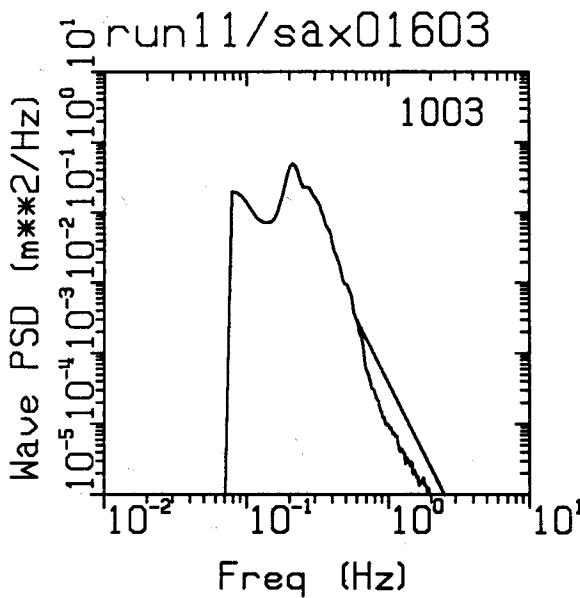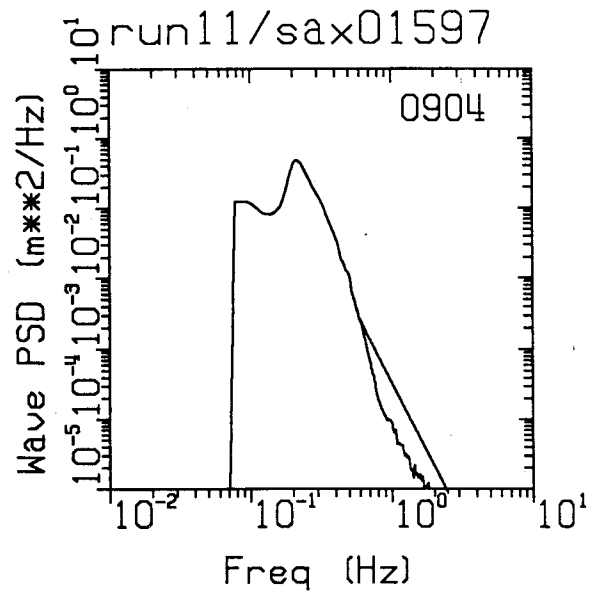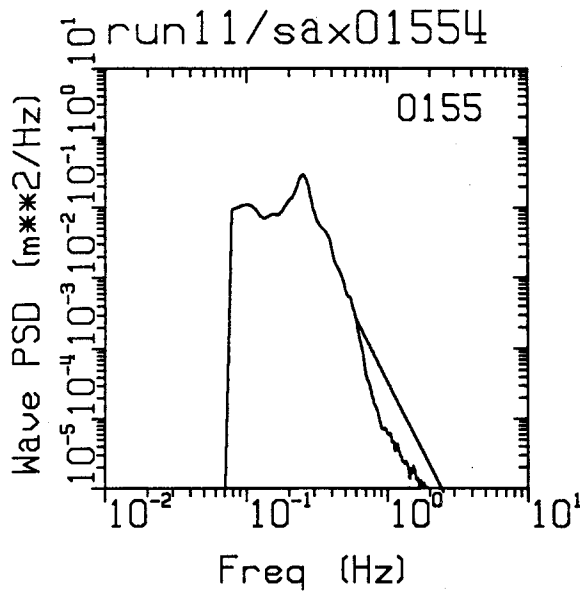
Figure 3.28b: Hourly surface displacement spectra derived from microwave measurements (equation 3.5) for RUN 11. Mid–time of measurement is indicated in upper right hand corner of each plot. Spectra have been extended from f=0.6Hz with an f^{-4} power law.

run11/sax01625

1352

Wave PSD (m**2/Hz)

Freq (Hz)

run11/sax01650

1759

Wave PSD (m**2/Hz)

Freq (Hz)
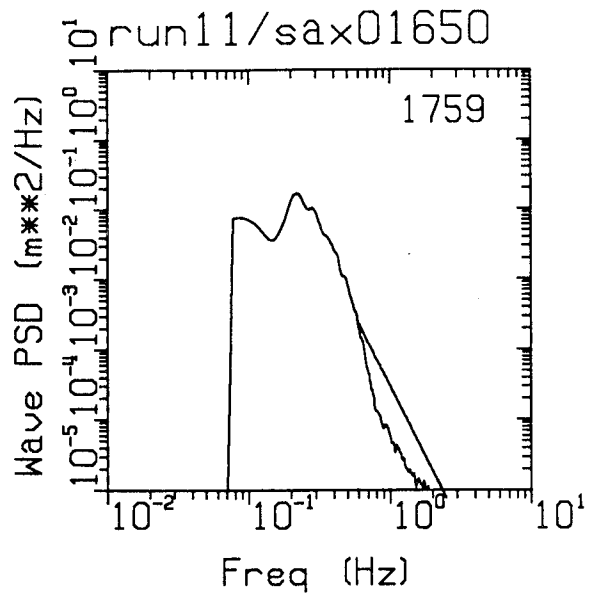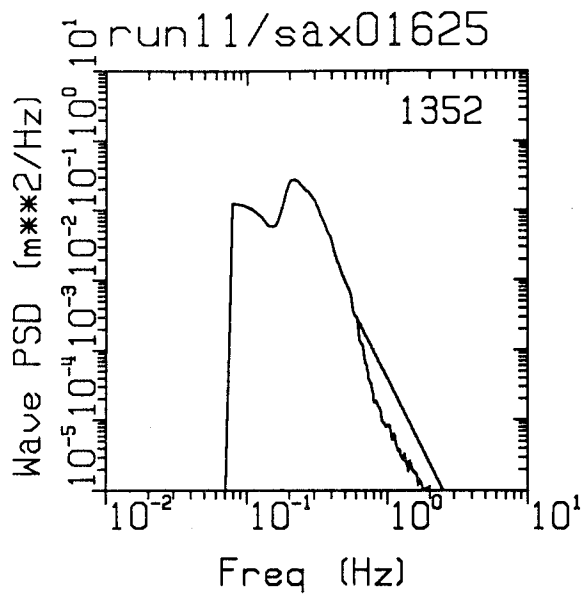
Figure 3.28b (continued): See caption, previous page.

Figure 3.29a: Time series of environmental measurements showing time period (horizontal line in upper graph) for RUN 12: friction velocity, u^*, and wind speed reference to 10m, U_{10}, computed using bulk formula method, wind direction, WD, and significant wave height, SWH.

SAXON RUN DURATION 10-13-88: RUN 12
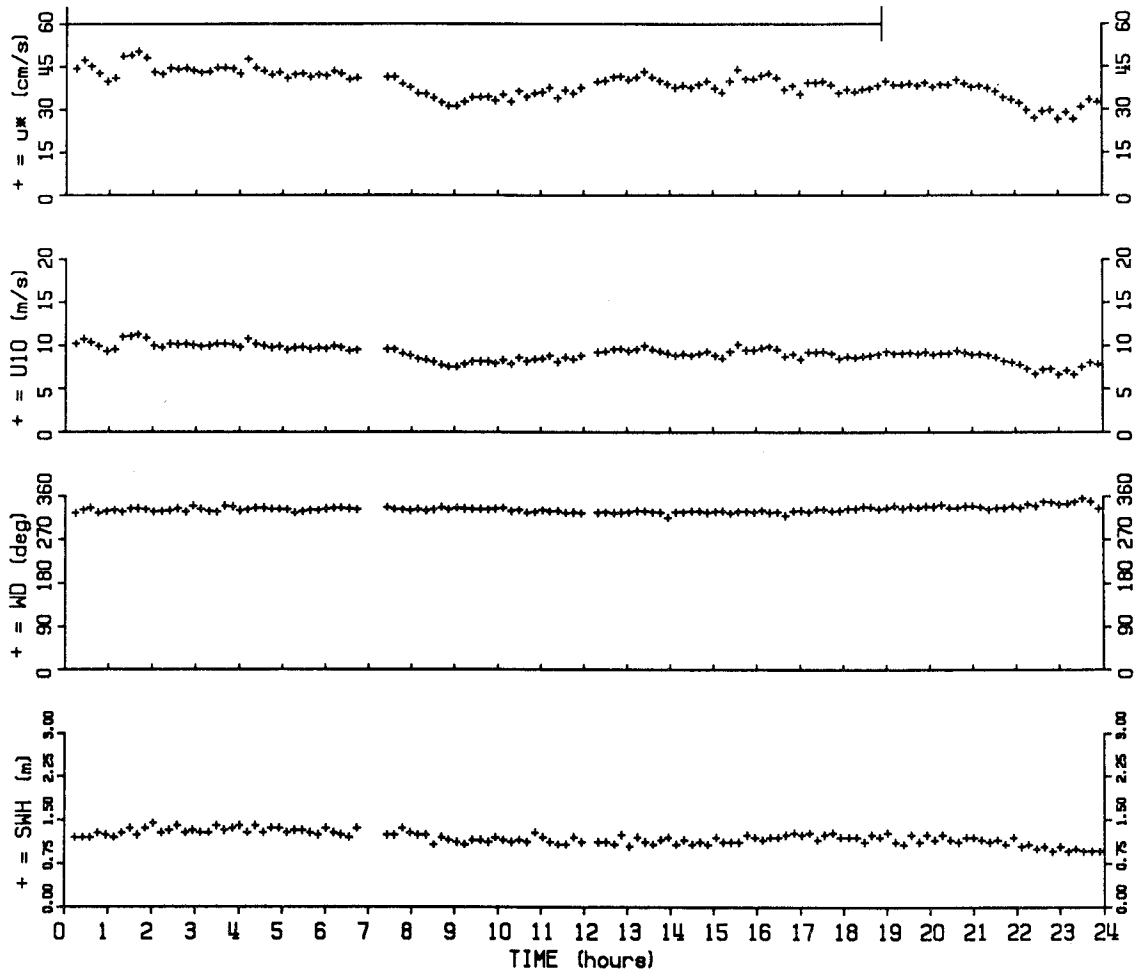
Figure 3.29a (continued): See caption, previous page.
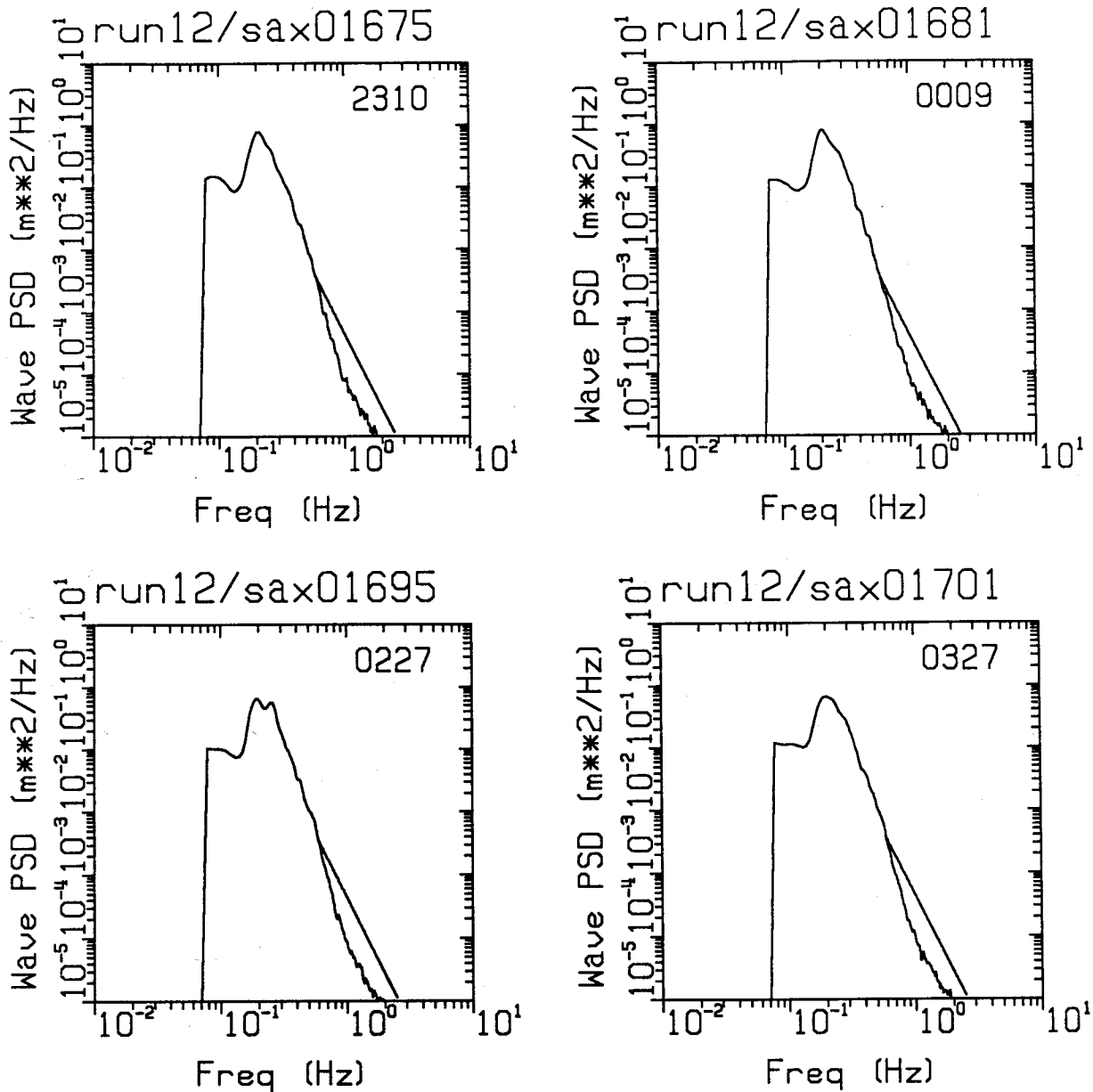
Figure 3.29b: Hourly surface displacement spectra derived from microwave measurements (equation 3.5) for RUN 12. Mid–time of measurement is indicated in upper right hand corner of each plot. Spectra have been extended from f=0.6Hz with an f^{-4} power law.
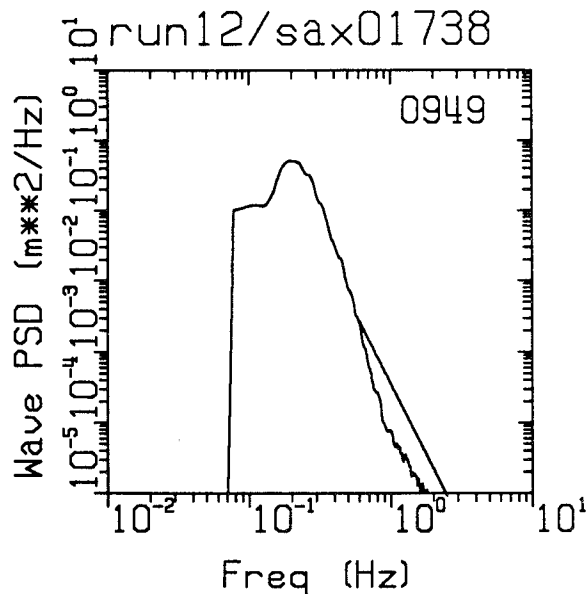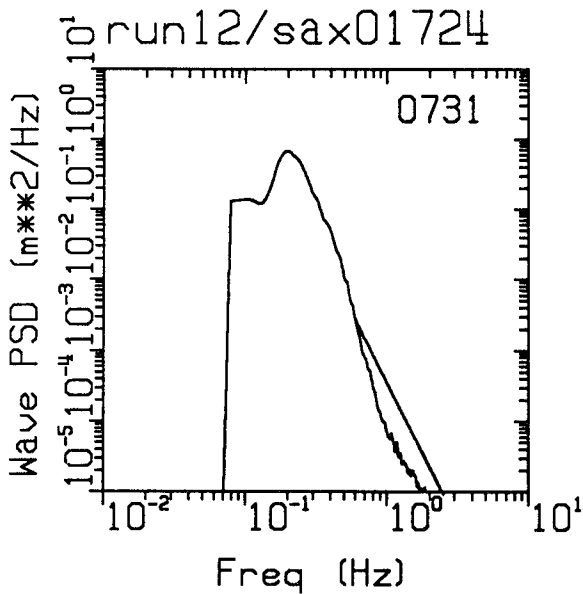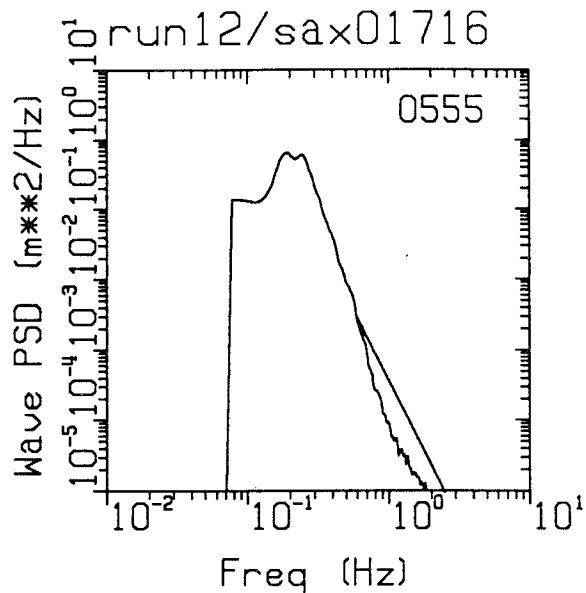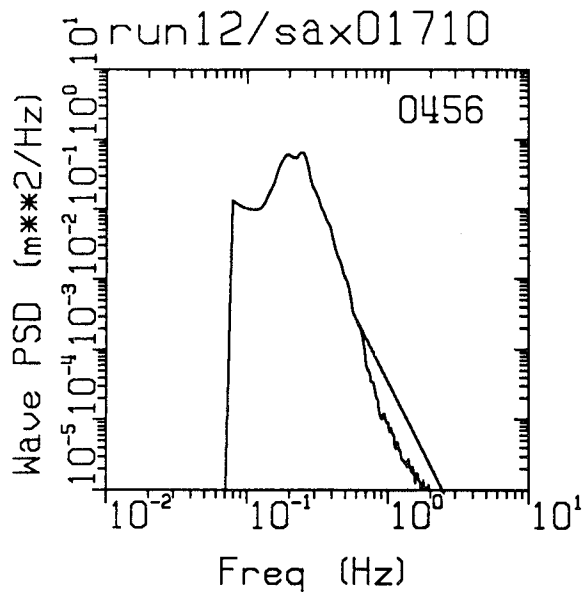
Figure 3.29b (continued): See caption, previous page.
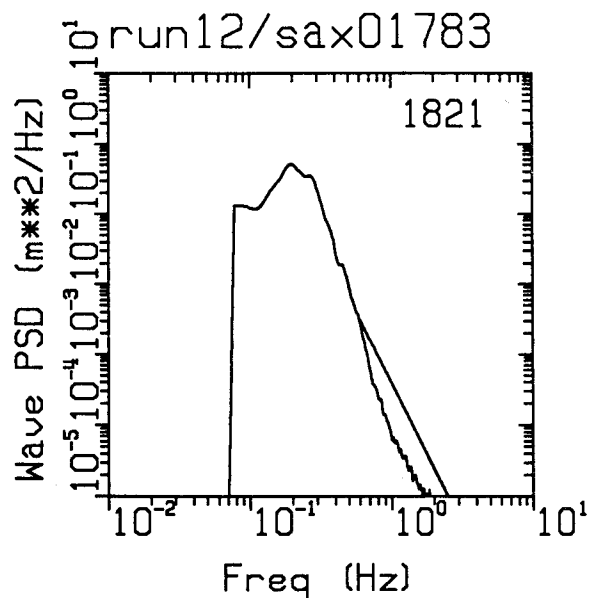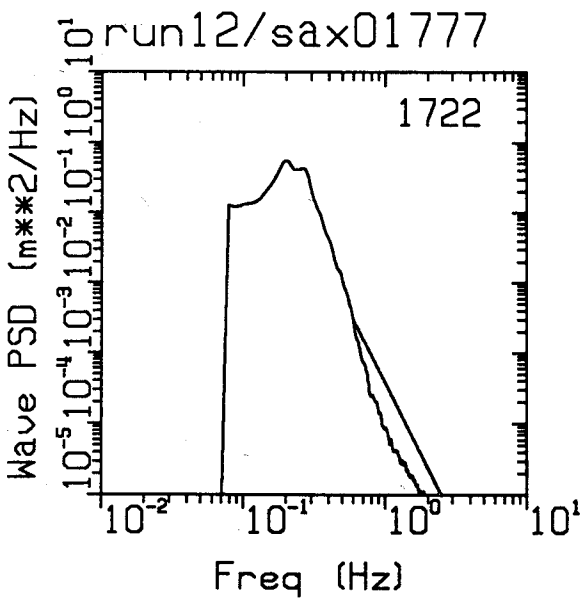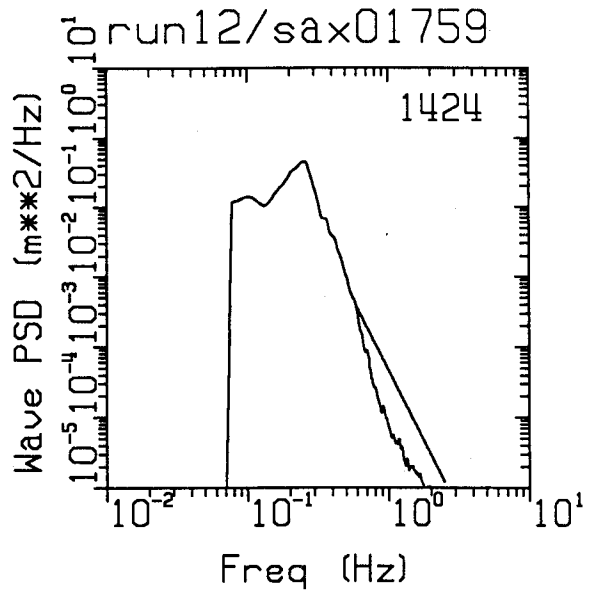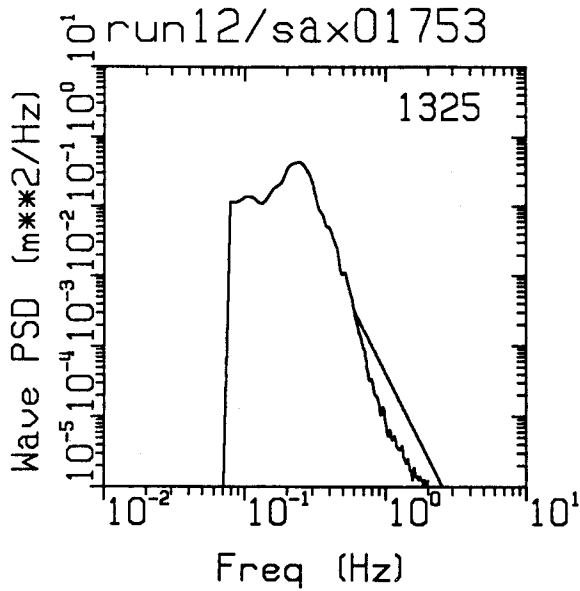
Figure 3.29b (continued): See caption, previous page.

CHAPTER 4

DETECTION OF SEA SPIKES ASSOCIATED WITH WAVE BREAKING

As shown in chapters 1 and 2, microwave backscatter at moderate incidence angles from steep and breaking waves can produce distinctive signatures in the return power and Doppler frequency spectrum. In this chapter, the characteristics of the microwave return associated with breaking events and the quantitative aspects of detection are discussed.

Figure 4.1 shows waterfall time series plots of the Doppler spectra for VV (top) and HH (bottom) return from the passage of a breaking wave. Each individual spectrum represent 0.25s, with time increasing up the page for a total duration of 15s. Positive frequencies on the right correspond to a line–of–sight velocity towards the antennas. Evident in both the VV and HH spectral maps is a large event with a mean Doppler shift of nearly 250 Hz (line–of–sight velocity 2.7 ms^{-1}) and increased bandwidth, indicating the range of power–weighted scatterer velocities. The magnitude of the backscattered power is comparable for VV and HH polarization during the breaking event in Figure 4.1, indicating a polarization ratio, $\sigma_{VV}^0/\sigma_{HH}^0$, near unity. The polarization ratio is clearly greater than unity at times away from the breaking event. Also apparent in Figure 4.1 is the spectral image of the extreme event reflected about zero frequency. The image is a result of the image rejection level discussed in Chapter 3, section 3.1 and is primarily due to the phase imbalance between the in–phase and quadrature demodulates of the receiver output.

The microwave signature of breaking waves identified from video recordings is illustrated in the time series of the mean values of radar cross–section, Doppler frequency, and bandwidth shown in Figure 4.2. The top
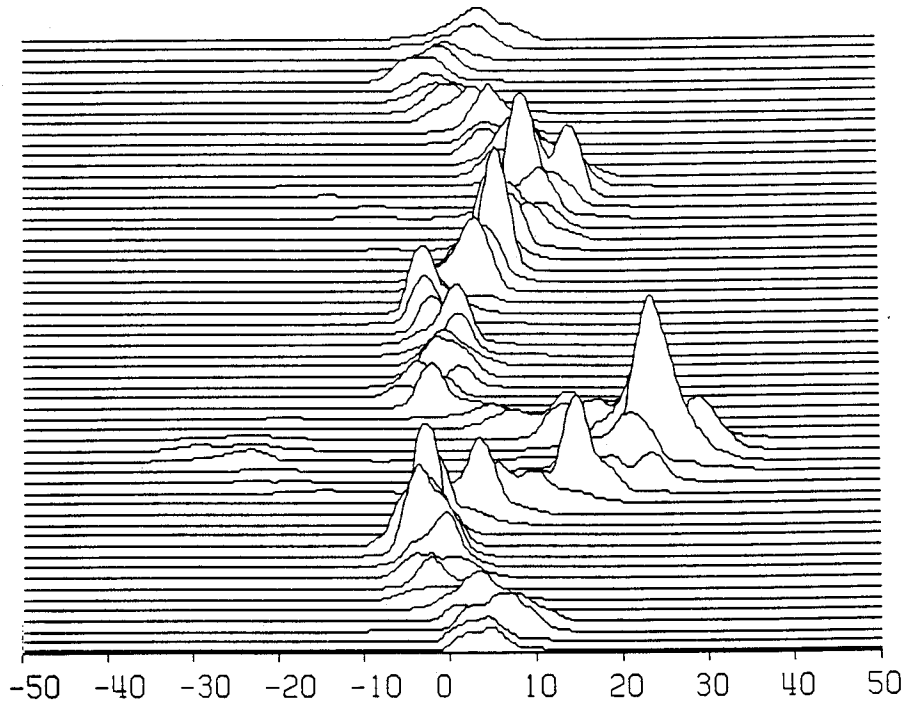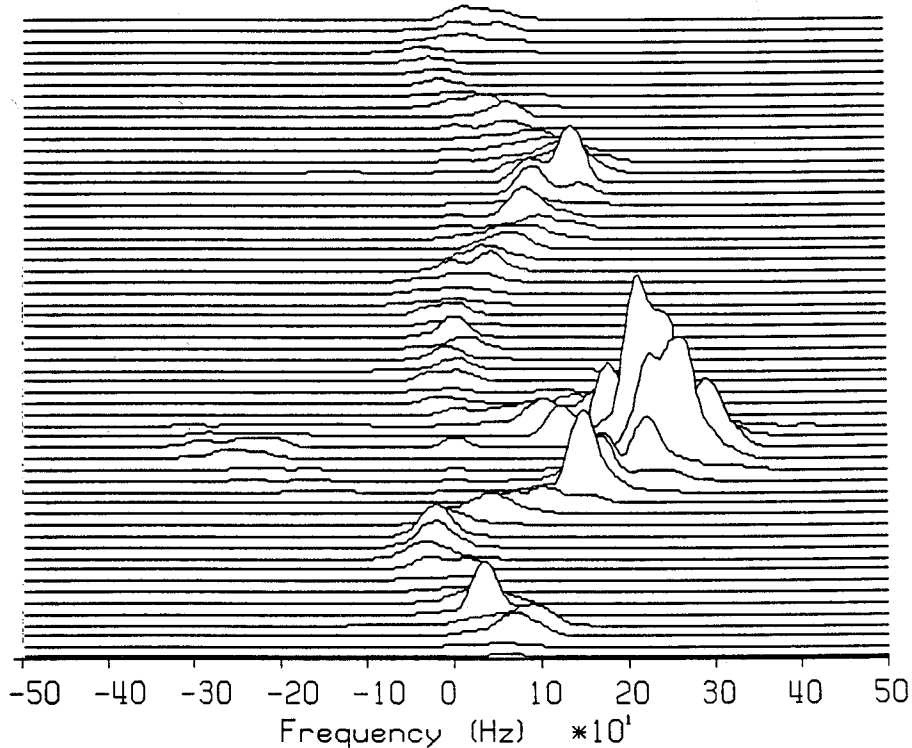
Figure 4.1: Doppler spectral map for VV (top) and HH (bottom) polarization illustrating the microwave signature of a breaking wave. Time increases up the page and the total elapsed time is 15s. Large amplitude event in both maps exhibits large Doppler shift, increased bandwidth, and comparble power for VV and HH polarization (from Jessup, 1988).

two traces show several sea spikes in σ^0 (linear scale) for VV and HH polarization. The mean Doppler frequency is shown in the third trace and the fourth trace is the Doppler bandwidth. The times in minutes and decimal seconds mark several large sea spikes in σ^0_{VV} and σ^0_{HH} and large excursions in bandwidth exceeding the thresholds indicated by dashed lines. The times of whitecaps appearing within the 3–dB illumination area are indicated on the axis of the mean Doppler frequency time series. These data from high wind conditions ($u_* = 55 cms^{-1}$) show numerous consecutive breaking events illustrating several important characteristics of the microwave return from breaking waves.

The five large sea spikes identified in the σ^0_{HH} time series in Figure 4.2 have been labelled A through E. The maximum amplitude of events A, B, and D are comparable for VV and HH polarization, suggesting scattering which is polarization independent. However, the HH return for events C and E is noticeably greater than that for VV. These examples are typical of events for which the polarization ratio, $\sigma^0_{VV}/\sigma^0_{HH}$, is <u>less</u> than unity, with minimum values near 0.70 (see Figure 4.11, discussed below in section 4.2). The cause of return for which σ^0_{HH} exceeds σ^0_{VV} is not obvious, since such events are not consistent with analytical models for backscatter from the ocean surface (see Chapter 1, section 1.3.5). The polarization ratio, $\sigma^0_{VV}/\sigma^0_{HH}$, is greater than unity when Bragg resonant scattering dominates, while specular reflections are polarization independent. The uncertainty in estimating the mean backscattered power may be responsible for events in which σ^0_{HH} exceeds σ^0_{VV} (see section 3.2.1). Differences in the VV and HH sea spikes as a function of the averaging or integration time may also contribute to the occurrence of these events, as discussed in section 5.8. An integration time of 0.125s was
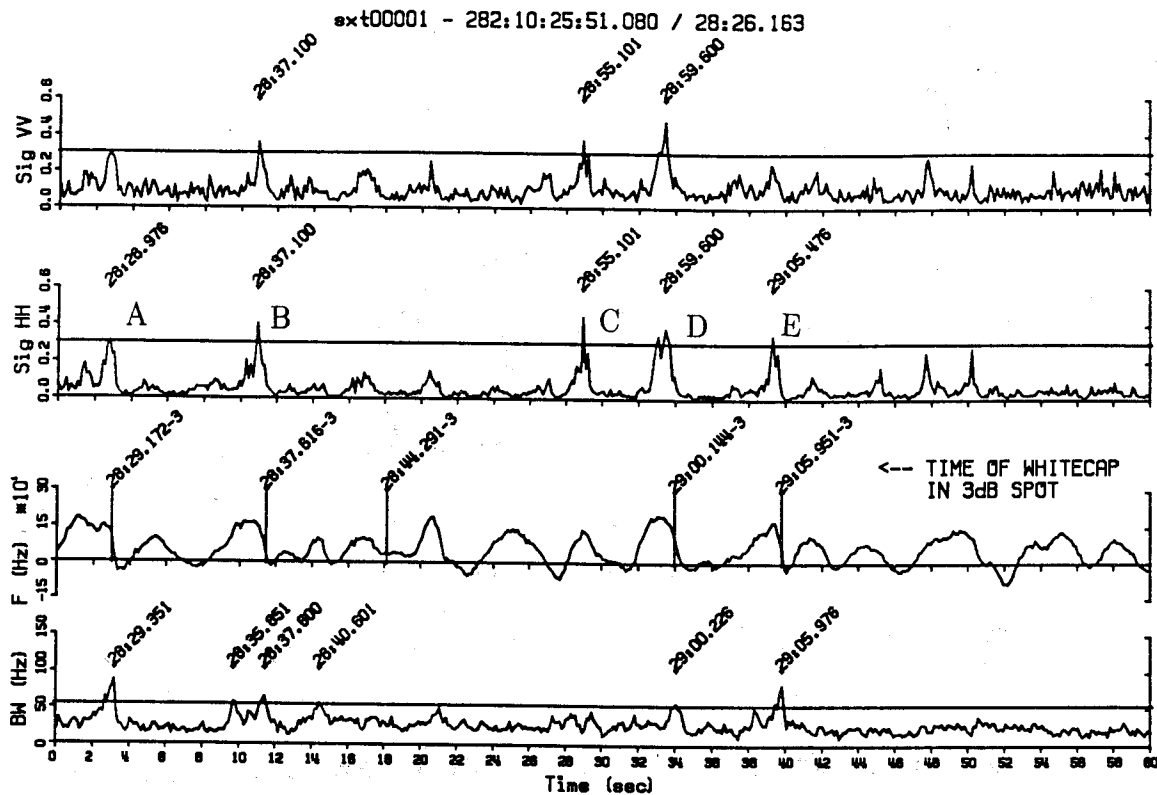
Figure 4.2: Time series of σ^{o}_{vv}, σ^{o}_{hh}, Doppler frequency, and bandwidth (u^{*}=55cms^{-1}). Events exceeding σ^{o}_{pol}=−5.2dB (0.30) and/or a bandwidth of 50Hz are identified by time (min & sec). Whitecaps in the 2−way, 3dB spot indicated on 3rd time axis from top. Notice 1: coincidence of σ^{o} and Doppler frequency maxima, 2: delay between bandwidth maxima and σ^{o} peak, 3: sea spikes may or may not accompany a whitecap in the 3dB spot, and 4: coincidence of whitecaps associated with a sea spike and bandwidth maxima.

used to process the data in Figure 4.2.

Important timing relationships between the sea spikes in σ^0 and maxima in the Doppler frequency and bandwidth are also apparent in Figure 4.2. The sea spike maxima tend to occur simultaneously with local maxima in the mean Doppler frequency. On the other hand, the occurrence of maxima in the bandwidth associated with the sea spikes tends to be delayed from the time of the local maxima in cross–section. The delay between the sea spike and bandwidth maxima is typically on the order of 0.25–0.50s. The appearance of a whitecap in the 3–dB spot also generally occurs later in time than the coincident local maxima in cross–section and Doppler frequency. Comparison between the times of the bandwidth maxima and the appearance of a whitecap in the 3dB spot indicates that these events tend to occur together.

The example in Figure 4.2 also shows that whitecaps in the 3–dB illumination area may not always be accompanied by a large sea spike in σ^0 and, vice versa, that a large sea spike may occur unaccompanied by a whitecap in the 3–dB spot. The third whitecap time noted in Figure 4.2 is not associated with a distinctive peak in either the cross–section or the bandwidth. The sea spike event labelled C is comparable in magnitude to the other events, yet no whitecap was observed in the 3–dB spot.

The general observations illustrated by the example in Figure 4.2 include:

1) sea spike maxima tend to occur close in time to local maxima in the mean Doppler frequency,

2) maxima in the bandwidth associated with sea spikes tend to be delayed from the sea spike maxima by 0.25–0.50s,

3) a large sea spike may be unaccompanied by the appearance of a whitecap in the 3–dB spot, and vice versa, and

4) when a sea spike is accompanied by a whitecap in the 3–dB spot, its appearance occurs close in time to the bandwidth maxima.

The significance of these observations are discussed in detail in the following sections.

4.1 SEA SPIKES IN THE RADAR CROSS-SECTION

4.1.1 SOURCES OF LARGE INTENSITY EXCURSIONS

When the dimensions of the illumination area are small compared to the wavelength of the dominant surface waves, the backscattered power is modulated as individual long wave crests pass through the measurement spot. Two sources of this modulation that have been recognized (see, e.g., Alpers et al., 1981) are relevant to the microwave signature of breaking waves. Tilt modulation is caused by the change in local incidence angle determined by the local wave slope. Hydrodynamic modulation of the radar cross-section is due to the amplitude modulation of short waves producing Bragg resonant scattering by the long waves upon which they are superimposed.

The evolution of the surface during the breaking process can create extremes in scattering geometry which may be responsible for the extremes in microwave scattering associated with breaking. Figure 4.3 illustrates the changes in surface geometry which can occur in the process of breaking. The profiles in Figure 4.3 were taken from photographs by Rapp (1986) of laboratory generated breaking waves in progressive stages of development (see also Rapp and Melville, 1990). These profiles illustrate how the stage of development of a breaking wave as it passes the illumination area will affect the scattering geometry.

The change in local incidence angle along the phase of a sharp-crested wave is illustrated in Figure 4.4 for one of the profiles from the sequence in
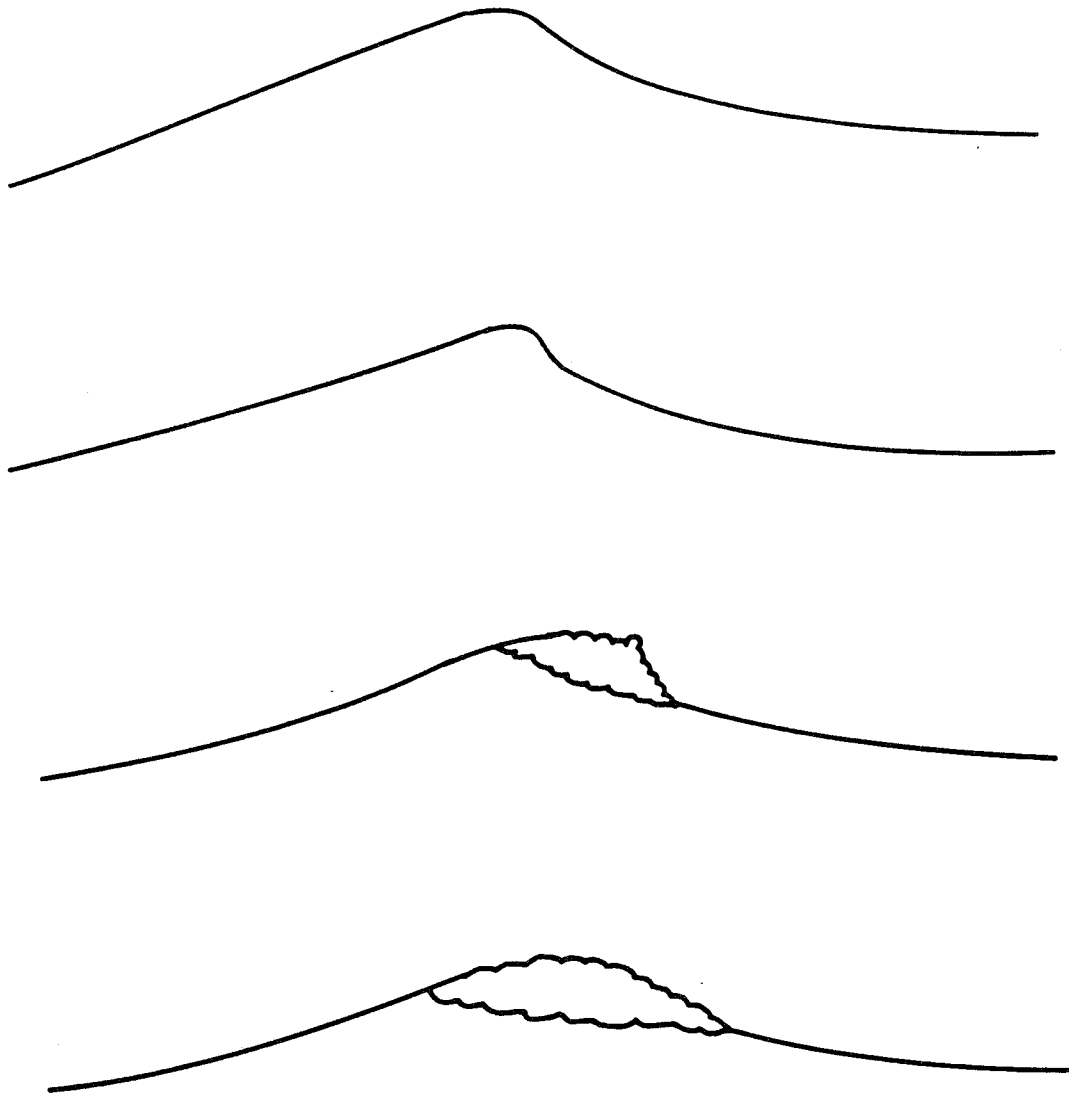
Figure 4.3: Sequence of surface profiles taken from laboratory generated breaking wave (Rapp, 1986) illustrating the variety of surface geometries associated with the evolution of a breaking crest.

Figure 4.3. The fixed or global incidence angle of the antenna look–direction with respect to the mean sea surface is denoted as θ_g. The extent of the two–way, 3–dB illumination area at various locations along the wave profile is indicated by the thick line. Clearly, the location of the illumination area with respect to the phase of the breaking wave as well as the stage of development can significantly influence the microwave scattering from a particular breaking event. Where the surface curvature is small over the extent of the illumination area, a local incidence angle, θ_l, can be defined, as indicated in Figure 4.4. As the forward face of a wave crest approaches the illumination area, the local incidence angle decreases to a minimum. The geometry becomes complicated when the illumination area straddles the crest and the definition of a local incidence angle is not simple. After the crest region, the local incidence angle is greater than the global value as the back side of the wave crest passes through the spot.

Evidence from the simultaneous microwave and video measurements indicates that the majority of large jumps in σ^0 associated with breaking occur on the steep forward face of waves that ultimately form a whitecap. This observation suggests that large sea spikes associated with breaking waves are primarily due to the change in local incidence angle. The dependence of the mean radar cross–section on incidence angle is shown in Figure 4.5. For measurements at a global incidence angle of 45°, Figure 4.5 indicates that changes in the local incidence angle of 10–15° would cause a moderate amount of tilt modulation. However, if the wave slope is such that the local incidence angle is reduced to 25° or less, then the scattering begins to enter the specular regime and a large jump in σ^0 may be expected.
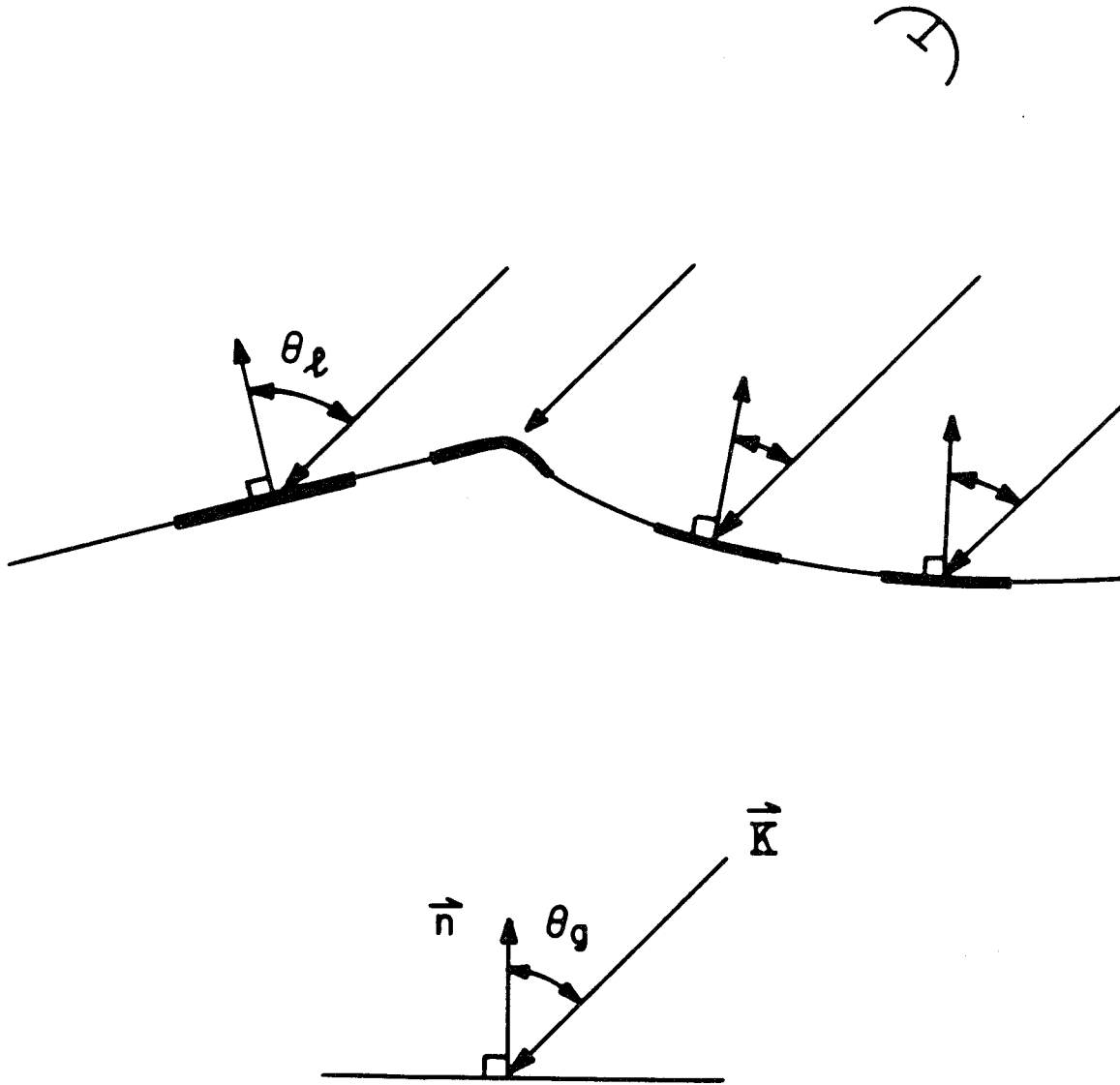
Figure 4.4: Illustration of the changes in the local incidence angle θ_l as a function of the location of the radar spot with respect to the phase of a breaking wave for one of the profiles in Figure 4.3. The extent of the 3dB spot is indicated by the thicker line. The lower sketch defines the global incidence angle θ_g as the angle between the antenna look direction, or trasmitted electromagnetic wavenumber κ, and the normal to the mean sea level **n**.
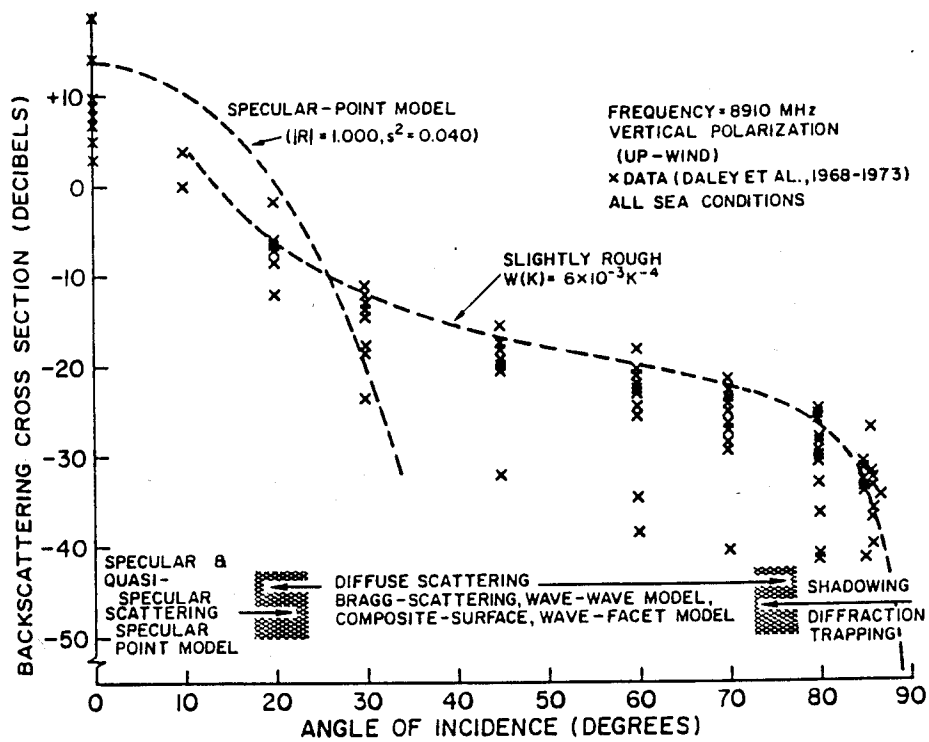
Figure 4.5: Incidence angle dependence of the mean radar cross–section σ^0 illustrating the three general scattering regimes: (1) near nadir, dominated by specular return, (2) moderate incidence, where Bragg scattering is important, and (3) near grazing incidence (from Valenzuela, 1978).

Rapp (1986) made laboratory measurements of the local slope of the forward face of breaking waves. Figure 4.6 shows the definition of the measured slope a/L, which ranged from 0.3 to 0.7 for spilling and plunging breaking events, respectively. For microwave measurements with a global incidence angle of 45°, these slopes would result in a local incidence angle in the range of 10°–30°. If the geometry of breaking waves generated in the laboratory is similar to those found in the field, then these measurements support the idea that sea spikes associated with the forward face of breaking waves are due to large changes in the local incidence angle.

However, some sea spikes occur closer in time to when the crest passes the center of the illumination area. These events tend to be associated with return from near the crests of low frequency swell exhibiting large modulations of short waves distributed over the crest region. The sea spikes associated with short wave modulation near such long wave crests may be due to increased Bragg resonant return at a reduced incidence angle.

4.1.2 FURTHER INTENSITY THRESHOLD CONSIDERATIONS

In Chapter 2, an argument was made for a detection scheme based on a radar cross–section threshold which identified large sea spikes with positive mean Doppler frequency. The polarization characteristics of return from breaking waves may also be used to establish a radar cross–section threshold to detect breaking events. Large, polarization independent sea spikes have been shown to be associated with breaking waves (see Chapter 1, Section 1.3.2). A threshold to detect polarization independent events may be found by considering the number of sea spikes in a given record as a function of
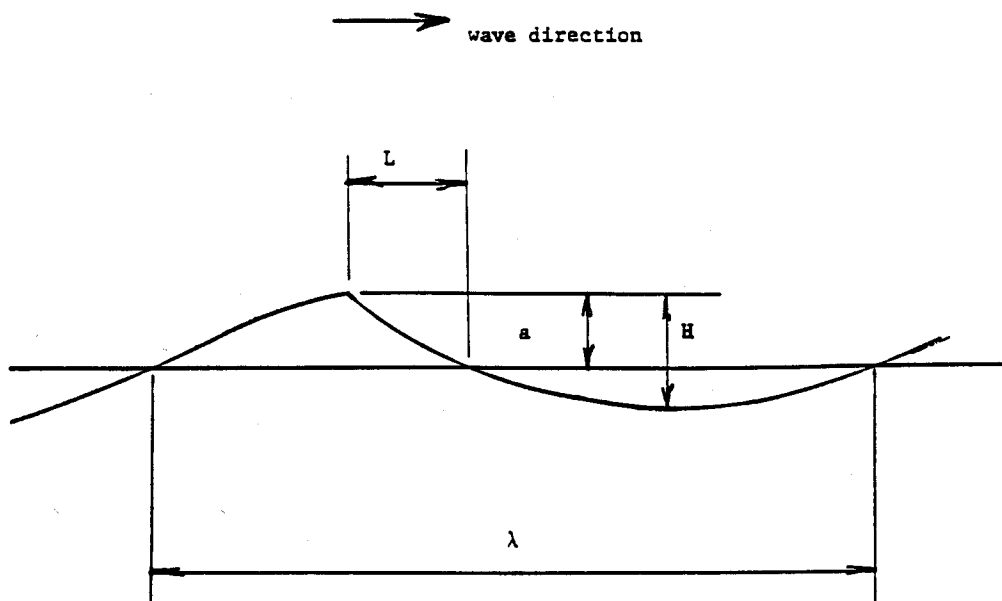
Figure 4.6: Schematic of steepness a/L of laboratory generated breaking waves (from Rapp, 1986). The steepness range of $0.3 \leq a/L \leq 0.7$ corresponds to a local incidence angle range of $10° \leq \theta_l \leq 30°$ for measurements at a global incidence angle θ_g of $45°$ (see Figures 4.4 and 4.5).

intensity and polarization. Fig. 4.7 shows the average number of sea spikes per hour versus the radar cross–section threshold for three different intervals of u_* for both VV (solid lines) and HH (dashed lines) polarization during the SAXON experiment. For a low threshold, more events are counted for VV than for HH since the mean polarization ratio of σ^0 is greater than unity (see Chapter 1, Section 1.3.3.). As the threshold is increased, approximately the same number of events are counted for both VV and HH over a range of u_*. If the polarization ratio for individual breaking events is indeed unity, then the point at which the VV and HH curves in Fig. 4.7 coincide is an appropriate threshold to count polarization independent sea spike. The coincidence of the VV and HH curves at slightly larger σ^0 thresholds for larger values of u_* suggests that the minimum threshold may be a weak function of u_*.

Results of this analysis for the preliminary measurements in the North Sea, shown in Fig. 4.8, are similar to those from the SAXON experiment. However, small differences between Figures 4.7 and 4.8 are apparent in both the threshold at which the VV and HH curves coincide and the spacing of the different u_* curves. For the SAXON data, the VV and HH curves in Fig. 4.7 begin to coincide at approximately –5dB, while the same point for the North Sea measurements in Fig. 4.8 occurs closer to –6dB. By shifting the two figures relative to one another by the difference between these two levels, the curves for the SAXON and the North Sea data roughly line up. The scatterometers used for the two measurements were different and thus the difference of 1dB or so may be due to calibration uncertainty, since the systems' accuracies are approximately ±1dB. The spacing of the curves for

SAXON THRESHOLD ANALYSIS: Ti = 0.25s
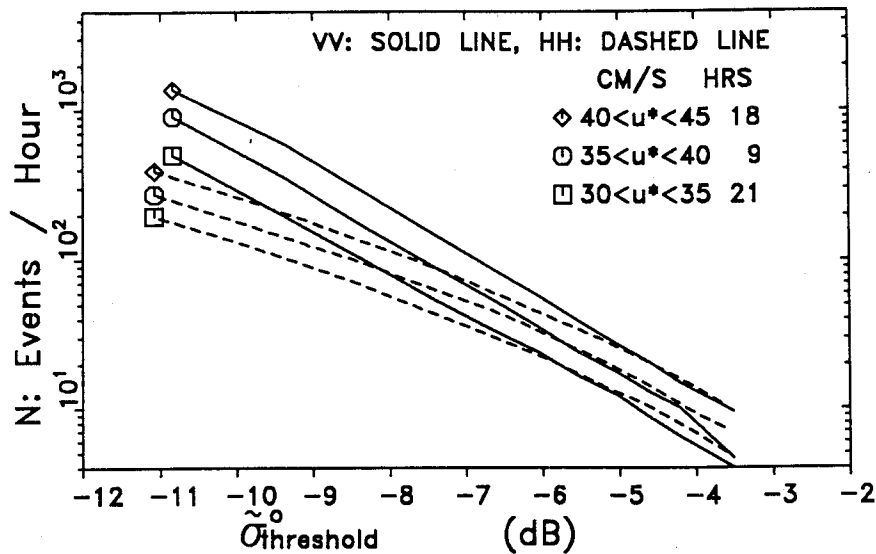
NORTH SEA THRESHOLD ANALYSIS: Ti = 0.25s
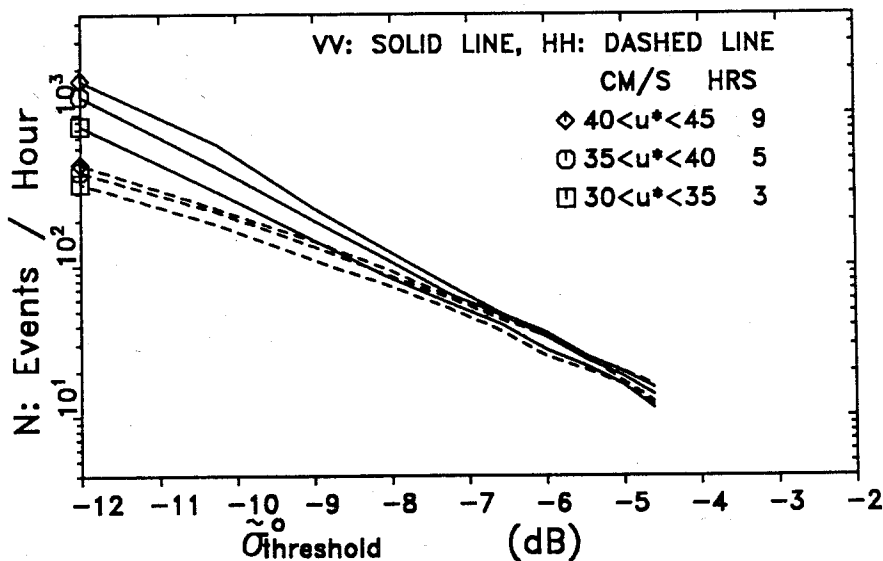
Figure 4.7 (top): Average number of events per hour N vs radar cross–section threshold for different u^* interval in SAXON. The same number of events are counted in VV and HH polarization near –5dB.

Figure 4.8 (bottom): Same as Figure 4.7 except for North Sea data and VV and HH curves begin to coincide near –6dB.

different u_* levels is a function of the u_* exponents of the frequency of sea spike occurrence. That the curves for different u_* are more tightly spaced for the North Sea data than for SAXON implies that the exponent for the former should be smaller than that of the latter, as is confirmed in the next chapter. In the following analysis, a threshold of $\sigma^0_{Pol}=-5.2dB$ (0.30) is used to detect large, polarization independent sea spikes.

4.1.3 VIDEO VERIFICATION

Two hours of video recordings from the SAXON experiment have been viewed in detail to identify visual evidence of wave breaking. These recordings correspond to measurement periods during Runs 11 and 12 for which the friction velocity was 30cms^{-1} and 40cms^{-1}, respectively. The recordings were first viewed independently of the microwave data to determine the number of whitecaps with a minimum dimension of roughly 0.5m which appeared within the two-way, 3-dB illumination area (1.5x2.2m^2). Table 4.1 summarizes this analysis, showing the number of events counted and the corresponding percentage of breaking crests, P_{3dB}, where the total number of crests is based on the peak frequency of the wave height spectrum. The values in Table 4.1 for the percentage of crests producing whitecaps in the 3-dB illumination area are consistent with the results of Holthuijsen and Herbers (1986) and Toba et al. (1971) shown in Figure 1.1.

As indicated in section 4.1, comparison of the time series of σ^0 with these video results showed that the whitecaps appearing within the 3-dB illumination area were not necessarily associated with large sea spikes in σ^0. Indeed, only about 10% of the whitecaps occurring within the 3-dB spot

Table 4.1: Whitecaps within 3—dB illumination area

RUN ID	u^* (cms^{-1})	U_{10} (ms^{-1})	Number of Whitecaps	P3dB: Percent of breaking crests
11	30	8.5	95	12.1%
12	40	11.3	184	21.1%

Table 4.2: Video Correlation of Sea Spikes: $\sigma_{vv}^0 \geq \sigma_{min}^0$

RUN ID	Total No. of sea spikes	Number of Non—breaking	Number of breaking	P5m: Percent of breaking crests
11	48	8	40	5.3%
12	228	70	158	18.1%

Table 4.3: Percentage of Sea Spike Breaking Events Detected

RUN ID	P_{ss}^1 $(\sigma_{vv}^0 > \sigma_{pol})$	P_{ss}^2 $(\sigma_{vv}^0 > -6dB)$	P_{ss}^3 $(BW > 50\ Hz)$	P_{ss}^4 $(\sigma_{vv}^0 > -6dB$ or $BW > 50Hz)$
11	15%	28%	70%	73%
12	19%	33%	66%	70%

corresponded to sea spikes detected by the threshold σ^0_{Pol}. Furthermore, large sea spikes in σ^0 sometimes occurred without the appearance of a whitecap in the 3–dB spot.

As noted above, the majority of large sea spikes occur when the steep forward face of a wave in the process of breaking is in the illumination area. The breaking process for such waves continues to evolve as the crest approaches the illumination area. Consequently, a wave whose forward face produces a large sea spike may not exhibit a whitecap until after its crest has passed the center of the illumination area. In other words, the whitecap associated with a given sea spike may occur 'downwave' of the center of the radar spot.

The video recordings show that all of the sea spikes detected with the threshold σ^0_{Pol} are due to waves which produce whitecaps within a distance of approximately 5m beyond the center of the radar spot. Therefore, the criterion for a given microwave event to be classified as being due to a breaking wave is taken to be the appearance of a whitecap within a distance of approximately 5m downwave of the radar spot. The distance of 5m is on the order of 10–20% of the wavelength of the dominant surface wave corresponding to the peak frequency of the surface displacement spectrum.

Despite the fact that all the sea spikes detected by the radar cross–section threshold σ^0_{Pol} are associated with breaking events identified from the video, the number of events detected is roughly one–tenth the number of whitecaps which were counted in the independent analysis of the video recordings summarized in Table 4.1. Furthermore, as indicated in discussing the example in Figure 4.2, the data reveal breaking events which produce

discernible sea spikes of a lesser magnitude than the threshold value σ^0_{Pol}.

In order to investigate improved discrimination, the microwave measurements for the two hours of video recordings were further analyzed to compile detailed statistics on all sea spikes which might be associated with the passage of a wave crest. The passage of an individual wave crest was taken as the time between zero up–crossings in the zero–mean time series of the Doppler frequency. A minimum threshold of $\sigma^0_{VV} > \sigma^0_{Pol}/2$ was imposed to eliminate false detections due to low–level random fluctuations. Using the criterion established above, the video recordings were then replayed and each sea spike was classified as being associated with either a breaking or a non–breaking wave.

Table 4.2 summarizes the results of this analysis in terms of the total number of sea spikes detected and the number of breaking and non–breaking waves identified. Also listed is the quantity P_{5m}, defined as the percentage of wave crests associated with sea spikes attributed to breaking waves (ie., sea spikes due to waves which produce a whitecap within 5m of the center of the radar spot). As in the independent analysis of the video recordings, the total number of wave crests was based on the peak frequency of the surface displacement spectrum. The percentage P_{5m} may be compared to P_{3dB}, the percentage of breaking crests identified independently from the video recordings and summarized in Table 4.1. For the higher friction velocity data in Run 12, the value of $P_{5m}=18.1\%$ is comparable to that of $P_{3dB}=21.1\%$, while the microwave–based percentage of $P_{5m}=5.3\%$ for Run 11 is roughly half that of the corresponding value of $P_{3dB}=12.1\%$. However, the values of P_{3dB} for both hours of video recordings analyzed are still within the range of measurements

by previous authors summarized in Figure 1.1. The appropriate comparison for evaluating the performance of a given microwave detection schemes is the number of unambiguously detected breaking events as a percentage of the total number of sea spikes caused by breaking waves. This percentage, denoted as P_{ss}, is tabulated in Table 4.3 for the cross–section threshold σ_{Pol}^{0}=–5.2dB and other detection schemes considered later in this chapter. As previously noted, all of the events detected by the VV radar cross–section threshold σ_{Pol}^{0}=–5.2dB were associated with breaking waves. However, these detected events comprise only 15–20% of the sea spikes associated with breaking waves identified in the video recordings.

Scatter plots showing the peak values of σ_{VV}^{0} versus σ_{HH}^{0} for seas spikes classified from the video recordings are given in Figure 4.9a and 4.9b for Run 11 and Run 12, respectively. The upper plot in each figure is for events classified as being due to breaking waves, while the lower plot is for those due to non–breaking waves. The distribution of non–breaking values indicates that a radar cross–section threshold somewhat lower than σ_{Pol}^{0}=–5.2dB (0.30) would continue to detect only breaking events. Furthermore, comparison between the VV and HH values in Figure 4.9 suggests that applying the threshold to either polarization would yield equivalent results.

Breaking events continue to be unambiguously detected as the VV radar cross–section threshold is lowered to a value of –6dB (0.25). However, the distributions of breaking events in Figure 4.9 indicate that a significant number of sea spikes associated with breaking events have still lower radar cross–section. The percentage of breaking events detected by the lower threshold of –6dB, summarized in Table 4.3, is approximately 30%. This
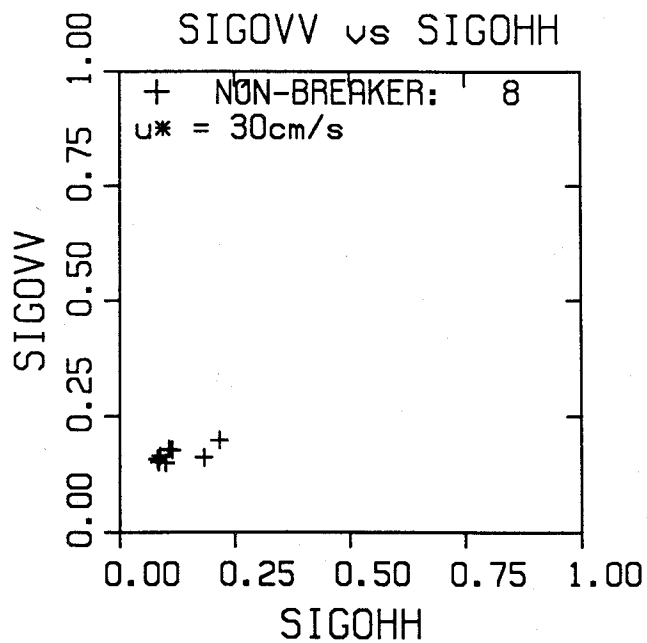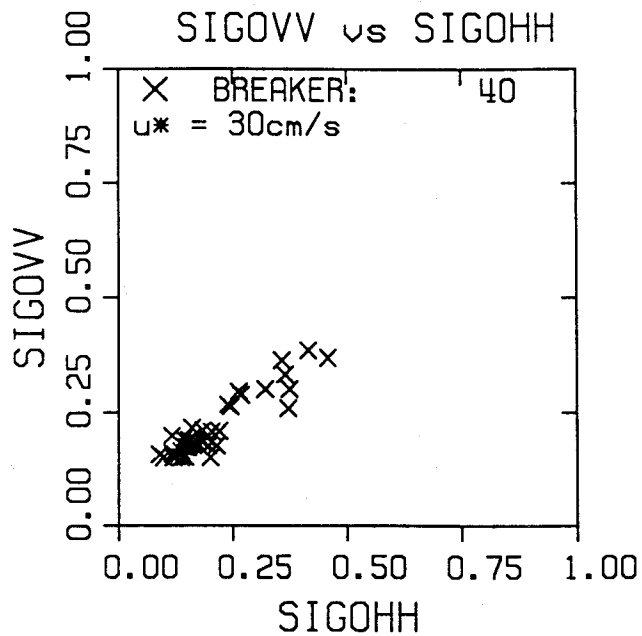
Figure 4.9a: Scatter plot of peak σ^o_{vv} vs σ^o_{hh} for sea spikes associated with waves identified as breaking (top) and non–breaking (bottom) for a one–hour video recording during Run 11 (u^*=30cms^{-1}).
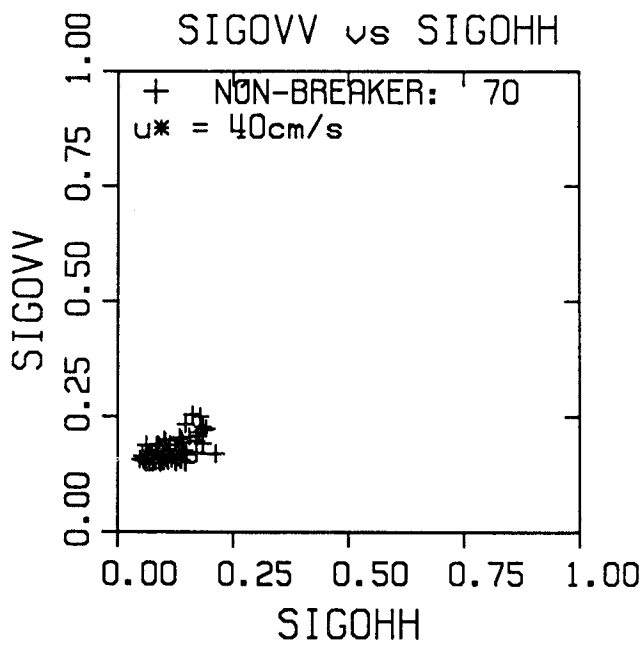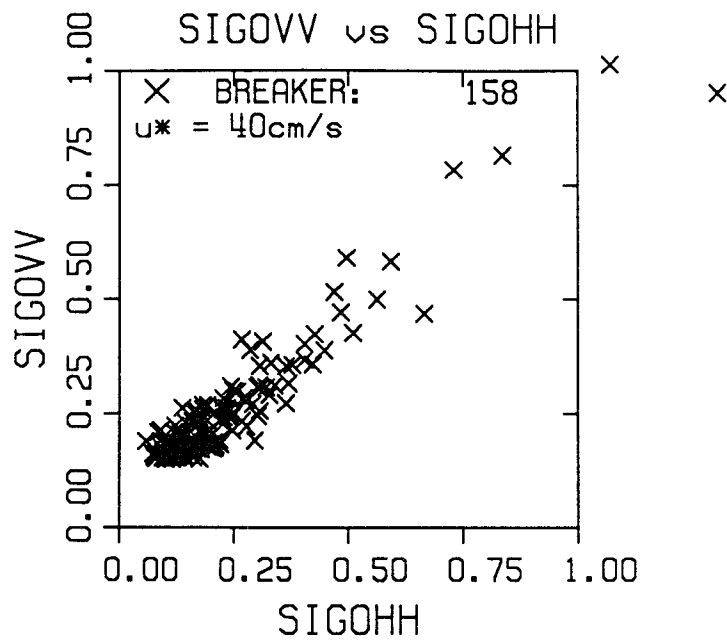
Figure 4.9b: Same as Figure 4.9a except for Run 12 (u^*=40cms^{-1}).

result indicates that, on the basis of radar cross–section alone, roughly 70% of the sea spikes which are attributable to breaking waves are not distinguishable from seas spikes of comparable magnitude which show no visual evidence of being due to wave breaking.

4.2 POLARIZATION RATIO

The polarization characteristics of the variation of the mean radar cross–section σ^0 with incidence angle are shown schematically in Figure 4.10. In the moderate incidence angle regime, the polarization ratio $\sigma^0_{VV}/\sigma^0_{HH}$ is greater than unity due to the dominance of the Bragg resonant scattering mechanism (Wright, 1966). However, the scattering becomes polarization independent as the incidence angle decreases and the specular scattering regime is approached, resulting in a polarization ratio of unity. As reported in chapter 1, previous authors have associated polarization independent sea spikes with breaking waves.

The data in the scatter plots in the upper graphs of Figure 4.9 show that many of the breaking events with large radar cross–section fall close to the line of $\sigma^0_{VV}=\sigma^0_{HH}$. However, the majority of sea spikes caused by breaking waves show σ^0_{VV} significantly greater than σ^0_{HH}. Furthermore, many of these events fall in the same region as the non–breaking events shown in the lower plots of Figure 4.9. The distribution of polarization ratio values is also illustrated in Figure 4.11, which shows scatter plots of the polarization ratio versus F_{max}, the Doppler frequency maximum associated with the detected events. (A discussion of the distribution of F_{max} follows in the next section.) These plots confirm that very few non–breaking waves have polarization ratios
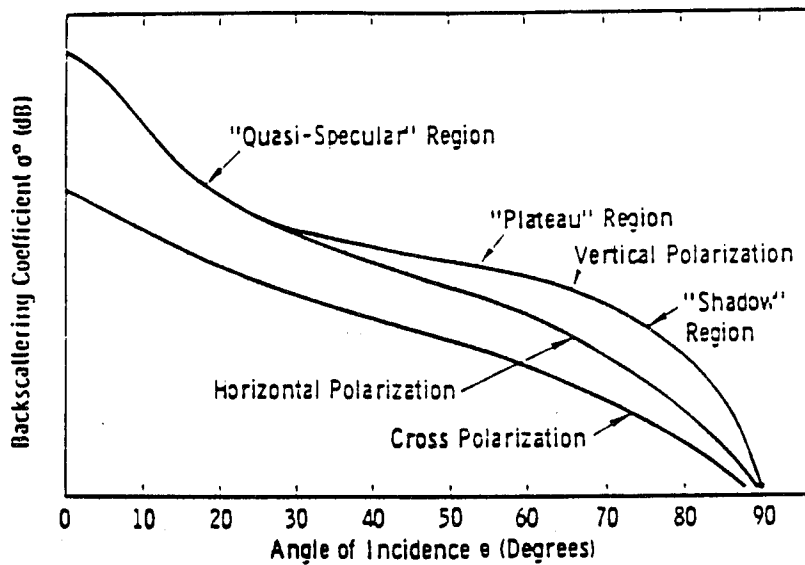
Figure 4.10: Schematic diagram showing polarization dependence of σ^o as a function of incidence angle. In general, $\sigma^o_{vv} > \sigma^o_{hh}$ for moderate incidence angle, while the return becomes polarization independent as the incidence angle decreases (from Ulaby et al., 1982).
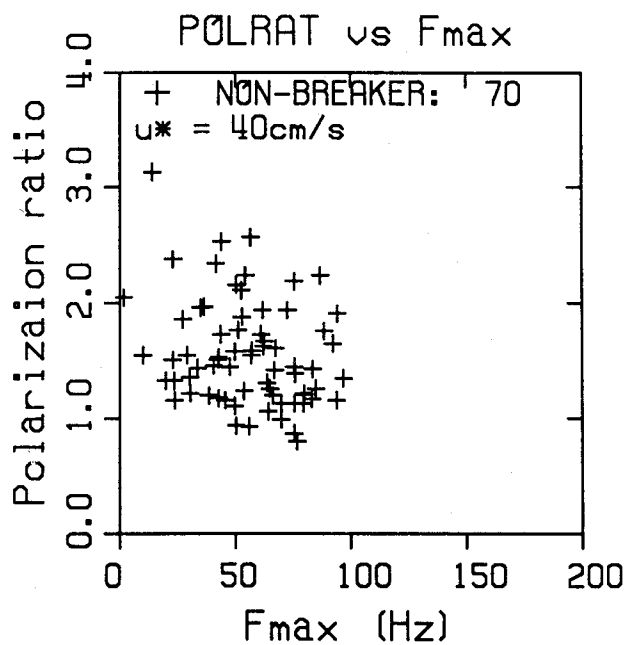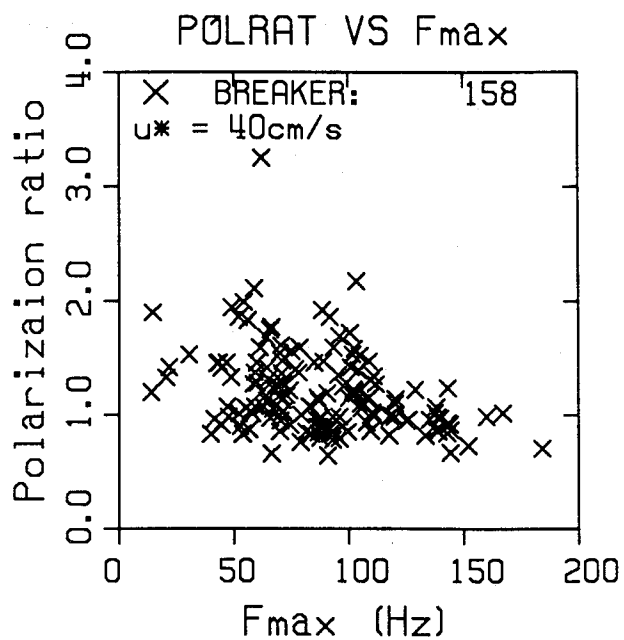
Figure 4.11: Scatter plot of polarization ratio of sea spike maxima versus the associated maximum Doppler frequency shift for breaking (top) and non–breaking (bottom) waves during the one–hour video recording for Run 12 ($u^*=40cms^{-1}$).

less than unity. However, a significant number of breaking events would be eliminated by a polarization ratio threshold of unity. These results discourage the use of the polarization ratio as a further discriminator of microwave events associated with wave breaking.

4.3 MEAN DOPPLER FREQUENCY

As noted in the discussion of Figure 4.2, the large sea spikes associated with the forward face of breaking waves occur very near in time to local maxima in the mean Doppler frequency. This observation is further illustrated by considering whether F_{max}, the maximum Doppler frequency associated with a given sea spike, is equal to F_{pk}, the Doppler frequency which occurs at the time of the sea spike peak. Figure 4.12 is a scatter plot of F_{pk} versus F_{max} for breaking and non–breaking waves identified the video recordings for Run 12. Most of the points in Figure 4.12 are clustered near the line $F_{pk}=F_{max}$, indicating that many of the Doppler frequency maxima are nearly coincident with the sea spike peak. This observation applies to both the breaking and non–breaking distributions in Figure 4.12.

The nearly simultaneous occurrence of the sea spike and Doppler frequency maxima is consistent with the assumption that the mean Doppler frequency is dominated by the line–of–sight component of the orbital velocity. Figure 4.13 shows the phase relationship between the surface displacement and the line–of–sight velocity V_r from linear wave theory (equation 3.4) for an incidence angle 45°. For a fixed observer, the maximum positive line–of–sight velocity occurs on the forward face at a phase of +45° relative to the crest. Notice also that the line–of–sight velocity is zero following the crest at phase
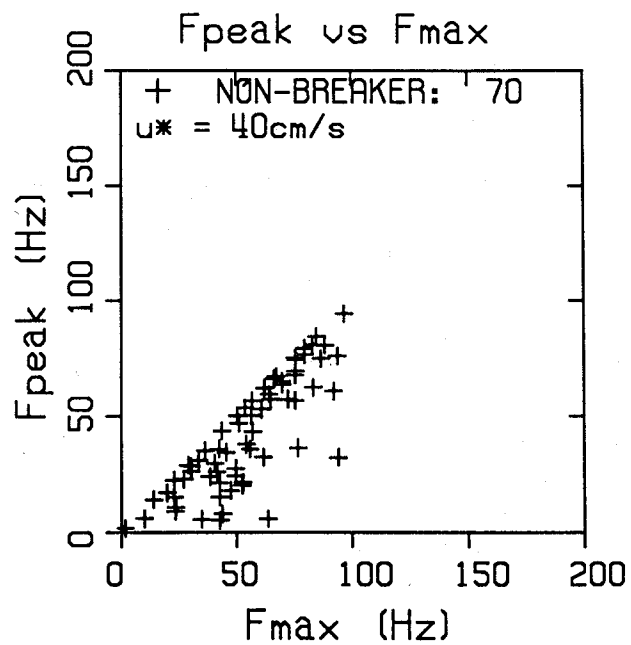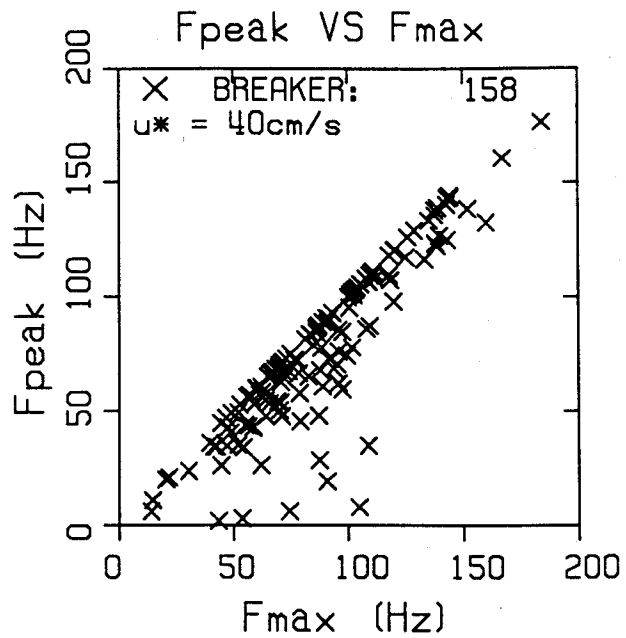
Figure 4.12: Scatter plot of the Doppler frequency at the time of the sea spike peak, F_{peak}, versus the Doppler frequency maximum, F_{max}, for breaking (top) and non-breaking (bottom) waves identified from the one-hour video recording during Run 12 ($u^*=40cms^{-1}$).
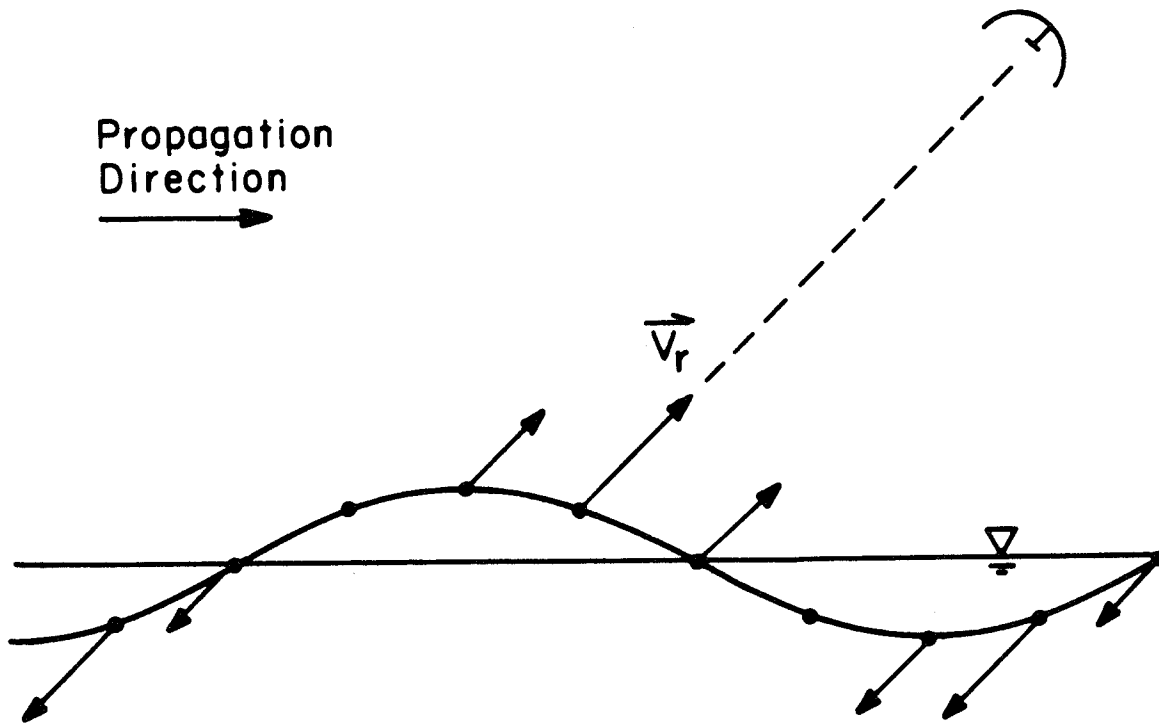
Figure 4.13: Variation with surface wave phase of V_r, the component of orbital velocity in the antenna look direction, from linear wave theory for an incidence angle of 45°. The velocity varies across the crest region from its maximum at $\pi/4$ ahead of the crest to zero at $\pi/4$ behind the crest.

angle $-45°$. (In a field situation, the orbital velocity will be superimposed on a surface drift current. The effect of this current is evident in the time series of the Doppler frequency in Figure 4.2, which has a positive long–term average.)

In addition to the contribution of the orbital velocity to the Doppler spectrum, the increased velocity of the active whitecap at the crest of a breaking wave is expected to be important. This additional scatterer velocity will generally occur later in time than the Doppler frequency maximum, since the latter is roughly coincident with the sea spike peak associated with the forward face of the wave crest. Note that if the whitecap velocity is nearly horizontal at the wave crest, its contribution to the measured line–of–sight velocity generally will be less than its magnitude. Nonetheless, the Doppler frequency due to the whitecap moving at a velocity on the order of the phase speed can be significantly larger than that due to the orbital velocity. The large velocities associated with active whitecaps superimposed on the orbital velocity contribution may be expected to increase the Doppler bandwidth, as discussed in the next section.

The joint scatter plot of the polarization ratio versus F_{max} in Figure 4.11 shows that the Doppler frequency maxima associated with breaking events can cover a wide range. The extent of this distribution may reflect the influence of the crest orientation on the measured line–of–sight scatterer velocity. Although a threshold criterion on the mean Doppler frequency apparently cannot increase discrimination, it may contain important information concerning the kinematics of the breaking process, as will be discussed in Chapter 5.

4.4 DOPPLER BANDWIDTH

A jump in the Doppler bandwidth often accompanies sea spikes which are caused by waves that break. The area–extensive nature of the scatterometer measurement produces a return whose frequency spectrum is the power–weighted velocity distribution of the scatterers within the illumination area. The bandwidth B as defined in Chapter 3 (section 3.2.2) is an indication of the range of velocities present. Unlike the mean Doppler frequency, however, the bandwidth maximum associated with a breaking wave generally occurs after the sea spike maximum in σ^0.

Comparisons of time series such as Figure 4.2 with simultaneous video recordings indicate that a bandwidth maximum generally occurs when the illumination area straddles the crest region. Even for a non–breaking wave, an increase in the bandwidth might be expected near the crest region due to the change in the line–of–sight velocity across the crest (see Figures 4.3 and 4.11). However, the velocity of an active whitecap will increase the range of velocities within the illumination area straddling the crest region and thus augment the bandwidth.

Doppler spectra computed from the archived scatterometer data support the idea that the characteristic jump in the bandwidth following a sea spike is due to an increased range of velocities near the crest. Figure 4.14 is a 1–minute time series of radar cross–section, mean Doppler frequency, and Doppler bandwidth computed directly from moments of the power spectral density of the microwave backscatter. Figures 4.15 through 4.17 show Doppler spectra corresponding to the three sea spike events identified in the time series of Figure 4.14 by the time in minutes and decimal seconds. The vertical axis
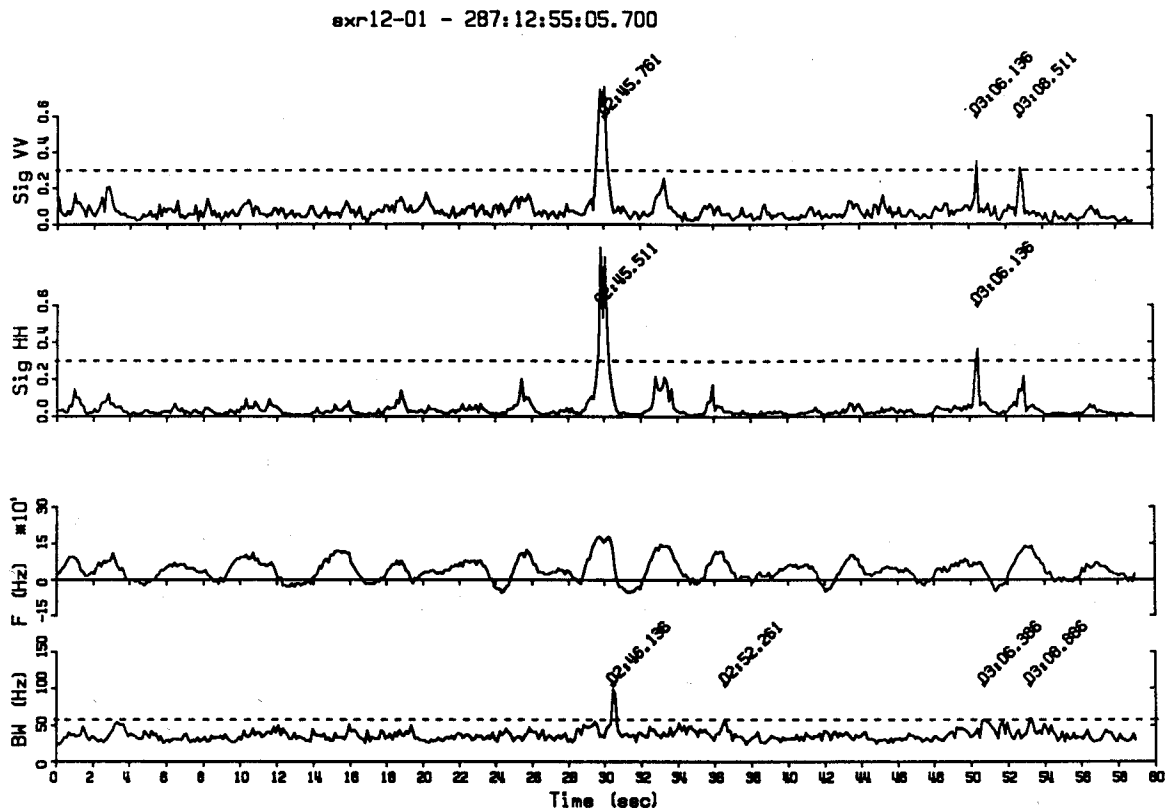
Figure 4.14: Example of one–minute time series of σ^0_{vv}, σ^0_{hh}, mean Doppler frequency, and bandwidth computed directly from Doppler spectra derived from the scatterometer data recorded on analog tape. Doppler spectra for the three sea spikes identified in the top trace are shown in Figures 4.15–4.17.
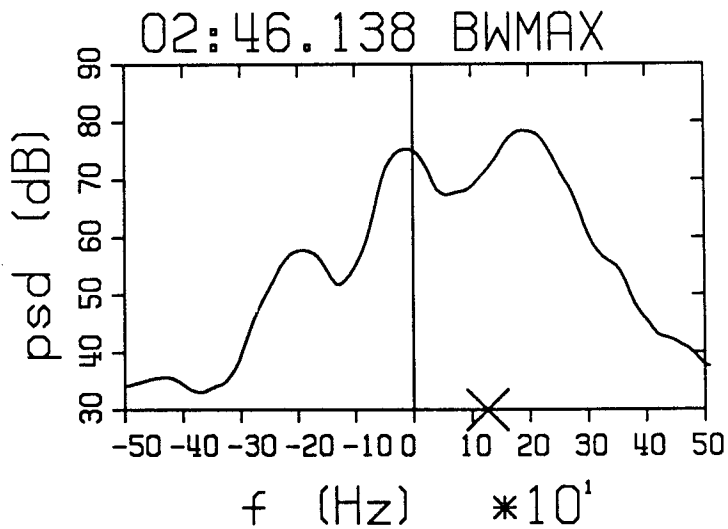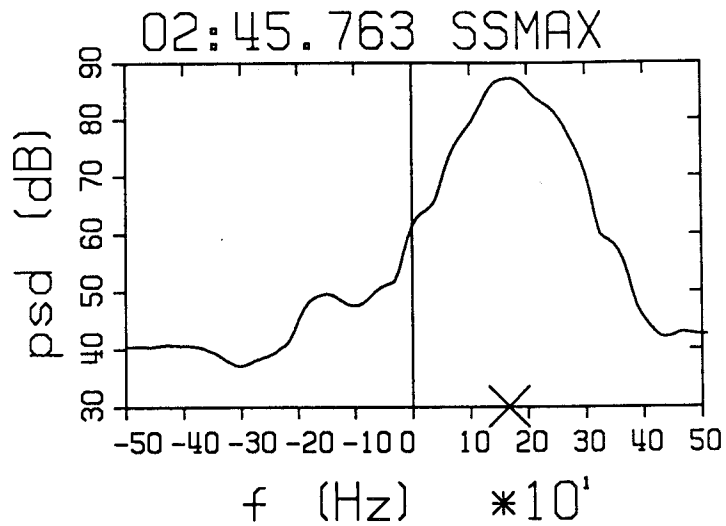
Figure 4.15: Doppler spectra for the first sea spike identified in Figure 4.14 (VV time 02:45:761) corresponding to the sea spike peak (top, labelled SSMAX) and the associated bandwidth maximum (bottom, labelled BWMAX). The mean frequency is marked with an (X) on the frequency axis. An image of the dominant peak reflected about zero frequency is evident on the left in each spetrum.
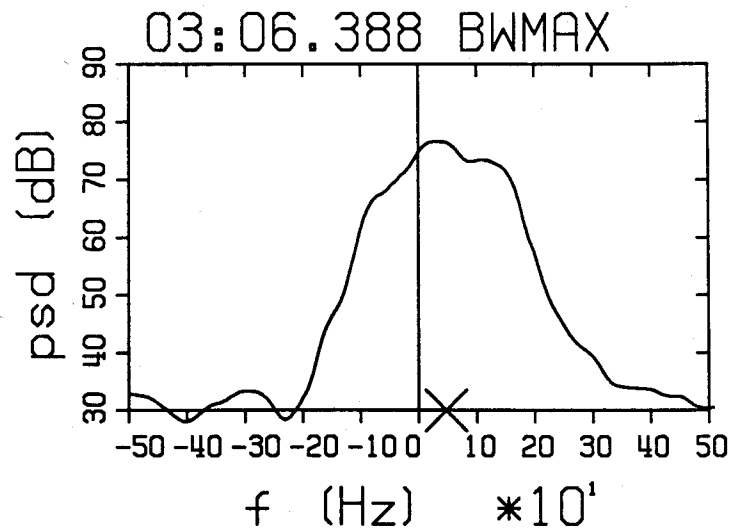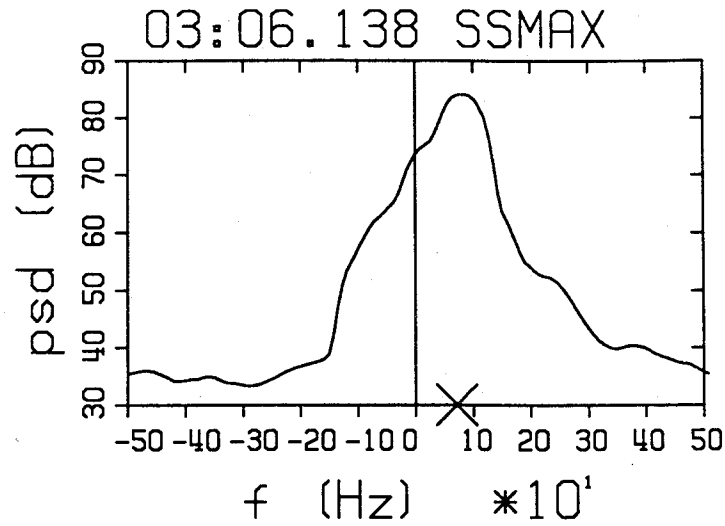
Figure 4.16: Doppler spectra for the second sea spike peak identified in Figure 4.14 (VV time 03:06.136) corresponding to the sea spike peak (SSMAX) and the associated bandwidth maximum (BWMAX). The mean frequency is indicated by an (X) on the frequency axis.
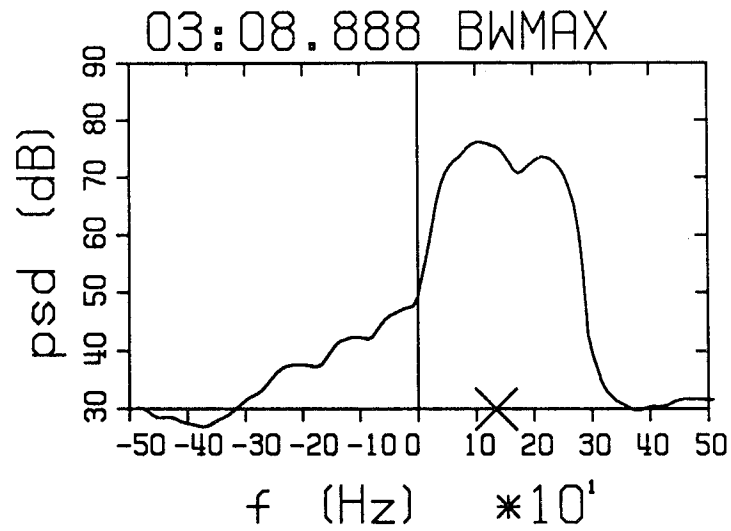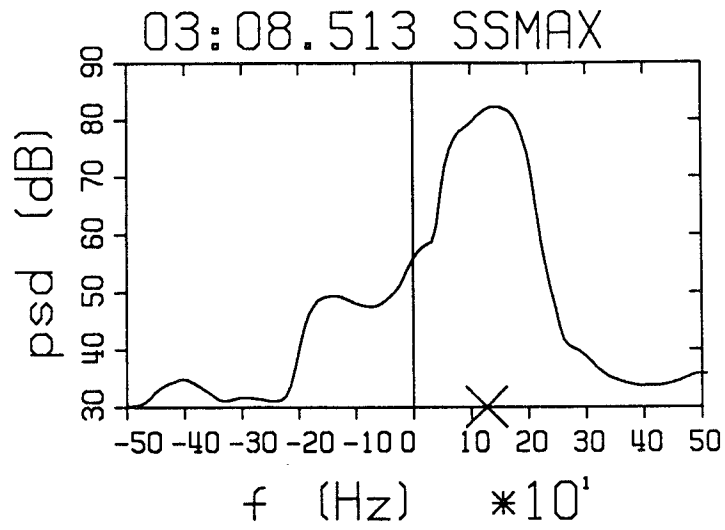
Figure 4.17: Same as Figure 4.16 except for the third sea spike identified in Figure 4.14 (VV time 03:08.511).

is the relative power spectral density in decibels (dB re arbitrary units) and the horizontal axis is the Doppler frequency in Hertz (Hz), with axis divisions of 100 Hz and zero frequency indicated by the vertical center line (recall that the Doppler conversion is 94Hz per m/s).

Rigorously, the spectra shown are estimates of the power spectral density, computed from the complex Fourier coefficients of the finite Fourier transform. The microwave data were digitally sampled at a rate of 1kHz per channel and subdivided into segments of 125 points, corresponding to a time length of 0.125s. A Hanning window was applied and each record was padded with zeros to a length of 128 points. The Fourier coefficients were calculated using an FFT algorithm and the estimate of the Doppler spectrum was computed from the magnitude of the coefficients. The spectrum was then smoothed using a weighted running average, resulting in a reduction of variance equivalent to 64 degrees of freedom.

The spectra in the upper plots of Figures 4.15 through 4.17, entitled SSMAX, coincide in time with the maximum in the radar cross–section for each sea spike considered. The lower spectra in the figures, entitled BWMAX, correspond to the bandwidth maxima for each event. The mean Doppler frequency for each spectrum is indicated by an (X) on the frequency axis.

The spectra corresponding to the first sea spike identified in Figure 4.14 are shown in Figure 4.15. The spectrum at the time of the sea spike maximum exhibits a single peak which is roughly coincident with the mean Doppler frequency. The small peak with a negative frequency is the image of the major peak. The spectrum corresponding to the bandwidth maximum is quite different, showing two major peaks widely separated in frequency.

(Again, the small, negative frequency peak is an image of the major peak.) The mean Doppler frequency is less than that for the sea spike maximum, even though the frequency of the highest peak is somewhat larger. The secondary peak lies very close to zero and shows significant contribution at negative frequencies. In contrast, the spectrum in Figure 4.16 corresponding to the bandwidth maximum for the second event in Figure 4.14 does not show two distinct frequency peaks. However, the spectrum does include significant return ranging from near zero frequency to approximately 150 Hz. The third example in Figure 4.17 shows a bimodal distribution with energy at frequencies exceeding 200Hz.

The bimodal nature of the spectra corresponding to the bandwidth maximum is consistent with the notion that the velocity distribution within the illumination area straddling a breaking crest will show a range of scatterer velocities. This range of velocities is likely to include contributions from higher velocities within the active whitecap as well as those of scatterers advected by the orbital velocity. A significant amount of energy near zero frequency in the spectra corresponding to a bandwidth maximum suggests return from the back side of the crest.

The scatter plots in Figures 4.18 and 4.19 show the peak VV sea spike radar cross-section, σ^0_{pk}, versus the corresponding maximum bandwidth, B_{max}, for Runs 11 and 12, respectively. The distribution of B_{max} in these figures suggests that a bandwidth threshold alone would unambiguously identify a larger number of breaking events than the radar cross-section threshold of -6dB used above. Indeed, a criterion that B_{max} exceed 50Hz successfully detects approximately 65–70% of the breaking events identified from the video

SIGMA0-VV VS BW

Peak sigma0 – VV

$\times$ BREAKER: 40
$u* = 30cm/s$
VV min = .15

BWmax (Hz)

SIGMA0-VV vs BW

Peak sigma0 – VV

$+$ NON-BREAKER: 8
$u* = 30cm/s$
VV min = .15

BWmax (Hz)
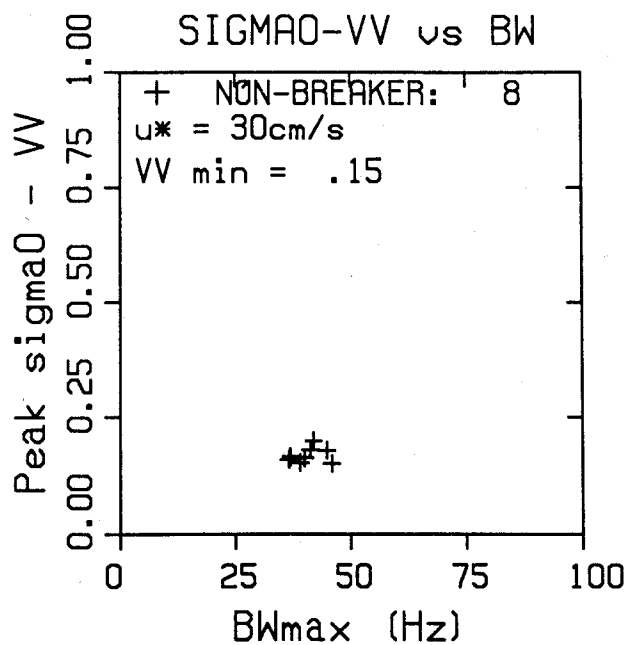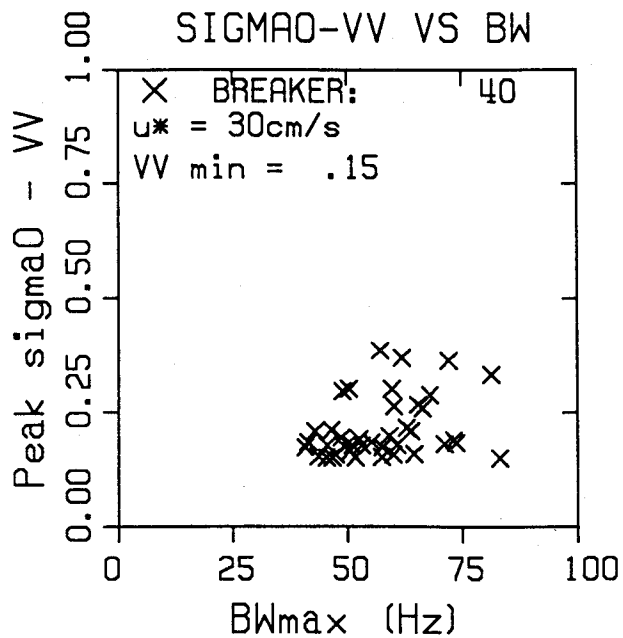
Figure 4.18a: Scatter plot of peak sea spike σ^0_{vv} versus B_{max}, its associated bandwidth maximum for breaking (top) and non-breaking (bottom) waves for the one-hour video recording from Run 11 ($u*=30cms^{-1}$).

SIGMA0-VV VS BW

SIGMA0-VV vs BW
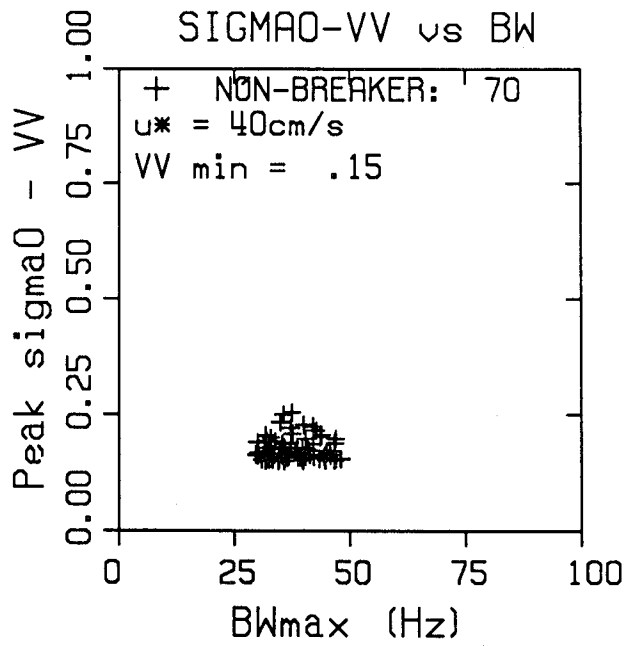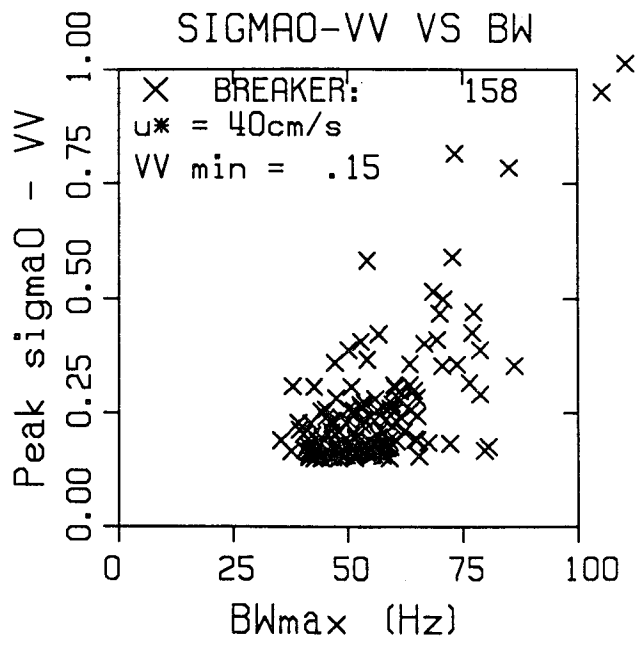
Figure 4.18b: Same as 4.18a except for Run 12 (u*=40cms^{-1}).

recording for Runs 11 and 12. By counting all events for which $\sigma^0_{VV} > -6$dB and/or B>50Hz, this success rate is increased slightly to a maximum of 73% (see Table 4.3). In other words, nearly 3 out of 4 breaking waves producing detectable microwave events are identified by a threshold−based scheme utilizing both radar cross−section and bandwidth information.

4.5 Detection Schemes to be Tested

The four threshold−based detection schemes considered in this chapter are:

1) $\sigma^0_{Pk} \geq \sigma^0_{Pol} = 0.30$ (polarization independent events, Figure 4.7)

2) $\sigma^0_{Pk} \geq 0.25$ (from distributions in Figure 4.9)

3) $B_{max} \geq 50$ Hz (from distributions in Figure 4.18)

4) $\sigma^0_{Pk} \geq 0.25$ or $B_{max} \geq 50$ Hz (from distributions in Figure 4.18)

The percentages of breaking events identified by these schemes are summarized in Table 4.3. While none of these detection schemes identify all microwave events attributable to breaking waves, scheme (4) is the most successful. Furthermore, for each scheme, the proportion of breaking events detected is roughly the same for both runs (see Table 4.3). That is, for the two different one−hour video recordings with $u_* = 30$cms^{-1} and $u_* = 40$cms^{-1}, the number of breaking events counted was proportional to the total number of sea spikes caused by breaking waves. To assess the impact of different detection schemes on the sea spike statistics, the analysis in the next chapter will be performed for all 4 detection schemes listed above. Note that schemes (3) and (4) may

be expected to provide better results than (1) and (2) by virtue of the larger sample size they provide.

CHAPTER 5

RESULTS AND DISCUSSION

The results from the simultaneous microwave and video measurements presented in Chapter 4 show that detection thresholds in radar cross-section as well as Doppler bandwidth can be used to identify individual breaking events. The location of the illumination area with respect to the phase of the breaking wave as well as the stage of breaking development will influence the detectability of a breaking event occurring in the vicinity of the radar spot. Also, the orientation of an individual crest with respect to the antenna look direction can affect detectability. Therefore, a microwave scatterometer cannot be expected to detect all waves that break near the illumination area. However, if the variability of the return due to such effects as crest orientation and spot location are random, then the scatterometer may provide a valid sample of the breaking events present.

The thresholds investigated in Chapter 4 do not detect all breaking wave crests in the vicinity of the microwave illumination area. However, for the two 1-hour video recordings analyzed in detail, the number of detected microwave events is proportional to the total number of sea spikes caused by wave breaking events. Therefore, if counting sea spikes caused by breaking waves is an indicator of the degree of wave breaking, then the detected sea spikes provide a relative measure. In this chapter, statistics of the detected microwave events are compared with modelling and measurements of wave breaking by previous investigators. Average normalized velocity and bandwidth which may be associated with the kinematics of wave breaking are also presented. Finally, the effect of decreasing the integration time used in processing is discussed.

As outlined in Chapter 3, section 3.2.3, the edited data set covers a wide range of sea conditions, none of which can be assumed to be fully–developed. Nonetheless, results from all runs are presented together because of the relatively limited amount of data available. In order to aid in identifying variations which might be a result of the wide range of conditions covered, data from each of the seven subsets are identified by a different symbol (each symbol represents the value corresponding to a one–hour record). Table 3.2 which summarizes the data runs has been reproduced as Table 5.1 for convenience.

Many of the results in this chapter are presented on log–log plots fitted with a straight line, illustrating a power law relation. These lines are the result of a linear regression analysis, following the method described by Bendat and Piersol (1986). The analysis provides a measure of the slope of the line, 95% confidence intervals on that slope, and a correlation coefficient. The linear regression parameter for power laws investigated are summarized in Table 5.2 and 5.3 as a function of detection threshold.

As outlined in Chapter 4 (section 4.5), four different detection schemes are used in presenting the quantitative results in this chapter. The detection criteria, repeated here for convenience, are:

1) $\sigma^0_{Pk} \geq \sigma^0_{Pol} = 0.30$

2) $\sigma^0_{Pk} \geq 0.25$

3) $B_{max} \geq 50$ Hz

4) $\sigma^0_{Pk} \geq 0.25$ and/or $B_{max} \geq 50$ Hz

Table 5.1: <u>DATA RUN CHARACTERISTICS</u>

RUN ID	HRS	FLO (Hz)	FHI (Hz)	SWH (m)	u* (cm/s)	U_{10} (m/s)	FETCH(km) look—dir
1	8	.13—.16	N/A	1.4—1.8	23—32	6.3—9.6	unlimited NE2/57°
4	4	.11	.27—.35	0.7—1.0	26—30	7.1—8.5	unlimited SW1/164°
5	6	.11	.25	1.0—1.1	26—31	6.3—7.9	32 NE1/342°
6	3	.09—.11	N/A	1.5—1.8	38—43	9.6—10.5	32 NE1/342°
9	5	0.10	.24—.27	1.1—1.3	42—46	10.4—11.5	28 SW3/220°
11	6	N/A	.22—.24	0.7—1.0	25—33	6.2—8.3	32 NE1/342°
12	12	N/A	.20—.25	1.0—1.2	38—48	8.4—11.7	32 NE1/342°

(See table 3.1 for key to table 5.1)

Schemes 1 and 2 are based on thresholds in radar cross–section and detect relatively low percentages of sea spikes caused by breaking waves. The use of a bandwidth threshold in schemes 3 and 4 significantly increases the percentage of breaking events detected (see Table 4.3). This larger sample size suggests that the statistical significance of the results using schemes 3 and 4 is greater than that of schemes 1 and 2.

The wind speed dependence of the sea spike statistics was presented in chapter 2 in terms of the friction velocity u_*. Phillips (1988) formulation for the sea spike frequency and contribution to the mean radar cross–section is in terms of a dimensionless friction velocity, $(u_*^2 \kappa/g)^{\frac{1}{2}}$, where κ is the electromagnetic wavenumber and g is the gravitational acceleration (see equations (1.25) and (1.26)). In this chapter, the power law relations expressing friction velocity dependence are presented in terms of this dimensionless variable, denoted a $\tilde{u}_*$. The plots of the computed quantities versus friction velocity have two x–axis scales: the top axis is the friction velocity, u_* (ms^{-1}) while the lower axis is the dimensionless friction velocity $\tilde{u}_*$.

5.1   FRICTION VELOCITY DEPENDENCE OF THE RADAR CROSS SECTION

The mean radar cross–section, σ^0, versus friction velocity is shown in Figure 5.1 for VV and HH polarizations. The SAXON results in Figure 5.1 are consistent with the corresponding preliminary measurements shown in Figure 2.6. The angle φ between the radar look–direction and the wind for the SAXON measurements was in the range $0^0 < \varphi < 25^0$, while for the preliminary results the angle φ was in the range $25^0 < \varphi < 45^0$. However, the variation of
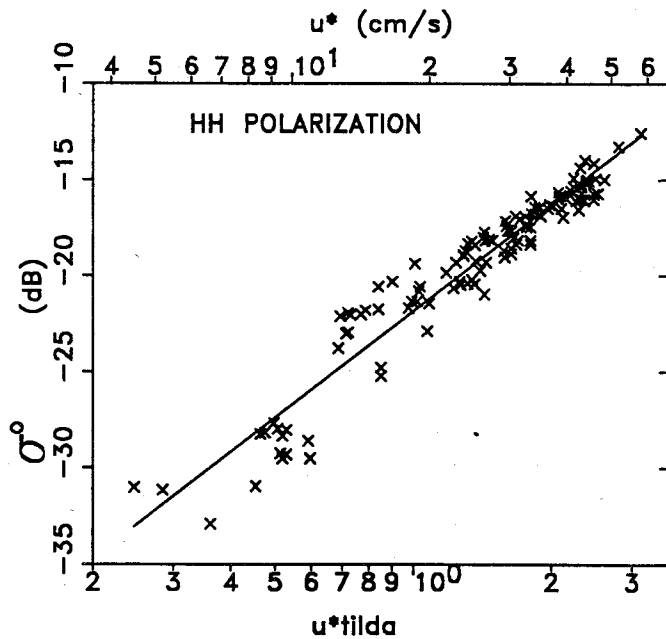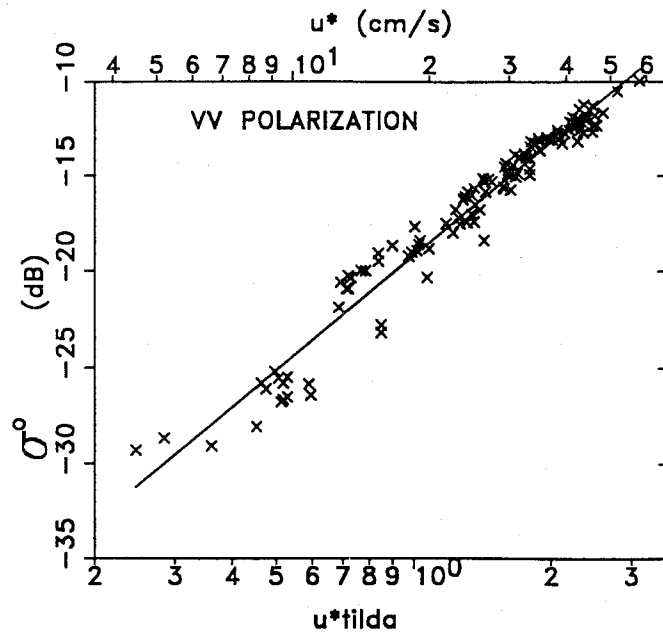
Figure 5.1: Mean normalized radar cross–section versus friction velocity for VV
(a:top) and HH (b:bottom) polarization, where each symbol represents a
one–hour average. The slope of the linear regression line is 2.0 for VV and
1.8 for HH polarization.

σ^o between the these two ranges of φ is less than 1dB, according to the Seasat–A satellite scatterometer model known as SASS II (Wentz, Peteherych, and Thomas, 1984). The calibration accuracy of the scatterometers used in both the preliminary and SAXON experiments has been estimated to be ±1dB (see Chapter 2, section 2.1 and Chapter 3, section 3.1.1).

For the relations

$$\sigma^o_{VV} = C_1 \, \tilde{u}_*^{a_1},$$ (5.1)

and

$$\sigma^o_{HH} = C_2 \, \tilde{u}_*^{a_2},$$ (5.2)

the exponents a_1 and a_2 with 95% confidence limits are $a_1 = 2.0 \pm 0.07$ ($\log C_1 = -1.9 \pm 0.02$, correlation coefficient $\rho_1 = 0.98$) for VV polarization and $a_2 = 1.8 \pm 0.09$ ($\log C_2 = -2.2 \pm 0.03$, correlation coefficient $\rho_2 = 0.96$) for HH polarization.

5.2   COMPARISON WITH PHILLIPS' (1988) PREDICTIONS

5.2.1   FREQUENCY OF SEA SPIKE OCCURRENCE

As outlined in Chapter 1, section 1.3.5, Phillips (1988) predicted a cubic dependence on friction velocity for the frequency of occurrence of sea spikes detected by an intensity threshold. The preliminary results from measurements in the North Sea presented in Chapter 2 were consistent with this expectation (Table 2.1 and Figures 2.10). Results from the SAXON experiment are given in Figures 5.2 as the number of detected events in a one–hour record versus

(a)

(b)

(c)

(d)
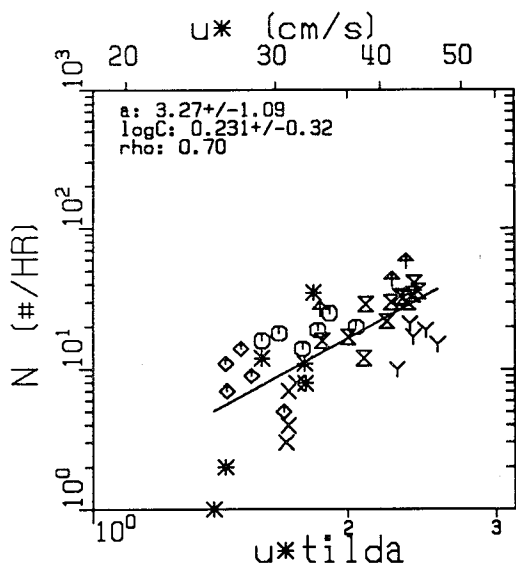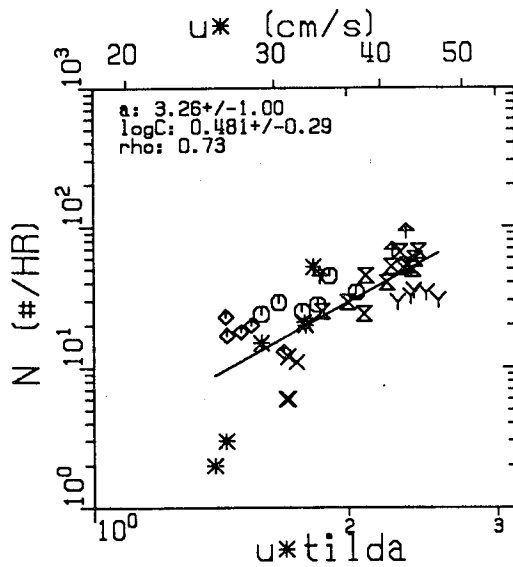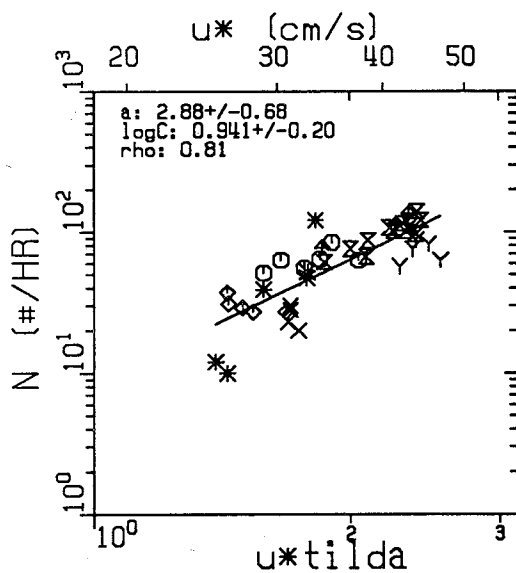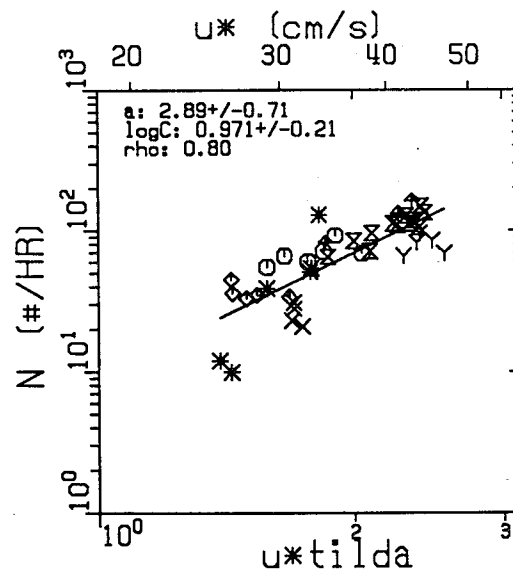
$\odot=1$, $\times=4$, $\diamond=5$, $\uparrow=6$, $Y=9$, $\ast=11$, $\boxtimes=12$

Figure 5.2: Frequency of sea spike occurrence N (number per hour) vs friction velocity for the detection schemes (a) $\sigma^{0}_{vv} > \sigma^{0}_{pol} = -5.2$dB, (b) $\sigma^{0}_{vv} >= -6.0$dB, (c) B>50Hz, and (d) $\sigma^{0}_{vv} >= -6.0$dB and/or B>50Hz. Each symbol represents one–hour with different symbols for each run. The linear regression parameters for equation (5.3) are in the upper left hand corner of each plot.

friction velocity, u_*, in log–log plots for the four different detection thresholds tested. For the relation

$$N = C_3\, \tilde{u}_*^{a_3},\tag{5.3}$$

the exponent a_3 is in the range $2.9 \leq a_3 \leq 3.3$ with correlation coefficient ρ_3 in the range $0.70 \leq \rho_3 \leq 0.81$ (see Table 5.2). These results are consistent with both the preliminary results presented in Chapter 2 and with Phillips' (1988) prediction.

5.2.2 CONTRIBUTION OF SEA SPIKES TO THE MEAN RADAR CROSS–SECTION

As outlined in Chapter 1, section 1.3.5, Phillips (1988) also predicted a cubic dependence on friction velocity for the contribution of sea spikes to the mean radar cross–section. The preliminary measurements in Chapter 2 also supported this prediction (Table 2.1 and Figures 2.7a–b). The two methods used to compute the sea spike contribution were outlined in Chapter 2, section 2.3. Both methods associate the contribution of an individual sea spike with the area under the spike above a specific value. For method 1 (see equation 2.3 and Figure 2.5a), the area under the sea spike is bounded by σ^0, the long–term mean radar cross–section. In method 2 (equation 2.4 and Figure 2.5b), the area under the sea spike is limited by the local minima on either side of the sea spike peak. In general, the contribution computed using method 2 will be greater than that given by method 1.

The sea spike contribution, σ_{ss}^0, as defined by method 1 is shown versus friction velocity, u_*, on a log–log plot in Figures 5.3 and 5.4 for VV and HH polarizations, respectively. For the relations

TABLE 5.2: <u>Linear Regression Results</u> ($T_i=0.25$s)

	$\sigma^0_{VV} > \sigma^0_{pol}$	$\sigma^0_{VV} > -6$dB	BW > 50 Hz	$\sigma^0_{VV} > -6$dB, BW > 50 Hz
$N=C_3\tilde{u}_*^{a_3}$:				
a_3:	3.3 ± 1.1	3.3 ± 1.0	2.9 ± 0.7	2.9 ± 0.7
$\log C_3$:	0.23 ± 0.32	0.48 ± 0.29	0.94 ± 0.20	0.97 ± 0.21
ρ_3:	0.70	0.73	0.81	0.80
$\sigma^0_{SSVV1}=C_4\tilde{u}_*^{a_4}$:				
a_4:	3.4 ± 1.2	3.2 ± 1.0	2.7 ± 0.7	2.7 ± 0.8
$\log C_4$:	-4.0 ± 0.4	-3.8 ± 0.3	-3.4 ± 0.2	-3.4 ± 0.2
ρ_4:	0.68	0.71	0.76	0.75
$\sigma^0_{SSHH1}=C_5\tilde{u}_*^{a_5}$:				
a_5:	3.3 ± 1.2	3.2 ± 1.0	2.7 ± 0.8	2.7 ± 0.8
$\log C_5$:	-3.9 ± 0.4	-3.7 ± 0.3	-3.4 ± 0.2	-3.4 ± 0.2
ρ_5:	0.68	0.71	0.76	0.75
$\sigma^0_{SSVV2}=C_6\tilde{u}_*^{a_6}$:				
a_6:	3.6 ± 1.2	3.5 ± 1.1	3.0 ± 0.8	3.0 ± 0.8
$\log C_6$:	-4.0 ± 0.4	-3.75 ± 0.3	-3.4 ± 0.2	-3.4 ± 0.2
ρ_6:	0.70	0.73	0.78	0.77
$\sigma^0_{SSHH2}=C_7\tilde{u}_*^{a_7}$:				
a_7:	3.5 ± 1.2	3.4 ± 1.0	3.0 ± 0.8	3.0 ± 0.8
$\log C_7$:	-3.9 ± 0.4	-3.7 ± 0.3	$-3.4 \pm .2$	-3.3 ± 0.2
ρ_7:	0.69	0.72	0.78	0.77
$P_{ss}=C_8\tilde{u}_*^{a_8}$:				
a_8:	3.4 ± 1.5	3.4 ± 1.4	3.0 ± 1.1	3.0 ± 1.1
$\log C_8$	$-.64 \pm .44$	$-.39 \pm .41$	$-.06 \pm .32$	$.10 \pm .33$
ρ_8:	0.59	0.62	0.66	0.66
$P_{ss}=C_9 Re_*^{a_9}$:				
a_9:	1.6 ± 0.3	1.6 ± 0.3	1.3 ± 0.2	1.3 ± 0.2
$\log C_9$:	-9.33 ± 1.8	-8.6 ± 1.7	-6.9 ± 1.3	-7.0 ± 1.3
ρ_9:	0.87	0.87	0.89	0.89

(a)

a: 3.44+/-1.19
logC: -4.04+/-0.35
rho: 0.68

(b)

a: 3.25+/-1.03
logC: -3.80+/-0.31
rho: 0.71

(c)

a: 2.71+/-0.75
logC: -3.44+/-0.22
rho: 0.76

(d)

a: 2.73+/-0.78
logC: -3.41+/-0.23
rho: 0.75
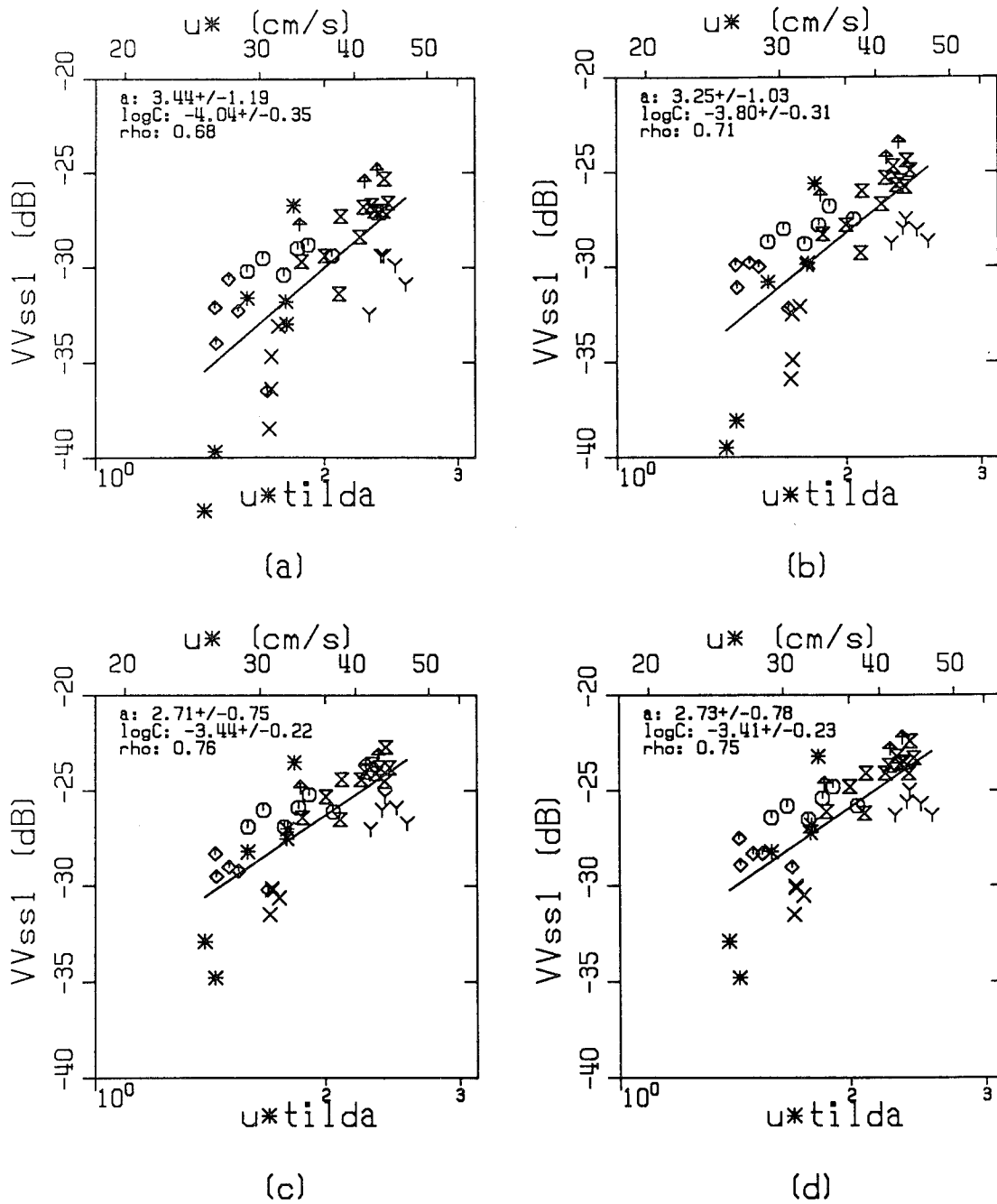
$\odot=1, \times=4, \diamond=5, \curlyvee=6, Y=9, *=11, \bowtie=12$

Figure 5.3: Sea spike contribution σ^0_{vvss1} (VV, method 1) versus friction velocity for the detection schemes (a) $\sigma^0_{vv} > \sigma^0_{pol} = -5.2$dB, (b) $\sigma^0_{vv} >= -6.0$dB, (c) B>50Hz, and (d) $\sigma^0_{vv} >= -6.0$dB and/or B>50Hz. Each symbol represents one–hour with different symbols for each run. The linear regression parameters for equation (5.4a) are in the upper left hand corner of each plot.
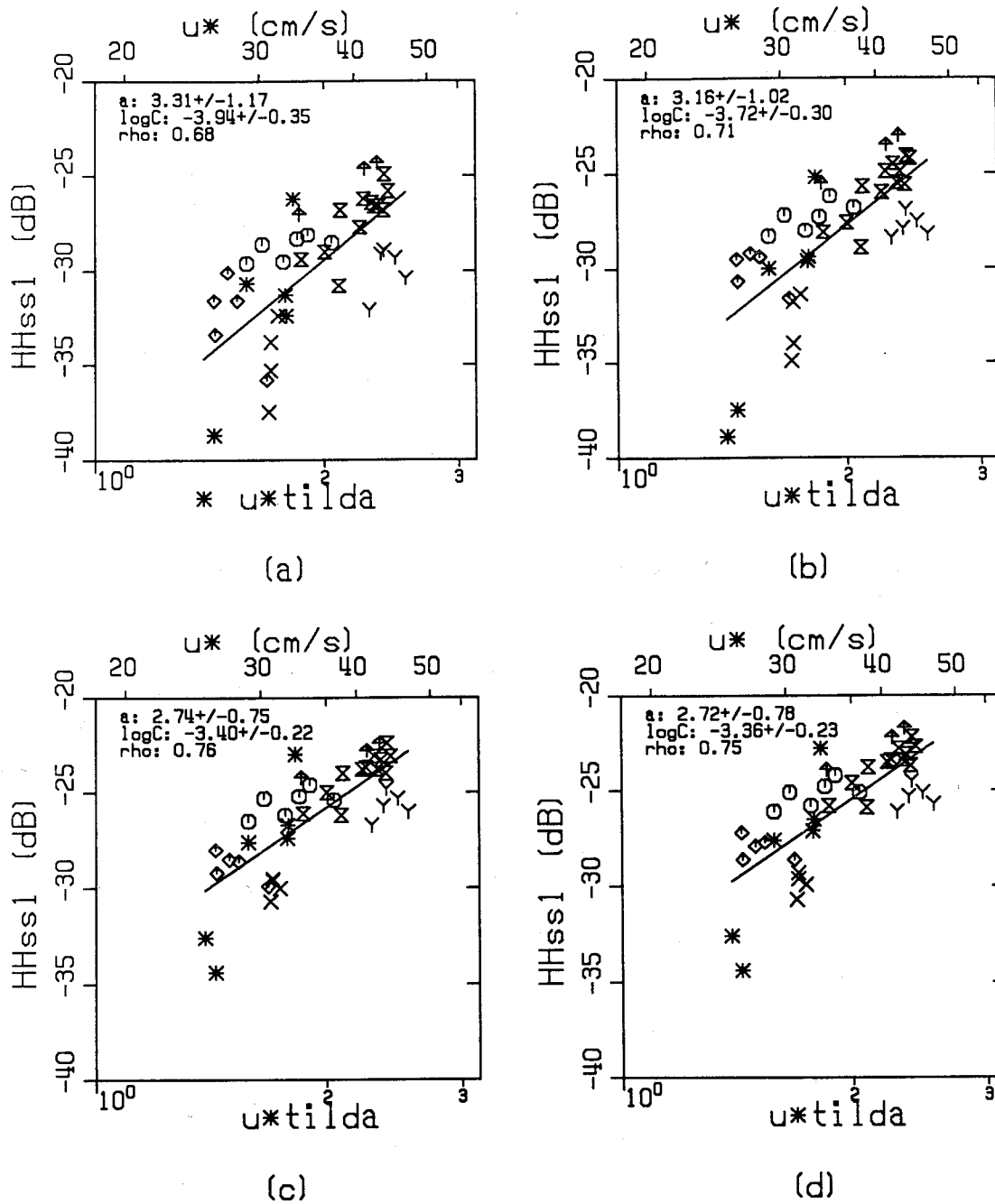
$\textcircled{}=1$, $\times=4$, $\diamondsuit=5$, $\text{\Lightning}=6$, $Y=9$, $\ast=11$, $\boxtimes=12$

Figure 5.4: Sea spike contribution σ^0_{hhss1} (HH, method 1) versus friction velocity for the detection schemes (a) $\sigma^0_{vv} > \sigma^0_{pol} = -5.2$dB, (b) $\sigma^0_{vv} >= -6.0$dB, (c) B>50Hz, and (d) $\sigma^0_{vv} >= -6.0$dB and/or B>50Hz. Each symbol represents one-hour with different symbols for each run. The linear regression parameters for equation (5.4b) are in the upper left hand corner of each plot.

$$\sigma^o_{SSVV1} = C_4 \, \tilde{u}_*^{a_4}, \qquad\qquad (5.4a)$$

and

$$\sigma^o_{SSHH1} = C_5 \, \tilde{u}_*^{a_5}, \qquad\qquad (5.4b)$$

the exponent a_4 is within the range $2.7 \leq a_4 \leq 3.4$ with correlation coefficient ρ_2 in the range $0.68 \leq \rho_4 \leq 0.76$ for VV polarization and the exponent a_5 is within the range $2.7 < a_5 < 3.3$ with correlation coefficient ρ_5 in the range $0.69 < \rho_5 < 0.77$ for HH polarizations (see Table 5.2). The corresponding results for method 2 are shown in Figures 5.5 and 5.6 for VV and HH polarizations, respectively. For the relations

$$\sigma^o_{SSVV2} = C_6 \, \tilde{u}_*^{a_6}, \qquad\qquad (5.5a)$$

and

$$\sigma^o_{SSHH2} = C_7 \, \tilde{u}_*^{a_7}, \qquad\qquad (5.5b)$$

the exponent a_6 is within the range $3.0 \leq a_6 \leq 3.6$ with correlation coefficient ρ_6 in the range $0.70 \leq \rho_6 \leq 0.78$ for VV polarization and the exponent a_7 is within the range $3.0 < a_7 < 3.5$ with correlation coefficient ρ_7 in the range $0.69 < \rho_7 < 0.78$ for HH polarizations (see Table 3.2). These results are consistent with the preliminary findings presented in Chapter 2 and with Phillips' (1988) prediction given by equation (1.14). The larger exponents and smaller correlation coefficients correspond to detections schemes 1 and 2, which detect a smaller percentage of breaking events causing sea spikes.
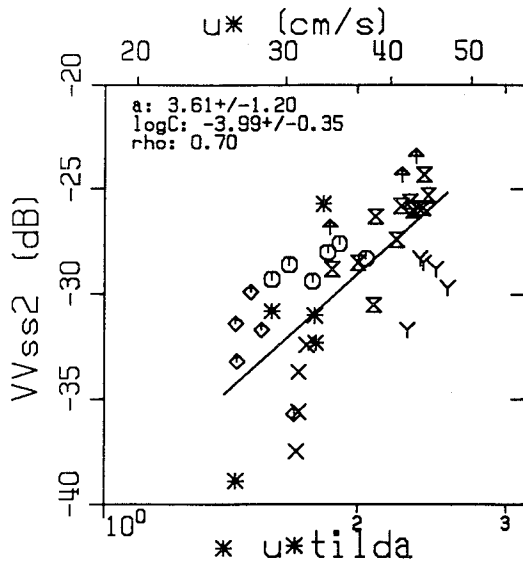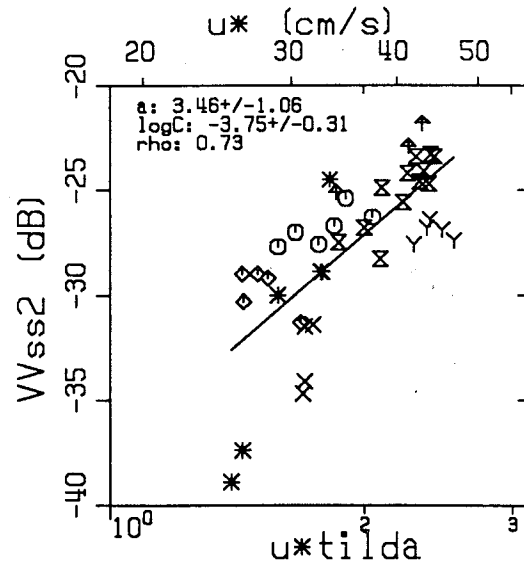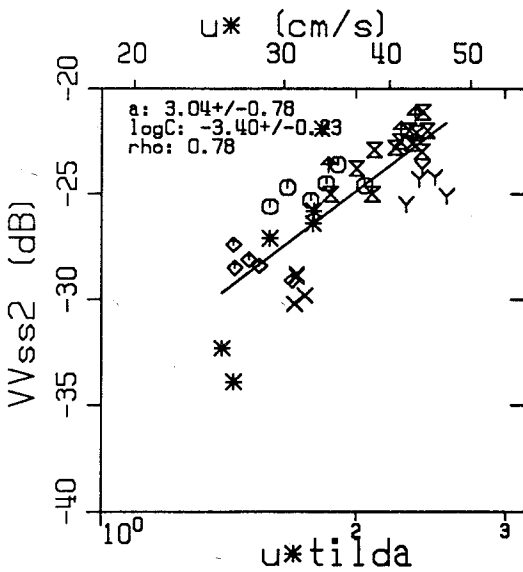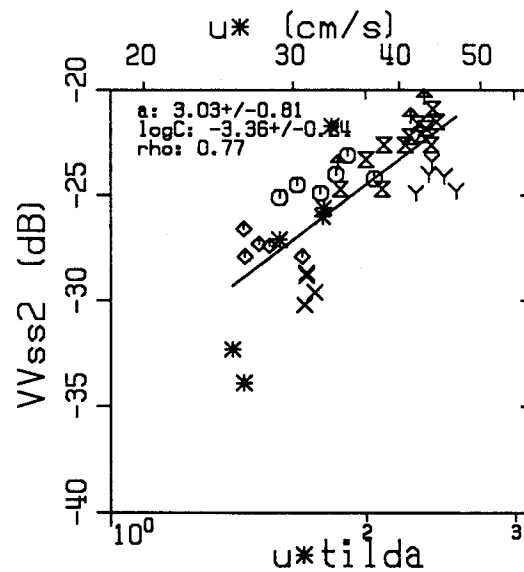
Figure 5.5: Sea spike contribution σ^0_{vvss2} (VV, method 2) versus friction velocity for the detection schemes (a) $\sigma^0_{vv} > \sigma^0_{pol} = -5.2$dB, (b) $\sigma^0_{vv} >= -6.0$dB, (c) B>50Hz, and (d) $\sigma^0_{vv} >= -6.0$dB and/or B>50Hz. Each symbol represents one–hour with different symbols for each run. The linear regression parameters for equation (5.5a) are in the upper left hand corner of each plot.

(a)

(b)

(c)

(d)
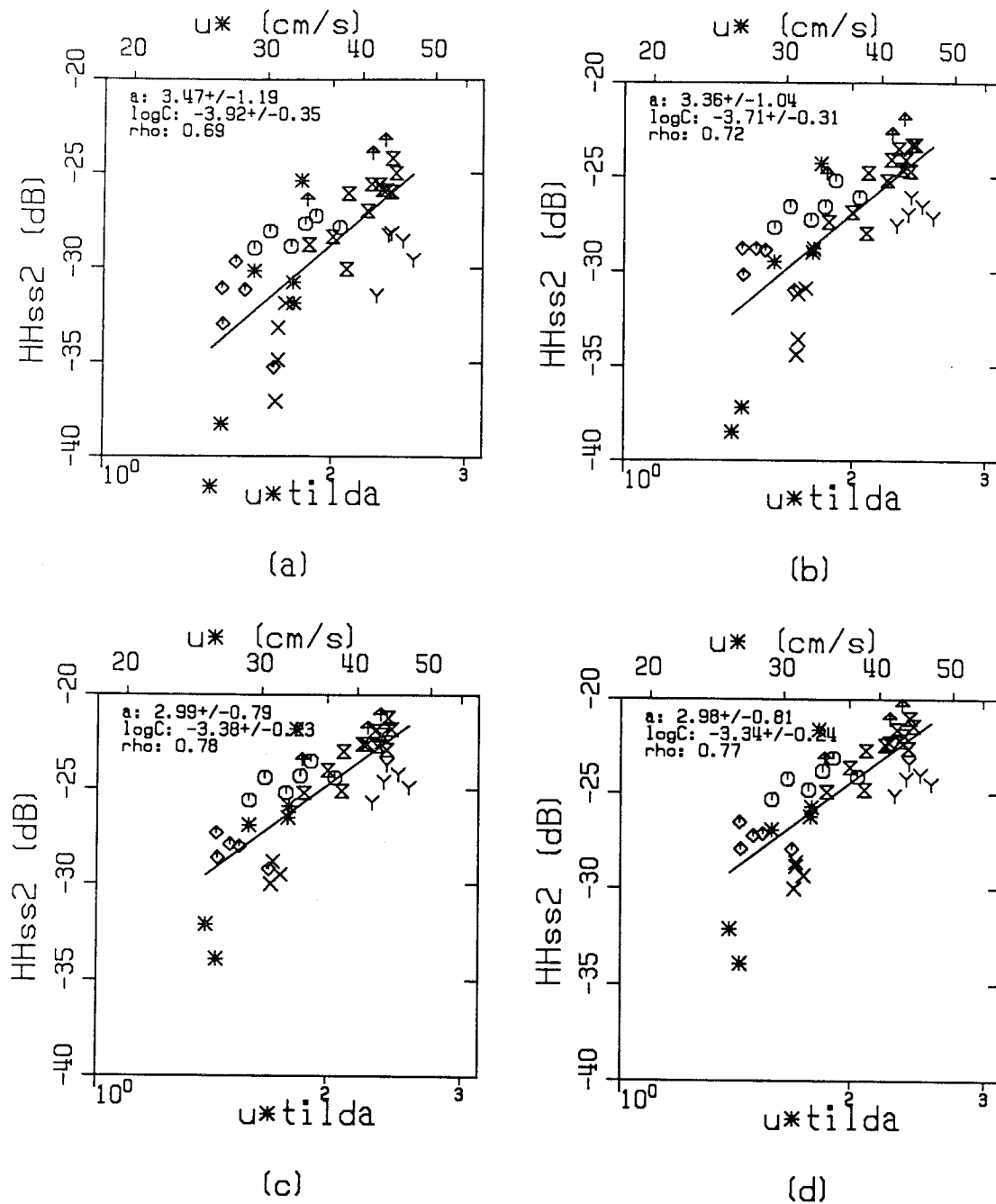
$\oplus=1$, $\times=4$, $\diamond=5$, $\uparrow=6$, $Y=9$, $*=11$, $\boxtimes=12$

Figure 5.6: Sea spike contribution σ^0_{hhss2} (HH, method 2) versus friction velocity for the detection schemes (a) $\sigma^0_{vv}>\sigma^0_{pol}=-5.2dB$, (b) $\sigma^0_{vv}>=-6.0dB$, (c) $B>50Hz$, and (d) $\sigma^0_{vv}>=-6.0dB$ and/or $B>50Hz$. Each symbol represents one–hour with different symbols for each run. The linear regression parameters for equation (5.5b) are in the upper left hand corner of each plot.

5.3 AVERAGE RADAR CROSS–SECTION OF AN INDIVIDUAL SEA SPIKE

As discussed in Chapter 2, the roughly cubic dependence on friction velocity of both σ^0_{ss}, the sea spike contribution to the mean radar cross–section, and N, the frequency of sea spike occurrence, implies that these two quantities may be linearly related. The slope of the lines fitted to log–log plots of N versus σ^0_{ss} in Chapter 2 (Figure 2.11) were consistent with this notion. This nearly linear relationship implied that the average radar cross–section of an individual sea spike, σ^0_{ss}/N, might be independent of friction velocity.

To further investigate this idea, the quantity σ^0_{ss}/N for the SAXON measurements is plotted directly as a function of friction velocity in Figures 5.7 through 5.10 for VV and HH polarizations using methods 1 and 2 described above. For the definitions of σ^0_{ss} and N used here, the scatter of approximately ±1dB in these plots indicates that the average contribution of an individual sea spike is not dependent on u_*.

5.4 FRACTIONAL CONTRIBUTION OF SEA SPIKES TO THE CROSS–SECTION

As discussed in Chapter 1, section 1.3, current models of microwave backscatter from the ocean surface generally do not include return from breaking events. Therefore, the relative importance of σ^0_{ss}, the sea spike contribution to the mean radar cross–section, is of interest. Figures 5.11 through 5.14 shows the friction velocity dependence of the fractional radar cross–section, σ^0_{ss}/σ^0, for VV and HH polarization using computation methods 1 and 2. These results are consistent with the preliminary measurements presented in Chapter 2 (Figure 2.8). In general, the relative importance of sea
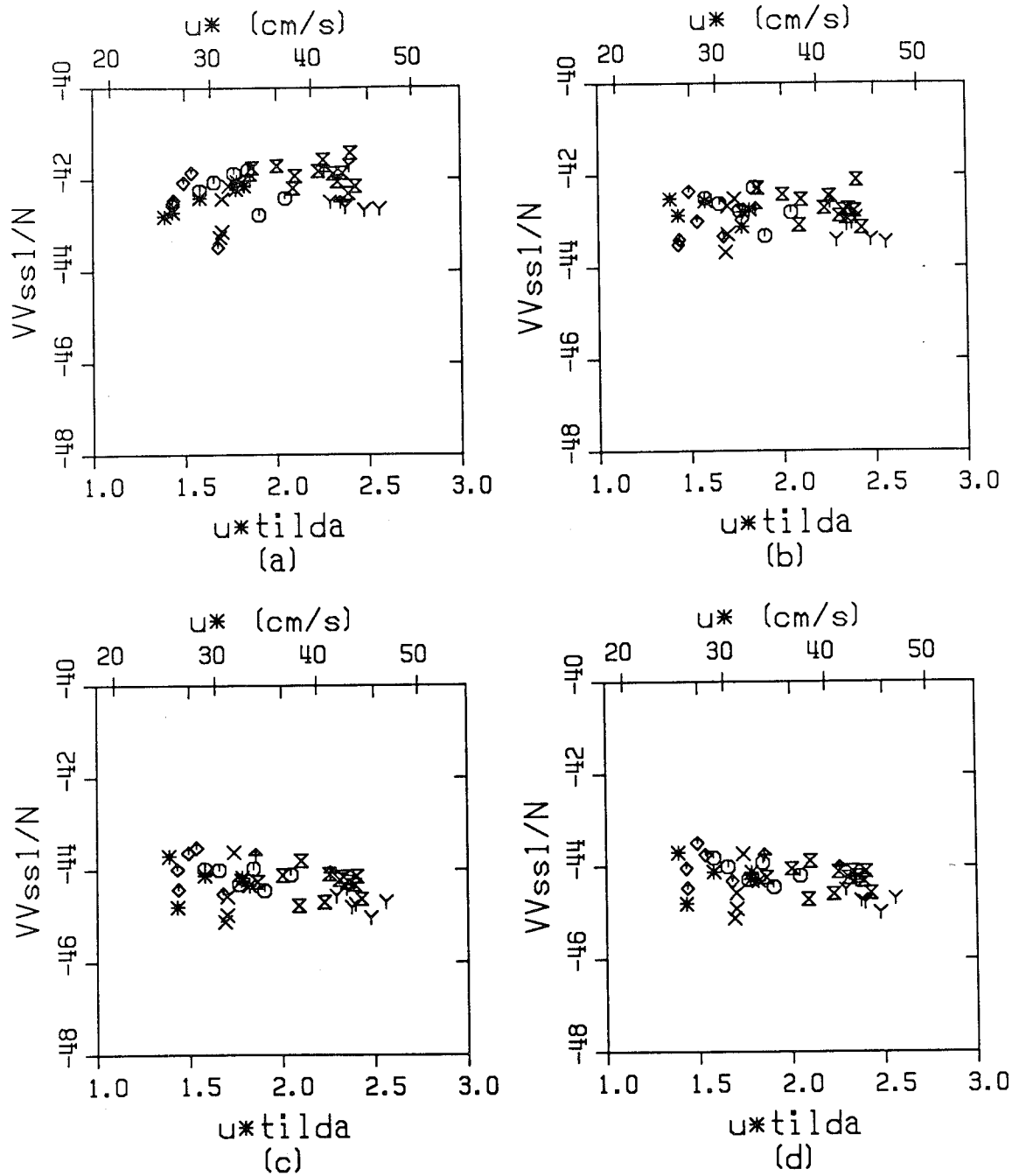
Figure 5.7: Average sea spike contribution $\sigma^0_{\mathrm{vvss1}}/N$ (VV, method 1) versus friction velocity for the detection schemes (a) $\sigma^0_{\mathrm{vv}} > \sigma^0_{\mathrm{pol}} = -5.2$dB, (b) $\sigma^0_{\mathrm{vv}} >= -6.0$dB, (c) B>50Hz, and (d) $\sigma^0_{\mathrm{vv}} >= -6.0$dB and/or B>50Hz. Each symbol represents one–hour with different symbols for each run.
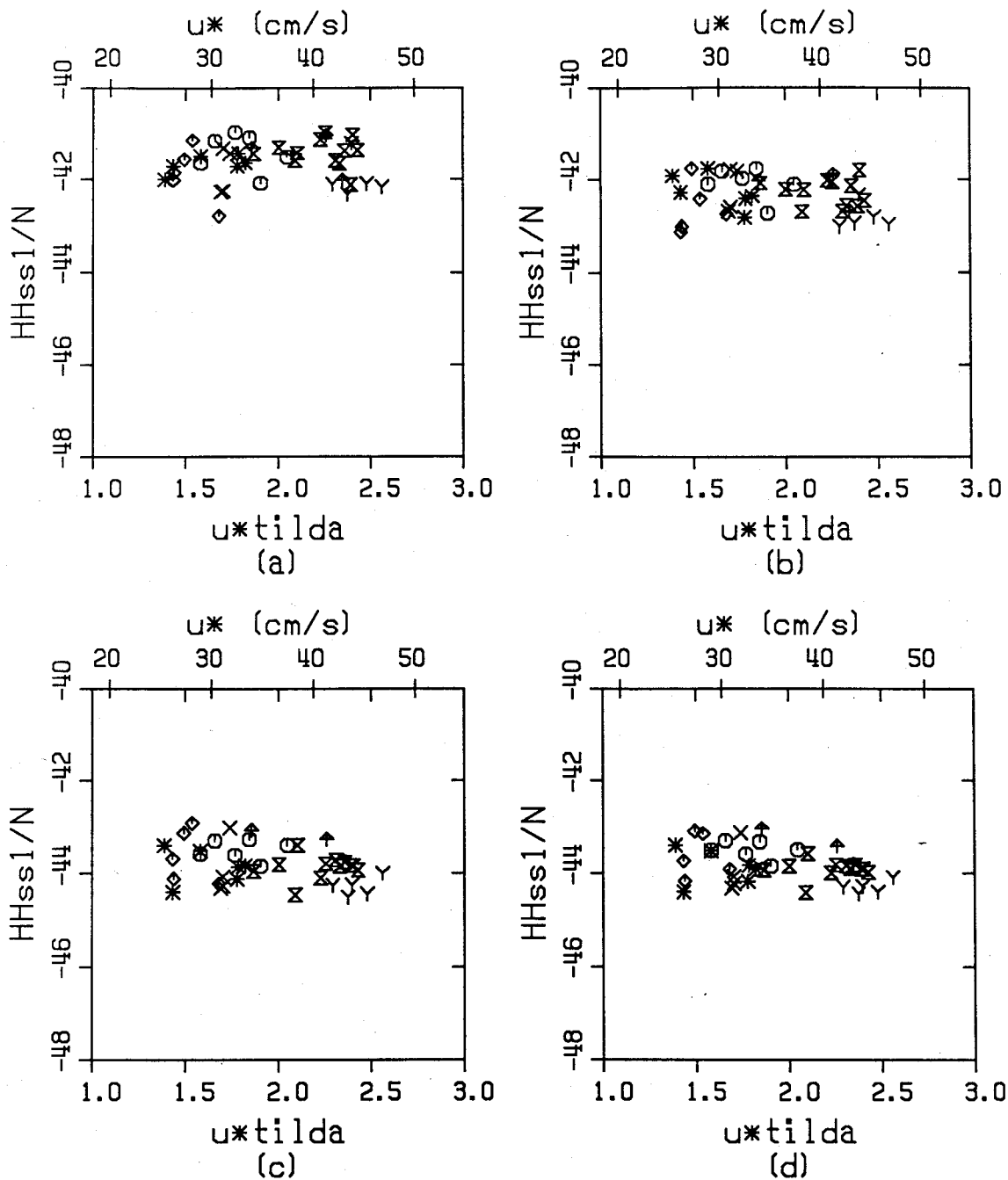
$\bigcirc=1$, $\times=4$, $\diamond=5$, $\Uparrow=6$, $Y=9$, $*=11$, $\boxtimes=12$

Figure 5.8: Average sea spike contribution σ^0_{hhss1}/N (HH, method 1) versus friction velocity for the detection schemes (a) $\sigma^0_{vv} > \sigma^0_{pol} = -5.2dB$, (b) $\sigma^0_{vv} >= -6.0dB$, (c) $B > 50Hz$, and (d) $\sigma^0_{vv} >= -6.0dB$ and/or $B > 50Hz$. Each symbol represents one–hour with different symbols for each run.
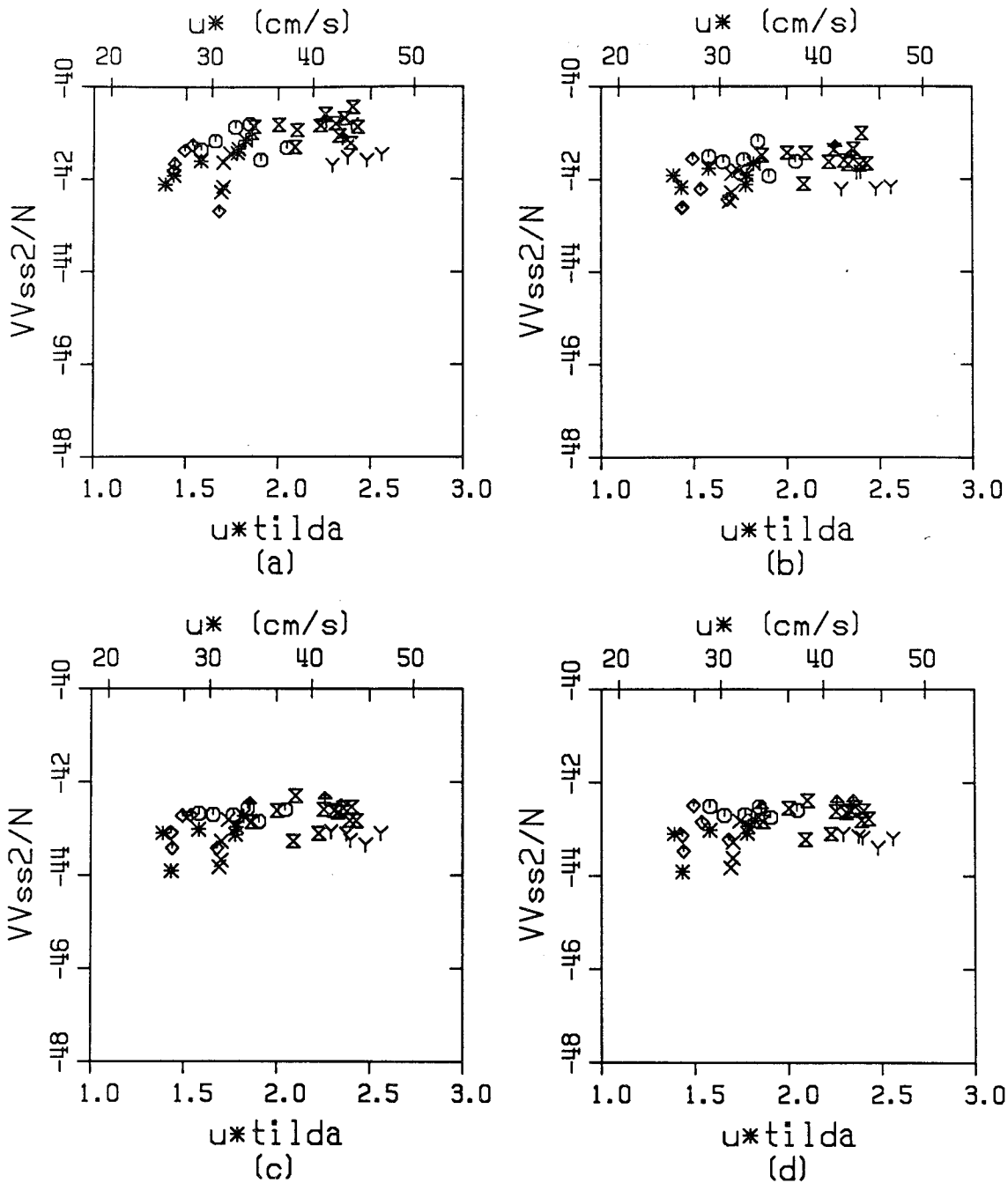
$\odot=1$, $\times=4$, $\diamond=5$, $\pitchfork=6$, $Y=9$, $\ast=11$, $\boxtimes=12$

Figure 5.9: Average sea spike contribution σ^0_{vvss2}/N (VV,method 2) versus friction velocity for the detection schemes (a) $\sigma^0_{vv} > \sigma^0_{pol} = -5.2$dB, (b) $\sigma^0_{vv} >= -6.0$dB, (c) B>50Hz, and (d) $\sigma^0_{vv} >= -6.0$dB and/or B>50Hz. Each symbol represents one–hour with different symbols for each run.
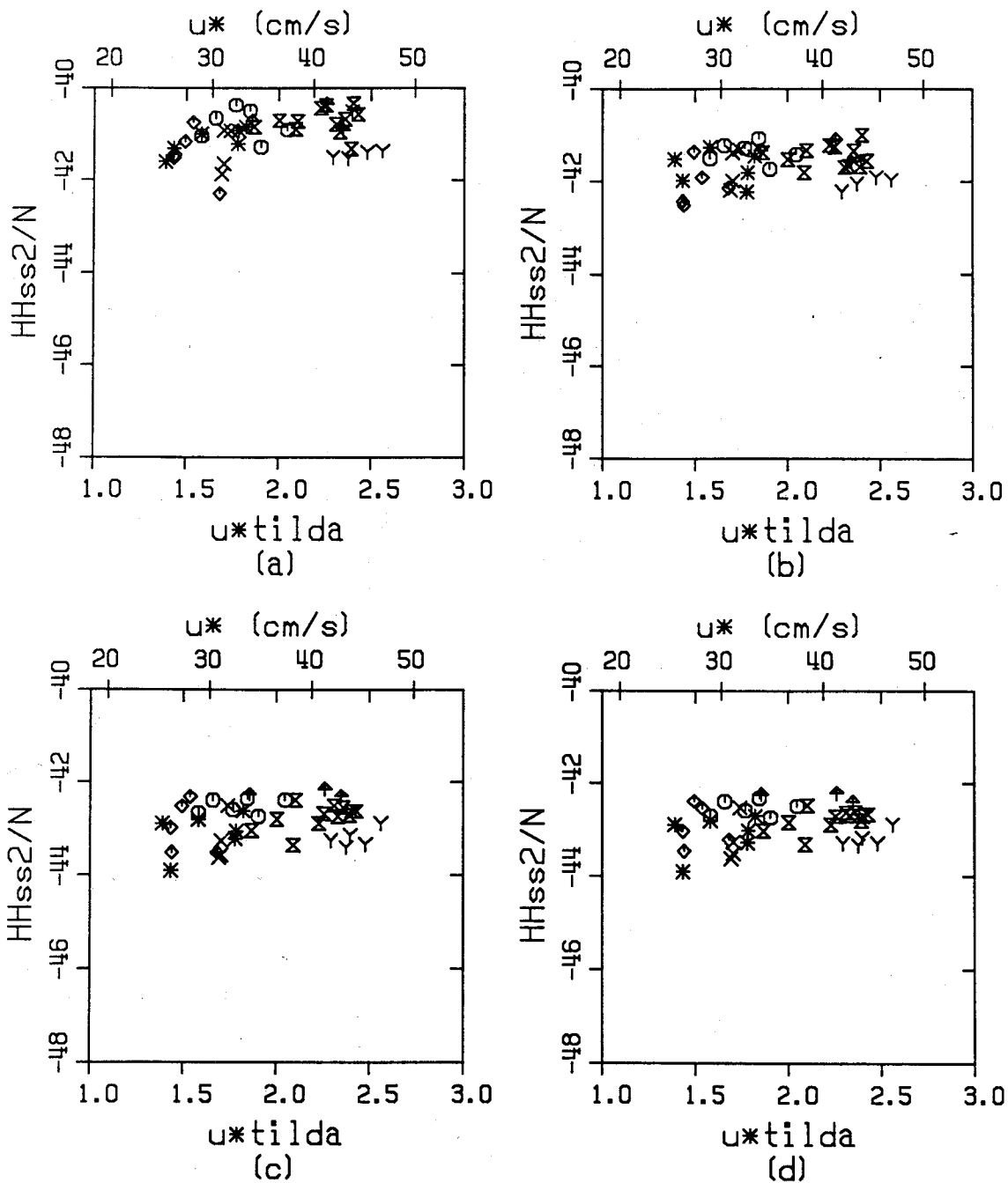
$\odot = 1$, $\times = 4$, $\diamondsuit = 5$, $\spadesuit = 6$, $Y = 9$, $* = 11$, $\boxtimes = 12$

Figure 5.10: Average sea spike contribution σ^o_{hhss2}/N (HH, method 2) versus friction velocity for the detection schemes (a) $\sigma^o_{vv} > \sigma^o_{pol} = -5.2$dB, (b) $\sigma^o_{vv} >= -6.0$dB, (c) B>50Hz, and (d) $\sigma^o_{vv} >= -6.0$dB and/or B>50Hz. Each symbol represents one-hour with different symbols for each run.
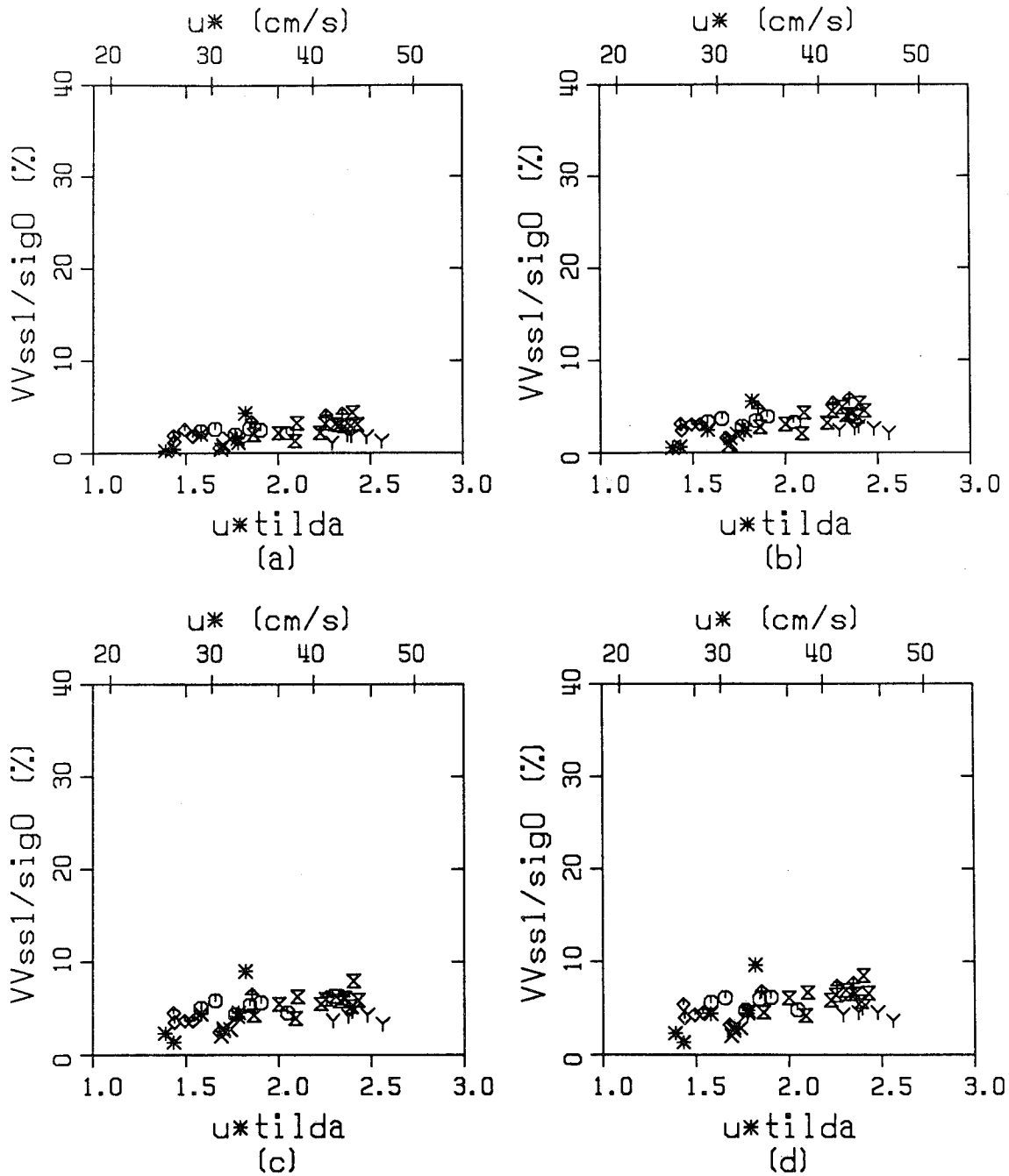
Figure 5.11: Fractional radar cross-section $\sigma^0_{vvss1}/\sigma^0_{vv}$ (VV, method 1) versus friction velocity for the detection schemes (a) $\sigma^0_{vv} > \sigma^0_{pol} = -5.2\text{dB}$, (b) $\sigma^0_{vv} >= -6.0\text{dB}$, (c) B>50Hz, and (d) $\sigma^0_{vv} >= -6.0\text{dB}$ and/or B>50Hz. Each symbol represents one-hour with different symbols for each run.
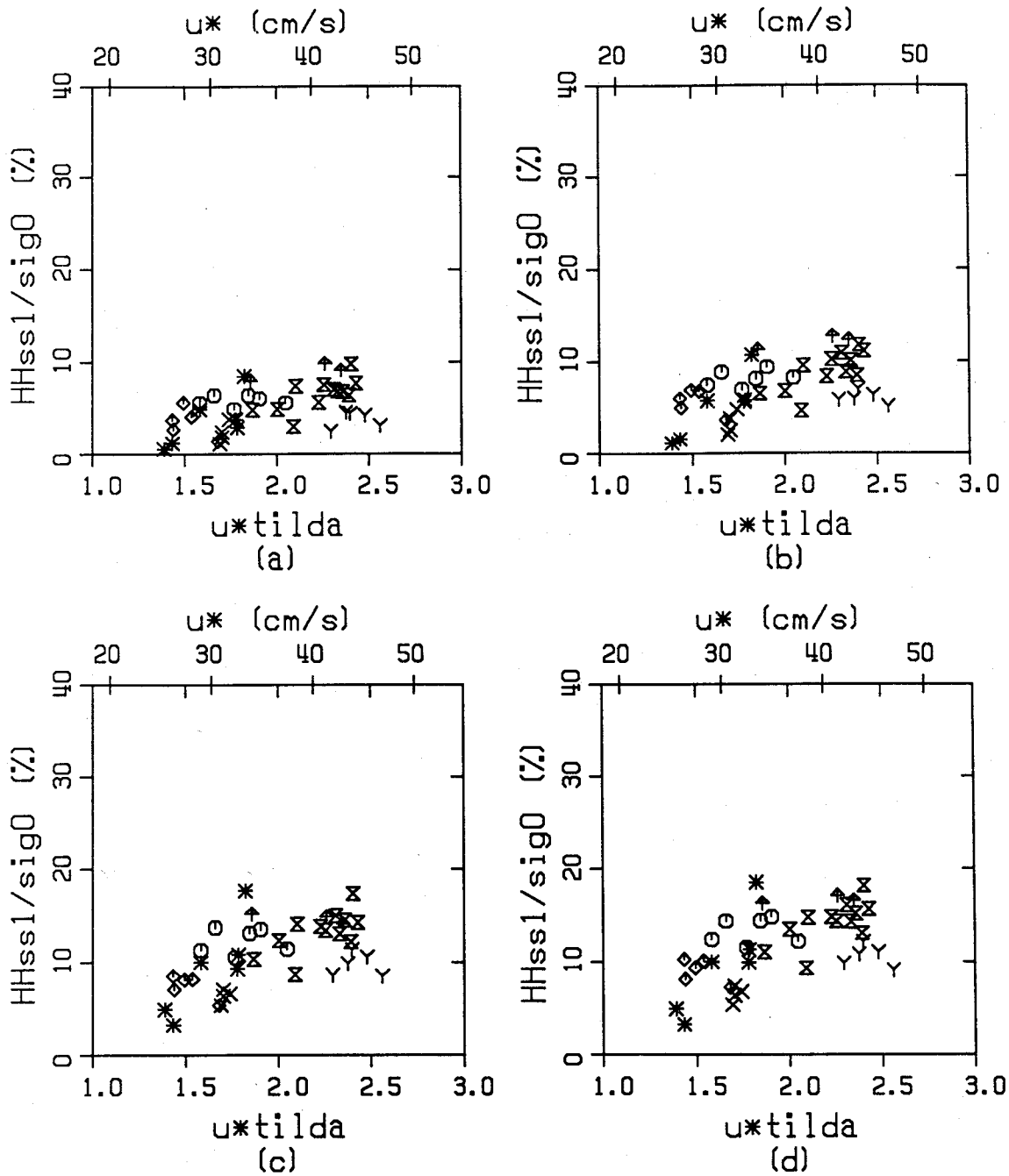
$$\odot=1, \times=4, \diamond=5, \text{↑}=6, Y=9, \ast=11, \boxtimes=12$$

Figure 5.12: Fractional radar cross–section $\sigma^0_{hhss1}/\sigma^0_{hh}$ (HH, method 1) versus friction velocity for the detection schemes (a) $\sigma^0_{vv}>\sigma^0_{pol}=-5.2\text{dB}$, (b) $\sigma^0_{vv}>=-6.0\text{dB}$, (c) B>50Hz, and (d) $\sigma^0_{vv}>=-6.0\text{dB}$ and/or B>50Hz. Each symbol represents one–hour with different symbols for each run.
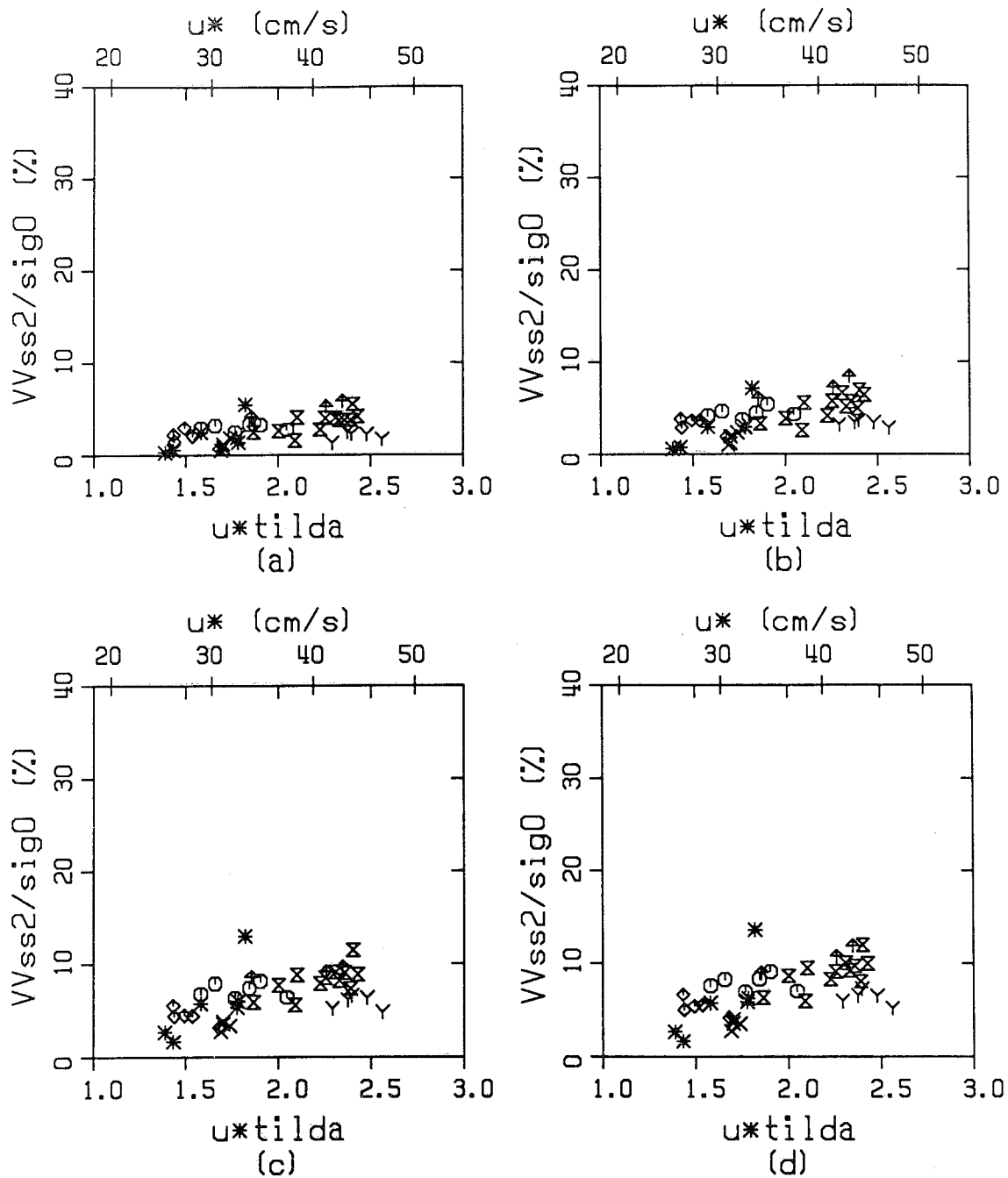
Figure 5.13: Fractional radar cross–section $\sigma^0_{vvss2}/\sigma^0_{vv}$ (VV, method 2) versus friction velocity for the detection schemes (a) $\sigma^0_{vv} > \sigma^0_{pol} = -5.2$dB, (b) $\sigma^0_{vv} >= -6.0$dB, (c) B>50Hz, and (d) $\sigma^0_{vv} >= -6.0$dB and/or B>50Hz. Each symbol represents one–hour with different symbols for each run.
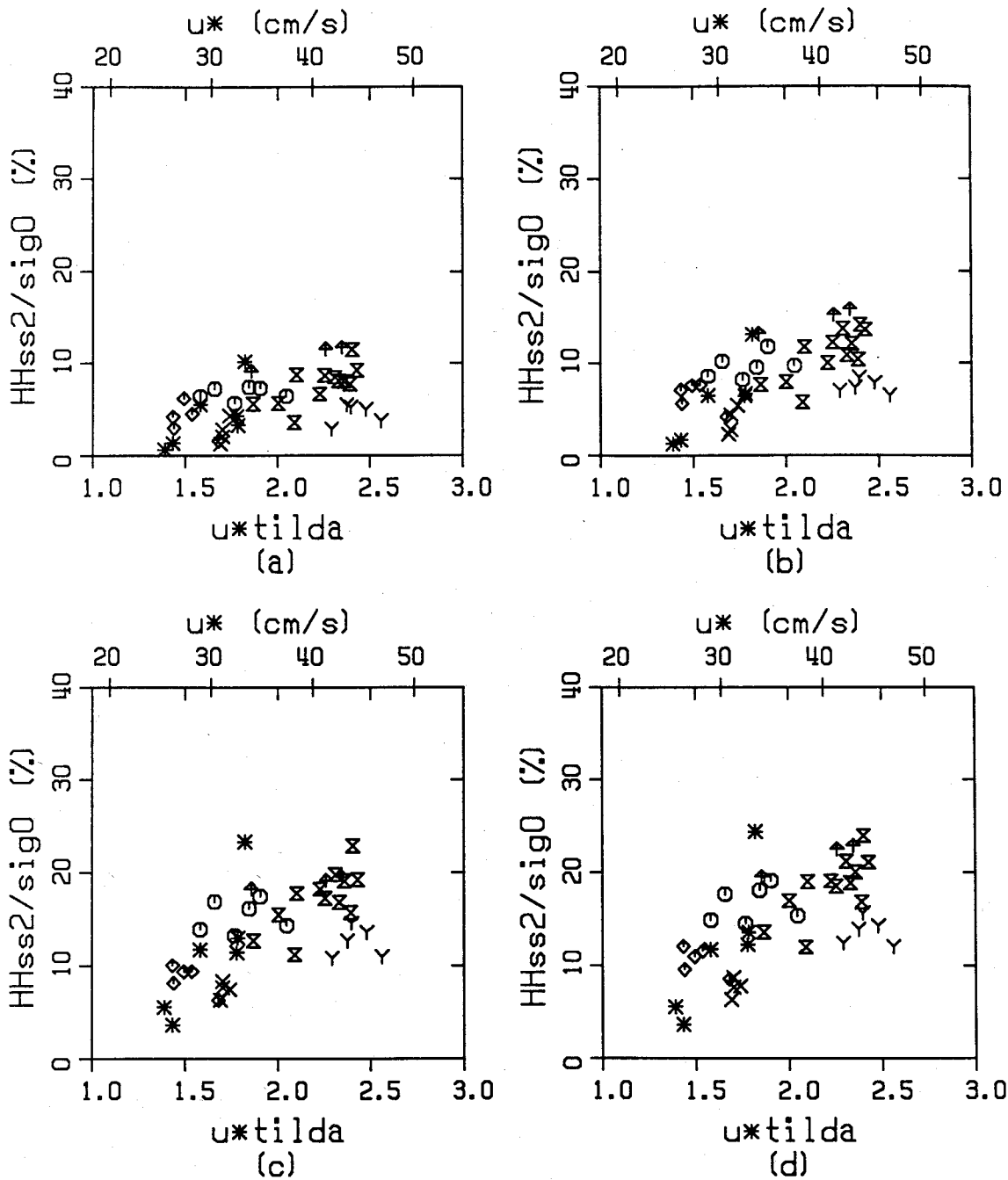
Figure 5.14: Fractional radar cross–section $\sigma^0_{hhss1}/\sigma^0_{hh}$ (HH, method 1) versus friction velocity for the detection schemes (a) $\sigma^0_{vv} > \sigma^0_{pol} = -5.2$dB, (b) $\sigma^0_{vv} >= -6.0$dB, (c) B>50Hz, and (d) $\sigma^0_{vv} >= -6.0$dB and/or B>50Hz. Each symbol represents one–hour with different symbols for each run.

spikes is greater for HH polarization than for VV. As discussed in Chapter 2, this result follows from the polarization characteristics of σ^0 and σ_{ss}^0. For HH polarization, the detected sea spikes contribute up to 20% of the received power, while for VV polarization that value is approximately 10%.

5.5 PERCENTAGE OF CRESTS PRODUCING SEA SPIKES

The fraction of breaking crests passing a fixed point has been used as a measure of the degree of wave breaking by a number of authors, as described in Chapter 1, section 1.1.2, and summarized in Figure 1.1. The total number of wave crests used in computing the fraction of breaking crests has been based on a number of definitions. Holthuijsen and Herbers (1986) defined individual waves from zero crossings in surface displacement measurements. Toba et al. (1971) used the average period of waves measured with a stop watch as the basis of defining the total number of wave crests passing the measurement site. The percentage of wave crests producing sea spikes, P_{ss}, may be compared to the fraction of breaking crests presented by previous investigators. The total number of wave crests used in computing this percentage is the number of waves in a given record with period equal f_{pk}^{-1}, where f_{pk} is the frequency of the peak of the surface displacement spectrum.

5.5.1 FRICTION VELOCITY DEPENDENCE OF P_{ss}

The percentage of wave crests producing sea spikes, P_{ss}, versus friction velocity is shown on log–log plots in Figures 5.15 for the four detection schemes used. For the expression
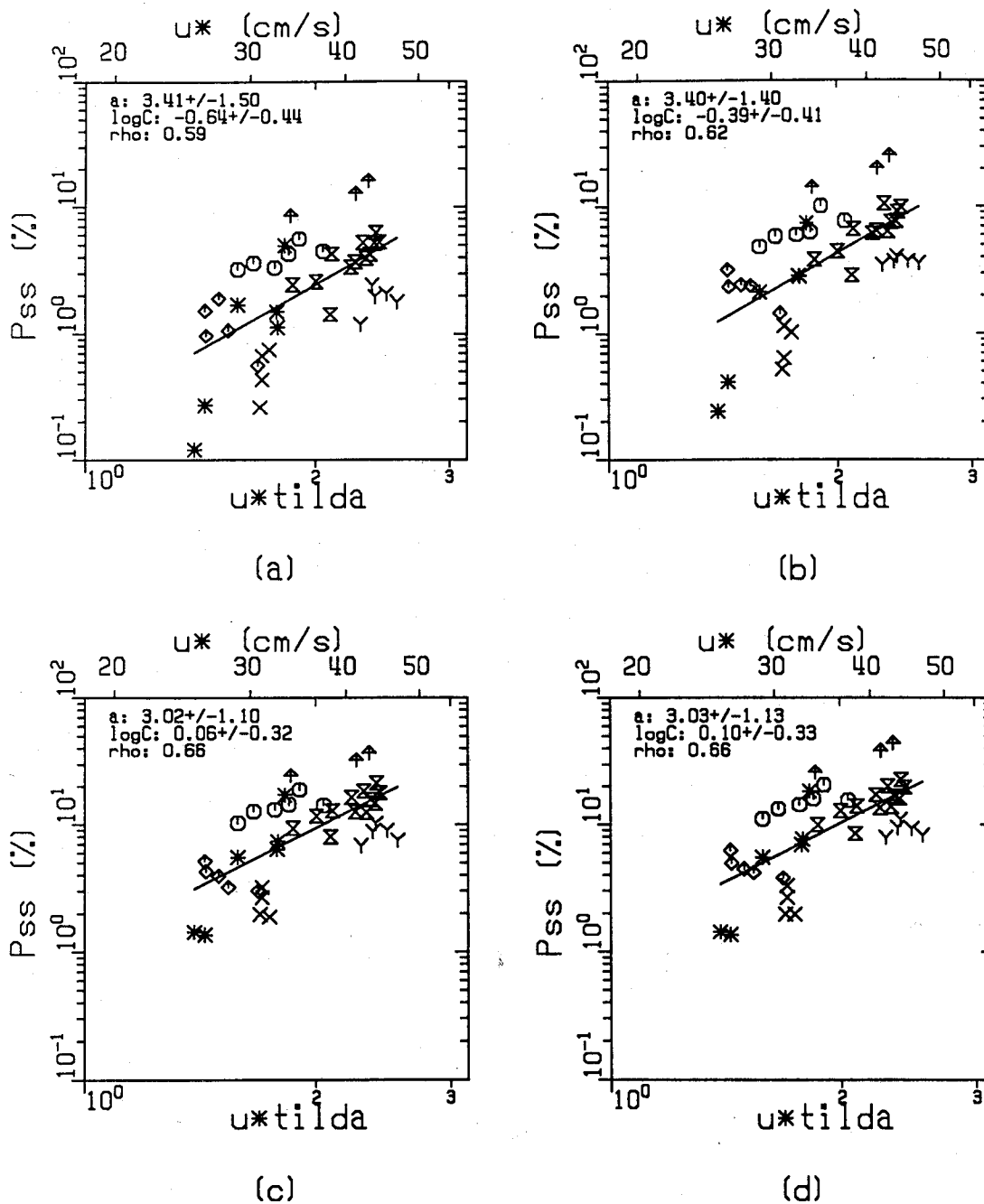
$\odot = 1$, $\times = 4$, $\diamondsuit = 5$, $\uparrow = 6$, $\curlyvee = 9$, $\divideontimes = 11$, $\boxtimes = 12$

Figure 5.15: Percentage of crest producing sea spikes, P_{ss} versus friction velocity for the detection schemes (a) $\sigma^0_{vv} > \sigma^0_{pol} = -5.2$dB, (b) $\sigma^0_{vv} >= -6.0$dB, (c) B>50Hz, and (d) $\sigma^0_{vv} >= -6.0$dB and/or B>50Hz. Each symbol represents one-hour with different symbols for each run. The linear regression parameters for equation (5.6) are in the upper left hand corner of each plot.

$$P_{ss} = C_8 \, \tilde{u}_*^{a_8}, \qquad\qquad (5.6)$$

the exponent a_8 is in the range $3.0 \leq a_8 \leq 3.4$ with correlation coefficient ρ_8 in the range $0.59 \leq \rho_8 \leq 0.66$ (see Table 5.2). The behavior of P_{ss} in Figures 5.15 is very similar to that of the frequency of sea spike occurrence, N, in Figure 5.2.

The percentage of wave crest producing sea spike may also be compared to the fraction of breaking crests reported by previous authors and summarized in Figure 1.1. The data of Holthuijsen and Herbers (1986) and Toba et al. (1971) from that figure have been replotted along with the results for the SAXON experiment in Figure 5.16. These data are presented as a function of U_{10}, wind speed referenced to 10m, and are plotted on linear axes. In general, the SAXON data compares well with the previous measurements in both magnitude and wind speed dependence. The three SAXON data points with the largest percentage values are for Run 6, which were the most extreme sea conditions encountered. Considering the difference in measurement techniques used, the overall agreement between the SAXON data and the previous measurements shown in Figure 5.16 is remarkable. This comparison is strong evidence to support the validity of counting sea spikes to measure the degree of wave breaking.

5.5.2 ROUGHNESS REYNOLDS NUMBER DEPENDENCE

Toba and Kunishi (1970) introduced a roughness Reynolds number Re_* to investigate the dependence of wave breaking on the combined effects of wind and wave conditions (see Chapter 1, section 1.2.1). The percentage of wave crests producing sea spikes, P_{ss}, is plotted versus $Re_* = u_* L / \nu$ in Figures
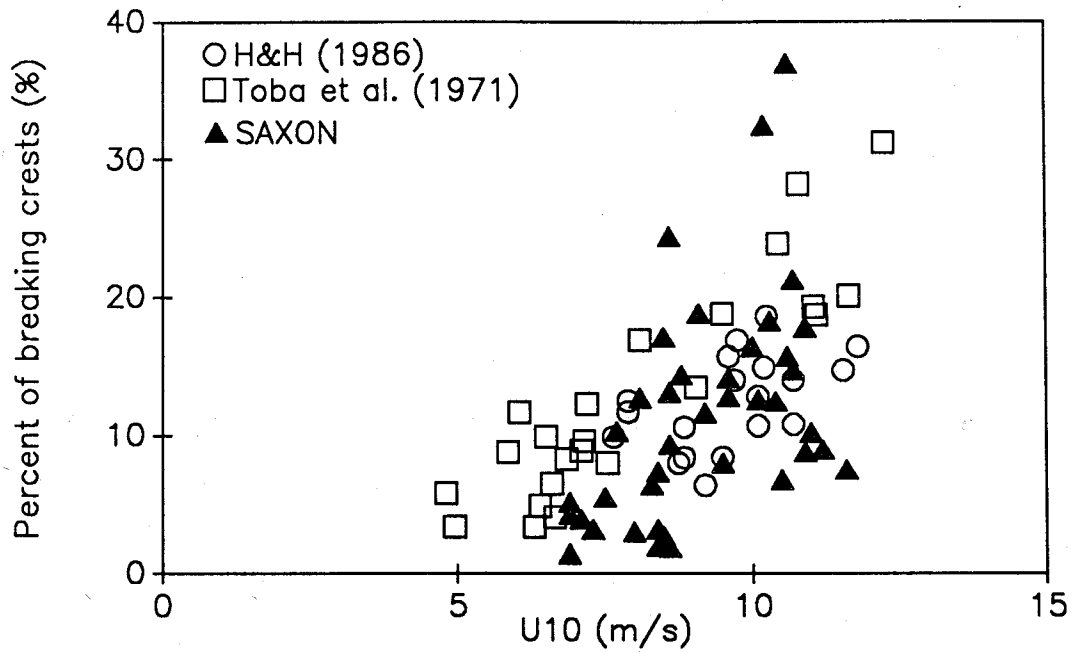
Figure 5.16: Comparison of results for SAXON with those of Holthuijsen and Herbers (1986) and Toba et al. (1971) (see Figure 1.1) as percentage of breaking crests versus U_{10}, wind speed referenced to 10m.

5.17. The characteristic wavelength L used in computing Re_* is that corresponding to the peak frequency of the surface displacement spectrum through the linear dispersion relation

$$\omega^2 = g \ k \ \tanh(kh), \tag{5.7}$$

where ω is the radian frequency $\omega=2\pi f$, k is the wavenumber $k=2\pi L$, h is the water depth, and g is the gravitational acceleration. In cases where the surface displacement spectrum was bimodal, the higher frequency peak was used to determine L. For the four detection schemes tested, the exponent a_9 in the expression

$$P_{ss} = C_9 \ Re_*^{a_9}, \tag{5.8}$$

is in the range $1.3 \leq a_9 \leq 1.6$ with a correlation coefficient ρ_9 in the range $0.87 \leq \rho_9 \leq 0.89$ (see Table 5.2).

The variation of the percentage of wave crests producing sea spikes, P_{ss}, as a function of the parameter Re_* in Figures 5.17 may be compared with the related results of previous authors shown in Figures 1.4 and 1.5. The fraction of breaking crests measured in a wind tunnel by Toba and Kunishi (1970) varied approximately as $Re_*^{1.4}$. Toba and Chaen (1973) reported a slope of 1.5 for a straight line fit on the log–log plot in Figure 1.5 of field measurements of the percentage of whitecap coverage versus Re_*.

As summarized in Table 5.2 and Figures 5.17, the exponent a_9 in equation (5.8) for the SAXON measurements is consistent with the results
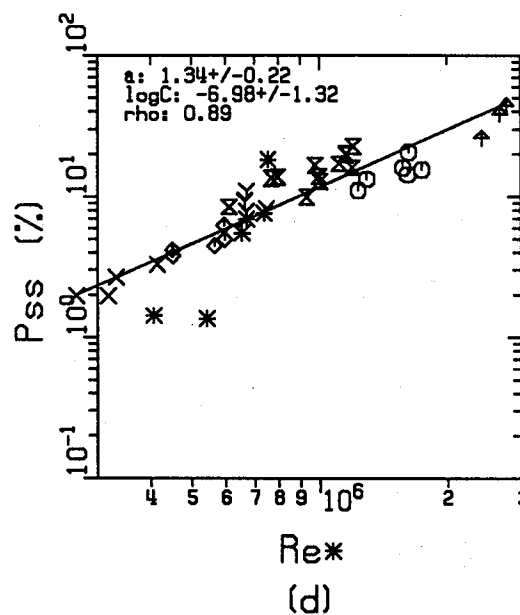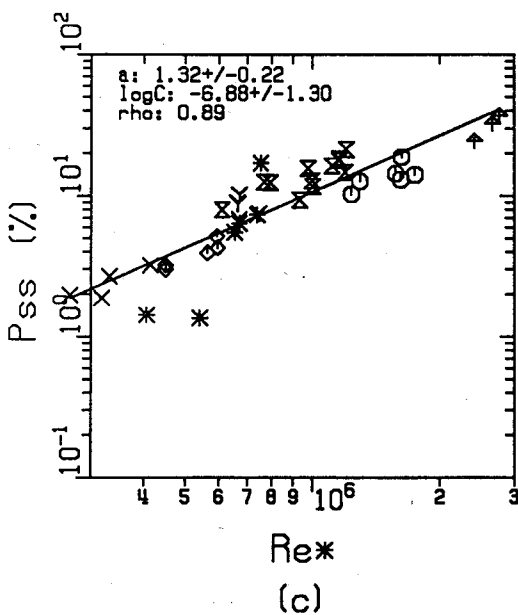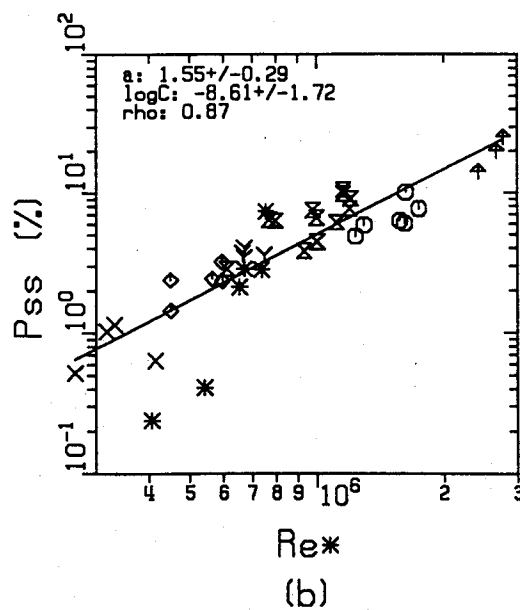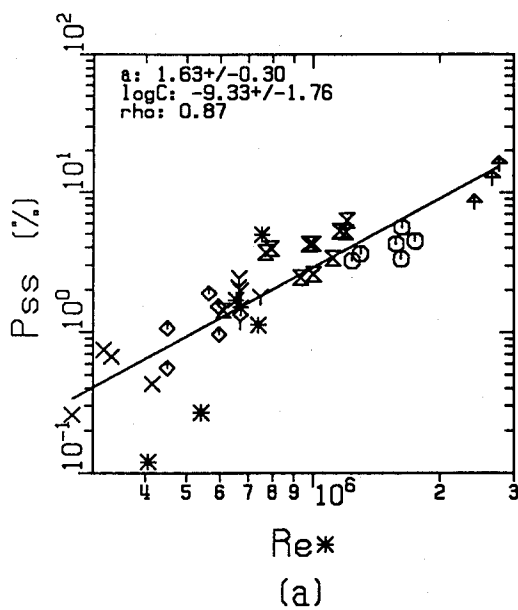
Figure 5.17: Percentage of crest producing sea spikes, P_{ss} versus the roughness Reynolds number Re* for the detection schemes (a) $\sigma^0{}_{vv} > \sigma^0{}_{pol} = -5.2$dB, (b) $\sigma^0{}_{vv} >= -6.0$dB, (c) B>50Hz, and (d) $\sigma^0{}_{vv} >= -6.0$dB and/or B>50Hz. Each symbol represents one–hour with different symbols for each run. The linear regression parameters for equation (5.8) are in the upper left hand corner of each plot.

reported by Toba and colleagues. Furthermore, the scatter of the data in Figures 5.16a–d is generally less than that of other sea spike quantities N versus u_* in Figure 5.2 as well as in P_{ss} versus u_* in Figure 5.15. This reduced scatter is also reflected in the confidence intervals and relatively large correlation coefficients for the exponent a_9 in equation (5.8).

As mentioned in chapter 1, a Re*–exponent of 1.5 is consistent with a cubic friction velocity dependence if $Re^*=u_*L/\nu$ is based on a wavelength L which is proportional to u_*. Thus, a formulation in terms of Re* effectively relaxes the constraint of a linear dependence of L on u_*. The improved correlation of P_{ss} versus Re* over that of P_{ss} versus u_* may be a reflection of this effect.

5.5.3 COMPARISON WITH SROKOSZ'S (1986) MODEL

Statistical models for the probability of wave breaking as a function of the dimensionless fourth moment of the surface displacement spectrum, m_4/g^2, given by equation (1.18) were reviewed in Chapter 1, section 1.2.2. In that treatment, the necessity of specifying an upper cutoff frequency, f_c, in computing m_4 was discussed. The percentage of crests producing sea spikes, P_{ss}, versus the dimensionless fourth moment, m_4/g^2, is plotted for two different cutoff frequencies in Figures 5.18 and 5.19. The solid curves in these figures correspond to equation (1.19), which is Srokosz's (1986) expression for the probability B that a breaking crest will occur at a given point on the sea surface. The curves correspond to values of the acceleration or steepness threshold parameter α of equation (1.19) in the range $0.20<\alpha<0.40$.

The surface displacement spectra computed from the time series of the
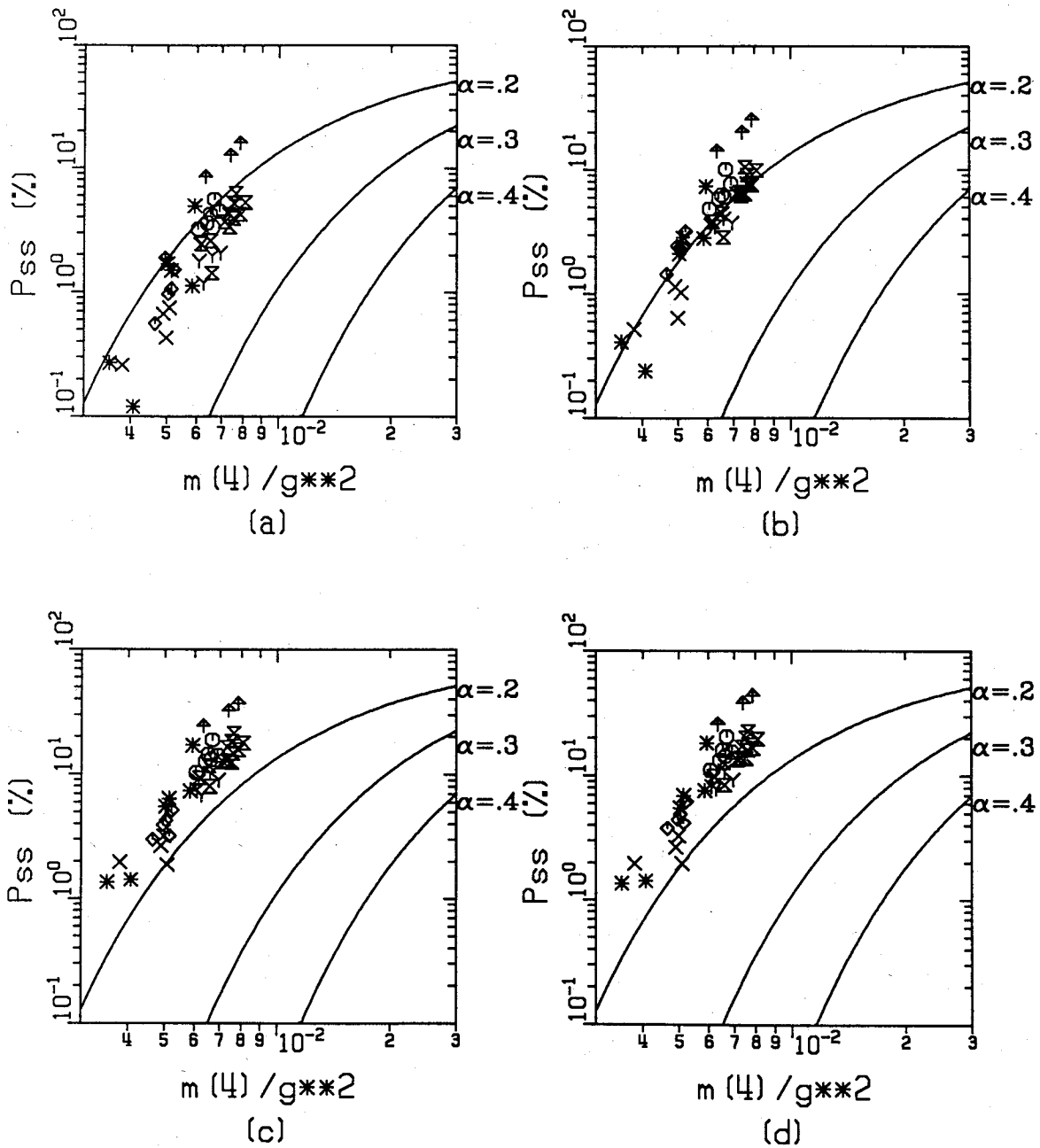
Figure 5.18: Percentage of crest producing sea spikes, P_{ss} versus m_4/g^2, the dimensionless fourth moment of the surface displacement spectrum (equation 1.19) for the detection schemes (a) $\sigma^0_{vv} > \sigma^0_{pol} = -5.2$dB, (b) $\sigma^0_{vv} >= -6.0$dB, (c) B>50Hz, and (d) $\sigma^0_{vv} >= -6.0$dB and/or B>50Hz. Curves correspond to Srokosz's model, equation (1.20), for $0.2 \leq \alpha \leq 0.4$. The cutoff frequency for the computation of m_4 is $f_c = 0.5$Hz.

$\odot=1$, $\times=4$, $\diamondsuit=5$, $\spadesuit=6$, $Y=9$, $*=11$, $\boxtimes=12$
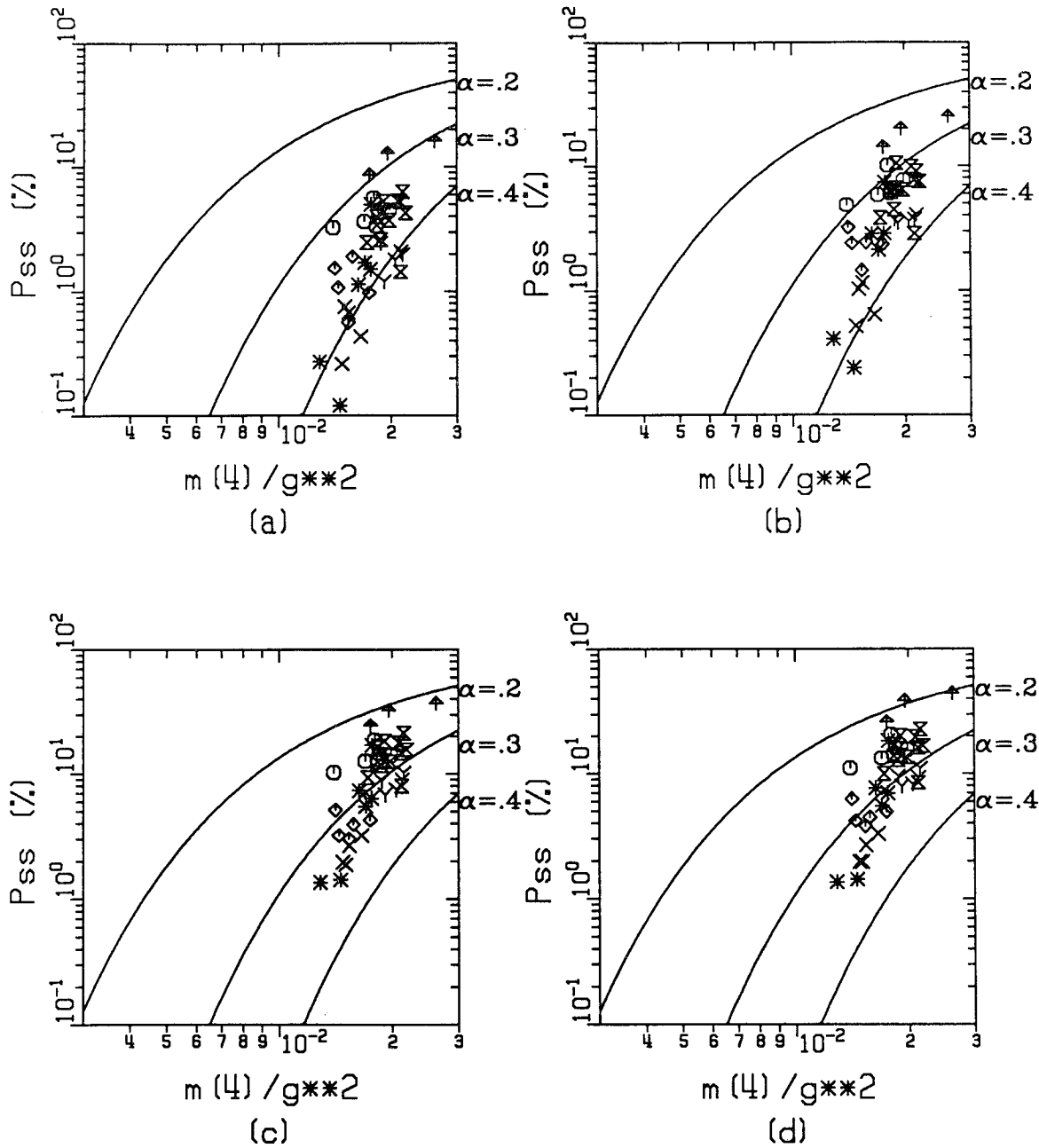
Figure 5.19: Same as Figure 5.18 except m_4 is computed using surface displacement spectra which have been extended by an f^{-4} power law with a cutoff frequency of $f_c=2.5\text{Hz}$ (see Figures 3.23b–3.28b).

mean Doppler frequency (equation 3.5) are valid up to a frequency of approximately 0.6Hz (see Chapter 3, section 3.1.2). Therefore, the value of m_4/g^2 in Figures 5.18 were computed with a cutoff frequency of $f_c=0.6$Hz. The values of m_4/g^2 in Figures 5.19 were computed with a cutoff frequency of $f_c=2.5$Hz by extending the measured spectra beyond 0.5Hz with an f^{-4} power law. This procedure is similar to that used by Kennedy et al. (1983) to address the importance of higher frequency components of the surface displacement spectrum (see Chapter 3, sections 3.1.2 and 3.2.3).

Over the range of values available, the data in Figures 5.18 corresponding to a cutoff frequency of $f_c=0.5$Hz show a functional dependence of P_{ss} on m_4/g^2 which is similar to that of the Srokosz model curves. On the other hand, a number of other curves (such as a straight line) could be reasonably fitted to the data. Also, the data in Figures 5.18 fall nearest to the curves corresponding to value of α on the order of 0.20, which is roughly one–half that of reported by previous investigators (see Chapter 1, section 1.2.2).

Increased emphasis is place on the higher frequency components of the surface displacement spectrum by computing m_4/g^2 with a cutoff frequency of $f_c=2.5$Hz. The scatter in the data of Figure 5.19 with $f_c=2.5$Hz increases somewhat over that of Figure 5.18. Although these data do fall nearer to the curves corresponding to the higher values of α, the data are not well represented by the model.

As discussed in Chapter 1, section 1.2.2, comparison between the various statistical models for the probability of wave breaking and measurements will tend to be ambiguous. This ambiguity is due to the combination of the

practical requirement of a cutoff frequency to compute m_4 and uncertainty in the appropriate value of the threshold parameter α. The comparisons shown in Figures 5.18 and 5.19 mainly serve to reinforce the drawbacks of this class of model.

5.6 KINEMATIC CONSIDERATIONS

5.6.1 NORMALIZED DOPPLER VELOCITY

The mean Doppler frequency measured by the scatterometer is proportional to the power–weighted line–of–sight velocity of the scatterers within the illumination area. When the illumination area is small compared to the wavelength of the dominant surface wave, the Doppler frequency provides a measure of the sea surface velocity. For non–breaking waves, the measured velocity is dominated by the orbital velocity of the long surface waves. A simple but useful model of a breaking wave asserts that the surface fluid particle velocity at the crest is on the order its phase speed. Therefore, the phase speed of the dominant surface wave may be an appropriate parameter for scaling the Doppler velocity measurements of breaking waves.

As shown in Chapter 4, large maxima in the mean Doppler frequency tend to occur with large sea spikes in the radar cross–section attributed to active breaking events. The average of the maximum Doppler velocity corresponding to detected sea spikes, $\overline{U}_{max}$, is given by

$$\overline{U}_{max} = \frac{1}{N}\sum_{i=1}^{N} U_{max}, \qquad (5.9)$$

where U_{max} is the line–of–sight velocity corresponding to the maximum Doppler frequency associated with a sea spike. The scaling of this average velocity associated with the detected breaking events may be relevant to the kinematics of the breaking process. For example, if it is dominated by the large velocities within the whitecap region, then it may be useful as a measure of the scale of the breaking. For purposes of scaling, the average maximum Doppler velocity $\overline{U}_{max}$ has been resolved to be horizontal. This procedure is motivated by the assumption that the actual surface velocity near the crest of a breaking wave is nearly horizontal. Furthermore, since the crest velocity of a breaking wave is expected to be on the order of its phase speed, the average velocity $\overline{U}_{max}$ is normalized by C_{pk}, the phase speed corresponding to the peak of surface displacement spectrum. In cases where the surface displacement spectrum is bimodal, the higher frequency peak has been used to determine C_{pk}.

The results of this scaling analysis are given in Figure 5.20, showing the friction velocity dependence of $\overline{U}_{max}/C_{pk}$. Although the data show a moderate amount of scatter, the values are generally clustered near $\overline{U}_{max}/C_{pk} = 0.25$. Considering the argument that the crest velocity of a breaking wave is on the order of its phase speed, one might expect a value of $\overline{U}_{max}/C_{pk}$ closer to unity. However, the average $\overline{U}_{max}$ should not be interpreted as the average velocity of the breaking crests. On the contrary, $\overline{U}_{max}$ is the average of the maximum mean Doppler frequency, or more precisely, the average of the maximum first moment of the Doppler spectrum. The Doppler spectrum reflects the power–weighted distribution of scatterer velocities within the
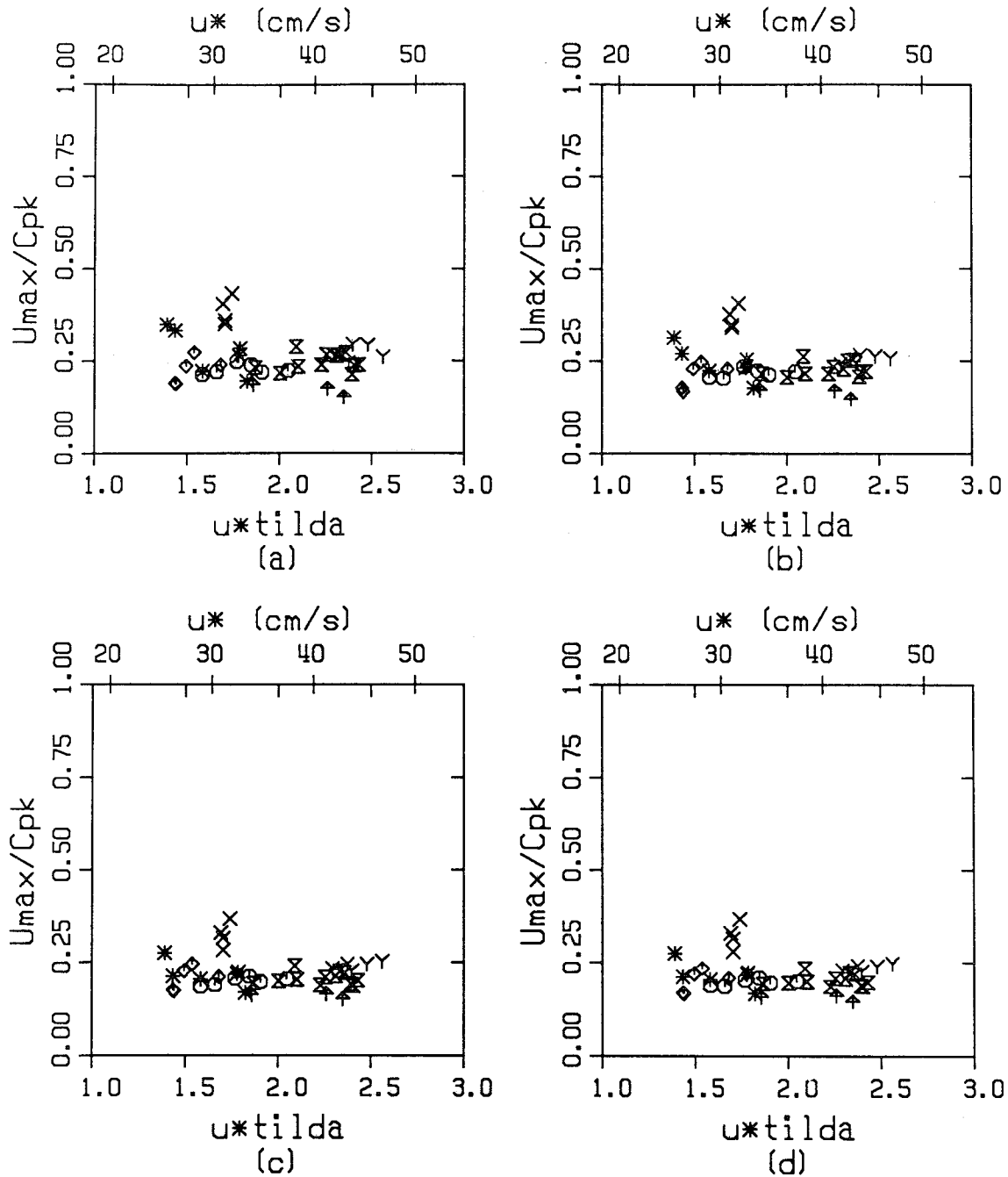
⊙=1, X=4, ◇=5, ⬆=6, Y=9, ✳=11, ⌧=12

Figure 5.20: Average maximum Doppler velocity (resolved to horizontal, see equation 5.9) associated with detected sea spikes normalized by the phase speed corresponding to the peak of the surface displacement spectrum for the detection schemes (a) $\sigma^0_{vv} > \sigma^0_{pol} = -5.2$dB, (b) $\sigma^0_{vv} >= -6.0$dB, (c) B>50Hz, and (d) $\sigma^0_{vv} >= -6.0$dB and/or B>50Hz.

illumination area. As discussed in Chapter 4, the influence of the active whitecap velocity on the Doppler spectrum depends on the location of the breaking crest with respect to the illumination area. Other factors affecting the relationship between the first moment of the Doppler spectrum and the actual whitecap velocity include crest orientation and the target strength of the breaking region relative to other sources of scattering. Thus the average of the maximum Doppler velocity should not necessarily be expected to reflect the whitecap velocity measured by the scatterometer.

The example of Doppler spectra for times of maximum bandwidth discussed in Chapter 4 (Figures 4.15 through 4.17) showed evidence of large velocities associated with the crest region of breaking waves. However, the mean Doppler frequency of those spectra is generally less than the maximum frequency (due to their large bandwidth). The Doppler spectrum in Figure 5.21 is an especially dramatic illustration of the point that the whitecap velocity measured by the scatterometer may not be reflected in the mean Doppler frequency. This spectrum includes the Doppler signature of a fast moving splash due to the crest of a breaking wave thrown forward and down into its forward face. The line–of–sight velocity corresponding to the frequency of the small peak on the right is roughly $4ms^{-1}$. This measured velocity would correspond to a horizontal velocity of $5.7 ms^{-1}$, which is on the order of the phase speed of roughly $8ms^{-1}$ corresponding to the peak of the wave height spectrum (see Figure 3.29a, Run12, file id SAX01710). However, the relative target strength of the splash is so low that its large velocity has negligible effect on the mean Doppler frequency, which is less than 100 Hz in this case.
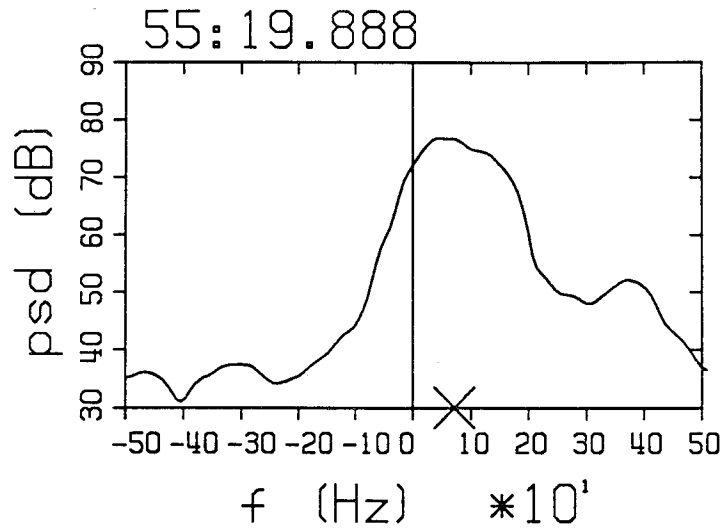
Figure 5.21: Doppler spectrum showing the signature of a fast moving splash caused by a breaking wave. The peak frequency in excess of 400Hz corresponds to a line–of–sight velocity of roughly 4ms^{-1}. The splash has negligble impact on the mean Doppler frequency, which is less than 100Hz.

5.6.2 NORMALIZED DOPPLER BANDWIDTH

The bandwidth of the Doppler spectrum is an indicator of the range of scatterer velocities within the illumination area. In chapter 4, section 4.4, large jumps in the bandwidth were found to be associated with the crest region of waves that break. In order to investigate the scaling of the bandwidth maxima associated with breaking events, a normalized bandwidth B_n has been computed. For each detected event, the bandwidth maximum was normalized by f_{max}, the maximum mean Doppler frequency associated with the event:

$$B_n = \frac{B_{max}}{f_{max}}. \tag{5.10}$$

For each one–hour record, the average normalized bandwidth $\overline{B}_n$ is then given by

$$\overline{B}_n = \frac{1}{N} \sum_{i=1}^{N} \left[\frac{B_{max}}{f_{max}} \right]_i , \tag{5.11}$$

where N is the total number of detected events. The variation of $\overline{B}_n$ with friction velocity, u_*, is shown in Figure 5.22. Except for one or two outlying points, the values of $\overline{B}_n$ indicate that, on average, the maximum bandwidth associated with the detected events is roughly 50–75% of the maximum Doppler frequency. The average (dimensional) maximum bandwidth was in the range of 60 to 70Hz.
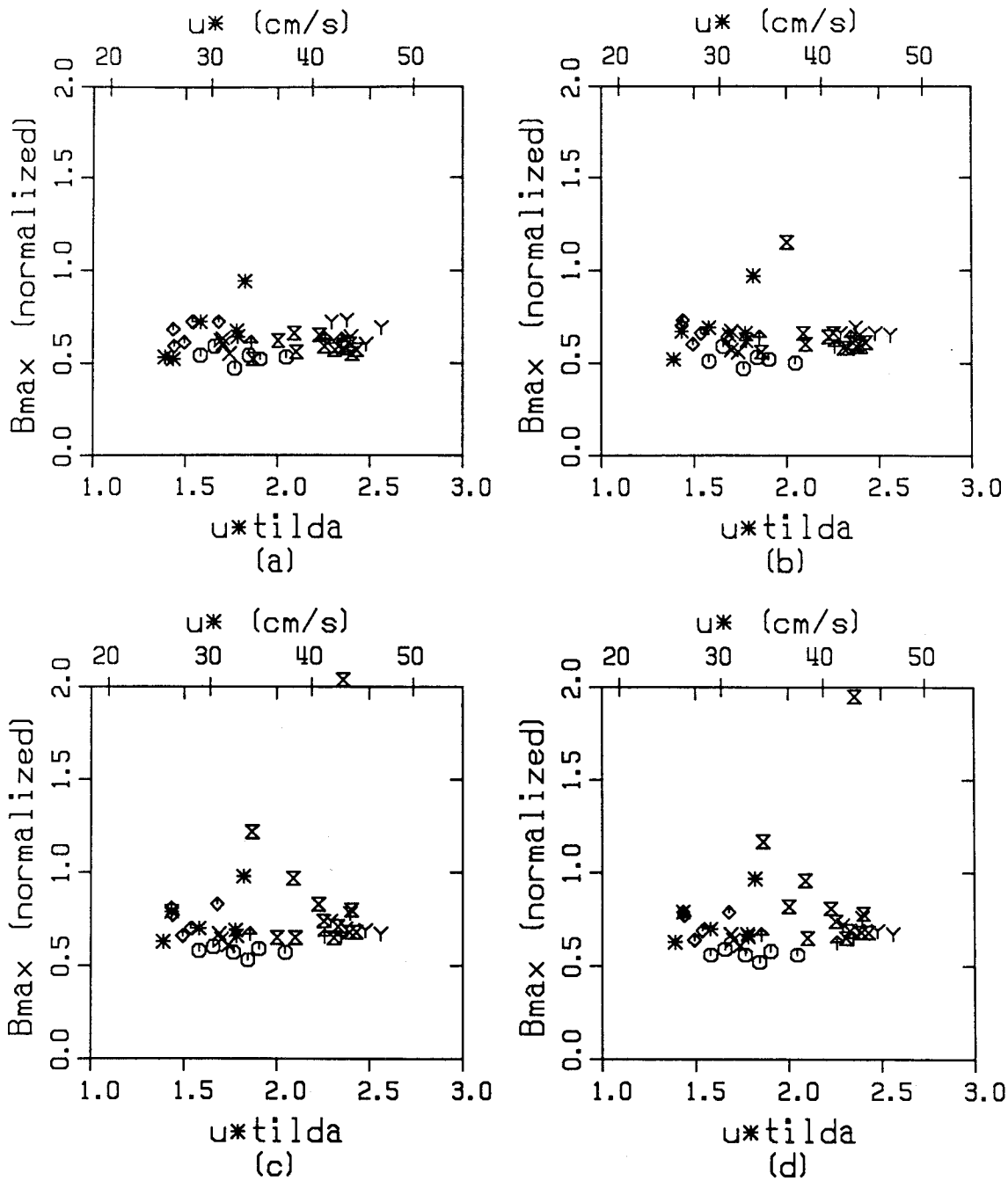
O=1, X=4, ◇=5, ⊁=6, Y=9, ✳=11, ☒=12

Figure 5.22: Average normalized bandwidth (see equations 5.10 and 5.11) associated with detected sea spikes for the detection schemes (a) $\sigma^0_{vv} > \sigma^0_{pol} = -5.2$dB, (b) $\sigma^0_{vv} >= -6.0$dB, (c) B>50Hz, and (d) $\sigma^0_{vv} >= -6.0$dB and/or B>50Hz.

5.7 SUMMARY PLOTS OF SELECTED RESULTS

Some of the major results of sections 5.1 through 5.6 have been replotted according to detection threshold in Figures 5.23 through 5.26. For each threshold, the following plots are shown:

a) Frequency of sea spike occurrence: N vs $\tilde{u}*$

b) Percentage of sea spike crests: P_{ss} vs $\tilde{u}*$

c) Sea spike RCS – VV, Method 1: σ^0_{SSVV1} vs $\tilde{u}*$

d) Sea spike RCS – HH, Method 1: σ^0_{SSHH1} vs $\tilde{u}*$

e) Fractional RCS – VV, Method 1: $\sigma^0_{SSVV1}/\sigma^0_{VV}$ vs $\tilde{u}*$

e) Fractional RCS – HH, Method 1: $\sigma^0_{SSHH1}/\sigma^0_{HH}$ vs $\tilde{u}*$

In general, the SAXON measurements are consistent with the preliminary findings reported in Chapter 2. Furthermore, the data support Phillips' predictions of a cubic friction velocity dependence for the frequency of sea spike occurrence as well as the contribution to the mean radar cross-section. The measurements are also in agreement with previous results by Toba and colleagues of the variation of the fraction of breaking crests with the Reynolds roughness number Re_*.

5.8 EFFECT OF DECREASING INTEGRATION TIME

As discussed in Chapter 3, section 3.2.1, an integration time of $T_i=0.25s$ was used to process data in the field in real-time. This choice of integration time was a compromise between the reduction of variance in the estimation of received power and resolution of the dynamics of the breaking process. A
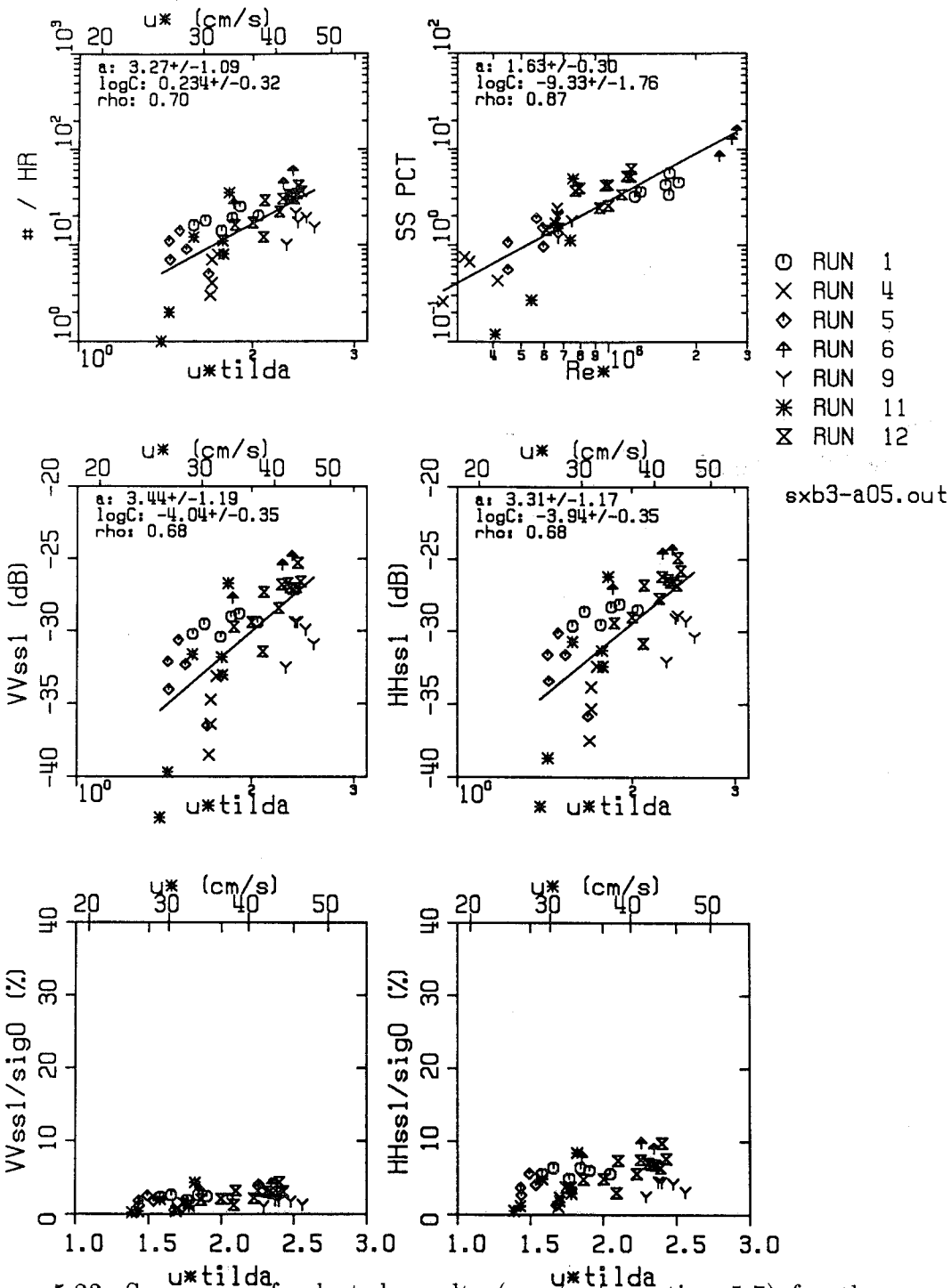
Figure 5.23: Summary of selected results (see text, section 5.7) for the detection scheme (1) $\sigma^o_{vv} > \sigma^o_{pol} = -5.2$dB.
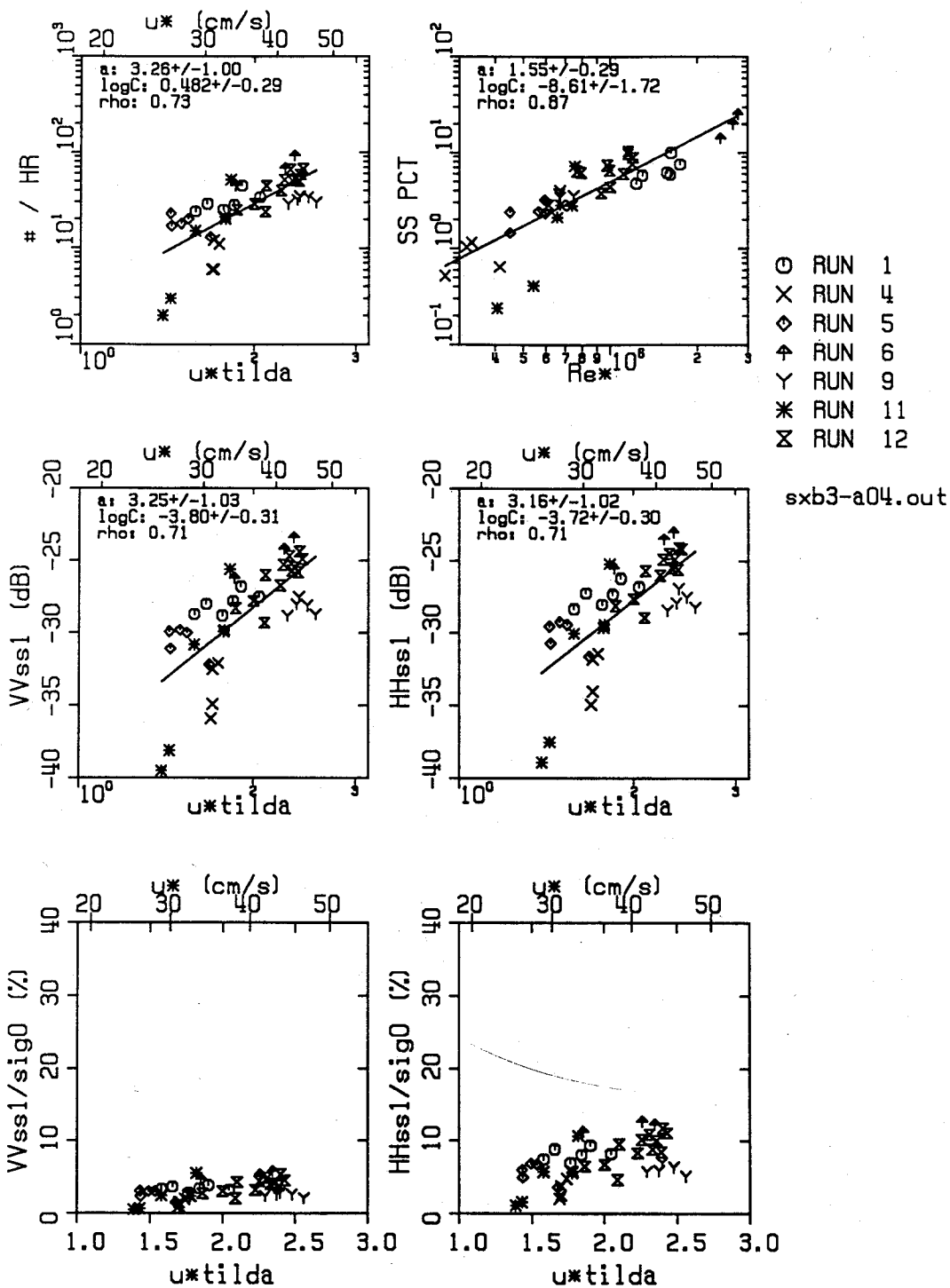
Figure 5.24: Summary of selected results (see text, section 5.7) for the detection scheme (2) $\sigma^0_{vv} >= -6.0$dB.
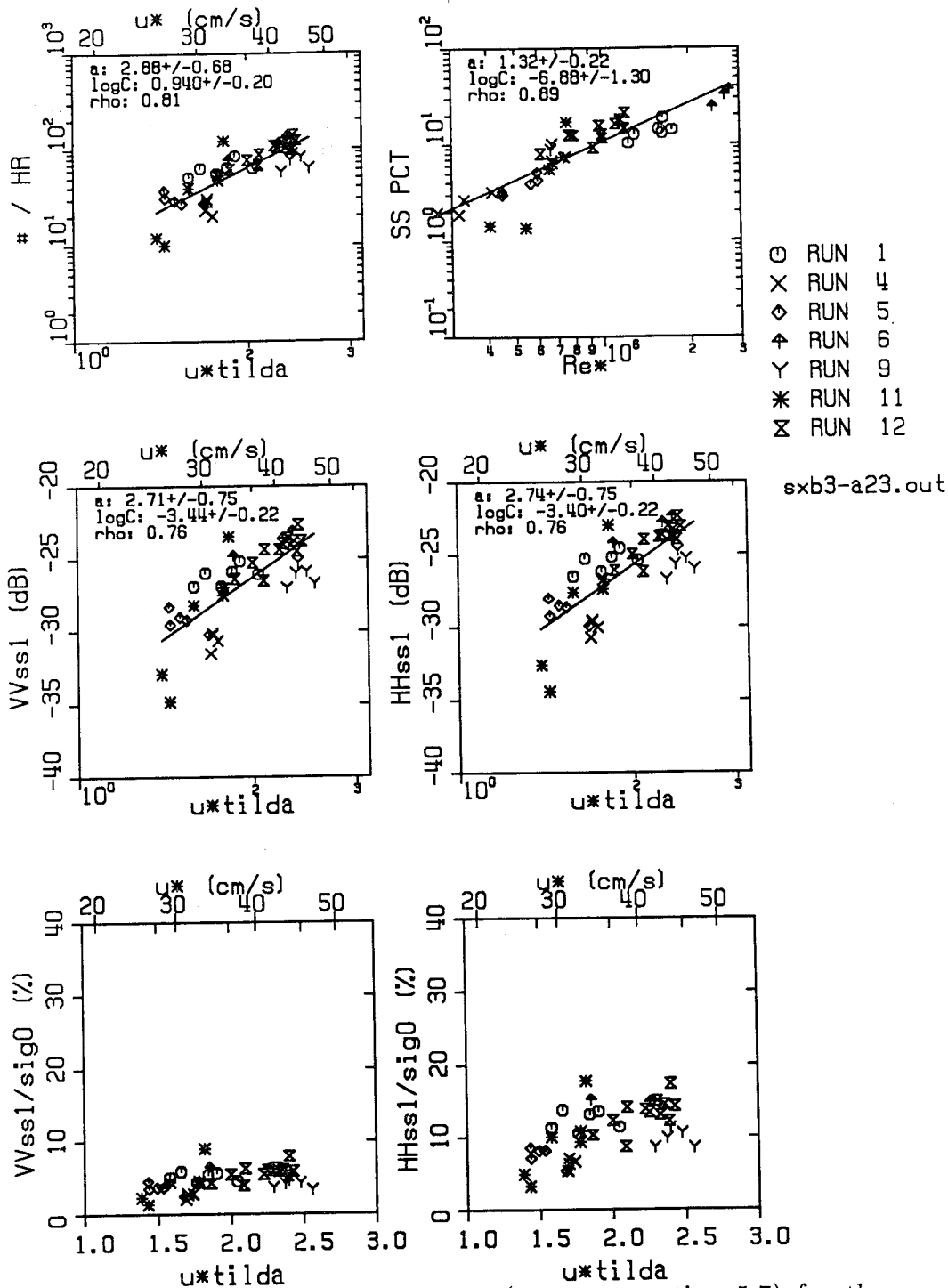
Figure 5.25: Summary of selected results (see text, section 5.7) for the detection scheme (3) B>50Hz.
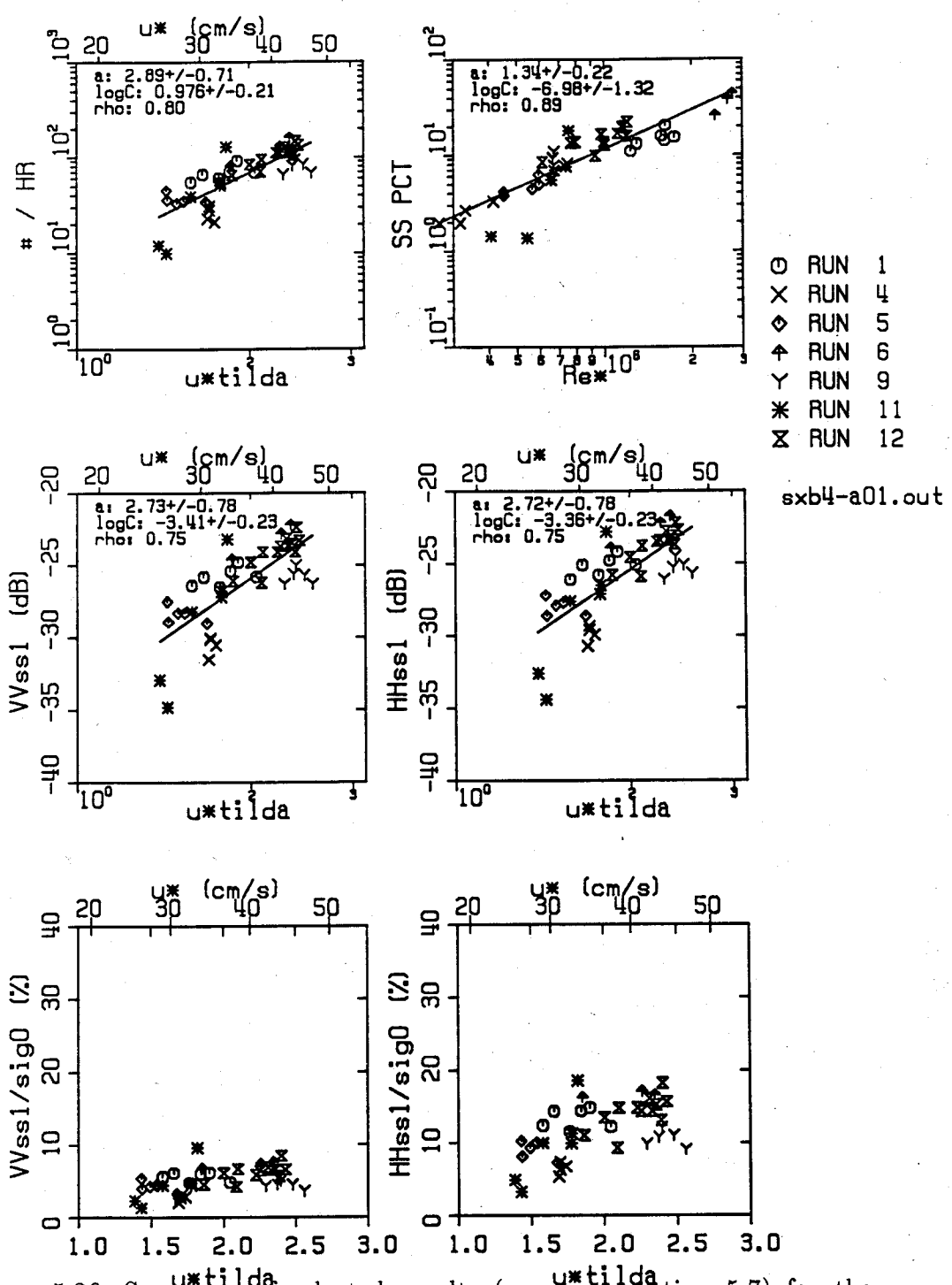
Figure 5.26: Summary of selected results (see text, section 5.7) for the detection scheme (4) $\sigma^0{}_{vv}>=-6.0$dB and/or B>50Hz.

shorter integration time might reveal more detail in individual sea spikes. However, this added detail would be at the expense of confidence in the estimate of the true mean power over the time interval T_i. During the SAXON experiment, a portion of the unprocessed output of the scatterometer was recorded on analog tape. The availability of this raw data permitted the processing done in real–time during the experiment to be repeated with a different integration time. An integration time equal to one–half that used in the field, or $T_i=0.125s$, was chosen to investigate the effect of a shorter integration time.

Figure 5.27 is a two–minute time series with $T_i=0.25s$ for the microwave quantities of VV and HH radar cross–section, mean Doppler frequency, and Doppler bandwidth. The same data processed with an integration time of 0.125s is shown in Figure 5.28. Comparison of the time series of $\sigma^o{}_{VV}$ and σ^o_{HH} in these figures reveals that the characteristics of some of the large sea spikes are indeed changed by the use of a shorter integration time.

In general, the time series of all quantities in Figure 5.28 with $T_i=0.125s$ exhibit increased random amplitude fluctuations over those in Figure 5.27 with $T_i=0.25s$. The shorter integration time reduces the effective number of independent samples, resulting in the overall appearance of added noise. However, the large radar cross–section sea spikes in Figures 5.28 tend to increase in maximum amplitude and exhibit amplitude fluctuations which are larger than the overall increase in background noise. Furthermore, the increase in maximum amplitude seems to be greater for HH spikes than for VV spikes.

These observations of the effect on individual sea spikes are reflected in
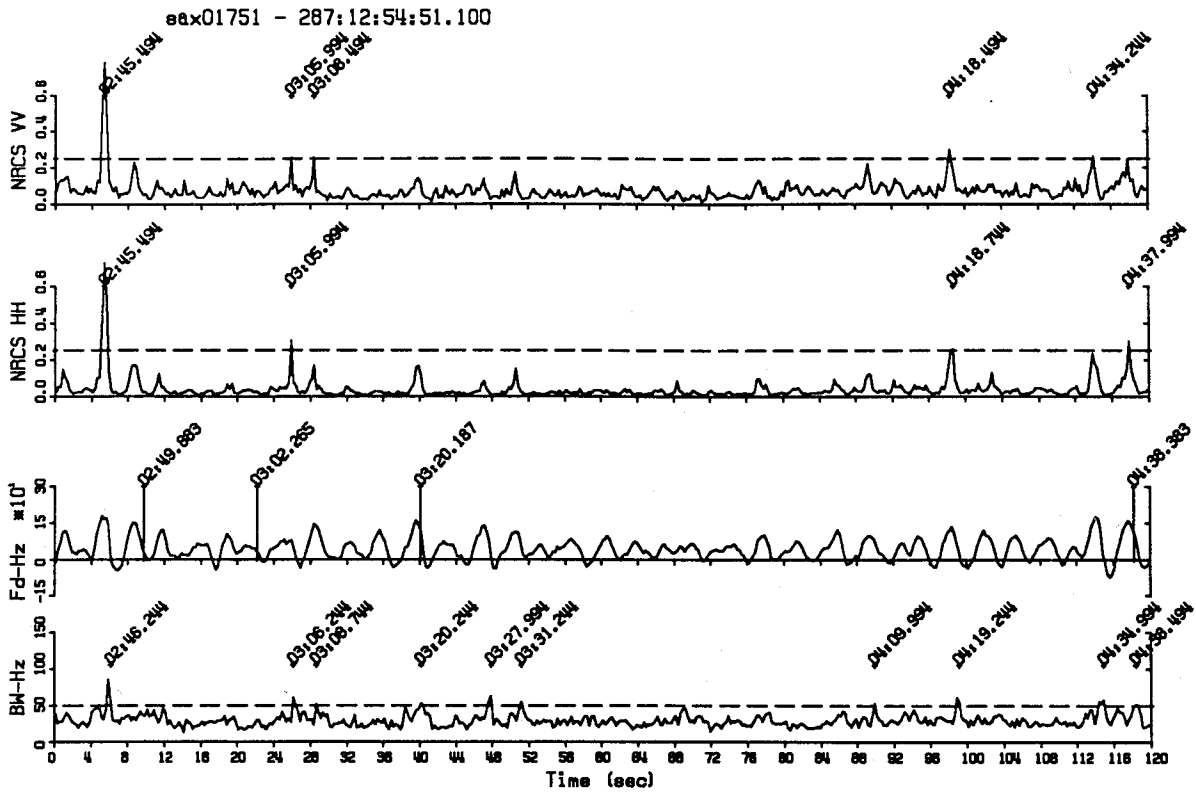
Figure 5.27: Example of time series of σ^0_{vv}, σ^0_{hh}, Doppler frequency, and bandwidth computed with an integration time of $T_i=0.25s$ (compare Figure 5.28).
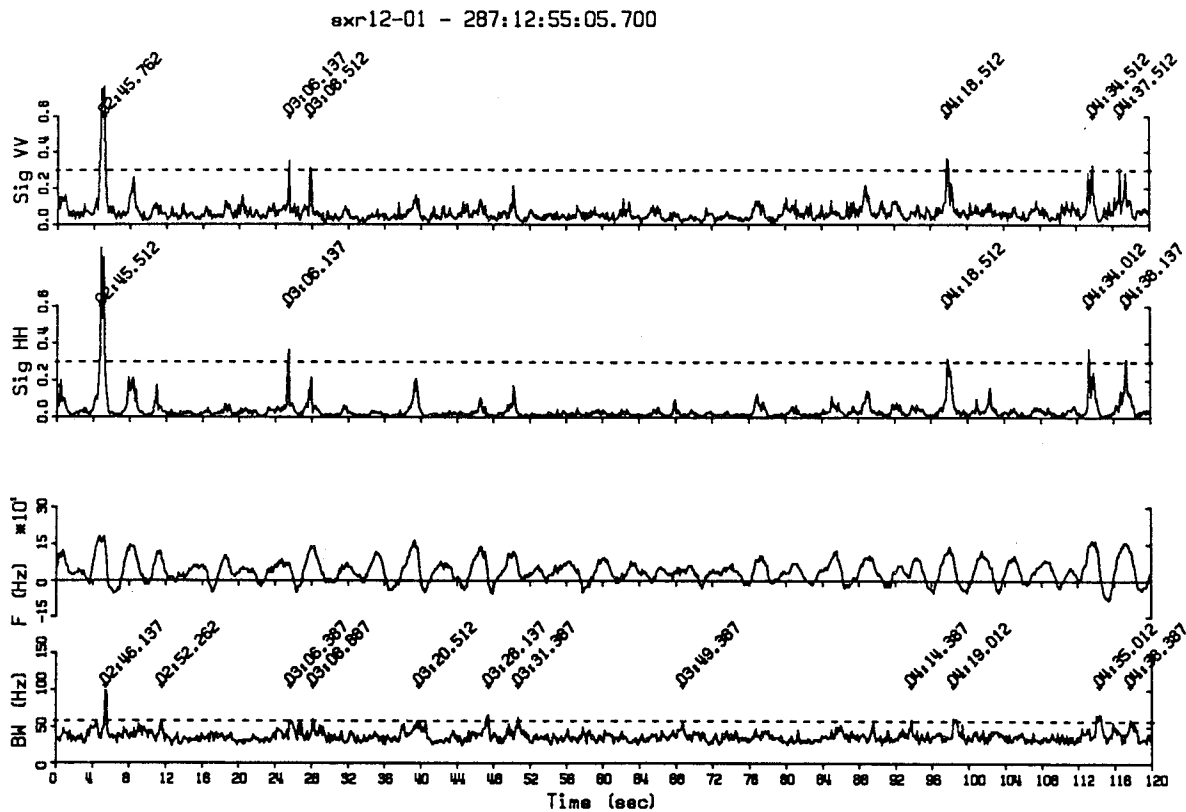
Figure 5.28: Example of time series of σ^0_{vv}, σ^0_{hh}, Doppler frequency, and bandwidth computed with an integration time of $T_i=0.125s$ (compare Figure 5.27).

Figure 5.29 which shows the result of the threshold analysis described in Chapter 4, section 4.1.2, repeated on 22 hours of data reprocessed with the shorter integration time. Comparison of Figure 5.29 with Figure 4.6 (reproduced with Figure 5.29) indicates that, for a given threshold, a larger number of sea spikes are detected for the data processed with a shorter integration time. For large threshold values, the increase in the number of detected events tends to be greater for HH than for VV polarization. The result of the greater increase in the number of HH events at large threshold values is that the VV and HH curves no longer converge in Figure 5.29 as they do in Figure 4.6.

The fact that the VV and HH polarization curves in Figure 4.6 tend to converge at large threshold values was used in Chapter 4 as the basis for choosing the threshold level σ^0_{Pol} to detect polarization–independent events. Thus, it is rather disconcerting that the HH curves in Figure 5.29 rise above the VV curves for large threshold values. Furthermore, this behavior implies that a significant number of sea spikes are produced by a scattering mechanism for which σ^0_{HH} exceeds σ^0_{VV}. As discussed in Chapter 1, the radar cross–section for VV polarization is greater than that for HH polarization when the Bragg resonant scattering mechanism dominates. Since specular reflections are polarization independent, measurements for which VV and HH backscatter are equal would not be unexpected. However, no current models of backscatter from the ocean surface include mechanisms for which HH return is greater than VV.

The interpretation of the result that σ^0_{HH} may exceed σ^0_{VV} raised by using the shorter integration time is complicated by uncertainty in the absolute calibration of the scatterometer. Notice that shifting the VV and HH

SAXON THRESHOLD ANALYSIS: Ti = 0.25s
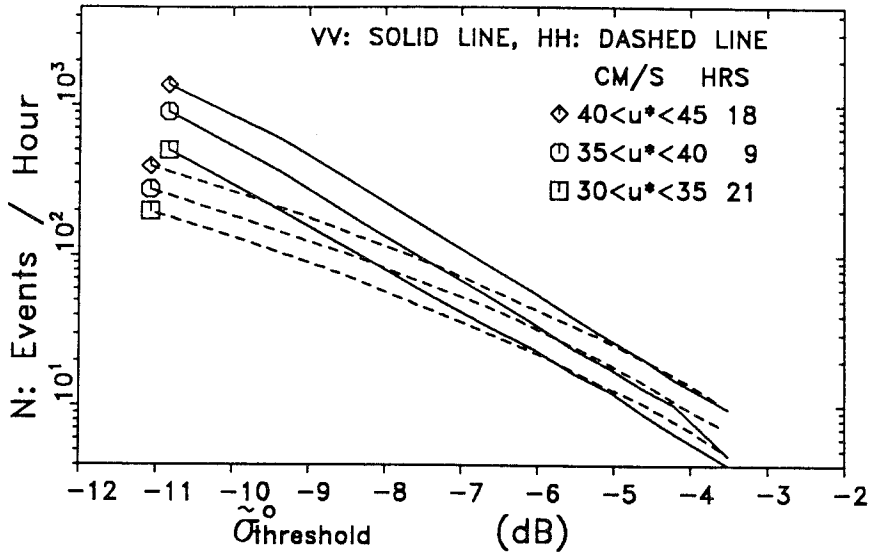
SAXON THRESHOLD ANALYSIS: Ti=0.125s
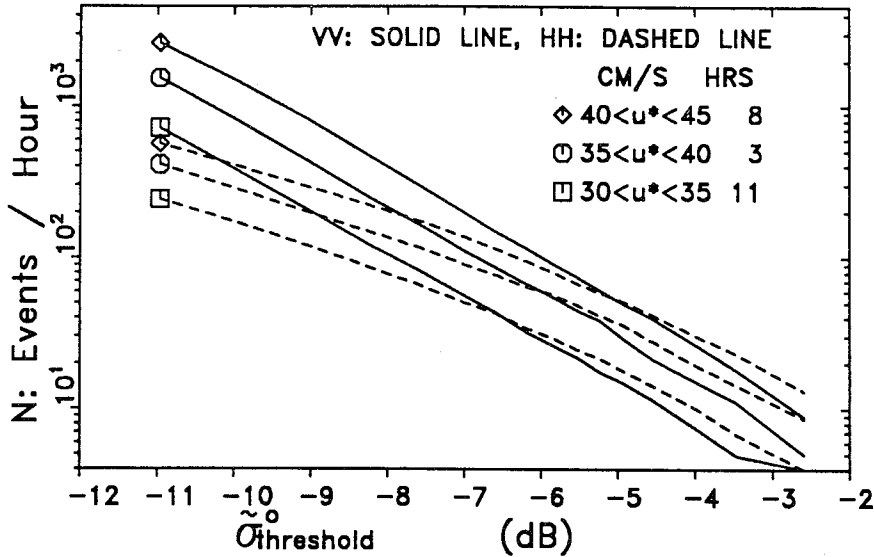
Figure 5.29: Top: threshold analysis from Chapter 4, section 4.1.2 repeated for SAXON data with an integration time of T_i=0.125s. Average number of events per hour N vs radar cross–section threshold for different u* interval in SAXON. Notice that the number of HH events exceeds that for VV at large threshold values. Bottom: Figure 4.6 (T_i=0.25s) is reproduced for comparison.

curves in Figure 5.27 by a few tenths of a dB would cause them to converge at large threshold values. As discussed in Chapter 3, the accuracy of the SAXON radar cross–section measurements is approximately ±1dB. Thus the events for which σ^o_{HH} exceed σ^o_{VV} might be the result of calibration uncertainty.

On the other hand, discrepancies between measurements and theoretical modelling of the polarization characteristics of the radar cross–section have been reported by previous authors(see Chapter 1, section 1.3). Most recently, Sylvester, Pierson, and Breitstein (1989) reported that maximum values of σ^o_{HH} exceeded those of σ^o_{VV} for approximately 8% of the measurements at an incidence angle of 40° from the Seasat–A satellite scatterometer. While the Seasat measurements are not necessarily directly comparable to the SAXON data, tower–based measurements have been used to calibrate space–based scatterometer systems (eg., Keller et al., 1989). The results reported by Sylvester et al. (1989) indicate that the possibility of σ^o_{HH} exceeding σ^o_{VV} is an important topic of current research interest. Unfortunately, the calibration uncertainty in the SAXON measurements has frustrated attempts to establish the validity of the cases for which σ^o_{HH} is greater σ^o_{VV}.

The changes in the large sea spikes due to the use of an integration time of T_i=0.125s do not invalidate the results based on data processed with T_i=0.25s. The primary basis of those results is the thresholds determined by detailed viewing of video recordings. However, the fact that the maximum amplitude of the sea spikes changes with integration time indicates that different thresholds might be appropriate in reanalyzing the data processed with a shorter integration time. A reanalysis based on a new set of thresholds

for the data processed with a shorter integration time would not eliminate the problems associated with the calibration uncertainty discussed above. Furthermore, only 16 hours of reprocessed data are available (roughly 1/3 the amount of original data used). Any reanalysis with a significantly smaller data set than the original is bound to increase the confidence levels associated with the results. The benefits of establishing a new set of thresholds for the reprocessed data are outweighed by these drawbacks.

Nonetheless, even a limited analysis of the reprocessed data based on the thresholds determined from the original data may indicate the sensitivity of the overall results to the effects of a smaller integration time. The results of the analysis of the reprocessed data with $T_i=0.125s$ are summarized in Table 5.3 and Figures 5.30 through 5.33. These results may be compared with those from the field processed data given in Table 5.2 and the summary Figures 5.23 through 5.26. In general, the results with the shorter integration time show an increased amount of scatter, as reflected in the larger confidence limits and smaller correlation coefficients. However, the general trends in the reprocessed data are consistent with the results from the data processed in field with $T_i=0.25s$. As discussed above, the smaller size of the data set with $T_i=0.125s$ and uncertainty in the scatterometer calibration combined to limit the conclusions to be drawn from this analysis. However, the ambiguities raised by using a shorter integration time serve to emphasize the need for further research into the detailed structure of individual sea spikes and improved instrument calibration.

TABLE 5.3: <u>Linear Regression Results</u> ($T_i=0.125s$)

	$\sigma^0_{vv} > \sigma^0_{Pol}$	$\sigma^0_{vv} > -6dB$	BW > 50 Hz	$\sigma^0_{vv} > -6dB$, BW > 50 Hz
$N = C_3 \tilde{u}_*^{a_3}$:				
a_3	3.4 ± 2.1	3.1 ± 1.9	2.9 ± 1.0	2.9 ± 1.2
$\log C_3$	0.37 ± 0.59	0.68 ± 0.54	1.1 ± 0.3	1.1 ± 0.3
ρ_3	0.66	0.66	0.84	0.80
$\sigma^0_{SSVV1} = C_4 \tilde{u}_*^{a_4}$:				
a_4	3.8 ± 2.1	3.4 ± 1.9	3.0 ± 1.2	3.0 ± 1.4
$\log C_4$	−3.8 ± 0.7	−3.5 ± 0.5	−3.2 ± 0.3	−3.2 ± 0.4
ρ_4	0.70	0.70	0.80	0.77
$\sigma^0_{SSHH1} = C_5 \tilde{u}_*^{a_5}$:				
a_5	3.8±2.1	3.4±1.8	3.1±1.2	3.0±1.3
$\log C_5$	−3.7 ± 0.6	−3.4 ± 0.5	−3.2 ± 0.3	−3.1 ± 0.4
ρ_5	0.71	0.72	0.82	0.78
$\sigma^0_{SSVV2} = C_6 \tilde{u}_*^{a_6}$:				
a_6	3.9 ± 2.1	3.6 ± 1.9	3.3 ± 1.2	3.2 ± 1.4
$\log C_6$	−3.7 ± 0.6	−3.5 ± 0.5	−3.2 ± 0.4	−3.1 ± 0.4
ρ_6	0.71	0.72	0.82	0.79
$\sigma^0_{SSHH2} = C_7 \tilde{u}_*^{a_7}$				
a_7	3.9 ± 2.1	3.6 ± 1.9	3.3 ± 1.2	3.3 ± 1.4
$\log C_7$	−3.7 ± 0.6	−3.4 ± 0.5	−3.1 ± 0.3	−3.1 ± 0.4
ρ_7	0.72	0.73	0.83	0.80
$P_{ss} = C_8 \tilde{u}_*^{a_8}$:				
a_8	1.3 ± 0.6	1.2 ± 0.5	0.8 ± 0.5	0.9 ± 0.5
$\log C_8$	−7.4 ± 3.3	−6.6 ± 3.0	−3.4 ± 2.8	−4.1 ± 2.7
ρ_8	0.80	0.80	0.66	0.72
$P_{ss} = C_9 Re_*^{a_9}$:				
a_9	1.3±0.6	1.2±0.5	0.8±0.5	0.9±0.5
$\log C_9$	−7.4 ± 3.3	−6.6 ± 3.0	−3.44 ± 2.8	−4.1± 2.7
ρ_9	0.80	0.80	0.66	0.72
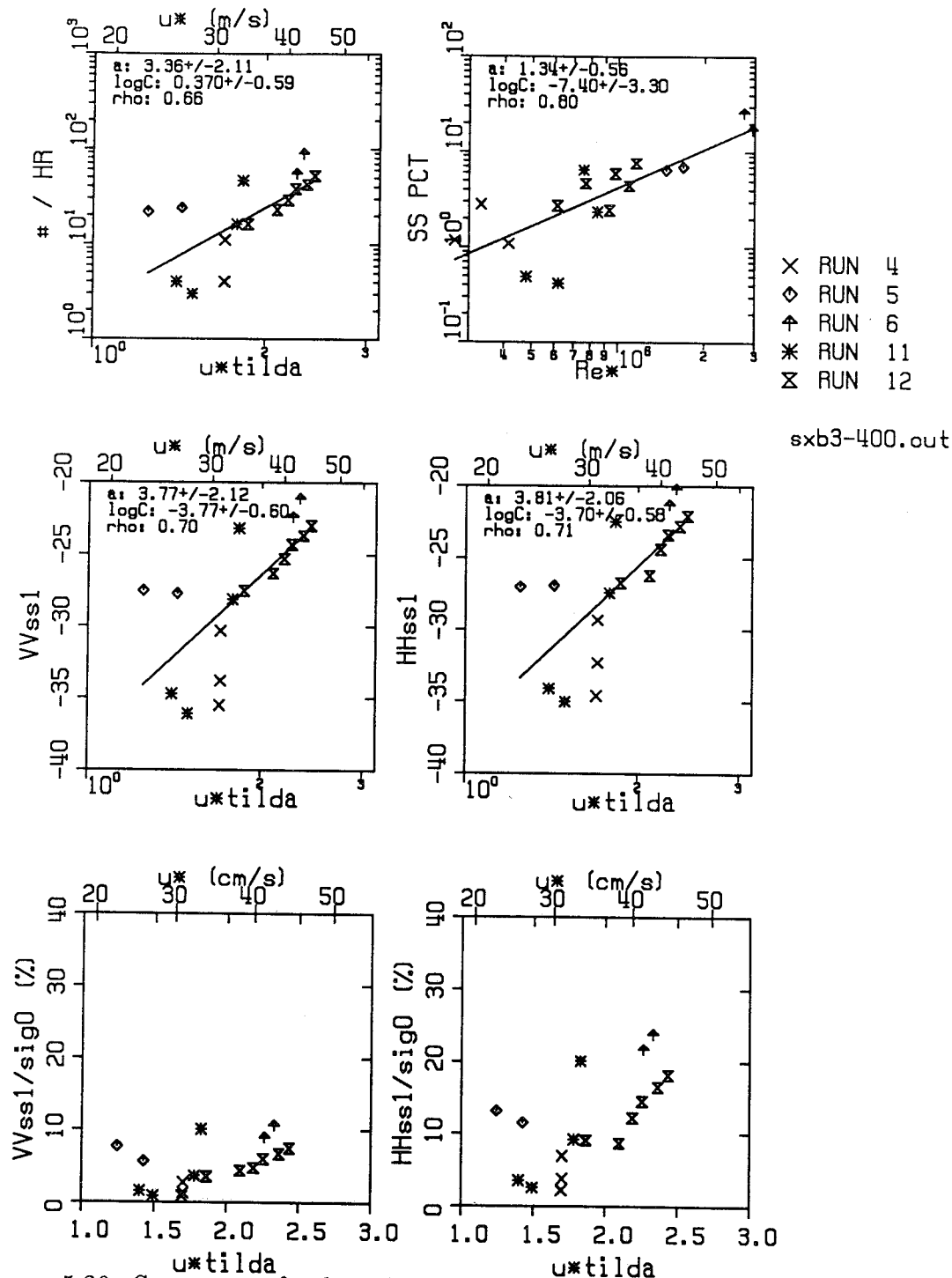
Figure 5.30: Summary of selected results (see text, section 5.7) for the detection scheme (1) $\sigma^0_{vv} > \sigma^0_{pol} = -5.2$dB (Integration time $T_i = 0.125$s).
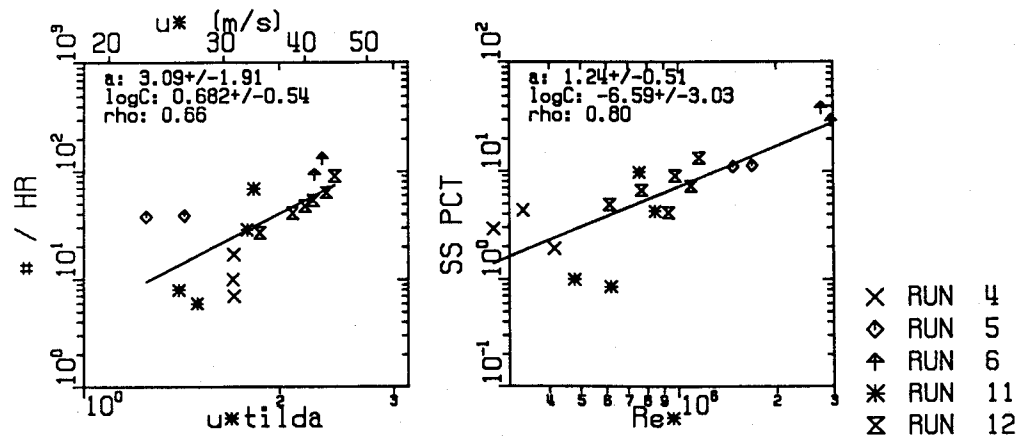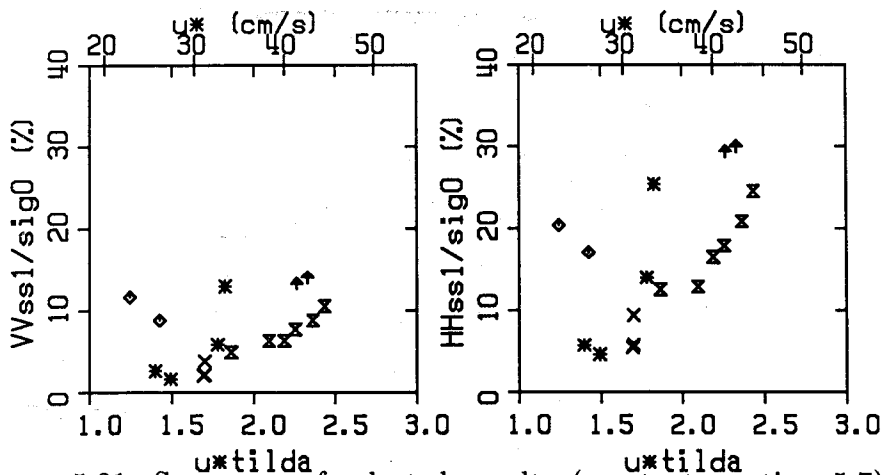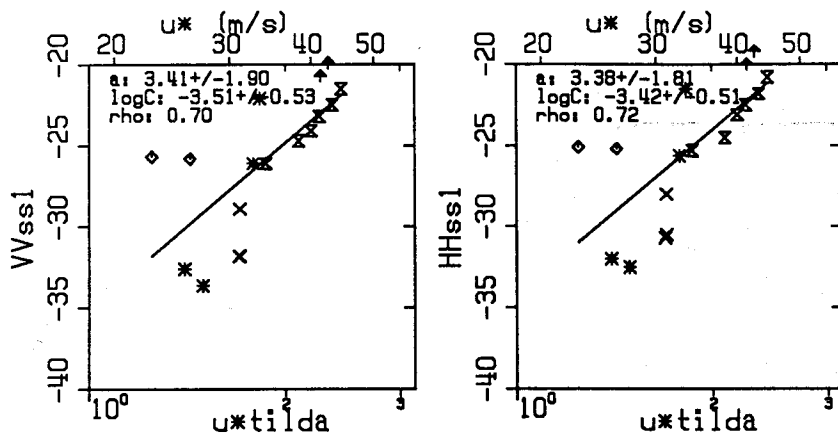
Figure 5.31: Summary of selected results (see text, section 5.7) for the detection scheme (2) $\sigma^0_{vv} \geq = -6.0$dB (Integration time $T_i = 0.125$s).
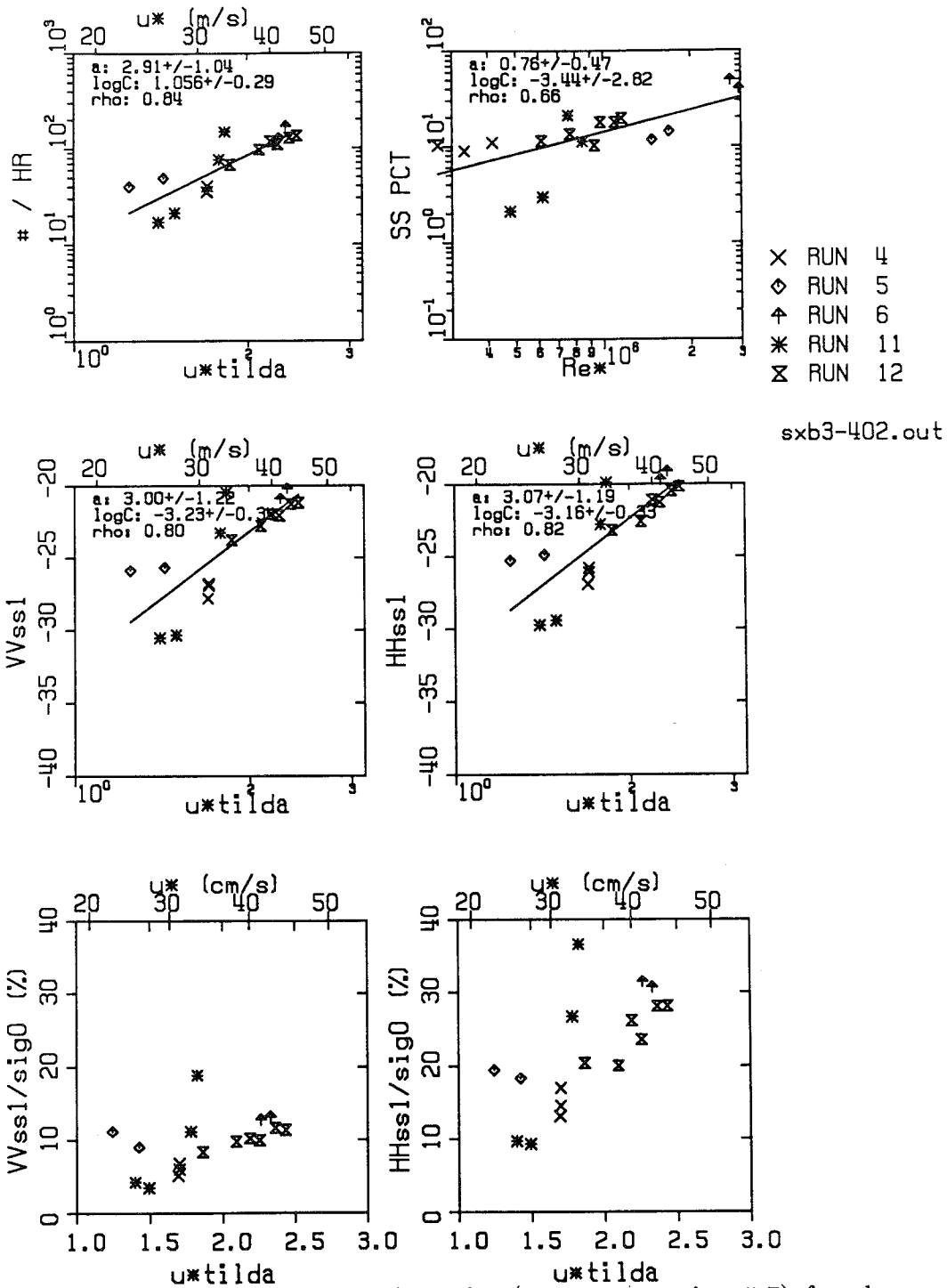
Figure 5.32: Summary of selected results (see text, section 5.7) for the detection scheme (3) B>50Hz (Integration time T_i=0.125s).
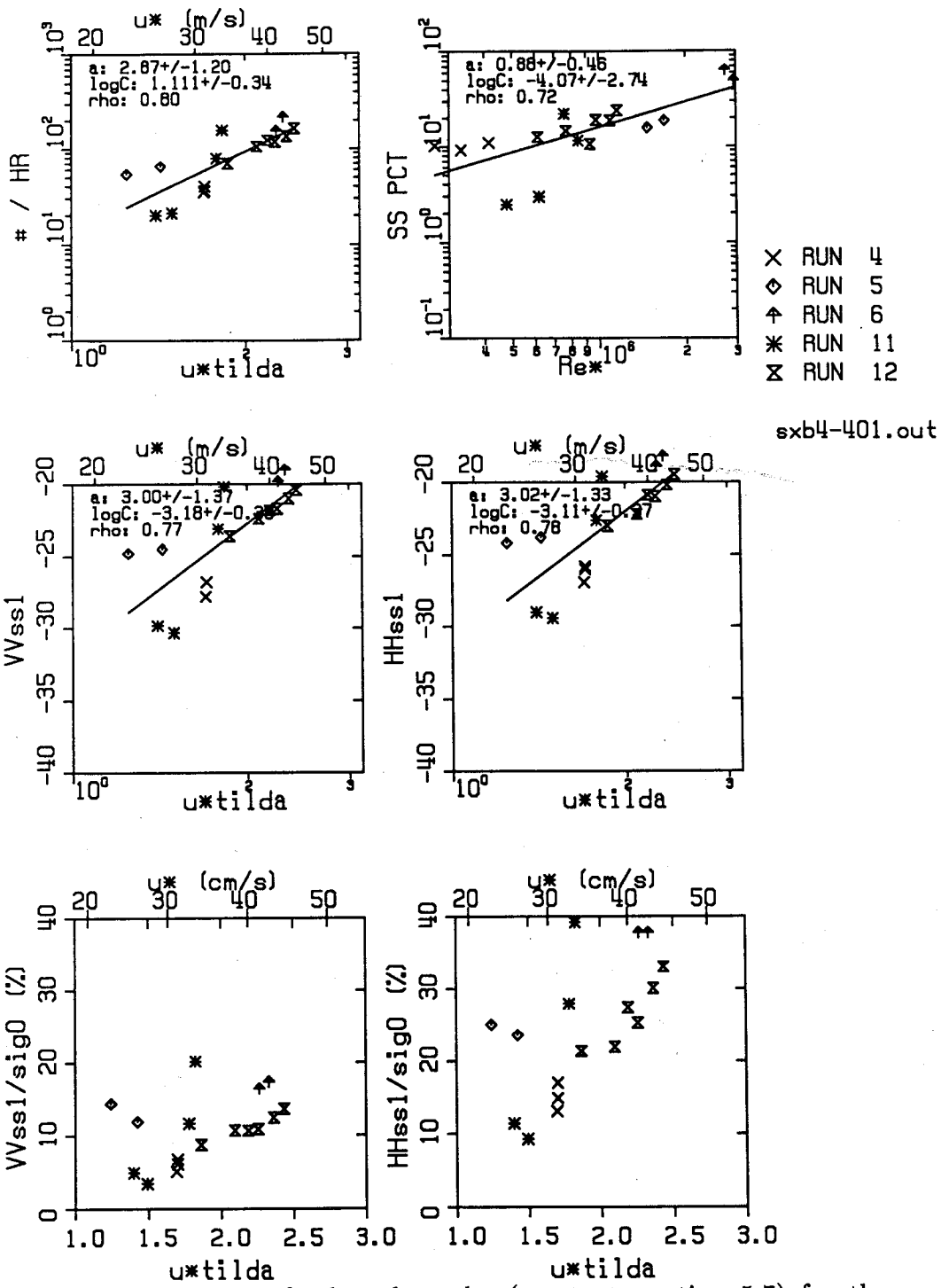
Figure 5.33: Summary of selected results (see text, section 5.7) for the detection scheme (4) $\sigma^{o}_{vv} \geq = -6.0$dB and/or B>50Hz (Integration time $T_i = 0.125$s).

CHAPTER 6

SUMMARY AND CONCLUSIONS

This thesis presents an investigation of large amplitude excursions in radar cross–section which occur in moderate incidence angle measurements of microwave backscatter from the ocean surface. The relationship between these microwave events, known as sea spikes, and breaking surface waves in the open ocean was examined using simultaneous microwave and video measurements with the camera field–of–view coincident with the radar illumination area. The sea spikes in radar cross–section were further characterized in terms of polarization and moments of the Doppler spectrum. This suite of microwave variables was used to investigate detection thresholds for identifying sea spikes associated with individual breaking events. The dependence of these detected events on wind and wave conditions was compared to other measurements of wave breaking and to analytical modelling by previous authors. The Doppler frequency and bandwidth measurements were used to inquire into the kinematics of the breaking process. Finally, the contribution of sea spikes to the mean radar cross–section was computed.

Two field experiments were performed to collect microwave measurements of breaking waves in the open ocean. A preliminary study was conducted using measurements made during a two week period in May, 1987, from the German research platform NORDSEE, which is located in 30m of water approximately 40nm off the German peninsula in the North Sea. A more extensive set of measurements was made over a six week period in the fall of 1988 during the SAXON experiment from the Chesapeake Light Tower, which is located in 12m of

water approximately 15nm offshore from the mouth of the Chesapeake Bay on the east coast of the United States. The major difference between the two data sets was the wave conditions, which for the North Sea were relatively uniform, dominated by low frequency swell, and of essentially unlimited fetch. The SAXON conditions consisted of swell-, mixed-, and wind-dominated seas for which fetch-limited conditions were common.

For both experiments, microwave measurements were made using a coherent, continuous-wave, dual-polarized scatterometer operating at Ku-band (transmit frequency 14GHz, wavelength 2.14cm) with a transmitted power of approximately 200mW. The instrument provided simultaneous complex output of like-polarized backscatter at vertical (VV) and horizontal (HH) linear polarization. The processing of the complex output of the scatterometer consisted of digitally sampling the in-phase and quadrature demodulates at 2kHz and computing time series estimates of the radar cross-section, mean Doppler frequency, and Doppler bandwidth in real-time with a time step, or integration time, of 0.25s. The mean Doppler frequency and bandwidth were computed using a covariance processing technique which compared well with spectral-based processing.

For the preliminary experiment in the North Sea, the angle φ between the wind and the antenna look-direction was in the range $25^\circ \leq \varphi \leq 45^\circ$. The incidence angle was 45° and the two-way, 3-dB elliptical illumination area, or radar spot, on the sea surface was small compared to the wavelength of the dominant surface wave, with dimensions of approximately 1.8m x 2.5m. Direct measurements of friction velocity were provided by a sonic anemometer, while wave height measurements were taken from the Baylor gauge permanently installed on the

tower. A total of 39 hours of microwave data were used in the final analysis of measurements from the preliminary experiment. In addition, a one–hour recording of poor quality video was used.

The azimuthal angle φ for the data analyzed from the SAXON experiment was in the range $0^o \leq \varphi \leq 25^o$. The incidence angle of 45° was the same as in the North Sea, but the spot size was somewhat smaller at 1.5m x 2.2m. Measurements of wind speed, air and sea temperature, and relative humidity were used to compute estimates of friction velocity. Surface displacement measurements were provided by an infrared ranging device and capacitance–type wire wave gauges. Surface displacement spectra computed from the time series of the mean Doppler frequency were also utilized. A total of 41 hours of microwave data and two hours of high quality video recordings were used in the analysis of the SAXON data.

In general, the sea spikes in the radar cross–section, σ^o, associated with breaking waves tend to be independent of polarization and accompanied by an increased mean Doppler frequency and large jumps in bandwidth. The video recordings indicate that the majority of sea spikes in σ^o associated with breaking occur on the steep forward face of waves that ultimately form a whitecap. This observation suggests that such large jumps in σ^o are primarily due to the change in local incidence angle and may be dominated by scattering in the specular regime. However, some sea spikes occur closer in time to when a long wave crest passes the center of the illumination area. These spikes may be due to Bragg resonant scattering at a reduced incidence angle.

The large sea spikes in σ^o associated with the forward face of breaking

waves tend to occur simultaneously with a maximum in the mean Doppler frequency. The coincidence of these maxima is consistent with the assumption that the mean Doppler frequency is dominated by the line-of-sight component of the orbital velocity. A large jump in the Doppler bandwidth often accompanies sea spikes in σ^0 which are caused by waves that break. Unlike the maximum in the mean Doppler frequency, the bandwidth maxima tend to occur after the maxima in σ^0. The video recordings show that the bandwidth maxima generally occur when the illumination area straddles the crest region. Time series of Doppler spectra indicate that the bandwidth maxima can be attributed the to large range of velocities associated with the crest region of wave that form a whitecap.

The video recordings were first viewed to determine the number of whitecaps with a minimum dimension on the order of 0.5m which appeared within the two-way, 3-dB illumination area. These results, expressed in terms of the percentage of breaking crests, summarized in Table 4.1, are consistent with the findings of previous investigators shown in Figure 1.1. However, comparison of the time series of σ^0 and these video results indicated that the waves producing whitecaps in the 3-dB radar spot were not necessarily associated with large sea spikes. Furthermore, large sea spikes in σ^0 are sometimes unaccompanied by a whitecap in the 3-dB spot.

As noted above, large sea spikes in σ^0 were generally associated with the forward face of waves in the process of breaking. Consequently, the whitecap associated with a give sea spike may occur 'downwave' of the radar spot, that is, after the crest of the wave responsible for the sea spike has passed the center of

the illumination area. Therefore, the criterion for a given microwave event to be classified as being due to a breaking wave was the appearance of a whitecap within a distance of approximately 5m downwave of the radar spot. The distance of 5m is on the order of 10–20% of the wavelength of the dominant surface wave corresponding to the peak frequency of the surface displacement spectrum.

A criterion that the peak sea spike radar cross–section, σ^0_{pk}, exceed –5.2dB was established to detect polarization independent sea spikes (see Figure 4.7). While results using this threshold value, designated σ^0_{Pol}, were given using VV polarization, comparison of the distributions of VV and HH radar cross–sections indicated that using HH polarization would be equivalent. The video recordings revealed that events detected by this threshold were indeed due with waves in the process of breaking. However, only 15–20% of the sea spikes associated with breaking waves identified in the video recordings were detected by the threshold σ^0_{Pol}. Breaking events continued to be unambiguously detected as the VV radar cross–section threshold was lowered to a value of –6dB. Approximately 30% of the sea spikes detected with the lower threshold of –6dB were associated with breaking events in the video recordings. On the basis of radar cross–section alone, roughly 70% of the sea spikes which were attributable to breaking waves were not distinguishable from sea spikes of comparable magnitude which showed no visual evidence of being due to wave breaking. Therefore, the distributions of the additional microwave quantities indicative of breaking were used to investigate detection schemes based on joint statistics.

The polarization characteristics of breaking events identified from the video were examined to determine if a useful threshold in the polarization ratio,

$\sigma^{o}_{VV}/\sigma^{o}_{HH}$, could be found. While many events were polarization independent, the polarization ratio exhibited a range of values distributed about unity (see Figures 4.9 and 4.11). The impact of measurement uncertainty on estimating the polarization ratio and the absence of an obvious threshold discouraged the use of the polarization ratio as a discriminator of microwave events associated with wave breaking.

The maximum mean Doppler frequency also proved to be inadequate as an indicator of breaking. Although a local maximum in the Doppler frequency is roughly coincident with the sea spike maximum associated with a breaking wave, the distribution of Doppler frequency maxima can cover a wide range. While this range of Doppler maxima may be due to the influence of crest orientation on the measured line–of–sight velocity, a quantitative study of this effect was judged to be beyond the scope of this thesis.

The characteristic jump in the Doppler bandwidth accompanying sea spikes caused by breaking waves was found to be a useful detection parameter. The joint distributions of radar cross–section and bandwidth were used to determine an appropriate bandwidth threshold (see Figure 4.18). A criterion that the maximum sea spike bandwidth, B_{max}, exceed 50Hz successfully detected approximately 65–70% of the microwave events associated with breaking waves identified from the video recordings. By counting all events for which $\sigma^{o}_{VV}>-6dB$ and/or $B>50Hz$, this success rate was increased to a maximum of 73%. In other words, roughly 3 out of 4 breaking waves producing detectable microwave events were successfully identified by a threshold–based scheme utilizing both radar cross–section and bandwidth information.

None of the detection schemes tested could identify all microwave events attributable to breaking waves. However, for each scheme, the proportion of those events which were detected was roughly the same regardless of friction velocity (see Table 4.3). That is, for the two different one–hour video recordings with $u_* = 30 cms^{-1}$ and $u_* = 40 cms^{-1}$, the number of breaking events counted was proportional to the total number of sea spikes caused by breaking waves. This result strongly supports the validity of using sea spikes detected with a threshold in radar cross–section and/or Doppler bandwidth as a measure of wave breaking.

Statistics of the detected breaking events were computed using the following four different threshold criteria:

1) $\sigma^0_{VV} > \sigma^0_{Pol}$ $(\sigma^0_{Pol} = -5.2 dB)$

2) $\sigma^0_{VV} > -6 dB$

3) $B_{max} > 50 Hz$

4) $\sigma^0_{VV} > -6 dB$ OR $B_{max} > 50 Hz$

Although the magnitude of the quantities of interest varied with each detection scheme, the exponents computed to express their dependencies on wind and wave conditions were not greatly affected by the particular method used (see Table 5.2).

The frequency of occurrence of sea spikes, N, was computed as the number of events counted in a one–hour record. The roughly cubic dependence on friction velocity is consistent with Phillips' (1988) model (equation 1.26) and with theoretical modelling and field measurements of whitecap coverage reported by other investigators.

The dependence on friction velocity of the sea spike contribution, σ^0_{ss}, to the mean radar cross–section was found to be consistent with Phillips' (1988) prediction of a cubic variation, equation (1.25). The fractional power for high friction velocities ($u_* = 40$–$50\,\mathrm{cms^{-1}}$) was found to be approximately 5–10% for VV polarization and 10–20% for HH polarization using the procedure designated method 1 (equations (2.2) and (2.3) and Figure 2.5a) and the detection scheme utilizing both radar cross–section and bandwidth information. These findings support the inclusion of wave breaking in scattering models, especially for HH polarization and high friction velocity. The data also suggest that the average radar cross–section of an individual sea spike is not dependent on u_*. Friction velocity exponent for the mean radar cross–section itself were computed to be 2.0 and 1.8 for VV and HH polarization, respectively (see Figure 5.1).

The percentage of crests producing sea spikes, P_{ss}, also exhibited a roughly cubic dependence on friction velocity. An exponent of approximately 1.5 was found for the dependence of P_{ss} on a roughness Reynolds number, Re_*, based on friction velocity and the dominant surface wavelength (equation 1.4). This result is consistent with laboratory measurements by Toba and Kunishi (1970) and field measurements by Toba and Chaen (1973). Furthermore, the scatter in the plots of P_{ss} versus Re_* was significantly less that of P_{ss} versus u_* and N versus u_*. A Reynolds number exponent of 1.5 was shown to be consistent with a cubic friction velocity dependence using published fetch dependent scaling relations.

Comparisons were made with the statistical models of Srokoz (1986) for the probability of wave breaking as a function of the dimensionless fourth moment, m_4/g^2, of the surface displacement spectrum (interpreted as an integrated measure

of the vertical acceleration). The results were inconclusive and serve mainly to highlight the ambiguity inherent in comparison of such models with field measurements. The ambiguity arises from the combined effect of specifying an upper cutoff frequency to compute m_4 and uncertainty in the appropriate value of the threshold parameter α in equation (1.19).

The average of the maximum mean Doppler velocity associated with the detected sea spikes was found to be less than 25% of the phase speed corresponding to the peak of the surface displacement spectrum. This result indicates that the mean Doppler frequency of breaking waves is not dominated by the large velocities associated with whitecaps. An average bandwidth was computed from the maximum Doppler bandwidth for each event normalized by the corresponding maximum mean Doppler frequency. This normalized bandwidth associated with the detected events ranged between 0.50 and 0.75 and showed no functional dependence of friction velocity. The average (dimensional) bandwidth corresponding to the sea spikes was in the range of 60–70Hz.

The effect of decreasing the integration time was considered by reanalyzing a unprocessed data which was recorded on analog tape. An integration time of $T_i=0.125$, equal to one–half that used in the original processing, was applied to 16 hours of archived data. The general trends in the reprocessed data were consistent with the results from data processed in the field. A significant number of the sea spikes showed maxima in HH polarization which exceeded VV polarization. The impact of a shorter integration time on individual sea spikes emphasizes the importance of accurate calibration when characterizing events in terms of the polarization ratio.

Many of the previous methods for measuring the degree of wave breaking have relied on visual techniques which tend to be laborious and subjective. One of the motivations of this thesis was a desire to overcome these limitations by utilizing objective criteria based on properties of microwave scattering from breaking waves. The use of thresholds in cross–section and bandwidth facilitate the analysis of a relatively large amount of data. The cross–section threshold established to count polarization independent sea spikes is solely based on the microwave measurements themselves and does unambiguously detect breaking events. However, the percentage of the total number of breaking events detected with this technique is relatively low. An acceptable level of detection was provided by the addition of a bandwidth threshold. The drawback of this scheme is that the bandwidth threshold was established by laboriously and subjectively correlating the microwave measurements with the video recordings to determine the bandwidth distribution. A potential criticism of the SAXON results lies in the fact that detailed viewing of the video recordings was done for only two hours. However, the merits of the analysis are supported by the favorable comparison of the SAXON results with those of previous investigators (see Figure 5.16).

Further research on the source of the bandwidth increase associated with wave breaking may lead to an objective basis for a bandwidth threshold. For example, improving the accuracy of the alignment between the video camera and antenna may aid in understanding the bandwidth increase. A ranging device bore–sighted with the antennas might be helpful in isolating the source the bandwidth increase which occurs when the radar spot straddles the crest region. Also, spectral based processing may be more appropriate for the second moment than the covariance processing technique employed here.

Laboratory measurements could also be helpful in investigating the source of the bandwidth increase. The importance of the location of the radar spot on the phase of the wave as well as its stage of development might also be clarified in the laboratory. A better understanding of the mechanisms which produce the distinctive Doppler signature of breaking waves may ultimately lead to useful information on the dynamics of the breaking process.

The experience gained in the SAXON experiment has contributed to improving the procedure for calibrating the scatterometer (see Appendix A). Better relative calibration between the VV and HH polarization channels may result in better discrimination based on the polarization ratio. The increased resolution provided by a shorter integration time may lead to a better rate of detection based on counting polarization independent events. These improvements should also be helpful in understanding the occurrence of cases where HH return exceeds that of VV. Further discrimination may also be possible by utilizing cross– as well as like–polarized microwave measurements.

The data analyzed in this thesis were restricted to an incidence angle 45° and an angle between the look–direction and the wind of 25°. Sea spikes associated with breaking wave were first reported for measurements at large incidence angle. Since the mean radar cross–section decreases with increasing incidence angle, detection may be enhanced as the incidence angle is increased.

The results concerning the contribution of sea spikes to the mean radar cross–section should be helpful in estimating and evaluating the errors in current algorithms used in scatterometry. The influence of return from breaking waves on

the modulation transfer function used in SAR imaging was not directly addressed in this thesis. However, a quantitative assessment seems worthwhile, given the correlation of the sea spikes with the Doppler frequency maxima and the large percentage of breaking crests under high sea conditions. Degraded azimuthal image resolution has been associated with localized scatterer coherence times on the order of 10^{-2}s (Lyzenga and Schuchman, 1983). The reciprocal of the average bandwidth associated with the detected sea spikes is of this same order.

In conclusion, this investigation has shown that individual wave breaking events can be meaningfully detected using microwave techniques. The radar cross–section and Doppler bandwidth were found to be the most useful discriminators of wave breaking. The dependence on wind and wave conditions of the detected breaking events was consistent with theoretical modelling and field measurements of wave breaking by other investigators. Information on the kinematics of the breaking process can be provided by microwave measurements of Doppler velocity and bandwidth. As far as we know, these are the first published measurements of the wind speed dependence and relative contribution of sea spikes due to breaking waves. The contribution of the detected sea spikes to the mean radar cross–section indicates that wave breaking should be included in models of microwave backscatter from the ocean surface.

REFERENCES

Alpers, W. and K. Hasselmann, The two–frequency microwave technique for measuring ocean wave spectra from an airplane or satellite, Bound. Layer Met., 13, 215–230, 1978.

Alpers, W. and W. L. Jones, The modulation of the radar backscattering cross–section by long ocean waves, Proc. of 12th Int. Symposium on Remote Sensing of Envir., Manila, Philippines, 1597–1607, ERIM, Ann Arbor, MI, 1978.

Alpers, W., D. B. Ross, and C. L. Rufenach, On the detectability of ocean surface wave by real and synthetic aperture radar, J. Geophys. Res., 86(C7), 6481–6498, 1981.

Banner, M. L. and E. H. Fooks, On the microwave reflectivity of small–scale breaking water waves, Proc. R. Soc. London, Ser. A, 399, 93–109, 1985.

Barrick, D. E., First–order theory and analysis of MF/HF/VHF scatter from the sea, IEEE Trans., AP–20, 2–10, 1972.

Barrick, D. E. and W. H. Peake, A review of scattering from surfaces with different roughness scales, Radio Science, 3, 865, 1968.

Bass, F. G., I. M. Fuks, A. E. Kalmykov, I. E. Ostrovsky, and A. D. Rosenberg, Very high frequency radio wave scattering by a disturbed sea surface, IEEE Trans., AP–16, 554–568, 1968.

Bendat, J. S. and A. G. Piersol, Random data: Analysis and measurement procedures, 2nd Edition, Wiley–Interscience, New York, 1986.

Blanc, T. V., Variation of bulk–derived surface flux, stability, and roughness results due to the use of different transfer coefficient schemes, J. Phys. Ocean., 15, 650–669, 1985.

Cartwright, D. E, and M. S. Longuet–Higgins, The statistical distribution of the maxima of a random function, Proc. Roy. Soc. London, A237, 212–232, 1956.

Crombie, D. D, Doppler spectrum of sea echo at 13.56 Mc/s, Nature, 175, 681–682, 1955.

Dahl, P. H., A. B. Baggeroer, P. N Mikhalevskym and I. Dyer, Measurement of the temporal fluctuations of cw tones propagated in the marginal ice zone, J. Acoust. Soc. Am., 83(6), 1988.

Donelan, M. and W. J. Pierson Jr., Radar scattering and equilibrium ranges in wind–generated wave with application to scatterometry, J. Geophys. Res., 92(C5), 4971–5092, 1987.

Doviak, R. J. and D. S. Zrnic', Doppler radar and weather observations, Academic Press, Orlando, 1984.

Duncan, J. R., W. C. Keller, and J. W. Wright, Fetch and wind speed dependence of Doppler spectra, Radio Sci., 9, 809–819, 1974.

Ewell, G. W., M. T. Tuley, and W. F. Horne, Temporal and spatial behavior of high resolution sea clutter 'spikes', IEEE Radar '84 Conf., 100–104, 1984.

Glazman, R. E., Statistical characterization of sea surface geometry for a wave slope field discontinuous in mean slope, J. Geophys. Res., 91, C5, 6629–6641, 1986.

Glazman, R. E. and P. B. Weichman, Statistical geometry of a small surface patch in a developed sea, J. Geophys. Res., 94(C4), 4998–5010, 1989.

Geernaert, G., L. Larsen, and F. Hansen, Measurements of wind stress, head flux, and turbulence intensity during storm conditions over the North Sea, J. Geophys. Res., 92(C12), 13,127–13,139, 1987.

Guinard, N. W. J. T. Ransome, and J. C. Daley, Variation of the NRCS of the sea with increasing roughness, J. Geophys. Res., 76, 1525–1538, 1971.

Hasselmann, K. and M. Schieler, radar backscatter from the sea surface, in Proc. of 8th Annual Symposium on Naval Hydrodynamics, ACR–179, 361–388, ONR, Dept. of Navy, Arlington, VA, 1970.

Holthuijsen, L. H. and T. H. C. Herbers, Statistics of breaking waves observed as whitecaps in the open sea, J. Phys. Ocean., 16, 290–297, 1986.

Jessup, A. T., W. C. Keller, and W. K. Melville, Measurements of sea spikes in radar backscatter at moderate incidence, to appear in J. Geophys. Res., 1990.

Jessup, A. T., Microwave detection and characterization of deep–water wave breaking, M.S. thesis, Massachusetts Institute of Technology, Cambridge, MA, 1988.

Kalmykov, A. I. and V. V. Pustovoytenko, On the polarization features of radio signal scattered from the sea surface at small grazing angles, J. Geophys. Res., 81, 1960–1964, 1976.

Katzin, M., On the mechanism of radar sea clutter, Proc. IRE, 45, 44–54, 1957.

Keller, W. C. and J. W. Wright, Microwave scattering and the straining of wind–generated waves, Radio Sci., 10, 139–147, 1975.

Keller, W. C, W. J. Plant, and G. R. Valenzuela, Observations of breaking ocean waves with coherent microwave radar, Wave Dynamics and Radio Probing of the Sea Surface, O. M. Phillips and K. Hasselmann, Eds., Plenum, 285–293, 1986)

Keller, W. C., W. J. Plant, and D. E. Weissman, The dependence of X band microwave sea return on atmospheric stability and sea state, J. Geophys. Res., 90–C1, 1019–1029, 1985.

Keller, W. C., V. Wissman, and W. Alpers, Tower–based measurements of the ocean C band radar cross–section, J. Geophys. Res., 94(C1), 1989.

Kennedy, R. M., A probabilistic description of deep water whitecaps, Ph.D. thesis, Nova University, Fort Lauderdale, FL, 1978.

Kennedy, R. M. and R. L. Snyder, On the formation of whitecaps by a threshold mechanism, 2, Monte Carlo experiments, J. Phys. Ocean., 13, 1493–1504, 1983.

Kitaigorodskii, S. A., Fizika Vzaimodestviya Atmosferi I Okeana, (Physics of air–sea interaction). Leningrad: Gidromet. Izdatel'stvo. (Engl. transl. (1973). Jerusalem: Israel Prog. Sci. Transl.), 1970.

Kwoh, D. S. and B. M. Lake, Microwave backscatter from short gravity waves: deterministic, coherent, dual–polarized study of the relationship between backscatter and water wave properties, Wave Dynamics and Radio Probing of the Sea Surface, O. M. Phillips and K. Hasselmann, Eds., Plenum, 1986; see also similar title in IEEE J. of Ocean. Eng., Vol. OE–9(5), 291–308, 1984.)

Kwoh, D. S., B. M. Lake, and Rungaldier, Microwave scattering from internal wave modulated surface waves: A shipboard real paerture coherent radar study in the Georgia Strait Experiment, J. Geophys. Res., 93(C10), 12,235–12,248, 1988.

Large, W. G. and S. Pond, Open ocean momentum flux measurements in moderate to strong winds, J. Phys. Ocean., 11, 324–336, 1981.

Lee, P. H. Y., Laboratory measurements of polarization ratios of wind wave surfaces, IEEE Trans., AP–26, 2, 302–306, 1978.

Lewis, B. L., and I. D. Olin, Experimental study and theoretical model of high–resolution radar backscatter from the sea, Radio Sci., 15, 815–828, 1980.

Long, M. W., Radar Reflectivity of Land and Sea, Artech House, Dedham, 1983.

Long, M. W., On the two–scatterer theory of sea echo, IEEE Trans., AP–22, 667–672, 1974.

Longuet–Higgins, M. S., The generation of capillary waves by steep gravity waves, J. Fluid Mech., 16, 138–159.

Longuet–Higgins, M. S. and J. S. Turner, An entraining plume model of a spilling breaker, J. Fluid Mech., 63, 1–20, 1974.

Longuet–Higgins, M. S. and N. D. Smith, Measurement of breaking waves by a surface jump meter, J. Geophys. Res., 88(C14), 9823–9831, 1983.

Lyzenga, D. R., A. L. Maffett, and R. A. Shuchman, The contribution of wedge scattering to the radar cross–section of the ocean surface, IEEE Trans., GE–21(4), 1983.

Lyzenga, D. R. and R. A. Shuchman, Analysis of scatter motion effects in Marsen X band SAR imagery, J. Geophys. Res., 88(C14), 9769–9775, 1983.

Mel'nichuk, Y.U. and A. A. Chernikov, Spectra of radar signals from the sea surface for different polarizations, Izvestia, Atmos. Oceanic Phys., 7, 17–24, 1971.

Melville, W. K., Wind stress and roughness length over breaking waves, J. Phys. Ocean., 7, 702–710, 1977.

Melville, W. K., M. R. Loewen, F. C. Felizardo, A. T. Jessup, and M. J. Buckingham, Acoustic and microwave signature of breaking waves, Nature, 336(6194), 54–59, 1988.

Michell, J. H., The highest waves in water, Phil. Mag., 36, 430–437, 1883.

Monahan, E. C., Laboratory comparison of fresh–water and salt–water whitecaps, J. Geophys. Res., 74(28), 1969.

Monahan, E. C., Oceanic whitecaps, J. Phys. Ocean., 1, 139–144, 1971.

Monahan, E. C. and I. G. O'Muircheartaigh, Whitecaps and the passive remote sensing of the ocean surface, Int. J. Remote Sensing, 7(5), 627–642, 1986.

Monahan, E. C., and D. K. Woolf, Comment on "Variations of whitecap coverage with wind stress and water temperature, J. Phys. Ocean., 19, 706–709, 1988.

Ochi, M. K., and C. H. Tsai, Prediction of occurrence of breaking waves in deep water, J. Phys. Ocean., 13, 2008–2019, 1983.

Papoulis, A., Probability, Random Variable, and Stochastic Processes, McGraw–Hill, New York, 1965.

Phillips, O. M., The Dynamics of the Upper Ocean, Cambridge University Press, 1977.

Phillips, O. M., Radar returns from the sea surface – Bragg scattering and breaking waves, J. Phys. Ocean., 18, 1065 –1074, 1988.

Phillips, O. M., Spectral and statistical properties of the equilibrium range in wind–generated gravity waves, J. Fluid Mech., 156, 505 – 531, 1985.

Phillips, O. M., and M. L. Banner, Wave breaking in the presence of wind drift and swell, J. Fluid Mech., 66(4), 625–640, 1974.

Pidgeon, V. W., Doppler dependence of radar sea return, J. Geophys. Res., 73, 1333–1341, 1968.

Pinkel, R., Observation of a strongly nonlinear motion in the open ocean using a range–gated Doppler sonar, J. Phys. Ocean., 9(4), 675–686, 1979.

Pinkel, R. Doppler sonar observations of internal waves: Wavefield structure, J. Phys. Ocean., 13(5), 804–815, 1983.

Plant, W. J., W. C. Keller, and J. W. Wright, Modulation of coherent microwave backscatter by shoaling waves, J. Geophys. Res., 83(C3), 1347–1352, 1978.

Plant, W. J. and W. C. Keller, The two–scale radar wave probe and SAR imagery of the ocean, J. Geo. Res., 88(C14), 9776–9784, 1983.

Plant, W. J., W. C. Keller, and A. Cross, Parametric dependence of ocean wave–radar modulation transfer functions, J. Geophys. Res., 88(C14), 9747–9756, 1983.

Plueddemann, A. J., Observations of the upper open using a multi–beam doppler sonar, Ph.D. thesis, Scripps Inst. Ocean., San Diego CA, 1987.

Rapp, R. J., Laboratory measurements of deep water breaking waves, Ph.D. thesis, Mass. Inst. of Tech., Cambridge, MA, 1986.

Rapp, R. J. and W. K. Melville, Laboratory measurements of deep–water breaking waves, to appear in Phil. Trans. Roy. Soc. Lond., 1990.

Rice, S. O., Mathematical analysis of random noise, Bell System Tech. J., 23, 282–332, 1944, and 24, 46–146,1945, both of which are reprinted in N. Wax (ed), Selected Papers on Noise and Stochastic Processes, Dover, New York, 1954.

Rice, S. O., Reflection of electromagnetic waves from slightly rough surfaces, Comm. Pure and Applied Math., 4, 351–378, 1951.

Ross, D. B. and V. Cardone, Observations of oceanic whitecaps and their relation to remote measurements of surface wind speed, J. Geophys. Res., 79(3), 444–452, 1974.

Rummler, W. D., Introduction of a new estimator for velocity spectral parameters, Tech. Memo MM–68–4121–5, Bell Tele. Lab., Whippany, NJ, 1968.

Schroeder, L. C., W. L. Jones, P. R. Schaffner, and J. L. Mitchell, Flight measurements and analysis of AAFE RADSCAT wind speed signature of the ocean, NASA Technical Memo., TM 85646, 144 pp., 1984.

Smith, S. D., Coefficients for sea surface wind stress, heat flux, and wind profiles as a function of wind speed and temperature, J. Geophys. Res., 93(C12), 15,467–15,472, 1988.

Snyder, R. L., and R. M. Kennedy, On the formation of whitecaps by a threshold mechanism, 1, Basic formalism, J. Phys. Ocean., 13, 1482–1492, 1983.

Snyder, R. L., L. Smith, and R. M. Kennedy, On the formation of whitecaps by a threshold mechanism, 3, field experiment and comparison with theory, J. Phys. Ocean., 13, 1505–1518, 1983.

Srokosz, M. A., On the probability of wave breaking in deep water, J. Phys. Ocean, 16, 382–385, 1986.

Stokes, G. G., On the theory of oscillatory waves, Mathematics, Physics Papers, 1, Appendix B, Cambridge University Press, 225–228, 1880.

Sylvester, W. B., W. J. Pierson, Jr., and S R. Breitstein, Techniques for evaluating the performance of models of radar backscatter from the ocean surface: suggestions for their development, IGARSS '89 (International Geoscience and Remote Sensing Symposium, Vancouver, Canada) 12th Canadian Symposium on Remote Sensing Proceedings, 5, 2991–2996, (IEEE No. 89CH2768–0), 1989.

Thorpe, S. A. and P. N. Humphries, Bubbles and breaking waves, Nature, 283, 463–465, 1980.

Toba, Y., Local balance in the air–sea boundary processes, 1, On the growth process of wind waves, J. Oceanogr. Soc. Japan, 28, 109–121, 1972.

Toba, Y. and H. Kunishi, Breaking of wind waves an the sea surface wind stress, J. Oceanogr. Soc. Japan, 26, 71–80, 1970.

Toba, Y. and M. Chaen, Quantitative expression of the breaking of wind waves on the sea surface, Rec. of Oceanogr. Works Japan, 12(1), 1973.

Toba, Y., M. Tokuda, K. Okuda, S. Kawai, Forced convection accompanying wind waves, J. Oceanogr. Soc. Japan, 31, 192–198, 1975.

Trizna, D. B., A model for Doppler peak spectral shift for low grazing angle sea scatter, IEEE J. Ocean. Eng., OE–10(4), 368–375, 1985.

Valenzuela, G. R., Theories for the interaction of electromagnetic and oceanic waves – A review, Bound–Layer Meteorol., 13, 61–83, 1978.

Valenzuela, G. R. and M. B. Laing, Study of Doppler spectra of radio sea echo, J. Geophys. Res., 75, 551–563, 1970.

Valenzuela, G. R., Theories of interaction of electromagnetic and oceanic waves – A review, Bound–Layer Metreorol., 13, 61–83, 1978.

Van Dorn, W. G. and S. E. Pazan, Laboratory investigations of wave breaking, 2, Deep water waves, Advanced Ocean Eng. Lab. Rep. 71, SIC, 105pp, 1975.

Wetzel, L. 0., On microwave scattering by breaking waves, Wave Dynamics and Radio Probing of the Sea Surface, O. M. Phillips and K. Hasselmann, Eds., Plenum, 1986)

Weissman, M. A., S. S. Atakturk, and K. B. Katsaros, Detection of breaking events in a wind–generated wave field, J. Phys. Ocean., 14, 10, 1984.

Wetz, F. J., S. Peteherych, and L. A. Thomas, A model function for ocean radar cross sections at 14.6 GHz, J. Geophys. Res., 89(C3), 3689–3704, 1984.

Wright, J. W., Backscattering from capillary waves with application to sea clutter, IEEE Trans. Antennas and Propagation, AP–14, 749–754, 1966.

Wright, J. W., A new model for sea clutter, IEEE Trans., AP–16, 217–223, 1968.

Wright, J. W. and W. C. Keller, Doppler spectra in microwave scattering from wind waves, Phys. Fluids, 14, 466–474, 1971.

Wright, J. W., W. J. Plant, W. C. Keller, and W. L. Jones, Ocean wave–radar modulation transfer functions from the West Coast Experiment, J. Geophys. Res., 85, 1980.

Wu, J., Wind–induced drift currents, J. Fluid Mech., 68, 1, 49–70, 1975.

Wu, J., Oceanic whitecaps and sea state, J. Phys. Ocean., 9, 1064–1068, 1979.

Wu, J., Variations of whitecap coverage with wind stress and water temperature, J. Phys. Ocean., 18, 1448–1453, 1988.

Wu, J. Reply, J. Phys. Ocean., 19, 710–711, 1989.

Zrnic, D. S., Spectral moment estimates from correlated pulse pairs, IEEE Trans. Aero. and Elect. Sys., AES–13(4), 344–354, 1977.

APPENDIX A: <u>Calibration Procedure</u>

This appendix gives details of the procedure used to calibrate the scatterometer for the SAXON experiment. Section A.1 is a brief discussion of the radar equation. The illumination integral for an area extensive target is developed in section A.2. Finally, the details of the calibration are outlined in section A.3. The development of the radar equation and the resulting illumination integral follows Ulaby, Moore, and Fung, (1982).

A.1   <u>Radar Equation</u>

The general form of the bistatic radar equation appropriate for both point and area targets expresses the received power, P_r, in terms of known system parameters and the radar cross–section $\sigma(R, \theta)$:

$$P_r = \frac{P_t \; G^2 \; \lambda^2}{(4\pi)^3 \; R^4} \; \sigma_{ij}(R, \; \theta), \qquad\qquad (A.1)$$

where P_t is the transmitted power, G is the antenna gain function, λ is the electromagnetic wavelength, R is the range, θ is the incidence angle, and the subscripts i and j indicate the polarization of the transmitted and received polarization, respectively. For convenience, the notation indicating the dependence of σ on the independent variables R, and θ will not be continued but remains implied. A summary of the derivation of equation (A.1) can be found in Jessup (1988).

When the illumination area, A_i, contains a large number of point scatters of comparable magnitude, the radar scattering coefficient or normalized radar

cross–section, σ^0, is defined by the time averaged, area–extensive form of the radar equation

$$\overline{P}_r = \frac{\lambda^2}{(4\pi)^3} \int_{A_i} \frac{P_t \ G^2 \ \sigma^0}{R^4} \ dA, \qquad (A.2)$$

where the integral is performed over the illumination are A_i. For a homogeneous sea surface and a narrow beamwidth system at moderate incidence angles, the transmitted power P_t, scattering coefficient σ^0, and range R are not expected to vary significantly over the illumination area and the radar equation becomes

$$\overline{P}_r = \frac{\lambda^4 \ P_t \ \sigma^0}{(4\pi)^3 \ R^4} \int_{A_i} G^2 \ dA. \qquad (A.3)$$

The average microwave return from the sea surface is characterized by the normalized radar cross–section σ^0, a dimensionless quantity defined by (A.2). In order to obtain a calibrated measure of the normalized radar cross–section, σ^0, the integral in equation (A.3) must be evaluated for the particular characteristics of the radar in use. When the assumptions that lead to equation (A.3) are valid and the integration performed, the radar equation can be inverted to express the normalized radar cross–section in terms of the received power and known system parameters as:

$$\sigma^0 = \frac{(4\pi)^3 R^4}{\lambda^2} \left[\frac{P_r}{P_t} \right] \frac{1}{\int_{A_i} G^2} \qquad (A.4)$$

A.2 Gaussian Illumination Integral

In practice, the remaining integral, referred to as an illumination integral, may be represented by a weighted area A_w given by

$$G_0^2 \, A_w = \int_{A_i} G^2 \, dA, \qquad (A.5)$$

where , $G = G_0 g(\theta,\varphi)$, G_0 is the maximum antenna gain, and the local coordinates θ and φ are relative to the antenna axis. This formulation is easily extended to include two-antenna systems by the substitution $G^2 = G_1 G_2$.

A common approximation for A_w is to use the area corresponding to the two-way, 3-dB illumination beamwidth. A more accurate estimate of A_w may be obtained by approximating the antenna pattern by an integrable function such as a Gaussian or sinc function. If the exact pattern in known, the most accurate method is to compute the integral numerically.

Due to the uncertainty inherent in the procedure employed to calibrate the scatterometer used in the SAXON experiment, numerical integration of equation (A.4) is unwarranted. However, to avoid the errors associated with simply using the area corresponding to the 3-dB beamwidth, A_w has been approximated by assuming that the beampattern of the individual antennas used is adequately approximated by a Gaussian function in spherical coordinates (r,θ,φ) of the form

$$G(\theta,\varphi) = G_0 \, g(\theta,\varphi), \qquad (A.6)$$

with

$$g(\theta,\varphi) = e^{-(\theta^2/\theta_0^2)} \qquad (A.7)$$

where θ is the angle measured from the antenna axis, φ is the azimuthal angle, and θ_0 is the one–way, e–folding value of θ determined from the antenna beampattern. As indicated in equation (A.7), the beampattern is assumed to be azimuthally symmetric. For the case of two antennas with different beam patterns, equation (A.5) becomes

$$A_w = \frac{1}{G_0^2} \int_{\cdot,i} g_1 \, g_2 \, dA \qquad (A.8)$$

with $G_0^2 = G_1 G_2$. For convenience, the product of the Gaussian functions g_1 and g_2 may be written as

$$g_0^2(\theta) = g_1 \, g_2 = e^{-2(\theta^2/\theta_0^2)}, \qquad (A.9)$$

where

$$\theta_0^2 = 2\,\frac{\theta_1^2 \, \theta_2^2}{\theta_1^2 + \theta_2^2} \qquad (A.10)$$

is now the effective one–way e–folding value of θ for the combined antenna system.

In spherical coordinates and for normal incidence, the integral in equation (A.8) becomes

$$A_w = \int_\theta \int_\varphi g^2(\theta) \, r \, \sin\theta \, d\varphi \, d\theta \qquad (A.11)$$

For a narrow beam system at long range, most of the contribution of the integral comes from a small range of θ for which

$$\sin\theta \approx \theta$$

and over which the distance r is approximately constant and given by

$$r \approx R.$$

The integral in equation (A.11) then reduces to

$$A_w \cong 2\pi R^2 \int_0^\pi \theta \, e^{-2(\theta^2/\theta_0^2)} \, d\theta \qquad (A.12)$$

Furthermore, since most of the contribution to the integral is for θ near 0, the upper limit may be replace by infinity, which results in the analytical solution

$$A_w = \frac{\pi}{2} R^2 \, \theta_0^2 \qquad (A.13)$$

For measurements off nadir, the illumination area increases by $(\cos\theta_i)^{-1}$, where

θ_i is the incidence angle. Then the general form of the weighted area A_w for a Gaussian beampattern is

$$A_w \approx \frac{\pi \, R^2 \, \theta_0^2}{2 \, \cos\theta_i}. \qquad (A.14)$$

From equation (A.10), we have that $\theta_0 = 2.0^{\circ}$ since from equation (A.7) we have $\theta_1 = 4.0^{\circ}$ for the 20cm horn (3–dB beamwidth of 6.7°) and $\theta_2 = 1.5^{\circ}$. For the SAXON measurements at an incidence angle of $\theta_i = 45^{\circ}$ and a range of R=36.4m, equation (A.14) yields $A_w = 3.61m^2$ ($5.6 dB m^2$). (Note that this value is approximately 1.7dB greater than the value of $2.47m^2$ which is the area of the elliptical area corresponding to the two–way 3–dB beamwidth.)

A.3 Calibration

The scatterometer was calibrated in an open area of a warehouse at the US Naval Research Laboratory, Washington, DC, in August, 1988. Since the scatterometer is an AC coupled device, a moving target was used to obtain a calibration signal. The target used was an aluminum sphere with diameter D=20cm, suspended on nylon line from the ceiling, at a horizontal range of 34m. Panels of microwave absorber material (Ecosorb VHP–2) were placed behind the target area to reduce the effect of reflections from background objects. The radar cross–section, σ (m^2), for a perfectly conducting sphere of diameter D is given by its cross–sectional area (Ulaby et al, 1982):

$$\sigma = \frac{\pi \, D^2}{4} \qquad (A.15)$$

A convenient method for manipulating the radar equation, (A.1), is to express it in terms of of decibels (dB). Strictly speaking, the unit of decibels expresses the ratio of two quantities of power, often the ratio of the quantity of interest, say P, to a reference power, P_o:

$$dB = 10 \log \left[\frac{P}{P_o} \right] \qquad (A.16)$$

Since power is proportional to voltage squared, an equivalent formulation in terms of voltage is given by

$$dB = 20 \log \left[\frac{V}{V_o} \right] \qquad (A.17)$$

Formally, the decibel is a dimensionless unit since it is proportional to the logarithm of the ratio of two quantities. A useful extension of the definition of the decibel is to use the particular unit of measure of a given quantity as the denominator in the ratio. For example, the dimensional quantity 100mW (mW=milliwatts) is expressed in decibels as 20 dB re mW, or more succinctly, 20dBmW Furthermore, any quantity which is a multiplier or divisor of power in an equation (such as the radar equation) can be expressed and manipulated in dB using equation (A.16).

The received power, P_r, in equation (A.1) is the power at the output port of the receiving antenna. For the calibration measurements of a 20cm diameter sphere made at a range of 34m, the known parameters of the radar

equation, (A.1), are:

$$(4\pi)^3 \qquad\qquad\qquad = 33.0\text{dB}$$

$$\sigma \quad = \quad \pi(0.1\text{m})^2 \quad = -15.0\text{dBm}^2$$

$$\lambda^2 \quad = \quad (.0214\text{m})^2 \quad = -33.4\text{dBm}^2$$

$$R^4 \quad = \quad (34\text{m})^4 \quad = 61.3\text{dBm}^2$$

$$G_1(\text{horn}) \qquad\qquad = 27.8\text{dB}$$

$$G_2(\text{parabola}) \qquad\quad = 37.0\text{dB}$$

$$P_t^v \quad = \quad 91.2\text{mW} \quad = 19.6\text{dBmW}$$

$$P_t^h \quad = \quad 100.0\text{mW} \quad = 20.0\text{dBmW}$$

The radar equation (A.1), with all quantities expressed in dB, becomes

$$P_r = P_t \; \frac{(27.8\text{dB})(37\text{dB})(-33.4\text{dBm}^2)(-15\text{dBm}^2)}{(33\text{dB})\,(61.3\text{dBm}^4)}, \qquad (A.18)$$

where multiplication implies addition and division implies subtraction.

Then the received power, P_r^i, is given in terms of the transmitted power P_t^i by

$$P_r^i \;(\text{dBmW}) \;=\; P_t^i \;(\text{dBmW}) \;\; - 77.9\text{dB}, \qquad (A.19)$$

where the superscript i denotes vertical or horizontal polarization.

The received power, P_r^i, is amplified by the net system gain, G_s^i, to produce the receiver output power, P_{out}^i, given by:

$$P_{out}^i \;(\text{dBmW}) \;=\; P_r^i \;(\text{dBmW}) \;+\; G_s^i \;(\text{dB}) \qquad (A.20)$$

The purpose of the calibration is to determine the system gain G_s^i using a

target of known radar cross–section.

Measurements of the receiver output were made over a range of power levels by attenuating the transmitted power in steps of 10dB. The sphere was set in motion and V_{p-p}, peak–to–peak voltage, was read from an oscilloscope. The average of two measurements made in this manner were used as the calibration value. The time–averaged output power for a sinusoidal signal is related to the RMS output voltage by

$$<P_{out}> \; = \; V^2_{rms}/R, \qquad\qquad (A.21)$$

where the brackets indicate the time average and R=50Ω is the output impedance of the receiver. A more convenient form of (A.20) expresses the power in mW in terms of V_{p-p} in volts for a 50Ω system as

$$<P>, \; (mW) \; = \; \frac{V^2_{p-p}}{0.40}, \; (V_{p-p} \text{ in volts}) \qquad (A.22)$$

which follows from $V^2_{p-p} = 8V^2_{rms}$ for sinusoidal signals. Tables A.1 and A.2 summarize the measurements and the calculated system gains for VV and HH polarization, respectively. The data are plotted in Figure A.1 as P^i_{out} versus P^i_t.

SAXON CALIBRATION: 8−88
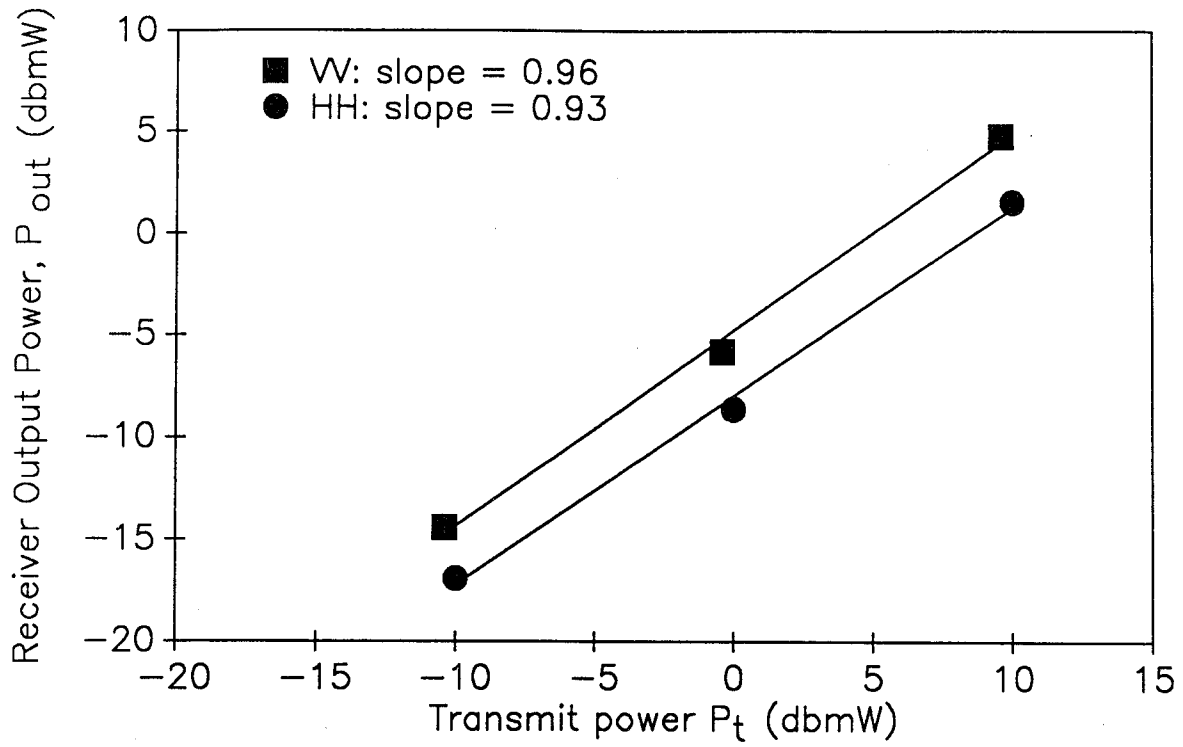
Figure A.1: Calibration curves for VV and HH polarization.

Table A.1: <u>VV Calibration Measurements</u>

Atten. (dB)	P_t (dBmW)	V_{P-P} (volts)	P_{out} (dBmW)	G_s (dB)
10	9.6	1.1	4.8	73.1
20	−0.4	0.33	−5.8	72.5
30	−10.4	0.12	−14.4	73.9

Table A.2: <u>HH Calibration Measurements</u>

Atten. (dB)	P_t (dBmW)	V_{P-P} (volts)	P_{out} (dBmW)	G_s (dB)
10	10.0	0.76	1.6	69.5
20	0.0	0.24	−8.6	69.3
30	−10.0	0.09	−16.9	71.0

The average values of the system gains from Table A.1 and A.2 are G_s^v=73.2dB and G_s^h=70.0dB for VV and HH polarization, respectively. The difference of 3.2dB between the average system gains for VV and HH polarization is not consistent with previous experience using scatterometers of similar design. Since the component of the VV and HH channels of the receiver are identical, the net system gains should be nearly the same for the same transmitted power. In this scatterometer, the transmitted power for horizontal polarization is 0.4dB greater than that of VV polarization. With a larger transmitted power and identical receiver components, the net gain for HH would be expected to be greater than that for VV, not vice versa, as was found for the calibration measurements summarized in Tables A.1 and A.2. Unfortunately, this inconsistency was not realized until after the calibration had been completed. Thus, the accuracy of the gain for the VV and/or HH channels is called into question.

A further indication that an error was made during the SAXON

calibration is the comparison between the measurements of mean radar cross-section, σ^0, from SAXON and those from the North Sea. The scatterometer used in the North Sea was calibrated in situ using a swinging sphere suspended from a crane mounted on the tower. A calibration measurement was obtained for the VV polarization channel only. The HH polarization measurements were calibrated by assuming/that the net system gain for the VV and HH channels was identical. The σ^0_{HH} values from SAXON using the average system gain from Table A.2 agree within a few tenths of a dB with the North Sea measurements. However, the σ^0_{VV} measurements using the average system gain from Table A.1 fall approximately 1.7dB below those from the North Sea.

The fact that the σ^0_{HH} measurements for SAXON and the North Sea are nearly the same indicates that the HH calibration values for SAXON may be valid. Furthermore, the fact that the σ^0_{VV} values for SAXON are lower than those from the North Sea is consistent with G^v_s for SAXON being too high (see equation A.9). If we assume that the VV system gain should be lowered by the difference of 1.7dB between the σ^0_{VV} measurements from the North Sea and SAXON, then the adjusted VV net system gain would be G^v_s=71.5dB. The difference of 1.5dB between this value and G^h_s computed from Table A.2 is a more reasonable difference to expect between the two receiver channels of identical components.

Based on the available information, the net system gain for HH polarization computed from the SAXON calibration is judge to be valid. The net system gain for VV polarization is discarded as being corrupted. Based on comparisons with the North Sea measurements, the adjusted system gain of

G_s^v=71.5 for VV polarization is used for SAXON.

The assumptions used to arrive at an adjusted VV gain increase the uncertainty associated with the accuracy of the VV polarization measurement. Furthermore, the difference on the order of 0.5–1.0dB expected between the SAXON and North Sea data due to the different range of the look–direction angle relative the wind has been ignored. The calibration uncertainty may be especially important when considering the polarization ratio $\sigma_{VV}^o/\sigma_{HH}^o$. Therefore, the results in this thesis concerning the polarization ratio have been interpreted cautiously.

The problems associated with the calibration technique used in the SAXON experiment have led to significant improvements in subsequent calibrations. A switch to change the scatterometer from an AC coupled device to a DC coupled device has been added to the audio circuit in the IF unit. By making the calibration with the scatterometer DC coupled, an improved method using a variety of corner reflectors of different sizes is possible. The corner reflector is placed on a dolly which is slowly moved along the antenna axis in order to remove the effect of background clutter. The in–phase (I) and quadrature (Q) outputs of the receiver are connected to the inputs of a 2 channel oscilloscope operating in x–y mode. Microwave absorber material is placed behind the target area to reduce background clutter from stationary objects.

The remaining return from stationary objects appears as a relatively small, constant offset on the oscilloscope. As the target is moved slowly in the line along the antenna look–direction, the resultant of the return from the corner reflector appears as a vector rotating about the constant offset vector of

the background clutter. The amplitude of the return due to the moving corner reflector can be read off the oscilloscope as the radius of the circle centered about the offset due to the clutter. This technique has been used several times since the SAXON experiment and is superior in terms of repeatability and reduction of contaminating effects of the surroundings.

A formula expressing the normalized radar cross–section, σ^o, in terms of the receiver output voltage, V_{out}, is derived from the approximation for the area–extensive form of the radar equation written as

$$P_r^i \approx \frac{P_t^i \ G_1 G_2 \ \lambda^2 \ A_w}{(4\pi)^3 \ R^4} \sigma_{ii}^o, \tag{A.23}$$

from equations (A.4) and (A.5). For convenience, let C denote the constant quantity

$$C = \frac{G_1 G_2 \ \lambda^2 \ A_w}{(4\pi)^3 \ R^4} = -58.4 \ dB. \tag{A.24}$$

Then equation (A.20) becomes

$$P_{out}^i(dBmW) = P_t^i(dBmW) + C(dB) + \sigma_{ii}^o(dB) + G_s^i(dB) \tag{A.25}$$

For the field measurements, the RG58 coaxial cable between the RF unit and the IF unit was 100' instead of the 75' used in the calibration setup. Since the attenuation for RG58 for a frequency of 60MHz is approximately 4dB/100', the net system gains for the field measurements are reduced by 1dB to

G_s^v=70.5dB and G_s^h=68.9dB. Also note that equation (A.25) can be converted from dBmW to dBW by subtracting 30dB from the left hand side. Then the receiver output power in <u>Watts</u> for VV polarization is given by

$$P_{out}^v \text{ (watts)} = 1.48\sigma_{VV}^o \qquad (A.26)$$

and for HH polarization by,

$$P_{out}^h \text{ (watts)} = 1.12\sigma_{HH}^o \qquad (A.27)$$

The receiver output power is given in terms of the output voltage as

$$P_{out} = V_{out}^2/R, \qquad (A.28)$$

where R is the output impedance of R=50Ω. By combining equations (A.27) and (A.28), we have the final result expressing the output voltage (in volts) in terms of the normalize radar cross-section:

$$(V_{out})_{VV}^2 = 74.0\sigma_{VV}^o \qquad (A.29)$$

$$(V_{out})_{HH}^2 = 56.0\sigma_{HH}^o. \qquad (A.30)$$

A.4 <u>IMAGE REJECTION</u>

This treatment of image rejection follows that of Doviak and Zrnic (1984). As mentioned in Chapter 3, section 3.1.1, an image spectrum can result from amplitude and phase imbalances between the in-phase (I) and

quadrature (Q) channel. In practice, the amplitude imbalance is less problematic, since its effect can be offset relatively easily in processing. The phase imbalance, however, can significantly affect the Doppler spectrum. The error is most consequential in the computation of the second spectral moment corresponding to the bandwidth. The quadrature hybrid device in the IF unit (see Figure 3.10) which does the phase shifting can introduce a phase imbalance. In the SAXON experiment, an additional phase imbalance was caused by the use of a sequentially sampling analog–to–digital converter. The use of a simultaneous sample and hold converter essentially eliminates this second source of phase imbalance.

The image effect is easily demonstrate by considering an individual term in the Fourier series expansion of a complex signal which is balanced in amplitude and phase:

$$A_i \, e^{j(\omega_i t + \theta_i)}, \tag{A.30}$$

where A_i is the ith coefficient and θ_i is its phase. If the gains of the I and Q channels are G_I and G_Q, respectively, and the Q channel is shifted by $\pm\Delta$ relative to the I channel, then equation (A.30) becomes

$$A_i K \, \cos(\omega_i t + \theta_i) \; + \; jA_i \sin(\omega_i t + \theta_i \pm \Delta) \; =$$

$$\tfrac{1}{2}A_i(K + e^{\pm j\Delta})e^{j(\omega_i t + \theta_i)} \; + \; \tfrac{1}{2}A_i(K - e^{\mp j\Delta})e^{-j(\omega_i t + \theta_i)} \tag{A.31}$$

where $K = G_I/G_Q$ is the ratio of the I and Q channel gains. The first term on the right of (A.31) corresponds to the original signal at frequency ω_i with

amplitude A_i in (A.30) modified in amplitude and phase. The second term on the right of (A.31) is the image signal at frequency ω_i. The ratio of the squared magnitude of the two terms on the right of (A.31) is defined as the image suppression, L:

$$|(K+e^{\pm j\Delta})| \; / \; |(K-e^{\mp j\Delta})|. \tag{A.32}$$

Figure A.2 shows the image suppression L as a function of both amplitude and phase imbalance (Doviak and Zrnic, 1984).

Because of the added phase error due to the sequential sampling mentioned above, the image suppression for the SAXON experiment was significantly dependent on frequency. The scatterometer was tuned to optimize the image suppression over the frequency range of interest by adjusting the line length between the quadrature hybrid device and the IF mixers (see Figure 3.10). Figure A.3 shows the image suppression computed from the output of the IF unit for sinusoidal test signals over a range of frequencies for both the VV and HH channels. The image suppression is generally better than 20dB over the frequency range of 0 to 400Hz. The experience with the scatterometer in the SAXON experiment has led to the use of simultaneous sample and hold converters. This improvement eliminates a large part of the dependence of the image suppression on frequency, resulting in image suppression better than 40dB over a 1kHz bandwidth.
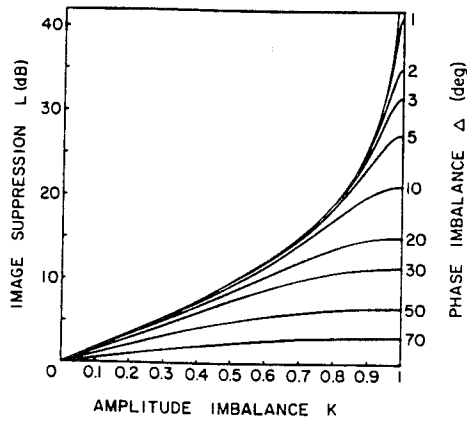
Figure A.2: Image suppression L as a function of amplitude and phase imbalance (from Doviak and Zrnic, 1984).
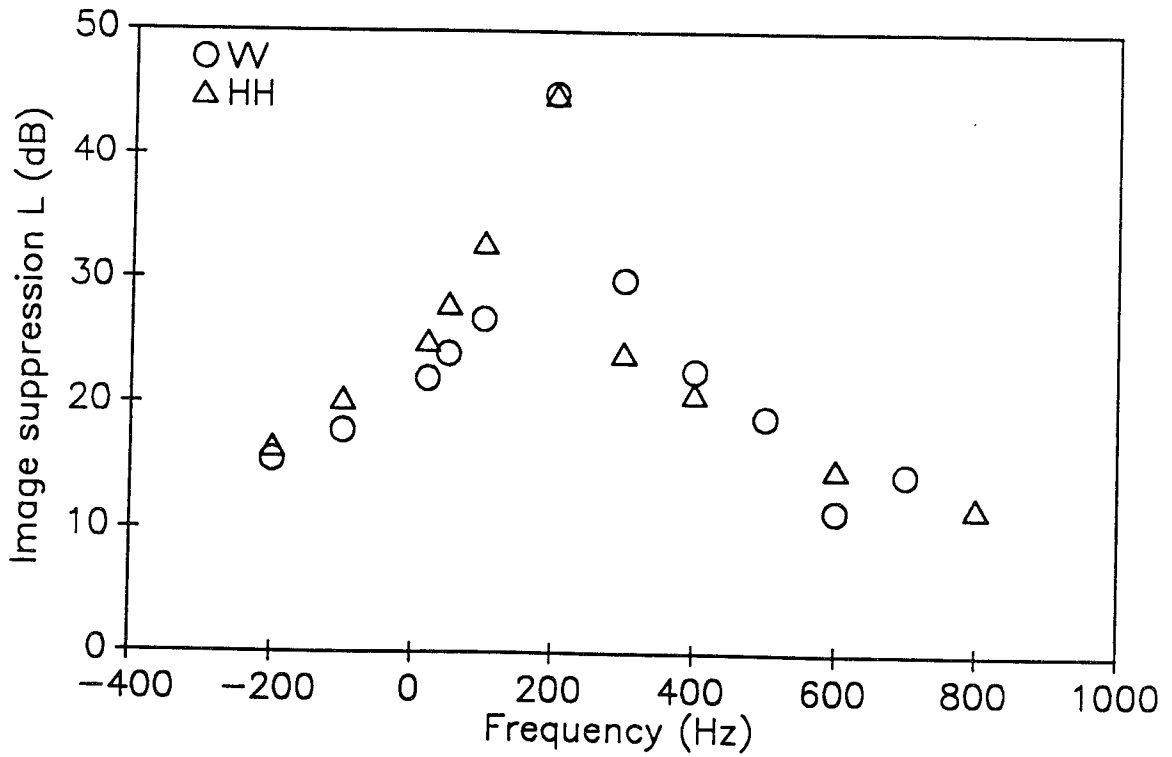
Figure A.3: Calibration of image rejection for SAXON scatterometer, 5–11–88.

APPENDIX B: <u>Bulk Method Formulation for Friction Velocity u_*</u>

The following description of the bulk aerodynamic method for computing friction velocity, u_*, and the wind speed reference to height $z=10m$, U_{10}, is based on the formulation given by Large and Pond (1981).

The transfer of momentum and heat across the air-sea interface due to the wind is described by the Reynolds fluxes:

Momentum flux:
$$\tau = -\rho <u'w'> \tag{B.1}$$

Sensible heat flux:
$$H_s = \rho \, C_p <w'T'>, \tag{B.2}$$

where ρ is the air density, C_p is the specific heat at constant pressure, u' and w' represent the fluctuating part of the horizontal and vertical velocities, respectively, T' is the fluctuating part of the air temperature at the surface, and the brackets indicate the ensemble average.

The friction velocity, u_*, is a velocity scale related to the momentum flux or shear stress, τ, at the surface by

$$\tau = \rho \, u_*^2. \tag{B.3}$$

Under conditions of neutral stability, the mean wind speed at height z, U_z, is well represented by the logarithmic expression

$$U_z = \frac{u_*}{\kappa} \ln(z/z_0), \tag{B.4}$$

where $\kappa=0.40$ is von Karman's constant and z_0 is a length scale corresponding to the surface roughness. The roughness length z_0 can be represented by the sum $z_0=z_s+z_c$, where z_s, a smooth surface contribution, and z_c, that due to form drag, are given by

$$z_s = \frac{0.11\ \nu}{u_*} \tag{B.5}$$

$$z_c = \frac{a\ u_*}{g}, \tag{B.6}$$

where ν is the viscosity of air, g is the gravitational acceleration, and a is an empirical constant. Accepted values of the 'constant' a include a=0.011 for deep water and values in the range $0.017{\leq}a{\leq}0.0185$ for shallow water (see Smith, 1988).

For conditions other than neutral, stability effects are accounted for by using the more general expression

$$U_z = \frac{u_*}{\kappa}\ \{\ \ln(z/z_0) - \Psi(z/L)\ \}. \tag{B.7}$$

The Monin–Obukov length scale L is given by

$$L = -\ \frac{u_*^3\ T_0}{\kappa g <wT_v>}, \tag{B.8}$$

where T_v and T_0 are the virtual temperature and its local average, respectively.

The definition of the Monin–Obukov length is such that $L > 0$ for stable conditions and $L < 0$ for unstable conditions. For stable conditions, $z/L > 0$, the function $\Psi_m(z/L)$ is given by

$$\Psi_m(z/L) = -5(z/L), \qquad\qquad (B.9)$$

for unstable conditions, $z/L < 0$, by

$$\Psi_m(z/L) = 2\ln[(1+X)/2 + \ln[(1+X^2)/2] - 2\tan^{-1}X + \pi/2 \qquad (B.10)$$

where $X = \{1 - 16(z/L)\}^{\frac{1}{4}}$, and for neutral conditions, $z/L = 0$,

$$\Psi_m(z/L) = 0. \qquad\qquad (B.11)$$

Estimates of the friction velocity, u_*, can be made from standard meteorological measurements by formulating the Reynold's fluxes as

$$- <u'w'> = C_D \, U_z^2 \qquad\qquad (B.12)$$

$$<w'T'> = C_T \, U_z \, \Delta\theta \qquad\qquad (B.13)$$

$$<w'Q'> = C_E \, U_z \, \Delta Q \qquad\qquad (B.14)$$

where θ is the potential temperature, Q is the humidity, C_D is the drag coefficient, C_T is the Stanton number, and C_E is the Dalton number. The potential air–sea temperature difference, $\Delta\theta$, is given in terms of the sea temperature T_s and the potential temperature at height z, θ_z, as

$$\Delta\theta \;=\; T_s \;-\; \theta_z. \tag{B.15}$$

The humidity difference, ΔQ, is given in terms of the absolute humidity Q_z at height z and the absolute humidity at the surface Q_s as

$$\Delta Q \;=\; Q_s \;-\; Q_z. \tag{B.16}$$

The air temperature at height z, T_z, and the air–sea temperature difference ΔT are given by

$$T_z \;=\; \theta_z \;-\; \gamma z \tag{B.17}$$

$$\Delta T \;=\; \Delta\theta \;+\; \gamma z \tag{B.18}$$

where γ is the adiabatic lapse rate, $\gamma=0.01 \mathrm{Km^{-1}}$.

A computational form of the stability parameter z/L is required in terms of the air temperature T_z and relative humidity H_R. According to Large and Pond (1981), the average virtual temperature T_v over temperate seas is approximately

$$T_o \;\simeq\; T_z \;+\; 1.72\mathrm{x}10^{-6} \; T_z^2 \; Q_z. \tag{B.19}$$

The absolute humidity Q_z is computed from

$$Q_z \;=\; H_R \; Q_{sat}(T_z), \tag{B.20}$$

where $Q_{sat}(T)$ is the saturation humidity given by

$$Q_{sat}(T) = 6.4038 \times 10^8 \exp(- 5107.4/T). \qquad (B.21)$$

The absolute surface humidity Q_s is computed by assuming 98% saturation at the surface so that

$$Q_s = 0.98 \ Q_{sat}(T_s). \qquad (B.22)$$

Expanding $<w'T_v>$ in equation (B.8) and using the bulk formulation for $<w'T'>$ leads to

$$z/L \cong - \frac{\kappa z g C_T U_z \Delta\theta}{u_*^3 \ T_o} \left[1 + 1.7 \times 10^{-6} \ T_o \ \frac{\Delta Q}{\Delta\theta} \right], \qquad (B.23)$$

where $C_T \approx 1 \times 10^{-3}$ for unstable conditions and $C_T \approx 0.86 \times 10^{-3}$ for stable conditions.

Using the above formulation, the friction velocity, u_*, and wind speed at height z, U_z, can be iteratively computed, except under extremely stable conditions (see Smith, 1988). The logarithmic profile given by equation (B.7) can now be formulated in terms of bulk measurement of wind speed at height z, air and sea temperature, and relative humidity. The resulting non-linear equation for u^* may be evaluated by iteration until a specified minimum estimation error is reached. The Fortran computer program CALUST in Appendix F uses Newton's iterative method and an error criterion that the difference between successive

estimates is less than 0.1%. The initial guess for u_* was computed by using a drag coefficient C_D in equation (B.12) from the formula for the neutral drag coefficient suggested by Geernaert, Larsen, and Hansen (1987) given by

$$1000C_{DN}=0.0847U_z + 0.577 \qquad \text{(B.24)}$$

For the SAXON experiment, measurements of wind speed and direction, air and sea temperature, and relative humidity were processed in real–time to produce average values at 10 minute intervals. The anemometer, air temperature sensor, and relative humidity probe were mounted at a height of approximately 42m above the sea surface, while the sea temperature sensor was tethered from a float to remain approximately 1m below the sea surface. Values of friction velocity, u_*, and wind speed referenced to a height of 10m, U_{10}, were iteratively computed using the 10 minute averages of wind speed, air–sea temperature difference, and relative humidity. The value of the parameter a in equation (B.6) of a=0.0185 suggested by Wu(1980) was chosen as being consistent with the limited fetch and shallow water depth at the Chesapeake Light Tower. The computed results were further averaged to produce average values of u_* and U_{10} corresponding to the 1–hour measurement periods of interest.

Appendix C: <u>Covariance Processing Formulas</u>

The continuous–time formulation for covariance–based spectral moment estimation is given in Chapter 3, section 3.2.2. In this brief appendix, the discrete–time equations used in the SAXON data processing are given. The covariance processing technique is based on the autocorrelation function $R(\tau)$ evaluated at lag $\tau = \Delta t$, where Δt is the time between samples. Consider a complex sequence $z(m)$ of M uniformly spaced samples:

$$z(m) = x(m) + iy(m), \tag{C.1}$$

where $x = Re(z)$ and $y = Im(z)$. An estimate of the autocorrelation function $R(\Delta t)$ is given by

$$\hat{R}(\Delta t) = \frac{1}{M} \sum z^*(m) \, z(m+1), \tag{C.2}$$

where (*) indicates the complex conjugate. The summations in equation (C.2) and all subsequent appearances in this appendix are from $m=1$ to $m=M-1$.

The sample pairs used in equation (C.2) are not required to be uniformly spaced. First moment estimates using an intra pair spacing, T_P, which is significantly larger than the time between samples have been used to recover aliased mean velocities (Doviak and Zrnic, 1984). Under circumstances of large signal–to–noise ratio, the variance of the first moment estimator is reduced by using staggered sample pairs in equation (C.2) (Zrnic, 1977). For this reason, the autocorrelation estimate used in the SAXON experiment was

based on a sample pair spacing of $\Delta t/T_P = 0.25s$.

From equation (3.19), the mean frequency based on the first moment estimator is given by

$$\hat{f} = \frac{1}{2\pi \; \Delta t} \; \tan^{-1}\left\{\frac{\sum \mathrm{Im}\{z^*(m) \; z(m+1)\}}{\sum \mathrm{Re}\{z^*(m) \; z(m+1)\}}\right\} \qquad (C.3)$$

The second moment estimator is based on the normalized covariance or correlation coefficient $\rho(\tau)$ evaluated at lag $\tau = \Delta t$. The correlation coefficient is equal to the autocovariance normalized by the total power, S. An estimate of $\rho(\Delta t)$ is

$$\hat{\rho}(\Delta t) = \frac{\hat{R}(\Delta t)}{\hat{S}}. \qquad (C.4)$$

and the estimate of the total power, $\hat{S}$, is

$$\hat{S} = \hat{R}(0) - \hat{N}, \qquad (C.5)$$

where $\hat{N}$ is the noise power estimate. Then the second moment estimator, from equation (3.21), is given by

$$\hat{B} = \frac{1}{\sqrt{2}\pi \; \Delta t} \; \ln\left|\left[\frac{\hat{S}}{|\hat{R}(\Delta t)|}\right]^{\frac{1}{2}}\right|, \qquad (C.6)$$

where $|\hat{R}(\Delta t)|$ is given explicitly by

$$|\hat{R}(\Delta t)| = \left\{ \left| \sum \mathrm{Re}\{z^*(m)z(m{+}1)\} \right|^2 + \left| \sum \{\mathrm{Im}(z^*(m)z(m{+}1))\} \right|^2 \right\}^{\frac{1}{2}}. \quad (C.7)$$

The above formulas are used in the Fortran program RTRAD, listed in Appendix F, which performed the real–time data acquisition and processing during the SAXON experiment.

Appendix D: Processed Results

The data used to produce the results presented in Chapter 5 are given in this appendix. The data are presented in tabulated form as a portion of the output from the Fortran computer programs SXBCHAR3 (schemes 1, 2, and 3) and SXBCHAR4 (scheme 4) listed in Appendix F. The following key lists the meaning of the column headers for Tables D.1–D.4, corresponding to detection schemes 1–4 (see Chapter 4, section 4.5). These data are for an integration time of $T_i=0.25s$ (see Chapter 3, section 3.2.1).

KEY TO PROCESSED DATA

Scheme: Detection scheme for this table: (1) $\sigma^o_{pk} \geq \sigma^o_{pol}=0.30$, (2) $\sigma^o_{pk} \geq 0.25$, (3)$B_{max} \geq 50Hz$, (4) $\sigma^o_{pk} \geq 0.25$ and/or $B_{max} \geq 50Hz$ (sec. 4.5)

No: Run identification number
file: File number identifying 1–hour record
brk: Number of events detected in record
pct: P_{ss}, percentage of crests producing detected events (sec. 5.5)
u10: Wind speed (ms^{-1}), 10m elevation based on u* (below) (App. B)
ustar: Friction velocity (ms^{-1}), bulk formulation (App. B)
uoc: Ratio of u10 (above) to phase speed corresponding to fpk (below)
fpk: Frequency (Hz) peak of surface displacement spectrum (Fig. 3.23b–3.29b)
m(4): $(m_4g^{-2})^{0.5}$dimensionless square root of 4th moment of E(f), $f_{cut}=0.5Hz$ (eq.1.19, 3.5)
L: Wavelength (m) given by fpk (above) in dispersion relation eq. (5.7)
vv0: σ^o_{vv} (linear), mean normalized VV radar cross–section (App. A)
hh0: σ^o_{hh} (linear), mean normalized HH radar cross–section (App. A)
prb: Average polarization ratio of detected events
fdb: Average max mean Doppler frequency (Hz) of detected events (eq. 5.9)
bwb: Average max Doppler bandwidth (Hz) for detected events
bwn: Normalized Doppler bandwidth for detected events (see eq. 5.11)
vss1: σ^o_{ssvv1} (dB), contribution to σ^o_{vv}, method 1 (eq. 2.2, 2.3, Fig. 2.5a)
vss2: σ^o_{ssvv2} (dB), contribution to σ^o_{vv}, method 2 (eq. 2.2, 2.4, Fig. 2.5b)
hss1: σ^o_{sshh1} (dB), contribution to σ^o_{hh}, method 1 (eq. 2.2, 2.3, Fig. 2.5a)
hss2: σ^o_{sshh2} (dB), contribution to σ^o_{hh}, method 2 (eq. 2.2, 2.4, Fig. 2.5b)

Table D.1: Processed Data for Detection Scheme 1

No-file	brk	pct	u10	ustar	uoc	fpk	m(4)	L	vv0	hh0	prb	fdb	bwb	bwn	vss1	vss2	hss1	hss2
1-0209	14	3.34	8.6	.323	.90	.125	.0814	75	.0468	.0228	.93	153	70	.47	-30.4	-29.4	-29.5	-28.9
1-0215	25	5.61	9.1	.348	.98	.133	.0818	70	.0538	.0256	.99	134	66	.52	-28.8	-27.6	-28.1	-27.3
1-0223	20	4.49	9.6	.374	1.03	.133	.0831	70	.0543	.0253	.96	137	68	.53	-29.4	-28.3	-28.5	-27.9
1-0229	19	4.26	8.8	.337	.94	.133	.0808	70	.0481	.0230	.99	147	75	.54	-29.0	-28.0	-28.3	-27.7
1-0235	18	3.63	8.1	.303	.84	.148	.0800	64	.0430	.0215	.94	138	77	.59	-29.5	-28.6	-28.6	-28.1
1-0241	16	3.23	7.7	.289	.81	.148	.0778	64	.0408	.0198	.97	133	67	.54	-30.2	-29.3	-29.6	-29.0
4-0484	3	.26	8.4	.309	1.84	.346	.0617	13	.0349	.0159	.89	120	74	.62	-38.5	-37.5	-37.5	-37.1
4-0490	7	.67	8.5	.311	1.61	.312	.0700	16	.0370	.0173	.85	115	70	.63	-34.7	-33.7	-33.8	-33.2
4-0496	4	.43	8.4	.311	1.45	.279	.0706	20	.0339	.0159	.84	132	78	.60	-36.4	-35.6	-35.3	-34.9
4-0510	8	.75	8.6	.318	1.69	.318	.0713	15	.0313	.0151	.96	136	71	.55	-33.1	-32.4	-32.4	-31.9
5-0901	5	.56	8.0	.307	1.35	.268	.0682	22	.0391	.0191	.98	93	65	.72	-36.5	-35.7	-35.8	-35.3
5-0907	9	1.07	7.3	.281	1.18	.250	.0717	24	.0329	.0169	.96	108	72	.72	-32.3	-31.7	-31.6	-31.2
5-0913	7	.97	6.9	.263	.93	.216	.0710	34	.0324	.0170	.94	91	52	.59	-34.0	-33.2	-33.4	-33.0
5-0923	14	1.90	7.1	.273	1.01	.220	.0704	31	.0345	.0174	.89	106	62	.61	-30.6	-29.9	-30.1	-29.7
5-0952	11	1.53	6.9	.262	.94	.214	.0723	34	.0330	.0186	1.05	91	54	.68	-32.1	-31.4	-31.6	-31.1
6-1202	59	16.15	10.6	.429	.99	.109	.0886	97	.0784	.0407	1.03	106	60	.63	-24.8	-23.4	-24.3	-23.2
6-1222	44	12.87	10.2	.413	1.03	.102	.0860	97	.0706	.0352	.99	114	65	.63	-25.4	-24.3	-24.6	-23.9
6-1234	27	8.57	8.6	.339	.86	.094	.0796	107	.0509	.0250	.97	123	71	.61	-27.7	-26.8	-27.0	-26.4
9-1421	17	1.97	11.0	.438	1.82	.258	.0813	23	.0630	.0292	1.09	115	68	.64	-29.4	-28.5	-28.9	-28.2
9-1427	21	2.43	10.9	.434	1.80	.258	.0784	23	.0606	.0273	1.13	96	64	.73	-29.4	-28.3	-29.1	-28.3
9-1433	15	1.79	11.6	.468	1.86	.250	.0781	24	.0642	.0295	1.02	103	65	.69	-30.9	-29.7	-30.4	-29.6
9-1445	19	2.08	11.2	.453	1.86	.273	.0834	22	.0598	.0279	1.06	116	65	.60	-29.9	-28.8	-29.3	-28.6
9-1451	10	1.19	10.5	.419	1.69	.250	.0791	24	.0544	.0249	1.01	105	63	.72	-32.5	-31.7	-32.1	-31.5
11-1555	1	.12	6.9	.254	1.11	.250	.0638	24	.0222	.0112	.96	138	72	.53	-42.8	-42.1	-42.0	-41.6
11-1598	8	1.13	8.4	.326	1.16	.211	.0765	34	.0442	.0198	1.01	134	81	.64	-33.0	-32.3	-32.4	-31.9
11-1604	35	4.95	8.5	.333	1.18	.211	.0770	34	.0497	.0283	.99	92	69	.94	-26.7	-25.7	-26.2	-25.4
11-1618	11	1.50	8.3	.325	1.19	.219	.0717	31	.0429	.0196	1.01	118	73	.67	-31.8	-31.0	-31.3	-30.8
11-1626	12	1.70	7.5	.289	1.04	.211	.0709	34	.0341	.0174	.89	105	72	.72	-31.6	-30.8	-30.7	-30.2
11-1651	2	.27	6.9	.262	.98	.219	.0593	31	.0249	.0113	.88	149	72	.52	-39.7	-38.9	-38.7	-38.3
12-1676	30	4.24	10.6	.431	1.47	.211	.0887	34	.0682	.0322	1.02	129	66	.58	-27.1	-25.9	-26.6	-25.9
12-1682	36	5.29	10.9	.444	1.36	.203	.0900	39	.0711	.0343	1.03	125	67	.57	-26.6	-25.3	-25.8	-25.0
12-1696	34	5.20	10.7	.437	1.30	.195	.0872	41	.0684	.0326	1.12	112	65	.60	-27.0	-25.9	-26.8	-26.0
12-1702	41	6.27	10.7	.439	1.31	.195	.0874	41	.0678	.0331	1.05	125	66	.55	-25.3	-24.3	-24.9	-24.2
12-1711	32	3.94	10.4	.426	1.53	.242	.0868	28	.0671	.0319	1.05	119	62	.59	-27.0	-26.0	-26.6	-25.9
12-1717	33	5.24	10.3	.422	1.31	.188	.0868	41	.0692	.0326	1.07	134	72	.57	-26.7	-25.6	-26.4	-25.6
12-1725	22	3.37	10.0	.407	1.22	.195	.0857	41	.0664	.0301	1.01	126	75	.65	-28.4	-27.4	-27.7	-27.0
12-1739	16	2.45	8.6	.341	1.05	.195	.0786	41	.0539	.0238	1.02	122	59	.52	-29.7	-28.8	-29.4	-28.8
12-1754	30	3.70	10.1	.412	1.49	.242	.0845	28	.0663	.0318	.99	119	67	.59	-26.8	-25.8	-26.2	-25.6
12-1760	12	1.43	9.5	.382	1.53	.250	.0812	24	.0570	.0276	1.01	114	68	.66	-31.4	-30.5	-30.8	-30.1
12-1778	29	4.26	9.6	.384	1.20	.203	.0855	39	.0582	.0282	1.04	122	65	.56	-27.3	-26.3	-26.8	-26.1
12-1784	17	2.60	9.2	.366	1.12	.195	.0809	41	.0541	.0257	1.00	114	61	.62	-29.4	-28.5	-29.0	-28.4

Table D.2: Processed Data for Detection Scheme 2

No-file	brk	pct	u10	ustar	uoc	fpk	m(4)	L	vv0	hh0	prb	fdb	bwb	bwn	vss1	vss2	hss1	hss2
1-0209	25	5.97	8.6	.323	.90	.125	.0814	75	.0468	.0228	.99	146	66	.47	-28.8	-27.6	-28.0	-27.3
1-0215	45	10.09	9.1	.348	.98	.133	.0818	70	.0538	.0256	1.05	131	64	.52	-26.8	-25.4	-26.2	-25.2
1-0223	34	7.63	9.6	.374	1.03	.133	.0831	70	.0543	.0253	1.03	136	64	.50	-27.5	-26.3	-26.8	-26.1
1-0229	28	6.28	8.8	.337	.94	.133	.0808	70	.0481	.0230	1.03	137	69	.53	-27.8	-26.7	-27.3	-26.6
1-0235	29	5.85	8.1	.303	.84	.148	.0800	64	.0430	.0215	.96	127	72	.59	-28.0	-27.0	-27.2	-26.6
1-0241	24	4.84	7.7	.289	.81	.148	.0778	64	.0408	.0198	1.00	129	62	.51	-28.7	-27.7	-28.3	-27.7
4-0484	6	.52	8.4	.309	1.84	.346	.0617	13	.0349	.0159	.90	112	72	.65	-35.9	-34.7	-34.9	-34.4
4-0490	12	1.15	8.5	.311	1.61	.312	.0700	16	.0370	.0173	.91	112	73	.67	-32.5	-31.5	-31.8	-31.2
4-0496	6	.64	8.4	.311	1.45	.279	.0706	20	.0339	.0159	.89	128	73	.57	-34.9	-34.1	-34.0	-33.6
4-0510	11	1.03	8.6	.318	1.69	.318	.0713	15	.0313	.0151	.93	128	69	.56	-32.1	-31.4	-31.4	-30.9
5-0901	13	1.45	8.0	.307	1.35	.268	.0682	22	.0391	.0191	.96	89	55	.64	-32.2	-31.3	-31.6	-31.0
5-0907	20	2.39	7.3	.281	1.18	.250	.0717	24	.0329	.0169	.97	98	59	.66	-30.0	-29.2	-29.4	-28.9
5-0913	17	2.35	6.9	.263	.93	.216	.0710	34	.0324	.0170	.98	81	54	.73	-31.1	-30.3	-30.7	-30.2
5-0923	18	2.44	7.1	.273	1.01	.220	.0704	31	.0345	.0174	.90	103	60	.60	-29.8	-29.0	-29.2	-28.8
5-0952	23	3.21	6.9	.262	.94	.214	.0723	34	.0330	.0186	1.00	85	54	.70	-29.9	-29.0	-29.5	-28.8
6-1202	93	25.45	10.6	.429	.99	.109	.0886	97	.0784	.0407	1.07	103	58	.64	-23.4	-21.8	-23.0	-21.9
6-1222	69	20.18	10.2	.413	1.03	.102	.0860	97	.0706	.0352	1.03	111	61	.59	-24.2	-22.9	-23.5	-22.7
6-1234	45	14.28	8.6	.339	.86	.094	.0796	107	.0509	.0250	1.00	114	68	.64	-26.2	-25.1	-25.5	-24.8
9-1421	35	4.05	11.0	.438	1.82	.258	.0813	23	.0630	.0292	1.06	104	62	.65	-27.5	-26.4	-26.9	-26.1
9-1427	32	3.70	10.9	.434	1.80	.258	.0784	23	.0606	.0273	1.13	96	62	.69	-28.0	-26.8	-27.9	-27.0
9-1433	30	3.58	11.6	.468	1.86	.250	.0781	24	.0642	.0295	1.07	102	61	.65	-28.7	-27.4	-28.2	-27.2
9-1445	34	3.72	11.2	.453	1.86	.273	.0834	22	.0598	.0279	1.05	104	62	.66	-28.1	-26.9	-27.5	-26.6
9-1451	29	3.46	10.5	.419	1.69	.250	.0791	24	.0544	.0249	1.05	96	57	.66	-28.8	-27.6	-28.4	-27.6
11-1555	2	.24	6.9	.254	1.11	.250	.0638	24	.0222	.0112	.94	124	64	.52	-39.5	-38.9	-38.9	-38.5
11-1598	20	2.83	8.4	.326	1.16	.211	.0765	34	.0442	.0198	1.03	120	71	.62	-29.8	-28.9	-29.4	-28.8
11-1604	52	7.35	8.5	.333	1.18	.211	.0770	34	.0497	.0283	1.00	84	66	.97	-25.6	-24.5	-25.2	-24.3
11-1618	21	2.86	8.3	.325	1.19	.219	.0717	31	.0429	.0196	1.03	104	64	.66	-29.9	-28.9	-29.6	-29.0
11-1626	15	2.12	7.5	.289	1.04	.211	.0709	34	.0341	.0174	.91	106	70	.69	-30.8	-30.0	-30.0	-29.5
11-1651	3	.41	6.9	.262	.98	.219	.0593	31	.0249	.0113	.96	121	70	.67	-38.1	-37.4	-37.5	-37.2
12-1676	53	7.49	10.6	.431	1.47	.211	.0887	34	.0682	.0322	1.04	120	65	.61	-25.5	-24.1	-24.9	-24.1
12-1682	67	9.85	10.9	.444	1.36	.203	.0900	39	.0711	.0343	1.12	116	64	.61	-24.9	-23.4	-24.2	-23.3
12-1696	50	7.65	10.7	.437	1.30	.195	.0872	41	.0684	.0326	1.10	110	63	.60	-25.8	-24.7	-25.6	-24.7
12-1702	59	9.03	10.7	.439	1.31	.195	.0874	41	.0678	.0331	1.10	116	63	.59	-24.4	-23.3	-24.1	-23.3
12-1711	51	6.29	10.4	.426	1.53	.242	.0868	28	.0671	.0319	1.16	112	58	.58	-25.7	-24.6	-25.5	-24.6
12-1717	66	10.47	10.3	.422	1.31	.188	.0868	41	.0692	.0326	1.16	116	63	.58	-24.7	-23.4	-24.5	-23.5
12-1725	40	6.12	10.0	.407	1.22	.195	.0857	41	.0664	.0301	1.05	114	67	.64	-26.7	-25.6	-26.0	-25.2
12-1739	25	3.82	8.6	.341	1.05	.195	.0786	41	.0539	.0238	1.07	114	59	.56	-28.3	-27.5	-28.1	-27.4
12-1754	52	6.41	10.1	.412	1.49	.242	.0845	28	.0663	.0318	1.07	105	62	.66	-25.3	-24.2	-24.9	-24.1
12-1760	24	2.86	9.5	.382	1.53	.250	.0812	24	.0570	.0276	1.02	104	62	.66	-29.3	-28.3	-28.9	-28.0
12-1778	45	6.61	9.6	.384	1.20	.203	.0855	39	.0582	.0282	1.09	113	62	.60	-26.0	-24.9	-25.7	-24.8
12-1784	29	4.44	9.2	.366	1.12	.195	.0809	41	.0541	.0257	1.06	109	61	1.15	-27.8	-26.8	-27.6	-26.9

Table D.3: Processed Data for Detection Scheme 3

N-file	brk	pct	u10	ustar	uoc	fpk	m(4)	L	vv0	hh0	prb	fdb	bwb	bwn	vss1	vss2	hss1	hss2
1-0209	55	13.13	8.6	.323	.90	.125	.0814	75	.0468	.0228	1.05	128	67	.57	-26.9	-25.3	-26.2	-25.2
1-0215	84	18.84	9.1	.348	.98	.133	.0818	70	.0538	.0256	1.04	121	65	.59	-25.2	-23.6	-24.6	-23.5
1-0223	63	14.13	9.6	.374	1.03	.133	.0831	70	.0543	.0253	1.05	126	65	.57	-26.1	-24.6	-25.4	-24.4
1-0229	64	14.36	8.8	.337	.94	.133	.0808	70	.0481	.0230	1.03	130	65	.53	-25.9	-24.5	-25.2	-24.3
1-0235	63	12.70	8.1	.303	.84	.148	.0800	64	.0430	.0215	1.02	118	67	.60	-26.0	-24.7	-25.3	-24.4
1-0241	51	10.28	7.7	.289	.81	.148	.0778	64	.0408	.0198	1.09	116	63	.58	-26.9	-25.6	-26.5	-25.6
4-0484	23	1.98	8.4	.309	1.84	.346	.0617	13	.0349	.0159	.99	98	64	.67	-31.5	-30.2	-30.7	-30.0
4-0490	28	2.68	8.5	.311	1.61	.312	.0700	16	.0370	.0173	1.05	104	65	.64	-30.1	-28.8	-29.6	-28.8
4-0496	30	3.21	8.4	.311	1.45	.279	.0706	20	.0339	.0159	1.00	104	64	.64	-30.2	-28.9	-29.5	-28.8
4-0510	20	1.88	8.6	.318	1.69	.318	.0713	15	.0313	.0151	.98	116	68	.61	-30.6	-29.8	-30.0	-29.5
5-0901	27	3.01	8.0	.307	1.35	.268	.0682	22	.0391	.0191	1.01	82	62	.83	-30.2	-29.1	-29.9	-29.2
5-0907	27	3.22	7.3	.281	1.18	.250	.0717	24	.0329	.0169	.99	97	63	.70	-29.2	-28.4	-28.6	-28.0
5-0913	31	4.28	6.9	.263	.93	.216	.0710	34	.0324	.0170	1.01	84	58	.77	-29.5	-28.5	-29.2	-28.6
5-0923	29	3.93	7.1	.273	1.01	.220	.0704	31	.0345	.0174	1.03	102	61	.66	-29.0	-28.1	-28.5	-27.9
5-0952	37	5.16	6.9	.262	.94	.214	.0723	34	.0330	.0186	.96	84	58	.81	-28.3	-27.4	-28.0	-27.3
6-1202	135	36.95	10.6	.429	.99	.109	.0886	97	.0784	.0407	1.08	106	61	.66	-23.1	-21.2	-22.4	-21.0
6-1222	111	32.47	10.2	.413	1.03	.102	.0860	97	.0706	.0352	1.06	108	63	.66	-23.6	-21.9	-22.8	-21.7
6-1234	77	24.44	8.6	.339	.86	.094	.0796	107	.0509	.0250	.99	108	66	.67	-24.8	-23.6	-24.2	-23.4
9-1421	88	10.18	11.0	.438	1.82	.258	.0813	23	.0630	.0292	1.14	89	61	.78	-25.3	-23.8	-24.8	-23.7
9-1427	76	8.79	10.9	.434	1.80	.258	.0784	23	.0606	.0273	1.15	96	62	.70	-26.0	-24.3	-25.7	-24.6
9-1433	63	7.52	11.6	.468	1.86	.250	.0781	24	.0642	.0295	1.10	100	62	.67	-26.7	-25.1	-26.0	-24.9
9-1445	82	8.96	11.2	.453	1.86	.273	.0834	22	.0598	.0279	1.12	97	61	.69	-25.9	-24.2	-25.3	-24.2
9-1451	57	6.80	10.5	.419	1.69	.250	.0791	24	.0544	.0249	1.13	92	61	.74	-27.0	-25.5	-26.7	-25.7
11-1555	12	1.43	6.9	.254	1.11	.250	.0638	24	.0222	.0112	.92	109	64	.63	-32.9	-32.3	-32.6	-32.1
11-1598	52	7.35	8.4	.326	1.16	.211	.0765	34	.0442	.0198	1.09	106	64	.66	-27.0	-25.8	-26.7	-25.9
11-1604	121	17.11	8.5	.333	1.18	.211	.0770	34	.0497	.0283	1.06	80	63	.98	-23.5	-21.9	-23.0	-21.8
11-1618	47	6.40	8.3	.325	1.19	.219	.0717	31	.0429	.0196	1.09	98	63	.69	-27.5	-26.4	-27.4	-26.5
11-1626	39	5.51	7.5	.289	1.04	.211	.0709	34	.0341	.0174	.99	97	63	.70	-28.2	-27.1	-27.6	-26.9
11-1651	10	1.36	6.9	.262	.98	.219	.0593	31	.0249	.0113	.99	95	69	.79	-34.8	-33.9	-34.4	-33.9
12-1676	111	15.69	10.6	.431	1.47	.211	.0887	34	.0682	.0322	1.10	105	63	2.04	-23.8	-22.1	-23.3	-22.1
12-1682	121	17.78	10.9	.444	1.36	.203	.0900	39	.0711	.0343	1.11	105	64	.68	-23.8	-22.0	-23.1	-21.8
12-1696	96	14.69	10.7	.437	1.30	.195	.0872	41	.0684	.0326	1.12	101	63	.68	-24.5	-23.0	-24.0	-22.9
12-1702	139	21.27	10.7	.439	1.31	.195	.0874	41	.0678	.0331	1.12	98	62	.80	-22.7	-21.1	-22.4	-21.2
12-1711	101	12.45	10.4	.426	1.53	.242	.0868	28	.0671	.0319	1.13	101	61	.71	-24.1	-22.6	-23.8	-22.7
12-1717	115	18.25	10.3	.422	1.31	.188	.0868	41	.0692	.0326	1.13	108	64	.65	-23.6	-22.0	-23.1	-21.9
12-1725	107	16.37	10.0	.407	1.22	.195	.0857	41	.0664	.0301	1.16	99	62	.83	-24.4	-22.8	-23.8	-22.6
12-1739	61	9.33	8.6	.341	1.05	.195	.0786	41	.0539	.0238	1.14	102	59	1.22	-26.4	-25.0	-26.1	-25.2
12-1754	102	12.57	10.1	.412	1.49	.242	.0845	28	.0663	.0318	1.16	94	60	.74	-24.0	-22.5	-23.7	-22.6
12-1760	67	8.00	9.5	.382	1.53	.250	.0812	24	.0570	.0276	1.09	95	63	.97	-26.5	-25.0	-26.2	-25.1
12-1778	87	12.79	9.6	.384	1.20	.203	.0855	39	.0582	.0282	1.05	106	63	.65	-24.4	-22.9	-24.0	-23.0
12-1784	76	11.63	9.2	.366	1.12	.195	.0809	41	.0541	.0257	1.04	105	61	.65	-25.3	-23.8	-25.0	-24.0

Table D.4: Processed Data for Detection Scheme 4

No-file	brk	pct	u10	ustar	uoc	fpk	m(4)	L	vv0	hh0	prb	fdb	bwb	bwn	vss1	vss2	hss1	hss2
1-0209	60	14.32	8.6	.323	.90	.125	.0814	75	.0468	.0228	1.05	126	65	.56	-26.5	-24.9	-25.8	-24.8
1-0215	92	20.64	9.1	.348	.98	.133	.0818	70	.0538	.0256	1.05	120	63	.58	-24.8	-23.1	-24.2	-23.1
1-0223	69	15.48	9.6	.374	1.03	.133	.0831	70	.0543	.0253	1.06	123	63	.56	-25.8	-24.2	-25.1	-24.1
1-0229	71	15.93	8.8	.337	.94	.133	.0808	70	.0481	.0230	1.04	129	63	.52	-25.4	-24.0	-24.8	-23.8
1-0235	66	13.30	8.1	.303	.84	.148	.0800	64	.0430	.0215	1.02	117	66	.59	-25.8	-24.5	-25.1	-24.2
1-0241	55	11.09	7.7	.289	.81	.148	.0778	64	.0408	.0198	1.09	118	62	.56	-26.4	-25.1	-26.1	-25.3
4-0484	23	1.98	8.4	.309	1.84	.346	.0617	13	.0349	.0159	.99	98	64	.67	-31.5	-30.2	-30.7	-30.0
4-0490	28	2.68	8.5	.311	1.61	.312	.0700	16	.0370	.0173	1.05	104	65	.64	-30.1	-28.8	-29.6	-28.8
4-0496	31	3.31	8.4	.311	1.45	.279	.0706	20	.0339	.0159	1.01	103	64	.64	-30.0	-28.7	-29.3	-28.6
4-0510	21	1.97	8.6	.318	1.69	.318	.0713	15	.0313	.0151	.97	116	68	.61	-30.5	-29.6	-29.9	-29.3
5-0901	34	3.78	8.0	.307	1.35	.268	.0682	22	.0391	.0191	1.00	81	59	.79	-29.0	-27.9	-28.6	-27.9
5-0907	35	4.18	7.3	.281	1.18	.250	.0717	24	.0329	.0169	.99	93	60	.69	-28.3	-27.4	-27.7	-27.1
5-0913	36	4.97	6.9	.263	.93	.216	.0710	34	.0324	.0170	1.00	81	56	.77	-28.9	-27.9	-28.6	-27.9
5-0923	33	4.47	7.1	.273	1.01	.220	.0704	31	.0345	.0174	1.01	99	59	.64	-28.3	-27.3	-27.9	-27.2
5-0952	45	6.27	6.9	.262	.94	.214	.0723	34	.0330	.0186	.99	81	55	.79	-27.5	-26.6	-27.2	-26.5
6-1202	162	44.34	10.6	.429	.99	.109	.0886	97	.0784	.0407	1.10	102	58	.65	-22.2	-20.3	-21.7	-20.3
6-1222	132	38.61	10.2	.413	1.03	.102	.0860	97	.0706	.0352	1.08	106	60	.63	-22.8	-21.2	-22.2	-21.0
6-1234	82	26.02	8.6	.339	.86	.094	.0796	107	.0509	.0250	1.00	105	64	.67	-24.6	-23.4	-23.9	-23.1
9-1421	95	10.98	11.0	.438	1.82	.258	.0813	23	.0630	.0292	1.14	89	60	.76	-25.0	-23.4	-24.5	-23.4
9-1427	82	9.48	10.9	.434	1.80	.258	.0784	23	.0606	.0273	1.14	95	61	.69	-25.6	-24.0	-25.3	-24.2
9-1433	69	8.23	11.6	.468	1.86	.250	.0781	24	.0642	.0295	1.11	98	61	.67	-26.3	-24.8	-25.7	-24.5
9-1445	85	9.29	11.2	.453	1.86	.273	.0834	22	.0598	.0279	1.11	95	60	.69	-25.7	-24.1	-25.1	-24.0
9-1451	66	7.88	10.5	.419	1.69	.250	.0791	24	.0544	.0249	1.13	91	59	.72	-26.3	-24.9	-26.1	-25.1
11-1555	12	1.43	6.9	.254	1.11	.250	.0638	24	.0222	.0112	.92	109	64	.63	-32.9	-32.3	-32.6	-32.1
11-1598	54	7.63	8.4	.326	1.16	.211	.0765	34	.0442	.0198	1.08	106	64	.66	-26.8	-25.6	-26.5	-25.7
11-1604	129	18.24	8.5	.333	1.18	.211	.0770	34	.0497	.0283	1.06	79	62	.97	-23.2	-21.7	-22.8	-21.6
11-1618	51	6.95	8.3	.325	1.19	.219	.0717	31	.0429	.0196	1.09	98	62	.67	-27.2	-26.0	-27.1	-26.2
11-1626	39	5.51	7.5	.289	1.04	.211	.0709	34	.0341	.0174	.99	97	63	.70	-28.2	-27.1	-27.6	-26.9
11-1651	10	1.36	6.9	.262	.98	.219	.0593	31	.0249	.0113	.99	95	69	.79	-34.8	-33.9	-34.4	-33.9
12-1676	118	16.68	10.6	.431	1.47	.211	.0887	34	.0682	.0322	1.10	104	62	1.95	-23.5	-21.8	-23.1	-21.9
12-1682	134	19.69	10.9	.444	1.36	.203	.0900	39	.0711	.0343	1.14	103	62	.68	-23.3	-21.5	-22.7	-21.4
12-1696	105	16.06	10.7	.437	1.30	.195	.0872	41	.0684	.0326	1.14	99	61	.68	-24.1	-22.6	-23.7	-22.6
12-1702	148	22.64	10.7	.439	1.31	.195	.0874	41	.0678	.0331	1.14	98	61	.78	-22.4	-20.9	-22.2	-21.0
12-1711	112	13.81	10.4	.426	1.53	.242	.0868	28	.0671	.0319	1.14	100	60	.69	-23.6	-22.1	-23.4	-22.2
12-1717	127	20.15	10.3	.422	1.31	.188	.0868	41	.0692	.0326	1.16	105	62	.65	-23.2	-21.6	-22.8	-21.6
12-1725	112	17.13	10.0	.407	1.22	.195	.0857	41	.0664	.0301	1.16	98	62	.81	-24.1	-22.6	-23.5	-22.4
12-1739	65	9.94	8.6	.341	1.05	.195	.0786	41	.0539	.0238	1.15	102	58	1.17	-26.1	-24.7	-25.8	-24.9
12-1754	110	13.56	10.1	.412	1.49	.242	.0845	28	.0663	.0318	1.17	93	59	.74	-23.7	-22.2	-23.4	-22.3
12-1760	71	8.47	9.5	.382	1.53	.250	.0812	24	.0570	.0276	1.08	93	62	.96	-26.2	-24.7	-25.9	-24.8
12-1778	95	13.96	9.6	.384	1.20	.203	.0855	39	.0582	.0282	1.09	104	61	.65	-24.1	-22.6	-23.8	-22.7
12-1784	84	12.85	9.2	.366	1.12	.195	.0809	41	.0541	.0257	1.06	103	60	.82	-24.8	-23.3	-24.6	-23.6

The participation in the SAXON experiment of investigators from the R. M. Parsons Laboratory in the Department of Civil Engineering at the Massachusetts Institute of Technology consisted of two separate studies concerning microwave scattering from the sea surface. The <u>altimeter study</u> was designed to measure the so–called sea–state or electromagnetic bias at nadir incidence at Ku–band frequency. The <u>scatterometer study</u> was primarily designed to investigate the microwave signature of wave breaking. A secondary aim of the scatterometer study was to measure the radar cross–section and modulation transfer function at Ku–band frequency. Both of these studies were carried out in collaboration with the Ocean Measurements Section of the US Naval Research Laboratory.

INSTRUMENTATION

The microwave instrument for the altimeter study was a 14 GHz dual–polarized coherent scatterometer mounted 23m above the sea surface on a boom extending 7m from the upper deck railing. An infrared wave height gauge was mounted adjacent to the microwave antennas to provide simultaneous surface elevation data coincident with the microwave illumination area. A video camera was also mounted adjacent to the antennas in order to assess tower interference and the influence of wave breaking. An array of three wire wave gauges was mounted on a 7m boom attached to the lower catwalk and offset from the altimeter illumination area by approximately 5m. This array provided wave slope and high frequency surface elevation information with which to model the electromagnetic bias.

The microwave instrument for the scatterometer study was similar in design to that used for the altimeter study. A video camera was mounted next to the antennas in order to provide visual documentation of the occurrence of whitecaps.

In addition to the microwave and wave gauge measurements, a meteorological station was established to record wind speed and direction, air and sea temperature, and relative humidity.

DATA RECORDING

The data recording system consisted of PC computer based real–time analysis, analog recording of unprocessed data, and VHS video recordings. These different recording systems were all synchronized with an IRIG time code. Table E.1 lists the time periods covered by each numbered recording method listed in the key to table E.1.

The environmental data (10–minute averages of RMS wave amplitude and meteorological measurements) have been made available for distribution to all SAXON participants. The attached memo describes the data in detail and daily plots of the environmental data are given in Figures E.1 through E.24.

TO: SAXON EXPERIMENT PARTICIPANTS
FROM: Andy Jessup, MIT, (617) 253-5450
SUBJECT: ENVIRONMENTAL DATA SUMMARY

This document is contained in a file called README.ENV on floppy SAXON-ENV and briefly describes the environmental data furnished by MIT. All values are 10 minute averages. All specifications below are those provided by the manufacturer. The data are:

1: Relative Humidity (%)
     - Rotronics MP-100 Humidity probe
     - Calibrated accuracy +/- 2%
     - Sensor Height 39m

2: RMS Wave Amplitude (m)
     - Thorn EMI Infra Red Wave Height Monitor
         (range measurement device)
     - Accuracy +/- 0.1m
     - Transmitter beamwidth 1 degree max
     - Instrument Height: 23 m
     - Maximum freq of wave measured: 5 Hz for 50m peak to trough
     - RMS Definition: sqrt(var(z(t)))
         where z(t) = surface elevation
     - N.B. Significant wave height (4 * RMS) is plotted in
         accompanying graphs

3: Wind Speed (m/s)
     - R. M. Young Model 05305
     - Instrument Height: 42m
     - Specifications available upon request

4: Wind Direction (degrees true)
     - same as 3

5: Air Temperature (degrees C)
     - R. M. Young 1000 Ohm Platinum sensor
     - Accuracy: +/- 0.5 deg C
     - Response time: 0.9 min
     - Instrument Height: 39m

6: Sea Temperature (degrees C)
     - R. M. Young 1000 Ohm Platinum sensor
     - Accuracy: +/- 0.5 deg C
     - Response time: 0.9 min
     - Instrument Depth: 1m

Environmental data were taken from 19 SEP to 14 OCT 14 1988. For each day there is an ASCI file named for the date as follows:
                    saxXX-YY.env
where XX = month and YY = day.

The first line of each file contains the number of time points in the file. The data were written with the following fortran format statements:

```
write(26, 3000) itime, jtime, ir, ws, wd, ta, ts, rh
format(2i4.4, 1x, f4.2, 1x, f4.1, 1x, f4.0, 1x, f5.1, 1x, f5.1, 1x, f5.0)
```

where:
itime = XXYY, XX = month, YY = day
jtime = ZZWW, ZZ = hrs, WW = mins (local start time of 10 min average)
ir   = RMS wave amplitude
ws   = Wind speed
wd   = Wind direction
ta   = Air temperature
ts   = Sea temperature
rh   = Relative humidity

The following column labels indicate the data format, followed by
the first few lines from file sax09-19.env for illustration (NB:
column labels are NOT in files and the first line of each file
is the number of time points in the file).

DATE mdhrmin	IRWG (m)	W.S. (m/s)	W.D. deg	A.T. (degrees C)	S.T.	R.H. (%)
22						
09191305	.07	3.9	160.	23.4	22.3	93.
09191333	.09	5.0	157.	23.7	22.4	92.
09191339	.08	5.0	158.	23.6	22.3	92.
09191735	.15	4.8	133.	23.5	22.8	91.
09191745	.15	5.2	130.	23.5	23.0	90.
09191756	.15	5.0	130.	23.4	23.1	90.

PROBLEMS:
   1: Wind direction algorithm
         Algorithm for computing average wind direction failed
         when the wind direction crossed back and forth between
         0 and 360 degrees. These instances are relatively obvious
         from the plots, for example on 09-22-88 between 1200 and 1400.

   2: Blocks of 'bad' wind speed and/or wind direction

      Wind speed   : 09-24-88 @ 0702 through 09-24-88 @ 1224
                        09-24-88 @ 1900 through 09-25-88 @ 1106
                        09-26-88 @ 0635 through 09-26-88 @ 0822
                        These value have been set to 99.9 in the
                        data files and are plotted as 0. in the plots.
                        These data are 'bad' because of a formatting
                        error in the output. From this knowledge,
                        we can say that the actual wind speed was
                        greater that 10 m/s.

      Wind direction: 09-23-88 @ 0758 through 09-25-88 @ 0835
                        09-26-88 @ 2157 through 09-27-88 @ 0913
                        These values have been set to 999. in the
                        data files and are plotted as 0. in the plots.
                        There is no information on what the values
                        should be.

3: Relative Humidity
   Water was found in the terminal box at the probe when the
   it was disassembled. This may explain the fact that the
   relative humidity reading was found to vary by 6 to 8 per cent at
   any given time. The average value may be correct, but these
   should be checked against other measurements such as NOAA.

If there are any problems or questions you have about the data,
please call me at the number above.

KEY TO TABLE E.1

1. Real–time, 10–minute averages of environmental and altimeter quantities:
   - wind speed
   - wind direction
   - air temperature
   - sea temperature
   - relative humidity
   - RMS wave amplitude
   - altimeter radar cross–section
   - EM bias

2. Real–time computation (time step 0.25 s) for altimeter and scatterometer:
   - radar cross–section
   - estimate of first moment of doppler spectrum
   - estimate of second moment of doppler spectrum

3. Analog tape recording of (bandwidth 625 Hz):
   - Altimeter: VV and HH polarization
   - Scatterometer: VV and HH polarization
   - Infrared and wire wave gauges
   - Meteorological data

4. VHS video recording of scatterometer illumination area

5. VHS video recording of altimeter illumination area

TABLE E.1 MIT MEASUREMENT PERIODS FOR SAXON EXPERIMENT

hourEDST/date	0919	0920	0921	0922	0923	0924	0925
0000					1	1	1
0100					1	1	1
0200					1	1	1
0300					1	1	1
0400					1	1	1
0500					1	1	1
0600					1	1	1
0700				1 3	1	1	1
0800				1 345	1 34	1	1 34
0900			345	1 345	1 34		1 34
1000	3		345	1 345	1 3	1 34	1 3
1100	3		3	1 345	1 3	1 34	1 3
1200	345		3	1 345	1	1 3	1
1300	345			1 34	1 3	1	1 34
1400				1	1 3	1 345	1 34
1500				1	1 3	1 345	1 3
1600					1 3	1 3	1 3
1700	1		345	1 3	1	1 3	1
1800	1		345	1 3	1 34	1	1 3
1900	1		3	1 3	1 34	1	1 3
2000	1		3	1 3	1 3	1 3	1 3
2100				1	1 3	1 3	1 3
2200				1	1	1 3	1
2300				1	1	1 3	1
2400				1	1	1 3	1

hourEDST/date	0926	0927	0928	0929	0930	1001	1002
0000	1	1	1		12	1	1
0100	1	1	1		12	1	1
0200	1	1	1		12	1	1
0300	1	1	1		12	1	1
0400	1	1	1		12	1	1
0500	1	1	1		12	1	1
0600	1	1	1		12	1	1
0700	1	1	1		12	1	1
0800	1	1	1		2	1	
0900	1 34	1 34	1 34		2	1	
1000	1 34	1 34	1 34		2	1 34	12345
1100	1 3	1 3	1 3	1	2	1 34	12345
1200	1 3	1 3	1	1	2	1 3	123
1300	1	1	1		2	1 3	123
1400	1	1	1		2	1	12345
1500	1 3	1	1		12345	1	12345
1600	1 3	1	1		12345	1	123
1700	1 3	1	1	1	123	1	123
1800	1 3	1	1		123	1	12
1900	1	1	1		12	1	12
2000	1 3	1	1		12	1	12
2100	1 3	1	1		12	1	123
2200	1 3	1	1	1	12	1	123
2300	1 3	1	1	12	1	1 3	123
2400	1	1	1	12	1	1 3	123

hourEDST/date	1003	1004	1005	1006	1007	1008	1009
0000	12	12	12	12	12	1 3	12
0100	12	12	1	12	12	1 3	12
0200	12	12	1	12	12	1	12
0300	12	12	1	12	12	1	12
0400	12	12	1	12	12	12	12
0500	12	12	1	12	12	12	12
0600	12	12	1	12	12	12	12
0700	12	1234	1 3	123	1234	12	12
0800		1234	1 3	1234	1234	12 4	12
0900		1234	1234	1234	123	12 4	12345
1000	1	1234	1234	123	123	1234	12345
1100	12345	12	12 4	1234	12	1234	123
1200	12345	12345	12 4	12 4	12	123	123
1300	123	12345	1234	1	12	123	12
1400	123	123	123	1	12 4	12	12
1500	123	123	1234	1234	12		1
1600	123	123	1234	1234	1234	12345	123
1700	123	1234	12	12	123	12345	123
1800	123	123	12	23	123	123	123
1900	123	123	12	23	123	123	123
2000	123	12	123	12	12	12	12
2100	123	123	123	12	12	123	12
2200	123	123	123	12	123	123	12
2300	123	123	123	12	123	123	12
2400	123	123	12	12	123	123	12

hourEDST/date	1011	1012	1013	1014
0000		123	12	1
0100		123	12	1
0200		123	12	1
0300		123	12	1
0400		12	12	1
0500		12	12	1
0600		12	12	1
0700		1234	1234	1 34
0800	1234	1234	1234	1 34
0900	123	1234	1234	1 3
1000	12345	1234	1234	1 3
1100	123 5	12 4	12 4	1
1200	12	12 4	12 4	1
1300	1 4	12 4	1234	1
1400	1 4	1234	1234	1
1500	1	1234	1234	1
1600	1	1234	1234	1
1700	1	1234	12 4	1
1800	1	12	12 4	1
1900	1	12	12	1
2000	1	12	1	1
2100	1	2	1	1
2200	1	12	1	1
2300	12	12	1	1
2400	12	12	1	1

FIGURE E. 1: SAXON ENVIROMENTAL DATA 09-19-88
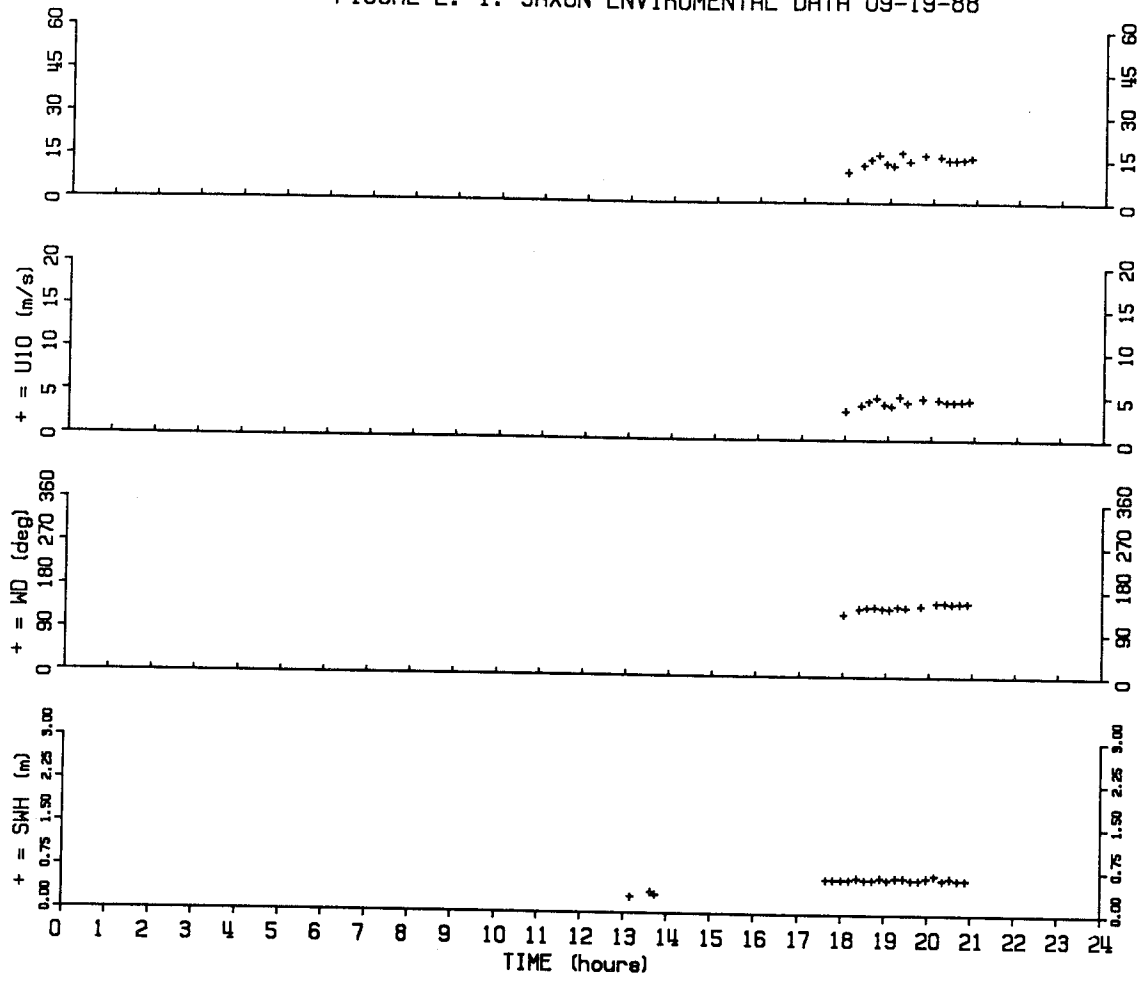
FIGURE E. 2: SAXON ENVIROMENTAL DATA 09-22-88
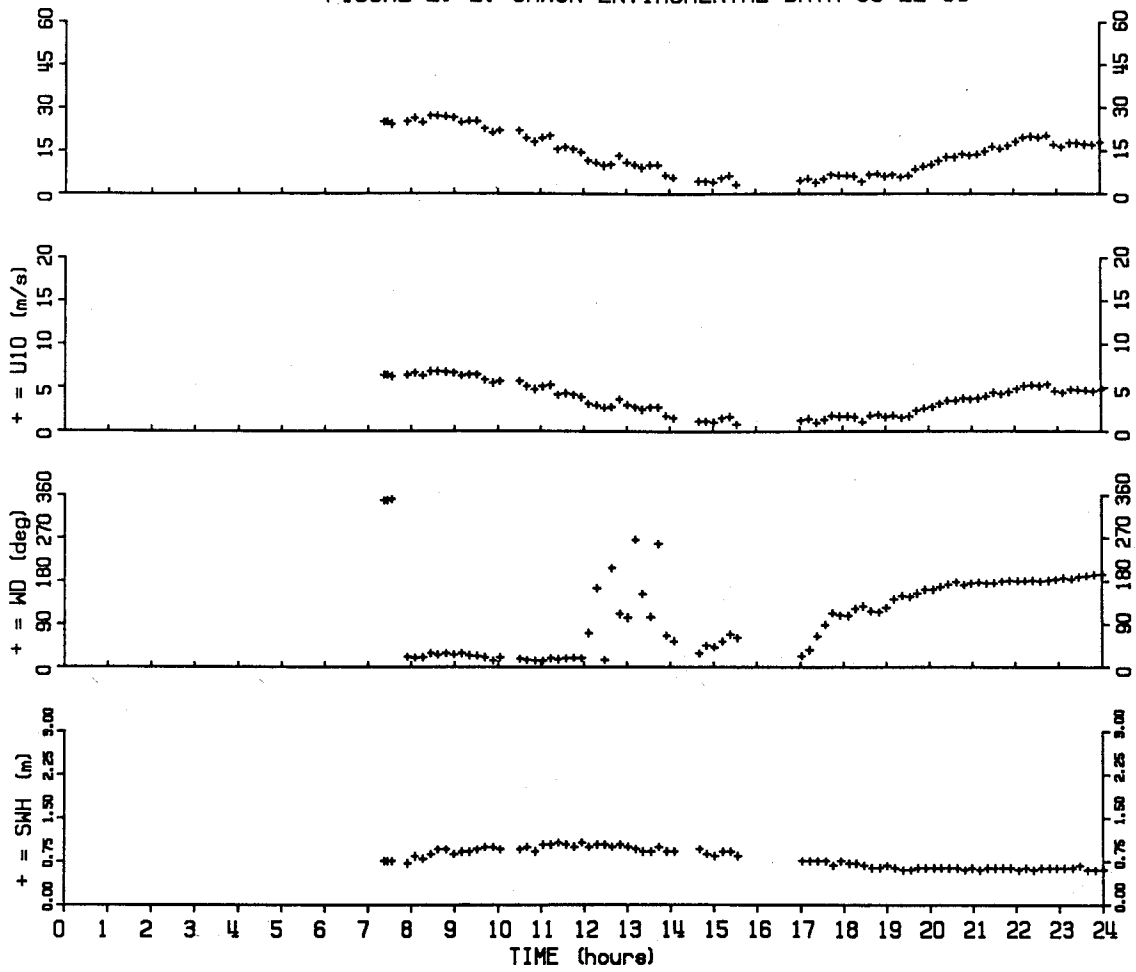
FIGURE E. 3: SAXON ENVIROMENTAL DATA 09-23-88
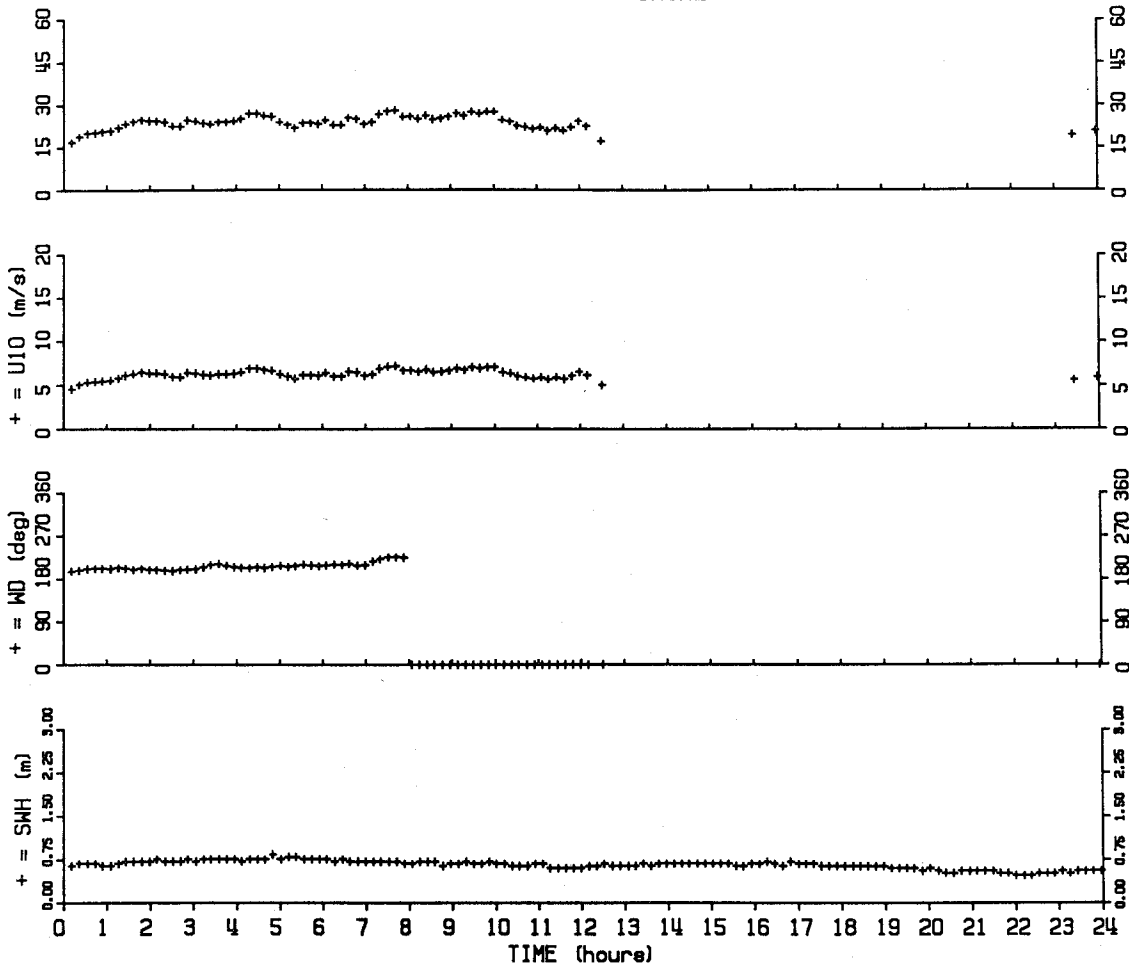
FIGURE E. 4: SAXON ENVIROMENTAL DATA 09-24-88
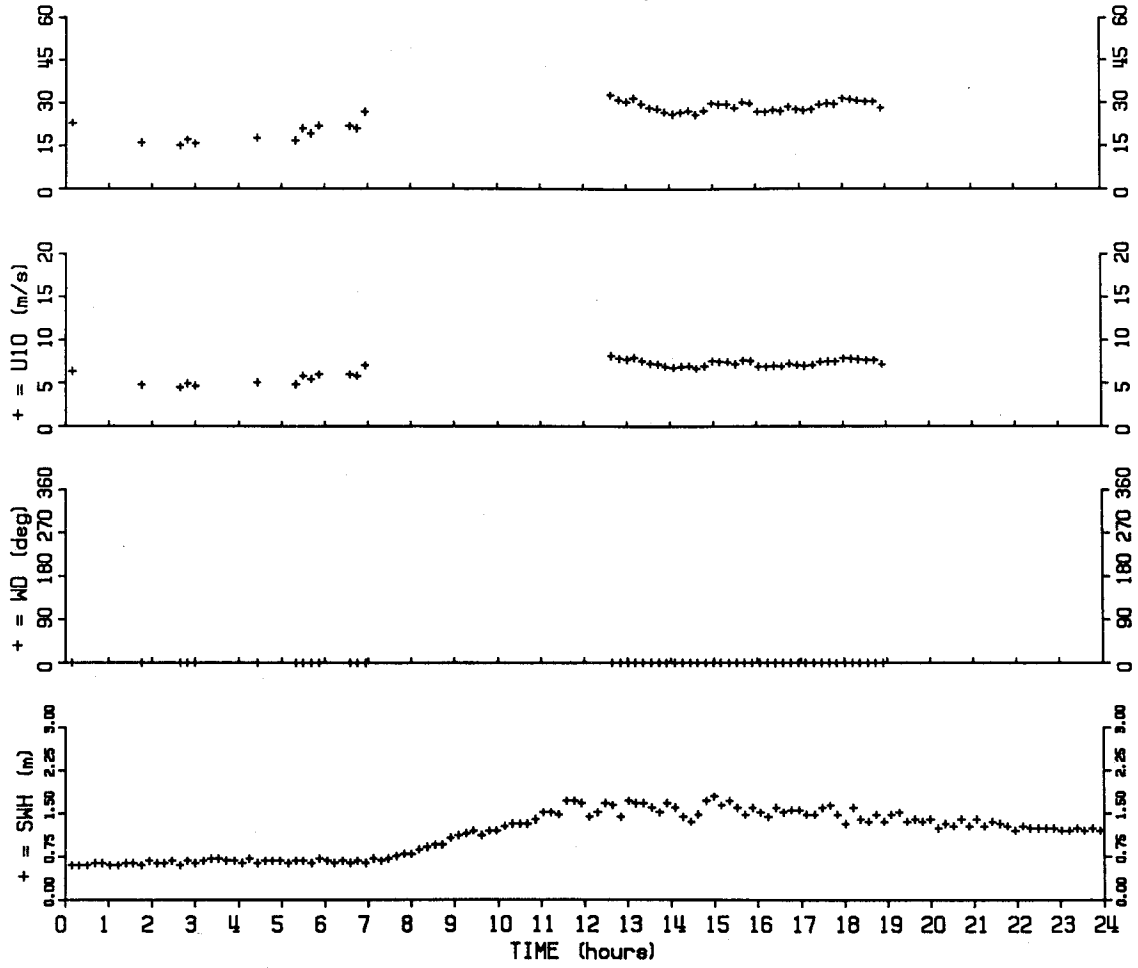
FIGURE E. 5: SAXON ENVIROMENTAL DATA 09-25-88
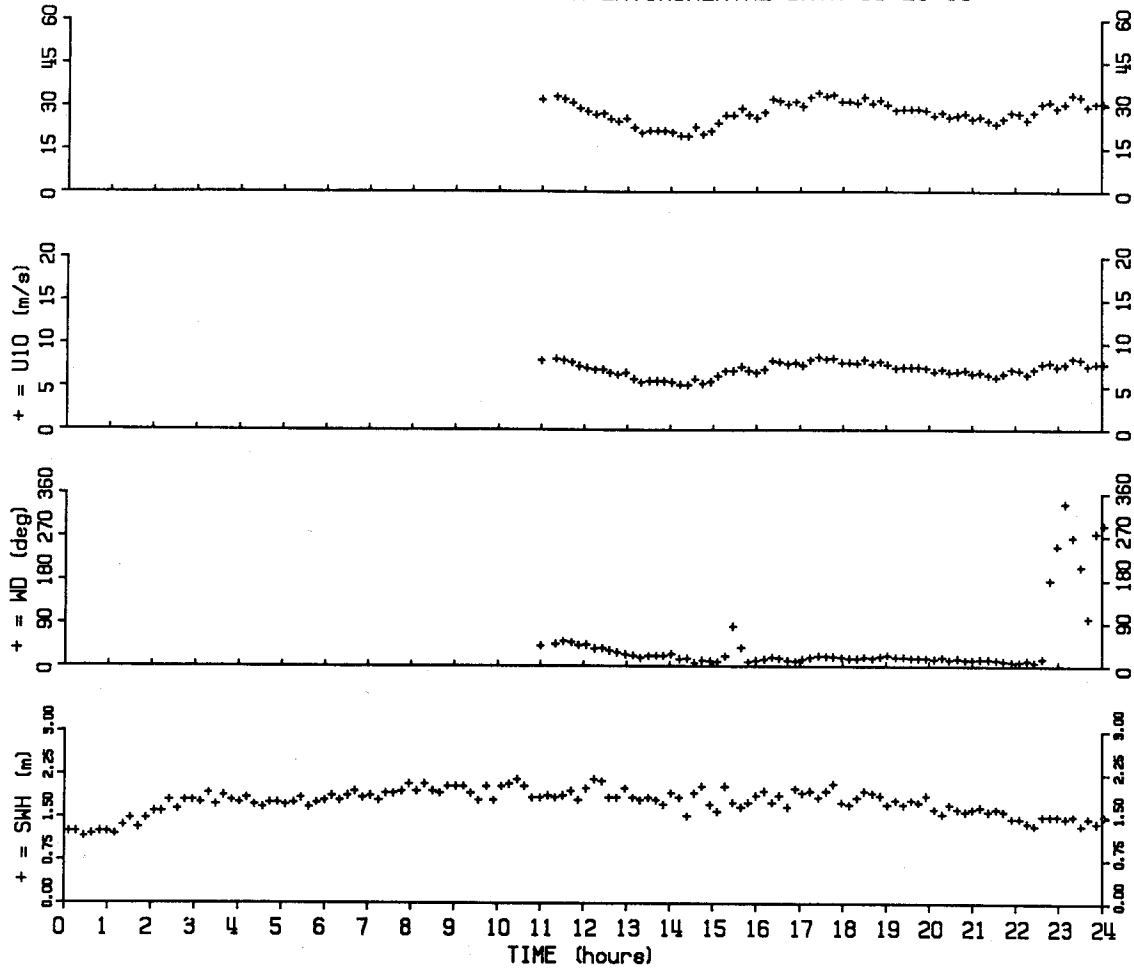
FIGURE E. 6: SAXON ENVIROMENTAL DATA 09-26-88
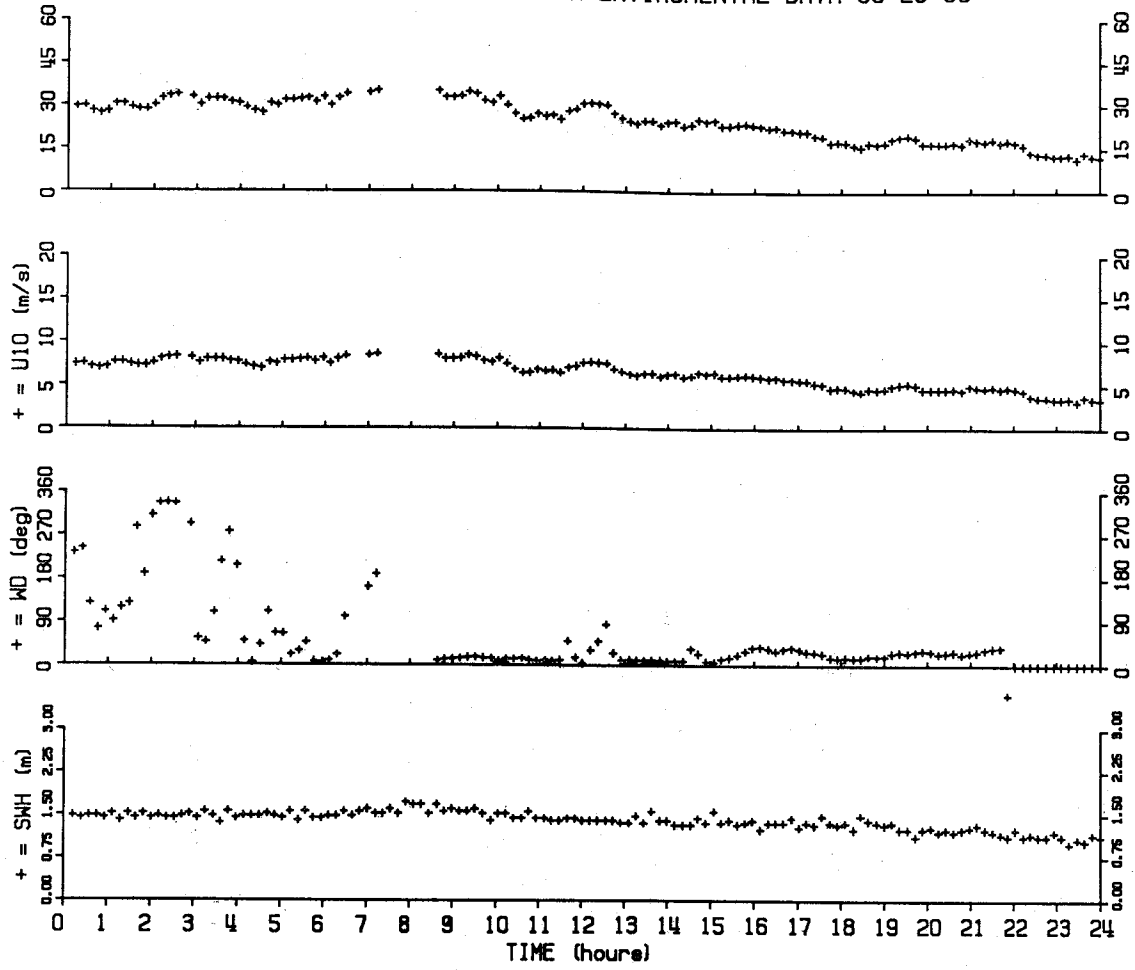
FIGURE E. 7: SAXON ENVIROMENTAL DATA 09-27-88
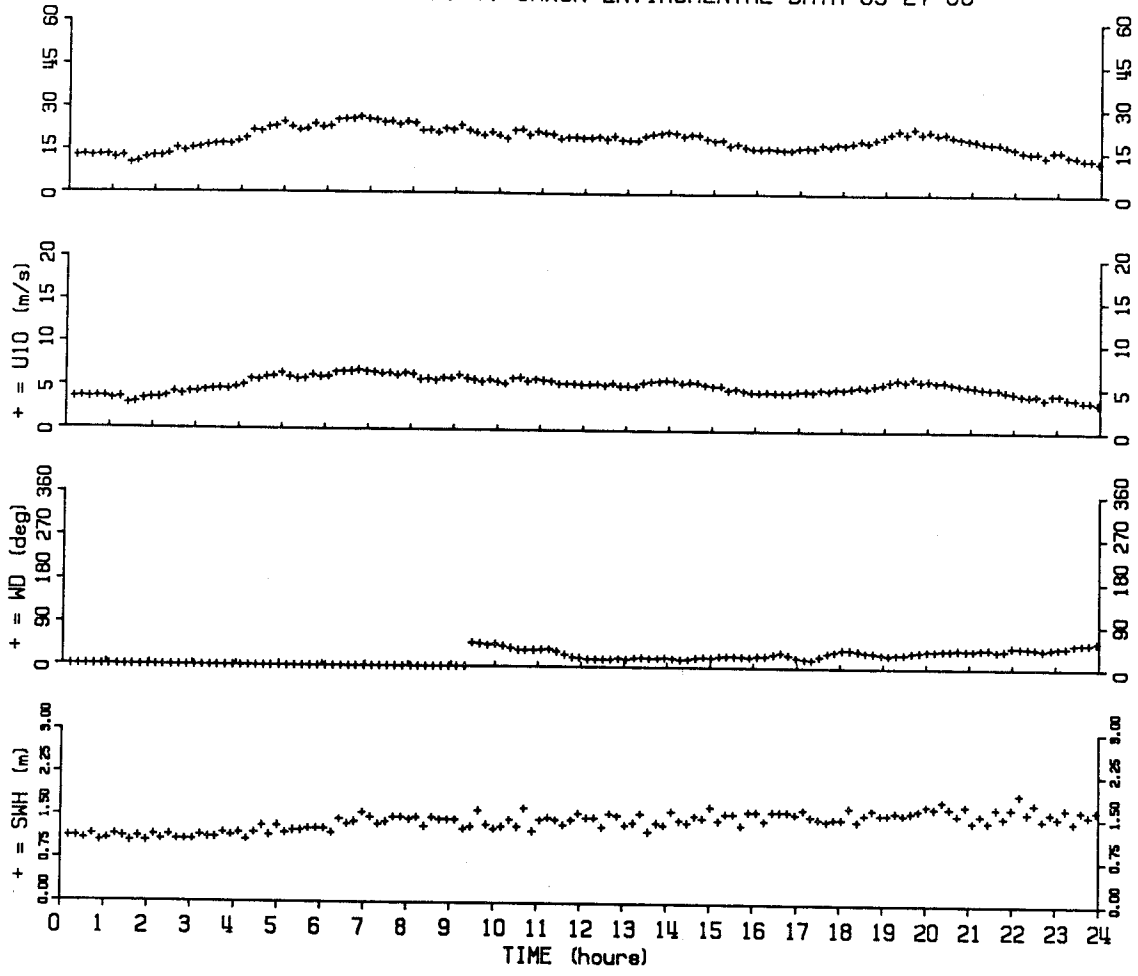
FIGURE E. 8: SAXON ENVIROMENTAL DATA 09-28-88
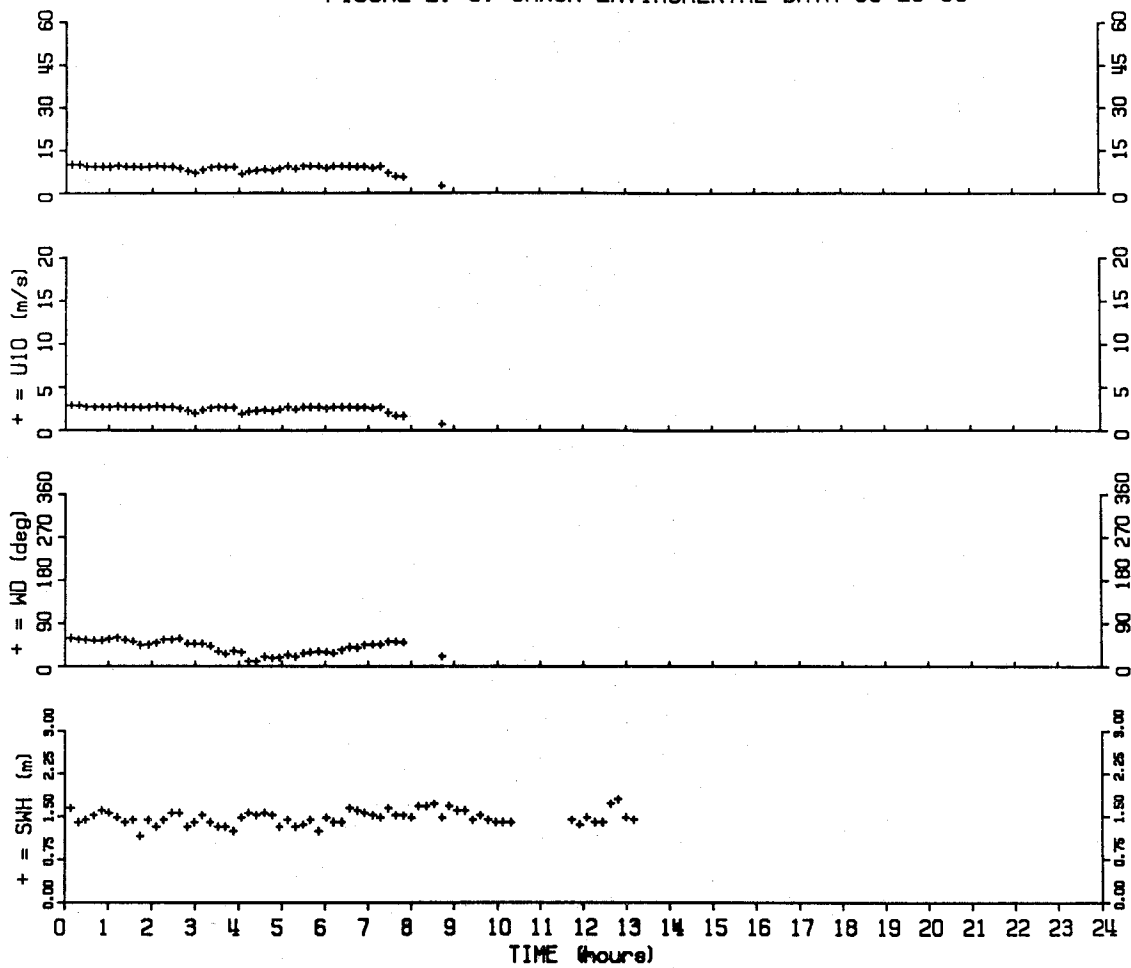
FIGURE E. 9: SAXON ENVIROMENTAL DATA 09-29-88
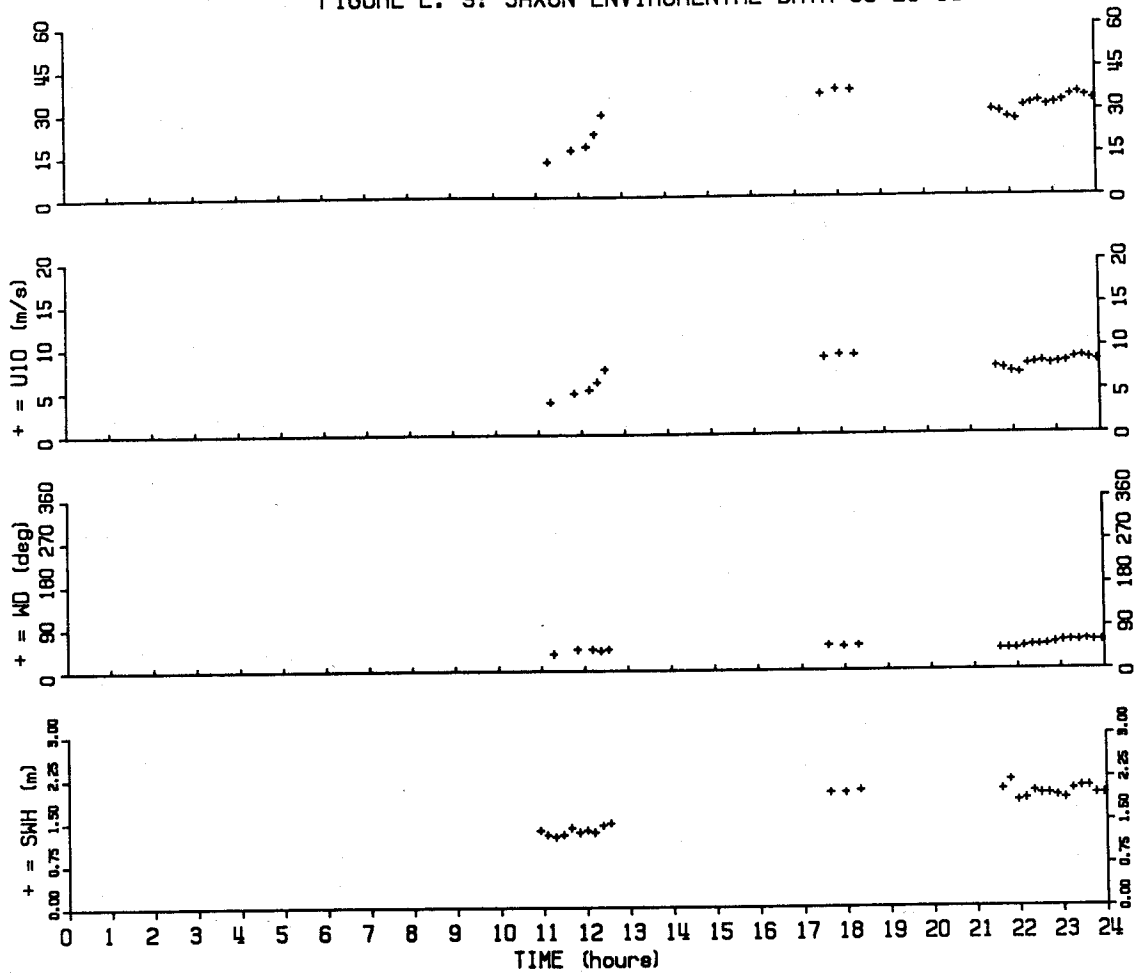
FIGURE E.10: SAXON ENVIROMENTAL DATA 09-30-88
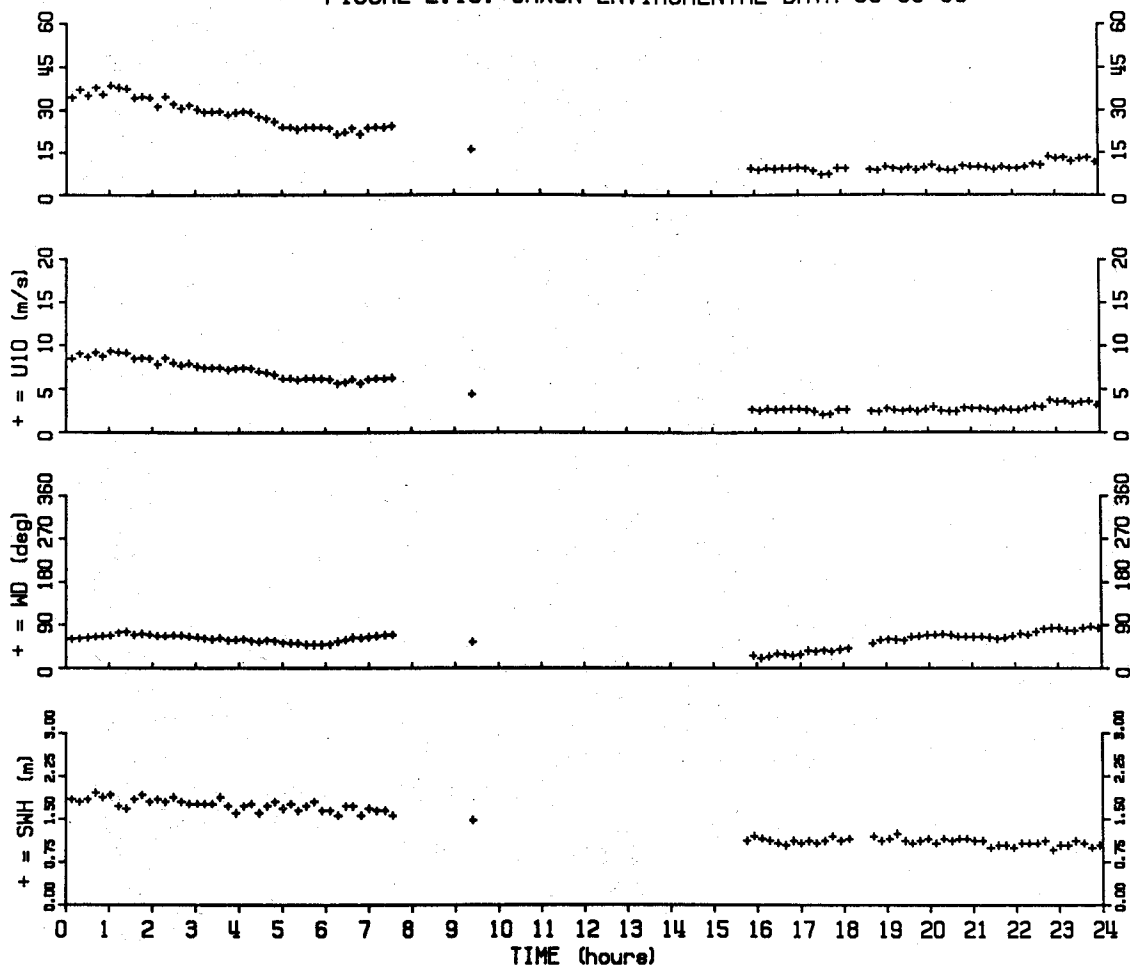
FIGURE E.11: SAXON ENVIROMENTAL DATA 10-01-88

TIME (hours)
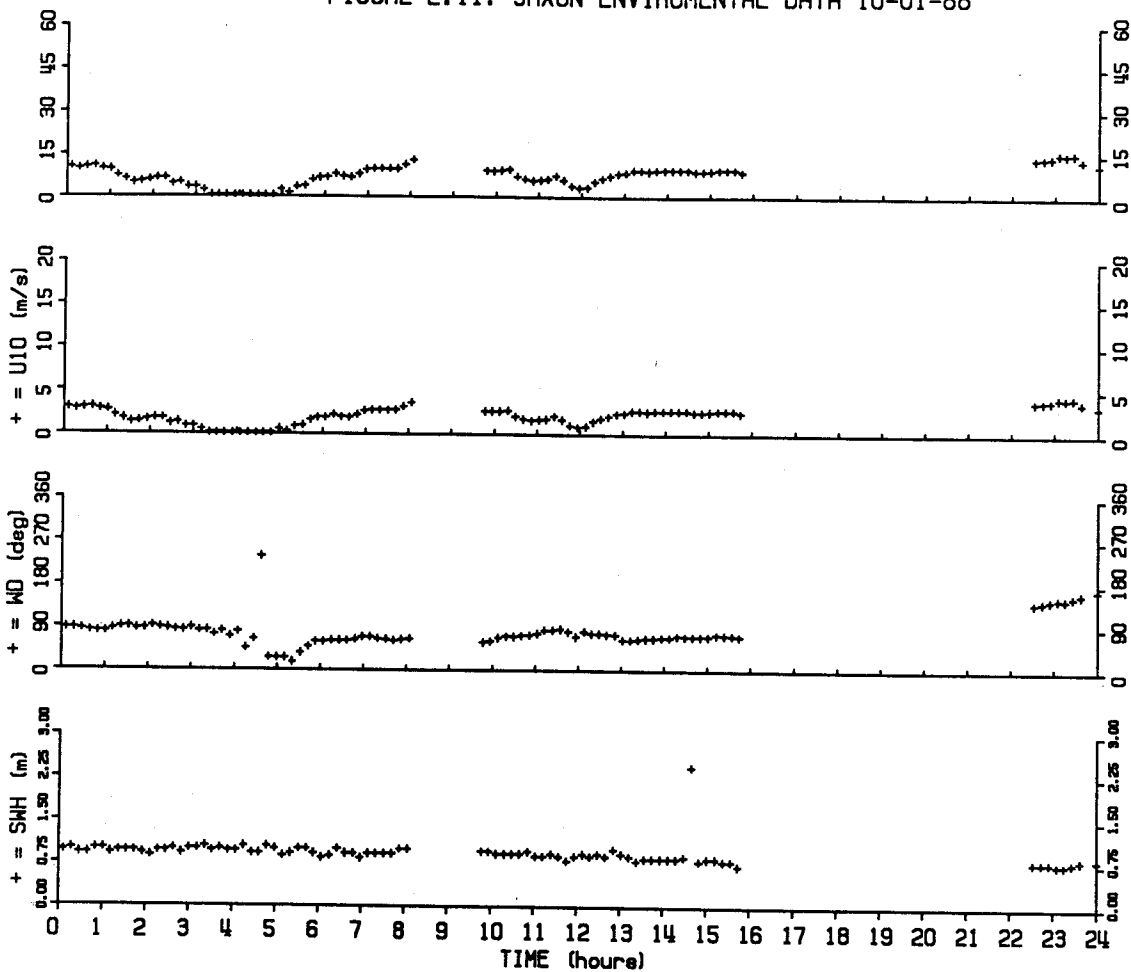
FIGURE E.12: SAXON ENVIROMENTAL DATA 10-02-88
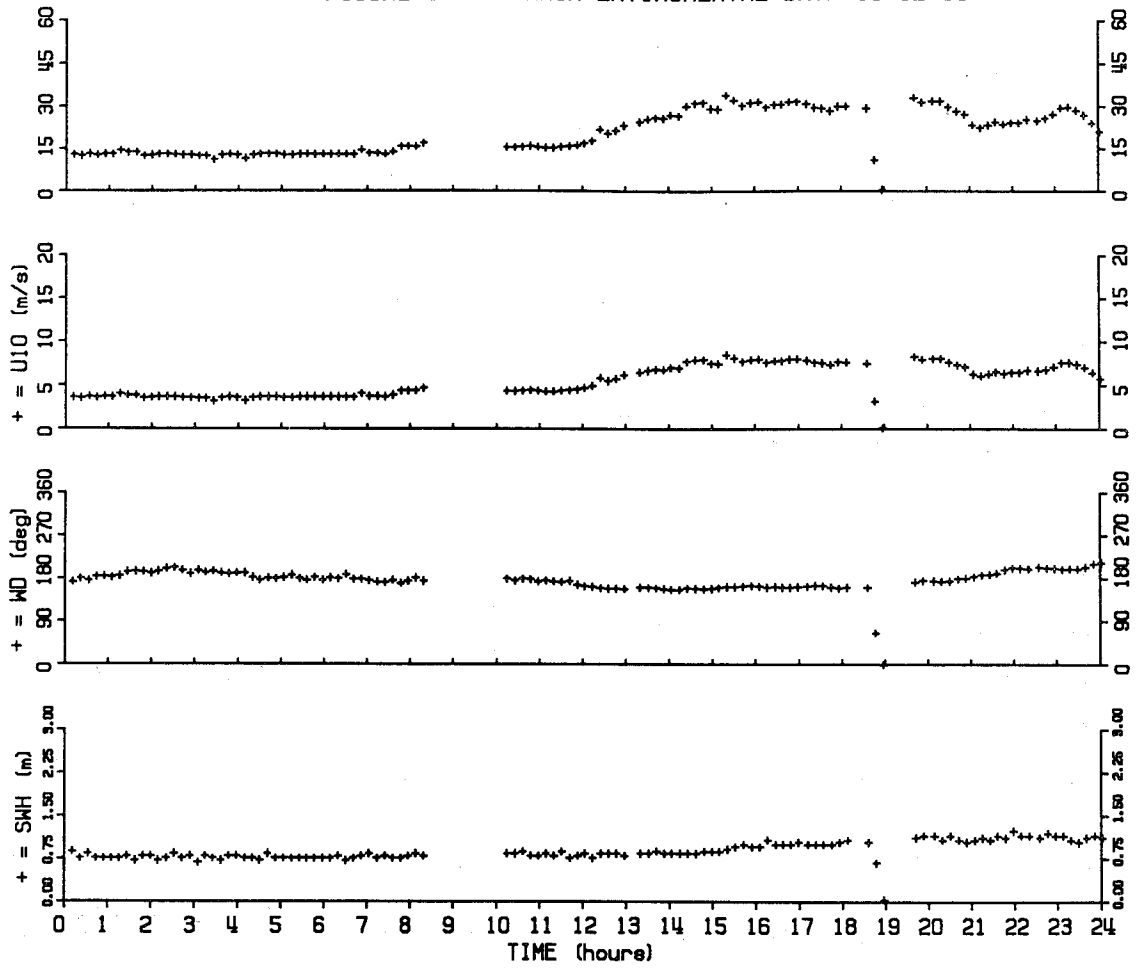
FIGURE E.13: SAXON ENVIROMENTAL DATA 10-03-88
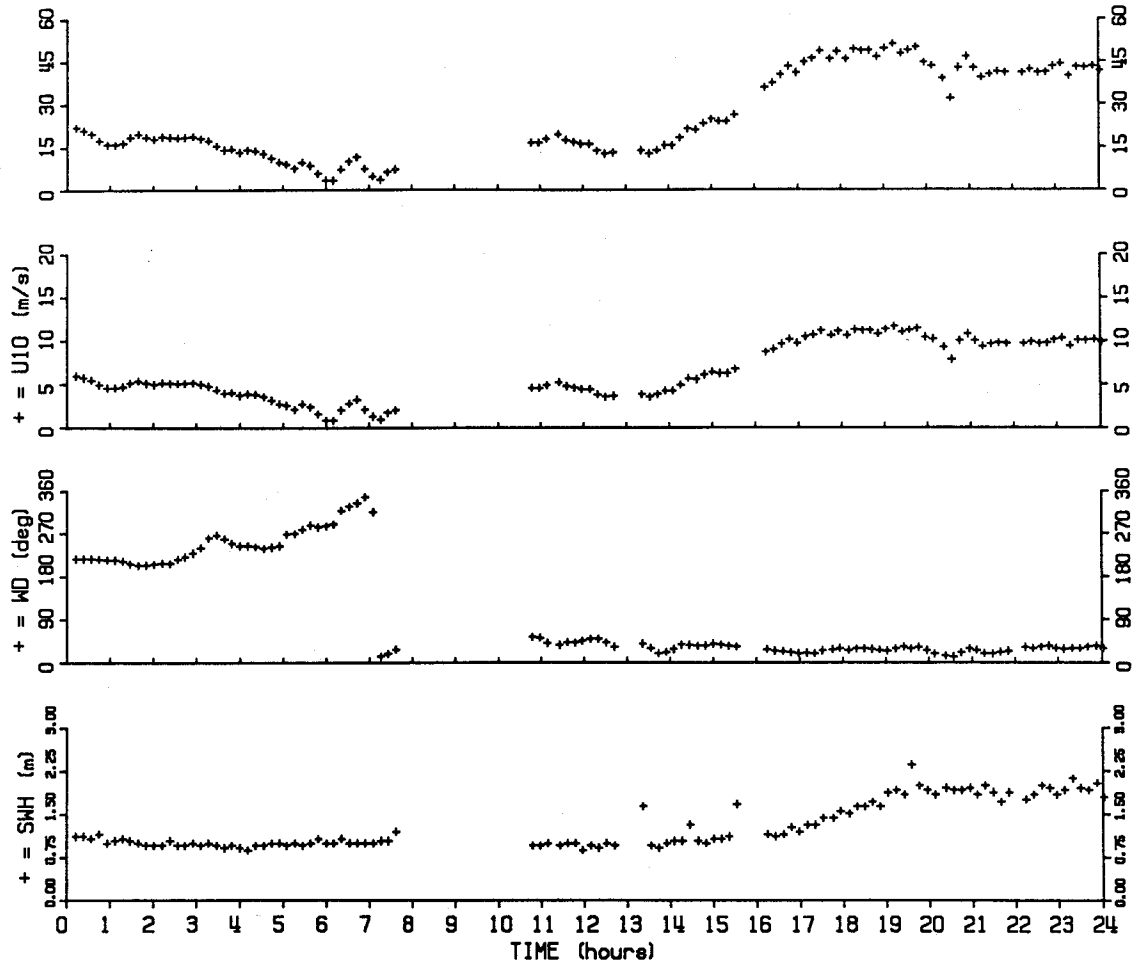
FIGURE E.14: SAXON ENVIRONMENTAL DATA 10-04-88
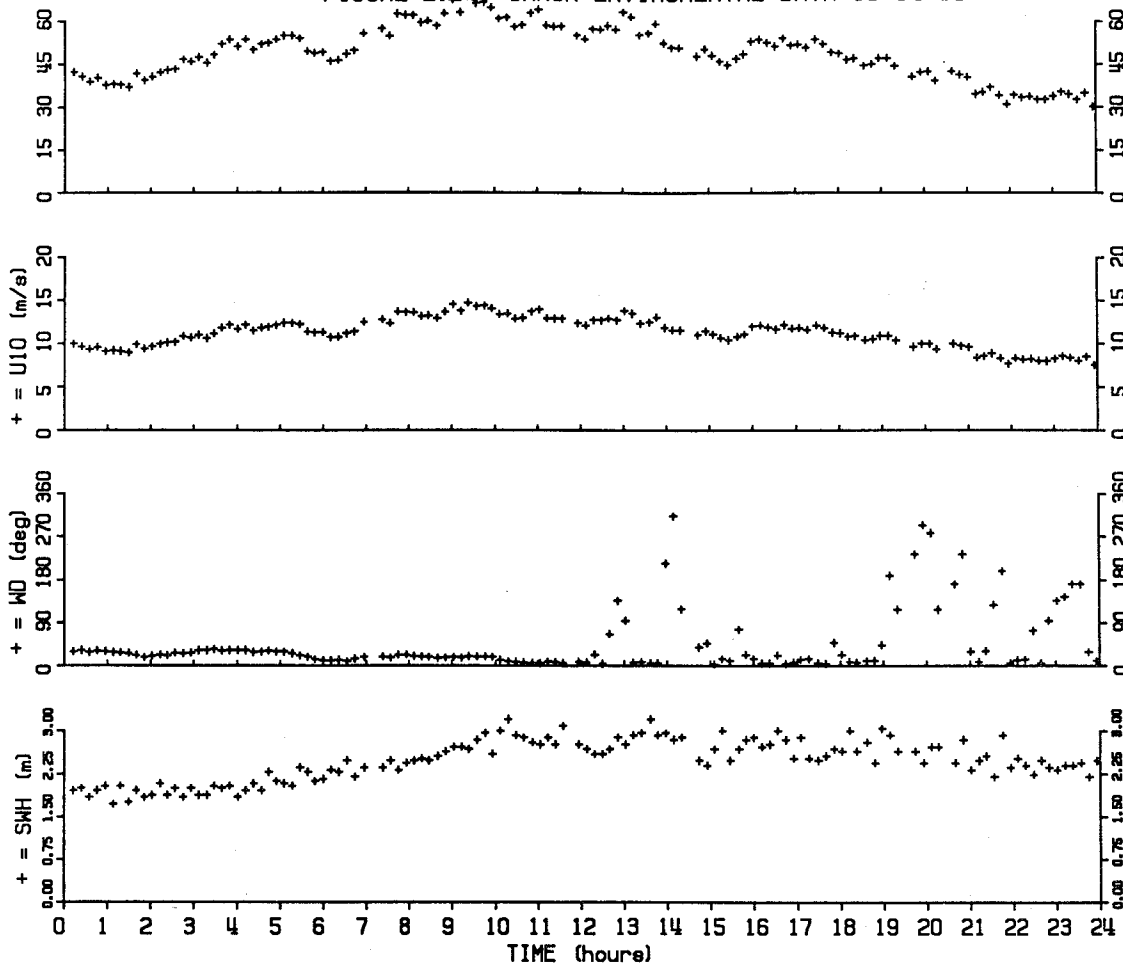
FIGURE E.15: SAXON ENVIROMENTAL DATA 10-05-88
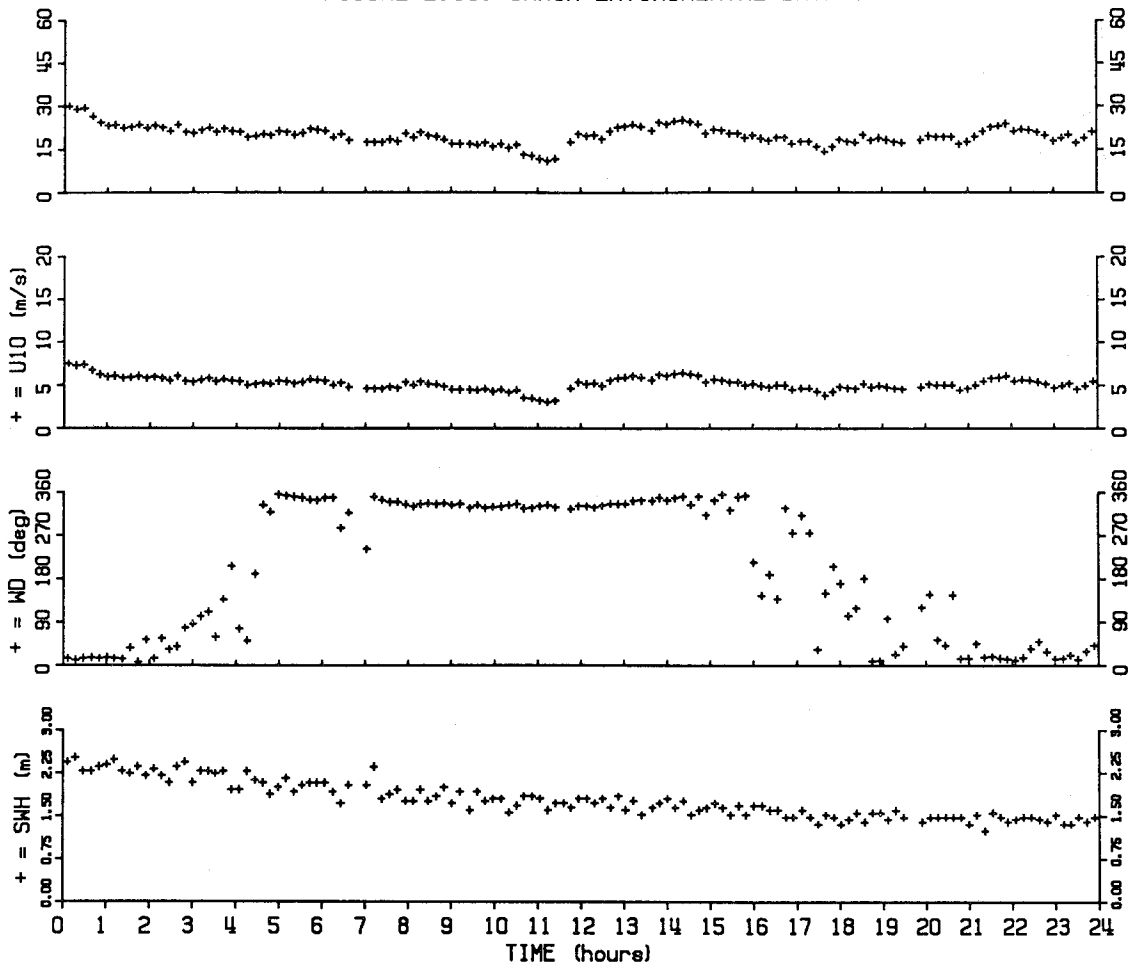
FIGURE E.16: SAXON ENVIROMENTAL DATA 10-06-88
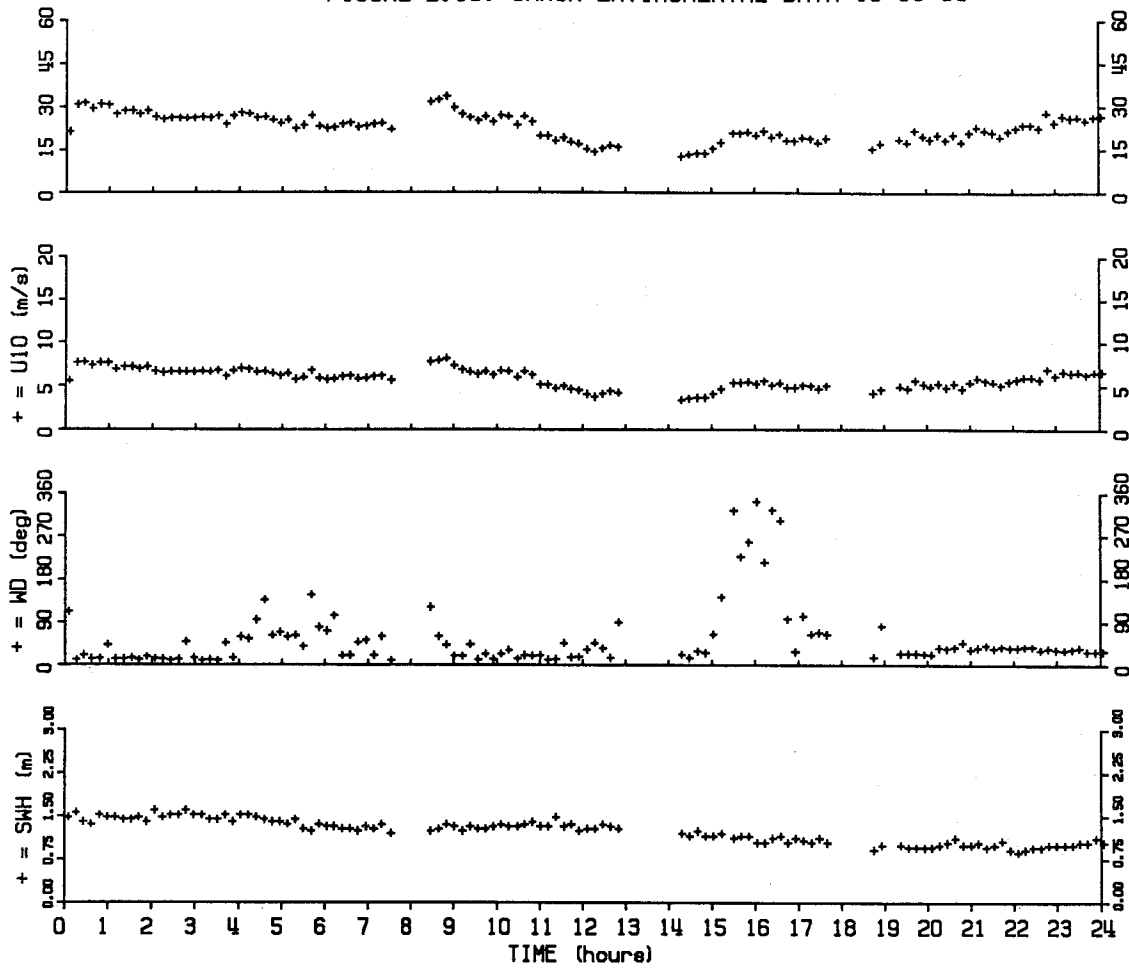
FIGURE E.17: SAXON ENVIROMENTAL DATA 10-07-88
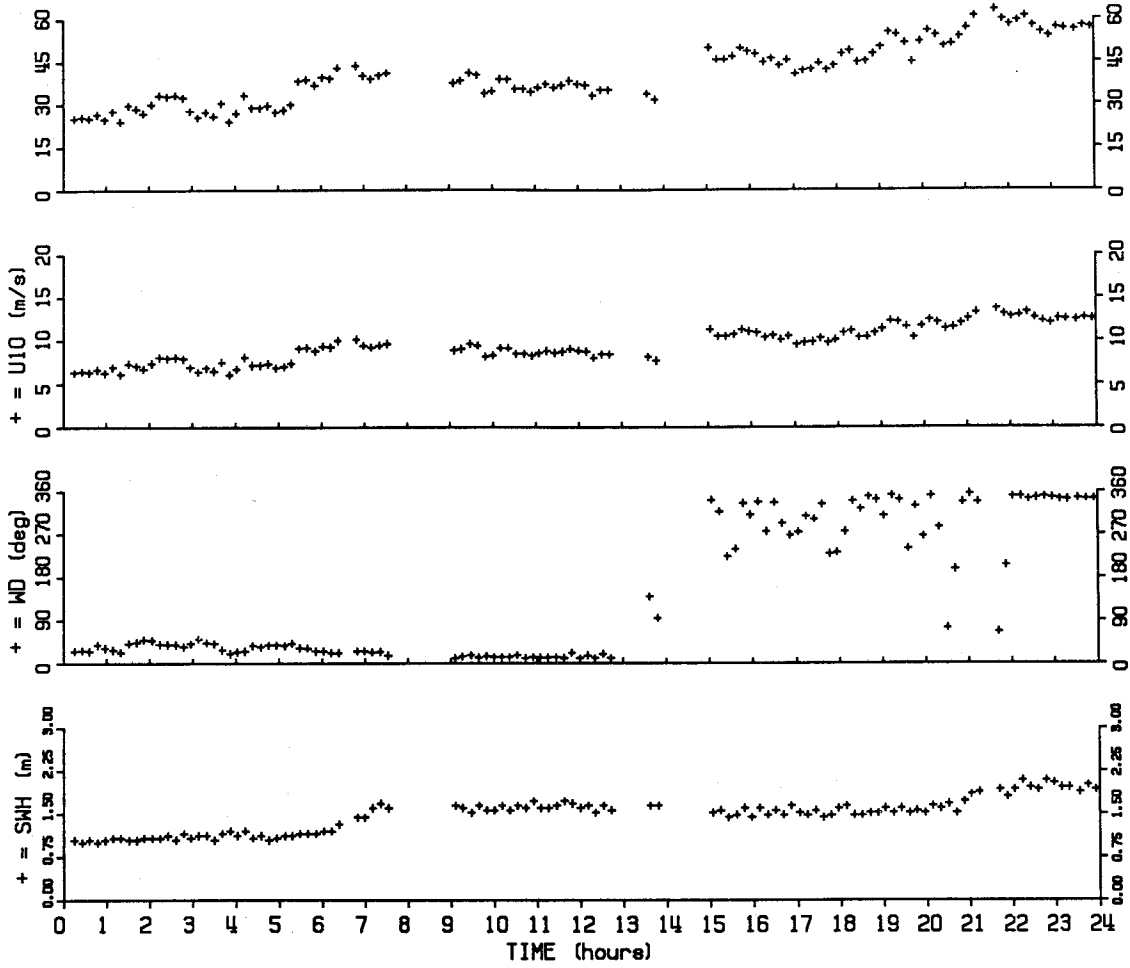
FIGURE E.18: SAXON ENVIROMENTAL DATA 10-08-88
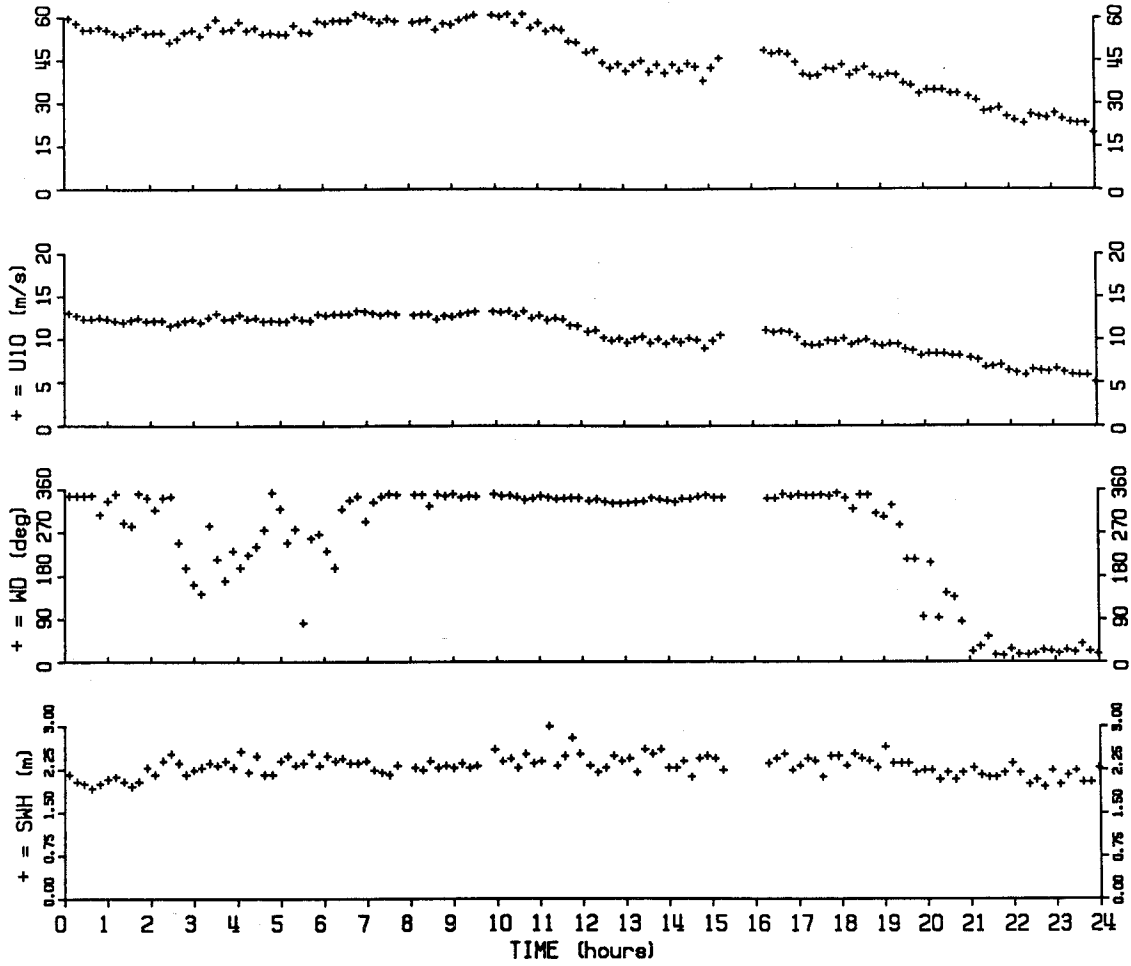
FIGURE E.19: SAXON ENVIROMENTAL DATA 10-09-88
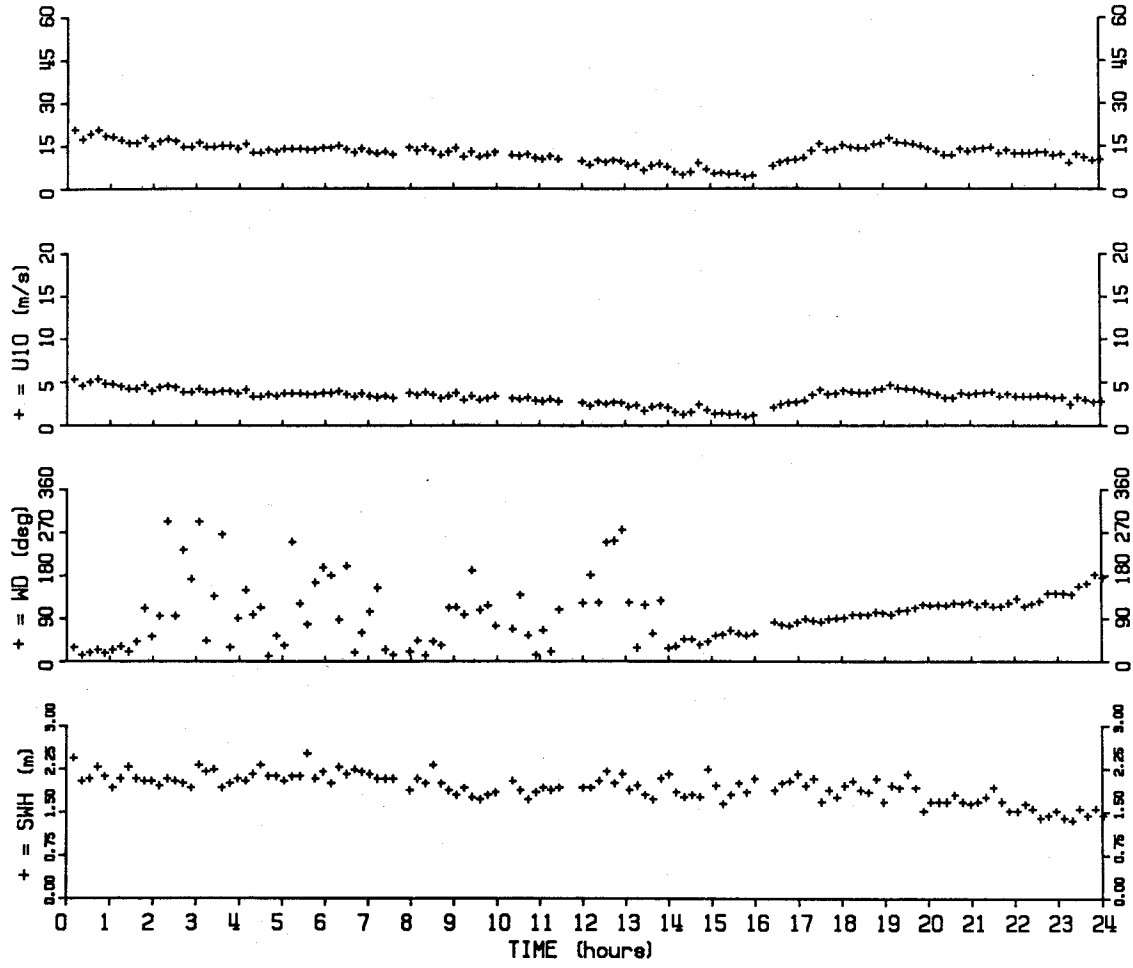
FIGURE E.20: SAXON ENVIROMENTAL DATA 10-10-88
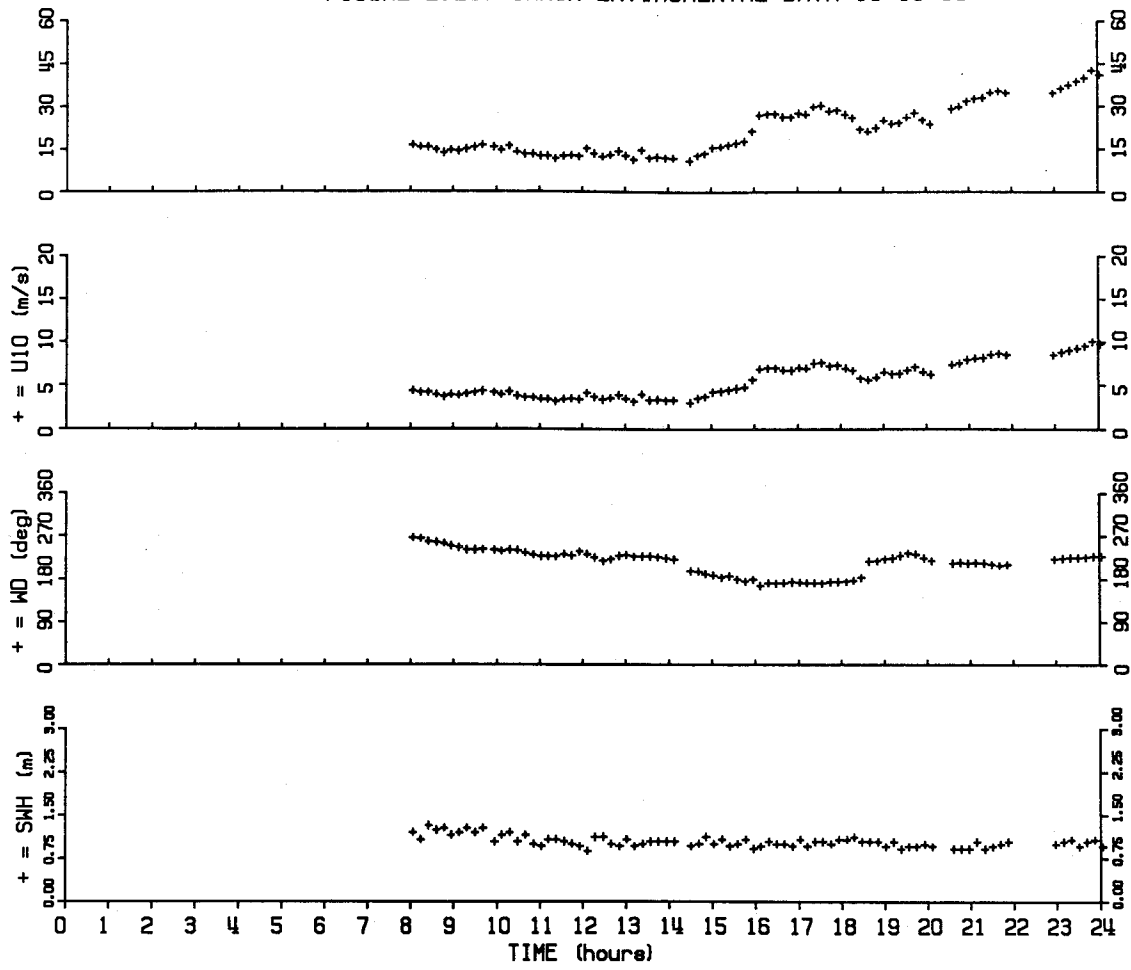
FIGURE E.21: SAXON ENVIROMENTAL DATA 10-11-88
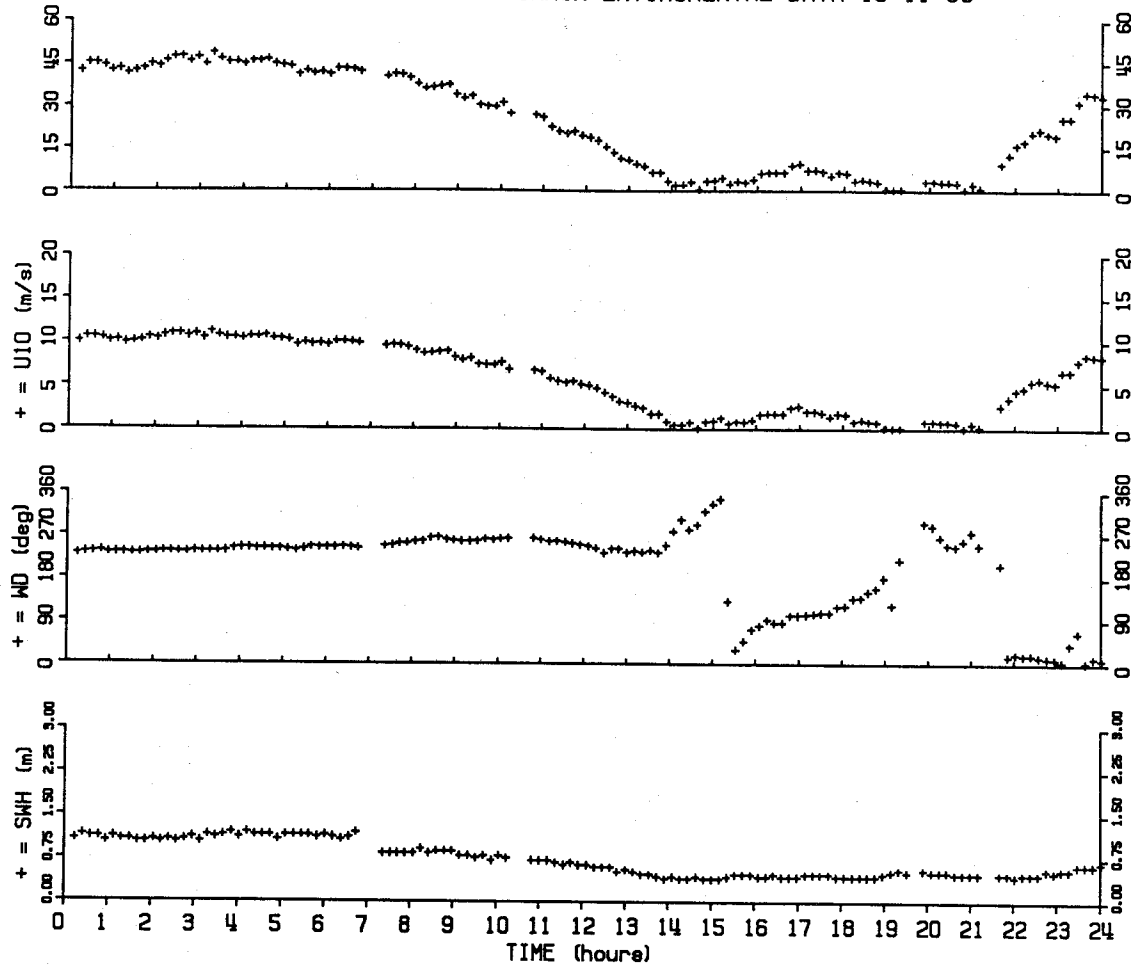
FIGURE E.22: SAXON ENVIROMENTAL DATA 10-12-88
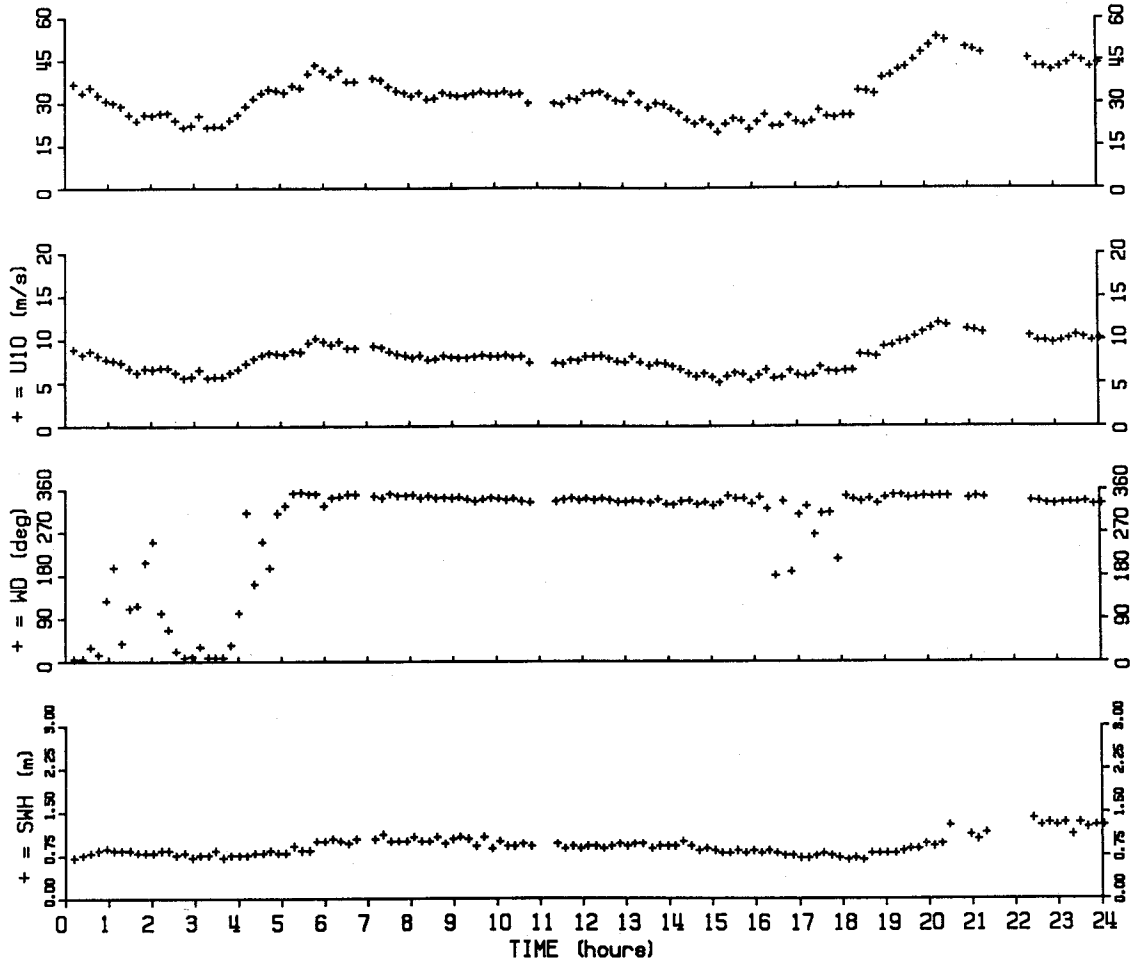
FIGURE E.23: SAXON ENVIROMENTAL DATA 10-13-88
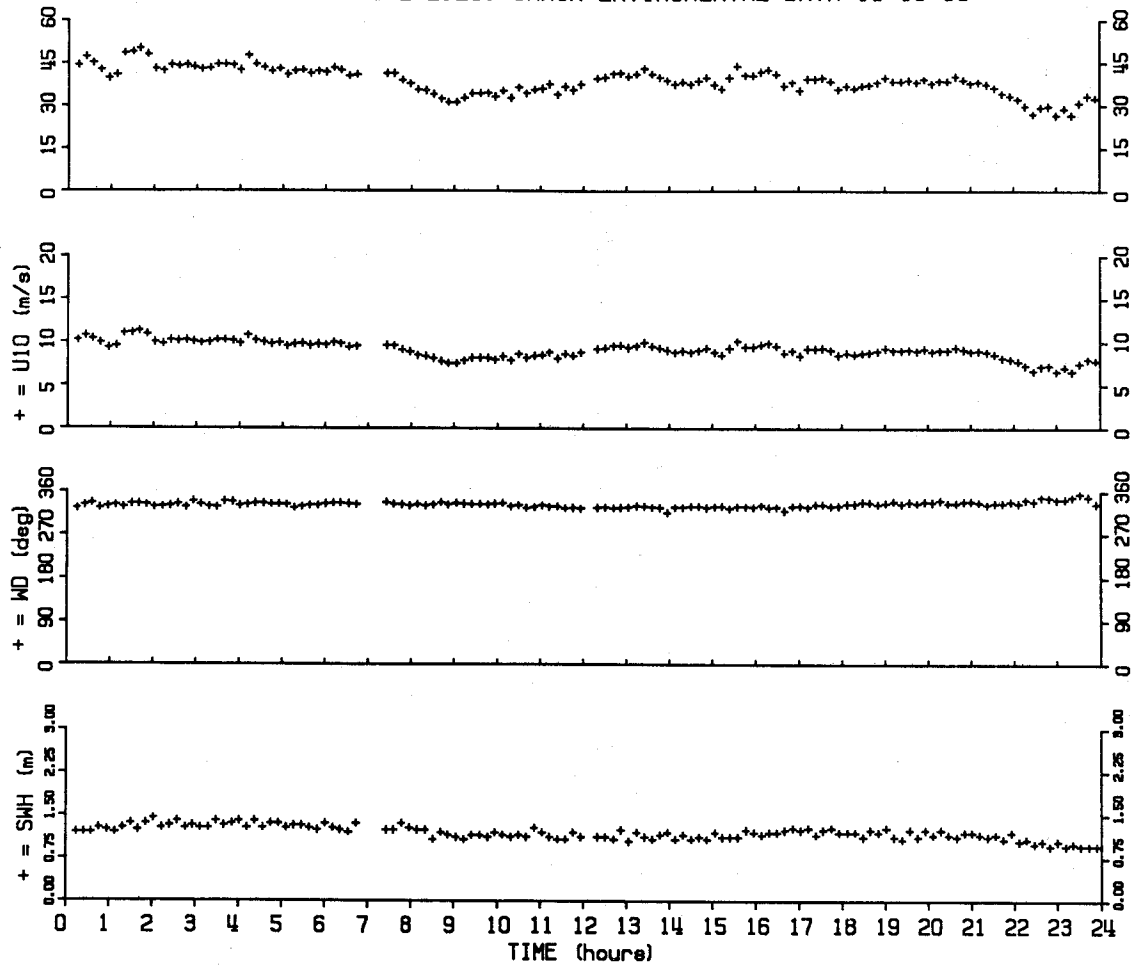
FIGURE E.24: SAXON ENVIROMENTAL DATA 10-14-88

TIME (hours)
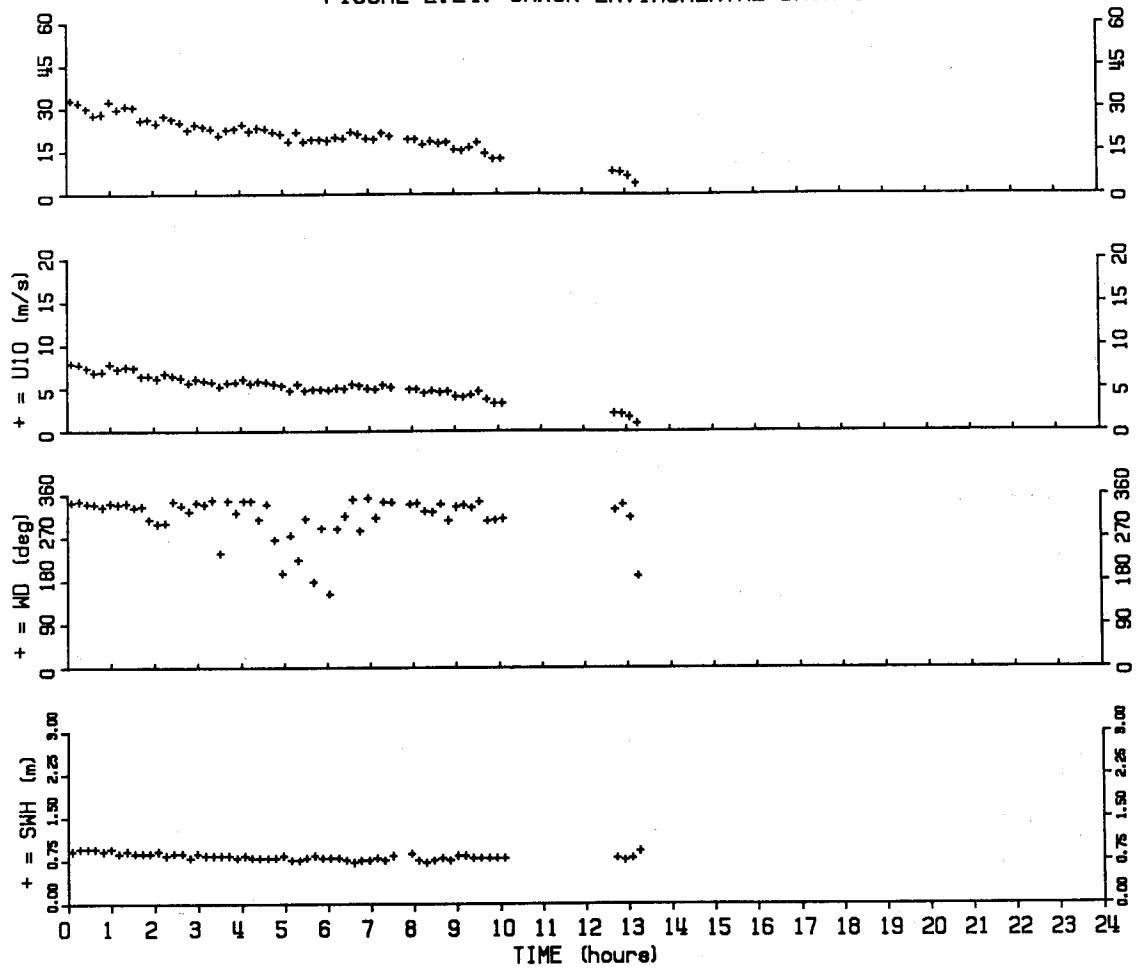
APPENDIX F: Computer Programs

This appendix contains the following Fortran computer programs and associated input files:

rtrad.for: real–time data acquisition and processing program (see Chapter 3)

rtrad.in: input file for program.for

sxbreak2.for: Program to compute statistics of microwave variables associated with individual waves passing the illumination area as defined by zero–crossings in the mean Doppler frequency record (see Chapter 4) Uses output of real–time data acquisition and processing program rtrad.for above.

sxbreak2.in: Input file for program sxbreak2.for

sxbchar3.for: Program to detect events using detection schemes number 1 through 3 (see Chapter 4). Program sxbchar4 to detect events using scheme number 4 is essentially the same except for conditional statements of eliminate events based on threshold values. Partial output of these detection programs are given in Appendix D.

sxbchar3.in: Input file for sxbchar3

calust.for: Program to compute estimates of friction velocity u^* using bulk aerodynamic formulation (see Appendix B).

calust.in   Input file for program calust.for

```
      Interface to integer*2 function getch [C] ()
      end
      Interface to integer*2 function tbhit [C] ()
      end
      Interface to subroutine comtop [C] ()
      end
      Interface to subroutine tcode [C] (time)
      character*16 time [REFERENCE]
      end
      program rtrad

C
C     PROGRAM FOR REAL TIME DATA ACQUISITION USING DAS-16 A/D BRD
C
C     PURPOSE:
C     COLLECT DATA IN BACKGROUND FROM CHANNEL 0 AND 7
C     COMPUTE MEAN, VAR, FCD, AND MSBW IN FOREGROUND
C     STORE TO DISK IN FILES OF 115200 BYTES = 20 MIN (96 BYTES /SEC)
C     IN THE FOLLOWING ORDER:
C           ipol = 1: xvar, fcd, msbw
C           ipol = 2: xvar, fcd, msbw
C           ipol = 3: xvar, fcd, msbw
C           ipol = 4: xvar, fcd, msbw
C
C           xvar     IN DIGITIZER UNITS (0 - 2048**2)
C           fcd      IN FREQUENCY UNITS (+/- 1000 HZ)
C           msbw     IN FREQUENCY UNITS (0 - 1000 HZ)
C
C     EACH FILE IS WRITTEN IN DATA BLOCKS OF 1568 BYTES (16 SEC)
C     ALL DATA ARE STORED AS I*2 BINARY NUMBERS AS FOLLOWS:
C           FOR IPOL = 1, 4:
C           dout(iout)     = int ( 2000. * int(xva-) )
C           dout(iout + 1) = int ( 10. * fcd )
C           dout(iout + 2) = int ( 10. * msbw )
C
C     INPUTS: (INITIALIZE FILE RTCV.INI)
C     filenum - NUMBER OF STARTING OUTPUT FILE
C     nstop   - NUMBER OF 20-MIN FILES TO WRITE
C     afact(4)- LONGTERM AMPLITUDE BALANCE FACTOR = SQRT(pxavg/pyavg)
C     xbarlast(4) - LONGTERM MEAN OF IN-PHASE COMPONENT
C     ybarlast(4)   LONGTERM MEAN OF OUT-OF-PHASE COMPONENT
C
C     NB:  THESE INPUTS ARE TO BE ARBITRARILY SET FOR THE 1ST DATA FILE
C          AFTER THE 1ST FILE IS GENERATED, SUBSEQUENT COMPUTATION WILL
C          USE THE MEANS AND SD FROM THE PRECEEDING 20 MIN FILE
C
C     COMPILER NOTES:
C     MUST BE COMPILED WITH DEFAULT INTEGER*2
C     USES MS 5.1 C RUNTIME LIBRARY FUNCTIONS
C
      integer iyr0, imon0, iday0
```

```
      integer ihr0, imin0, isec0, ihsec0
      integer ihr1, imin1, isec1, ihsec1
      integer iyr2, imon2, iday2
      integer ihr2, imin2, isec2, ihsec2
      integer base, intlev, dmalev
      integer ach, fch, nch
      integer bsize, fnch
      integer cntx, icnt
      integer n, trig, rcyc, ncyc, nwrite
      integer ix, ix1, ix2, ix3, iy, iy1, iy2, iy3
      integer nch11, nch12, nch13
      integer icyc, i, npts, npol, j
      integer rcode, das16, ibuf, nstart, ipol
      integer sqadr, nxoff, nyoff, nch1
      integer mode6, mode7, mode8, mode9, mode, baddr
      integer kbhit, getch
      integer nfile, iwrtml, icycml, istop, keyint, nstop
      integer iout, iwrite, filenum
      real fcd, msbw, sig0, polrat, xmean, ymean, varx, vary
      real fnpts, fnptml, dt, pi, s2pidt, pidt2
      real zzre, zzim, shat, xshat, yshet, rhmag
      real xi, xi1, xi2, xi3, yi, yi1, yi2, yi3
      real afact, af, cfac2
      real srate, n1rate, n2rate
      real fnbar, fnpavg
      real xbarlast, ybarlast
      real holdvx, holdvy
      integer data
      integer dout
      integer buffer
      real pavg, xbar, ybar
      integer param
      character*1 key
      character*8 fileid
      character*12 sumfil
      character*16 time0
      character*16 time1
      character*16 time2
C
C
C
C     ARRAY buffer MUST BE DIMENSIONED 32K TO ENSURE THAT IT STARTS AT
C     A PAGE BOUNDARY
C
      dimension buffer(32768)
      dimension data(4000)
      dimension dout(768)
      dimension pavg(2,4)
      dimension xber(4)
      dimension ybar(4)
      dimension xbarlast(4)
      dimension ybarlast(4)
```

```fortran
      dimension efact(4)
      dimension param(5)
c
      data base/#340/, intlev/3/, dmalev/1/, trig/1/, sch/0/, fch/7/
      data mode0/6/, mode7/7/, mode8/8/, mode9/9/, rcyc/1/
      data ((pavg(i,j), i=1, 2), j=1,4)/8*0./
      data nwrite /75/, ncyc/32/
      data srate/1000000./, nfrate/5/, n2rate/125/
      data fstop/0./, nfile/0/
      data time0/'    :    :    '/
      data time1/'    :    :    '/
      data time2/'    :    :    '/
c
c     ENTER INPUT PARAMETERS
c
      print *, 'REAL TIME PROCESSING rtrad: Eight channels'
      print *, 'Enter number of 16 sec records to write:'
      read(5,*) nwrite
      open(15, file = 'c:\usr\andy\rt\rtcv.ini', status = 'old')
      read(15,*) filenum
      read(15,*) nstop
      read(15,*) efact
      read(15,*) xbarlast
      read(15,*) ybarlast
c
c     OUTPUT INITIALIZING INFO TO USER
c
      print *, 'Beginning file number: ', filenum + 1
      print *, 'Number of 20-min records to write: ', nstop
      print *, 'Amplitude balance factors:'
      print *,    'pol 1: ', efact(1)
      print *,    'pol 2: ', efact(2)
      print *,    'pol 3: ', efact(3)
      print *,    'pol 4: ', efact(4)
      print *, 'DC offset adjustment:'
      print *,    'pol 1: xoff = ', xbarlast(1), ' yoff = ', ybarlast(1)
      print *,    'pol 2: xoff = ', xbarlast(2), ' yoff = ', ybarlast(2)
      print *,    'pol 3: xoff = ', xbarlast(3), ' yoff = ', ybarlast(3)
      print *,    'pol 4: xoff = ', xbarlast(4), ' yoff = ', ybarlast(4)
      print *, ' '
c
c     INITIALIZE COM1 PORT FOR TIME CODE INPUT
c
      call comlop
c
c     INITIALIZE DAS-16 A/D BOARD
c
      param(1) = base
      param(2) = intlev
      param(3) = dmalev
```

```fortran
c
      mode = 0
      rcode = das16(mode, param)
c
c     SET CHANNEL SCAN LIMITS
c
      param(1) = sch
      param(2) = fch
      nch = fch - sch + 1
      fnch = float(nch)
      mode = 1
      rcode = das16(mode, param)
c
c     SET CLOCK RATE
c
      param(1) = nfrate
      param(2) = n2rate
      srate = srate / ( param(1) * param(2) )
      bsize = int( srate / 2 )
      n = bsize / 2
      npts = n / nch
      fnpts = float(npts)
      fnptsl = fnpts - 1.
      npol = nch / 2
      mode = 17
      rcode = das16(mode, param)
c
c     SET CONTANTS FOR COVARIANCE PROCESSING
c
      dt = fnch / srate
      pi = 4. * atan(1.)
      a2pidt = sqrt(2.) * pi * dt
      p1dt2 =      2. * pi * dt
c
c     SET UP BUFFER POINTER
c
      baddr = segadr(buffer)
c
c     OPEN OUTPUT, LOG AND SUMMARY FILE (FIRST TIME)
c
      filenum = filenum + 1
      write(fileid, 40) filenum
      write(sumfil, 41) filenum
40    format('sax', i5.5)
41    format('sax', i5.5, '.sum')
      open (26, file = fileid // '.dat', access = 'direct', recl = 1536,
     1     blocksize = 1536, form = 'binary', status = 'new', err =
     1     990)
      write(26) dout
      open(16, file = fileid // '.log', status = 'new', err = 991)
```

```fortran
      open(36, file = sumfil, status = 'new', err = 992)

c
c     BEGIN DMA CONVERSION (BACKGROUND OPERATION)
c
      param(1) = bsize
      param(2) = baddr
      param(3) = trig
      param(4) = rcyc
      pause 'Press return to begin sampling:'
      write (6,5000)
      write(36,5000)
      close(36)
50    continue
      call tcode (time0)
      call gettim(ihr0, imin0, isec0, ihsec0)
c
c     BEGIN DMA CONVERSION
c
      rcode = das16(mode6, param)
      if (rcode .ne. 0)
1       print *, 'Error starting DMA, mode6: rcode = ', rcode
c
c     ENTER MAIN RECYCLE LOOP
c
      do 600 iwrite = 1, nwrite
        iout = -2
c
c     LOOP 400 IS FOR COMPUTING AND STORING  dout(7684) = 16 SEC
c
      do 400 icyc = 1, ncyc
      icnt = (iwrite - 1) * ncyc + icyc
      do 400 ibuf = 1, 2
        nstart = (ibuf - 1) * n
c
c     CHECK TO SEE IF HALF OF BUFFER IS FULL
c
100     continue
        rcode = das16(mode8, param)
        if (ibuf .eq. 1 .and. param(3) .lt. n .or.
1          (ibuf .eq. 2 .and. param(3) .gt. n) then
           go to 100
        else
c
c     TRANFER HALF OF BUFFER TO ARRAY DATA
c
        cntx = param(3)
        if (iwrite .eq. 1 .and. icyc .eq. 1 .and. ibuf .eq. 1)
1         then
          call tcode( time1 )
          call gettim(ihr1, imin1, isec1 ,ihsec1 )
```

```fortran
        endif
        if (iwrite .eq. nwrite .and. icyc .eq. ncyc .and.
1          ibuf.eq. 2) then
           call tcode( time2 )
           call gettim(ihr2, imin2, isec2, ihsec2 )
        endif
        do 390 ipol = 1, npol
          iout = iout + 3
          af = afact(ipol)
          xmean = xbarlast(ipol)
          ymean = ybarlast(ipol)

          nyoff = nch - 2*ipol
          nxoff = nyoff + 1
c
c
c     SEPERATE CHANNELS INTO TWO ARRAYS
c     SUBTACT MEAN, COMPUTE VAR, FCD, AND MSBW
c
          zzim  = 0.
          zzre  = 0.
          shat  = 0.
          xshat = 0.
          yshat = 0.
          varx  = 0.
          vary  = 0.
          do 160 i = 1, npts-3, 4
            nchi  = nch * i + nstart
            nchi1 = nchi + nch
            nchi2 = nchi + 2. * nch
            nchi3 = nchi + 3. * nch
            ix  = buffer(nchi  - nxoff)
            ix1 = buffer(nchi1 - nxoff)
            ix2 = buffer(nchi2 - nxoff)
            ix3 = buffer(nchi3 - nxoff)
            iy  = buffer(nchi  - nyoff)
            iy1 = buffer(nchi1 - nyoff)
            iy2 = buffer(nchi2 - nyoff)
            iy3 = buffer(nchi3 - nyoff)
            if ( ix .lt. 0 ) then
              xi = float( isha(ix, -4) + 2048 )
            else
              xi = float( isha(ix, -4) - 2048 )
            endif
            if ( ix1 .lt. 0 ) then
              xi1 = float( isha(ix1, -4) + 2048 )
            else
              xi1 = float( isha(ix1, -4) - 2048 )
            endif
            if ( ix2 .lt. 0 ) then
```

```fortran
          xi2 = float( isha(ix2, -4) + 2048 )
        else
          xi2 = float( isha(ix2, -4) - 2048 )
        endif
        if ( btest(ix3, 15) ) then
          xi3 = float( isha(ix3, -4) + 2048 )
        else
          xi3 = float( isha(ix3, -4) - 2048 )
        endif
        if ( iy .lt. 0 ) then
          yi = float( isha(iy, -4) + 2048 )
        else
          yi = float( isha(iy, -4) - 2048 )
        endif
        if ( iy1 .lt. 0 ) then
          yi1 = float( isha(iy1, -4) + 2048 )
        else
          yi1 = float( isha(iy1, -4) - 2048 )
        endif
        if ( iy2 .lt. 0 ) then
          yi2 = float( isha(iy2, -4) + 2048 )
        else
          yi2 = float( isha(iy2, -4) - 2048 )
        endif
        if ( iy3 .lt. 0 ) then
          yi3 = float( isha(iy3, -4) + 2048 )
        else
          yi3 = float( isha(iy3, -4) - 2048 )
        endif
c
c     COMPUTE MEAN (DC OFFSET)
c
        xbar(ipol) = xbar(ipol) + xi + xi1 + xi2 + xi3
        ybar(ipol) = ybar(ipol) + yi + yi1 + yi2 + yi3
c
c     REMOVE MEAN BASED ON LAST RECORD
c
        xi  = xi  - xmean
        xi1 = xi1 - xmean
        xi2 = xi2 - xmean
        xi3 = xi3 - xmean
        yi  = yi  - ymean
        yi1 = yi1 - ymean
        yi2 = yi2 - ymean
        yi3 = yi3 - ymean
c
c     LINEAR INTERPOLATION TO CORRECT FOR TIME DELAY DUE TO SEQUENTIAL
c     SAMPLING OF A/D BOARD
c
        yi2 = yi2 - (yi2-yi1) / fnch
```

```fortran
c
        yi1 = yi1 - (yi1-yi) / fnch
        zzim = zzim + xi1 * yi2 - xi2 * yi1
        zzre = zzre + xi2 * xi1 + yi2 * yi1
        xshat = xshat + xi1 * xi1 + xi2 * xi2
        yshat = yshat + yi1 * yi1 + yi2 * yi2
        varx = varx + xi*xi + xi3*xi3
        vary = vary + yi*yi + yi3*yi3
160     continue
        rhmag = sqrt( zzim * zzim + zzre * zzre )
        holdvx = (varx + xshat) / fnptm1
        dout(lout) = int( 2000. * alog(holdvx) )
        dout(lout+1) =
1       int( 10. * atan2 ( zzim, zzre ) / pidt2 )
        dout(lout+2) =
1       int ( 10. * sqrt( abs( alog( (xshat+yshat)
1                    / rhmag / 2. ) ) ) / s2pidt )
        pavg(1,ipol) = pavg(1,ipol) + holdvx
        pavg(2,ipol) = pavg(2,ipol)
1                    + (vary + yshat) / fnptm1
390     continue
        endif
c
c     CHECK TO SEE THAT COMPUTATION COMPLETES BEFORE NEXT BUFFER FILLS
c
        rcode = das16(mode8, param)
        if( ibuf .eq. 1 .and. param(3) .lt. n .or.
1          ibuf .eq. 2 .and. param(3) .gt. n) then
          write(16,*)                      '****WARNING****'
          write(16,*) 'Buffer ', ibuf, ' has been over run'
          write(16,*)                  lcnt = ', lcnt
          write(16,*)                  fill count = ', cntx
          write(16,*)                  end proc count = ', param(3)
        endif
        rcode = das16(mode8, param)
400     continue
c
c     WRITE 1536 BYTES TO OUTPUT FILE
c
        write(26) dout
c
c     CHECK TO SEE THAT WRITE WAS COMPLETED BEFORE NEXT BUFFER FILLS
c
        rcode = das16(mode8, param)
        if( param(3) .gt. n) then
          write(16,*) 'Write has overrun Buf 2 '      '****WARNING****'
          write(16,*)                  lcnt = ', lcnt
          write(16,*)                  fill count = ', cntx
          write(16,*)                  end write count = ', param(3)
        endif
```

```
600 continue
c
c     SHUT DOWN DMA
c
      rcode = das16(mode7,param)
      nfile = nfile + 1
      close (26)
      write(16,*) '"SAXON EXPERIMENT FALL 1988: MIT/NRL SCATTEROMETERY"'
      write(16,*) 'REAL TIME DATA AQUISITION AND PROCESSING'
      write(16,*)'OUTPUT FILE ID: ', fileid // '.dat'
      write(16,*)'Amplitude balance factors:'
      write(16,*)    pol 1: ', afact(1)
      write(16,*)    pol 2: ', afact(2)
      write(16,*)    pol 3: ', afact(3)
      write(16,*)    pol 4: ', afact(4)
      write(16,*)'DC offset adjustment:'
      write(16,*)    pol 1: i = ', xbarlast(1), ' q = ', ybarlast(1)
      write(16,*)    pol 2: i = ', xbarlast(2), ' q = ', ybarlast(2)
      write(16,*)    pol 3: i = ', xbarlast(3), ' q = ', ybarlast(3)
      write(16,*)    pol 4: i = ', xbarlast(4), ' q = ', ybarlast(4)
      write(16,*)'TRIG TIMING:'
      write(16,54) time0
      write(16,55) time1
      write(16,56) time2
      write(16,*) 'COMPUTER TIMING:'
      write(16,57) ihr0, imin0, isec0, ihsec0
      write(16,58) ihr1, imin1, isec1, ihsec1
      write(16,59) ihr2, imin2, isec2, ihsec2
54 format(' DMA start : ', a16)
55 format(' First buf1: ', a16)
56 format(' Last buf2 : ', a16)
57 format(' DMA start : ', i3.3, ':', i2.2, ':', i2.2, '.', i2.2)
58 format(' First buf1: ', i3.3, ':', i2.2, ':', i2.2, '.', i2.2)
59 format(' Last buf2: ', i3.3, ':', i2.2, ':', i2.2, '.', i2.2)
      iwrtal = iwrite - 1
      icycm1 = icyc   -1
c
c     SET CONSTANTS AND FACTORS FOR NEXT 20 MIN RECORD
c
      write(16,*) 'VARIANCE AND DC OFFSET BY POL FOR FILEID: ', fileid
      fnpavg = float(2 * iwrtal * icycm1)
      fnbar = fnpavg * fnpts
      do 610 i = 1, 4
      xbarlast(i) = xbar(i) / fnbar
      ybarlast(i) = ybar(i) / fnbar
      afact(i) = sqrt( pavg(1,i) / pavg(2,i) )
      pavg(1,i) = pavg(1,i) / fnpavg
      pavg(2,i) = pavg(2,i) / fnpavg
      write(16,607) i, 10. * alog10( pavg(1,i) ), xbarlast(i)
      write(16,608) i, 10. * alog10( pavg(2,i) ), ybarlast(i)
```

```
c
c     NOTE: FOLLOWING ZERO ASSIGNMENTS SHOULD BE REMOVED FOR FINAL RUN
c
c
      xbarlast(i) = 0.
      ybarlast(i) = 0.
      afact(i) = 1.
610 continue
      close(15)
      write(6,5001) time1,
     1    ( (10. * alog10( pavg(i,j) ), i = 1, 2 ), j = 1, 4)
      open(36, file = sumfil)
      do 615 ilin = 1, nfile
      read (36,*)
      write(36,5001) time1,
     1    ( (10. * alog10( pavg(i,j) ), i = 1, 2), j = 1, 4)
615
      close(36)
      do 616 i = 1, 4
      pavg(1,i) = 0.
      pavg(2,i) = 0.
      xbar(i) = 0.
      ybar(i) = 0.
616 continue
      open(15, file = 'c:\usr\andy\rt\rtcv.ini', status = 'old')
      write(15,*) filenum,            FILE NUMBER: 5 DIGIT MAX
      write(15,*) nstop,              NUMBER OF 10 MIN RECORDS TO WRITE
      write(15,*) afact,              AFACT
      write(15,*) xbarlast,           XBAR
      write(15,*) ybarlast,           YBAR
      close(15)
      if (istop .eq. 1) go to 620
c
c     CHECK IF KEYBOARD HAS BEEN STRUCK
c
      if (kbhit() .gt. 0) then
        keyint = getch()
        if (keyint .eq. 83 .or. keyint .eq. 115) then
          write(16,*) 'Program terminated from keyboard CODE 2'
          go to 620
        else
          key = keyint
          write(16,*) 'KEY ', key, ' WAS PRESSED'
        endif
      endif
      close(16)
c
c     CHECK TO SEE IF NUMBER OF FILES REQUESTED HAVE BEEN WRITTEN
c
      if (nfile .ge. nstop) then
        go to 620
      else
```

```
c
c     OPEN NEXT OUTPUT AND LOG FILE
c
        filenum = filenum + 1
        write(fileid, 40) filenum
        open (26, file = fileid // '.dat', access = 'direct',
     1       recl = 1536, blocksize = 1536, form = 'binary',
     2       status ='new', err = 990)
        open(16, file = fileid // '.log', status = 'new', err = 991)
617     do 617 izero = 1, 768
        dout(izero) = 0
        write(26) dout
        param(1) = bsize
        param(2) = baddr
        param(3) = trig
        param(4) = rcyc
        go to 50
        endif
620     continue
607     format(' sigma0-i-', i1, ':', f6.2, ' dB   mean:', f6.1)
608     format(' sigma0-q-', i1, ':', f6.2, ' dB   mean:', f6.1)
5000    format(
     1' day:hr:min:sec.msc sct1-i sct1-q sct2-i sct2-q slt1-i slt1-q'
     1' slt2-i slt2-q ')
c  XX:XX:XX:XX.XXX XXX.XX XXX.XX XXX.XX XXX.XX XXX.XX XXX.XX
c  12345678901234567890123456789012345678901234567890
5001    format(1x, a15, 8(1x, f6.2))
c
3000    format(a)
        go to 999
990     write(16,*) 'Error 990 - opening output file, unit 26',
     1        fileid // '.dat'
        print *,   'Error 990 - opening output file, unit 26',
     1        fileid // '.dat'
        go to 999
991     write(16,*) 'Error 991 - opening log file, unit 16',
     1        fileid // '.log'
        print *,   'Error 991 - opening log file, unit 16',
     1        fileid // '.log'
        go to 999
992     write(16,*) 'Error 992 - opening log file, unit 16',
     1        sumfil
        print *,   'Error 992 - opening log file, unit 16',
     1        sumfil

999     end
```

FILE NUMBER: 5 DIGIT MAX
NUMBER OF 10 MIN RECORDS TO WRITE
XBAR
YBAR

```
2
1
2.904625      -24.658890
23.842170     -45.824540
```

```
      program sxbreak2

c     12-8-89: MDFY TO DO SAXTAPE FILES IF DESIRED
c            - CHANGED DIMENSION OF ARRAYS LIKE sigvv
c            - MAKE SURE NUMBER OF POINTS npts IS CHANGED IN INPUT
c            - ASSIGN spdfac BASED ON FILENAMES AND RUN NUMBER
c
c     10-29-89: MDFY FRM sxbreak1 FOR FINAL COMPUTATIONS:
c            - COMPUTE SLOPE AND ACC FOR FCUT=0.6 ONLY
c            - COMPUTE VARIANCE OF USTAR AND U10
c
c     9-26-89: PROGRAM TO COMPUTE JOINT STATISTICS OF WAVES DEFINED BY
c     ZERO CROSSING IN DOPPLER FREQ.  ALSO COMPUTES PEAK FREQ  AND
c     RMS SLOPE FROM PREVIOUSLY COMPUTED WAVE HEIGHT SPECTRA FROM DOP
c
c     FOR USE WITH SAXON DATA PROCESSED IN THE FIELD
c
      real sigvv(4736), sighh(4736), fd(4736), bw(4736), pr(4736)
      real svmax(1000), shmax(1000), fdmax(1000), bwmax(1000)
      real fdpk(1000), prmin(1000)
      real vss1(1000), vss2(1000), hss1(1000), hss2(1000)
      real kah(257), wpad(257)
      real junk(300)
      real u10(6), ustar(6)
      integer idata0(28416)
      integer karray(2)
      real sfreq, deltaf, fpk, fcut1, fcut2, fcut3, g, fact
      real vvcal, hhcal, gain, spdfac, u10bar, usbar, u10var, usvar
      real fdbar, fdchk, svbar, shbar, bwbar, ss1, ss2
      real svchk, shchk, fdcut, vacc3, vvsig0, hhsig0
      real fdavg, bwchk, rms, srms3, ymax
      integer nfile, npts, nwave, istart, npath, nsmth
      integer i, ipt, iteft, j, ifile, nhrs, ihr, lpk, icut
      integer iout, iwave, nspec, no2p1, nwidth
      integer ivmax, ihmax, ifmax, ibmax
      integer ncut3
      character*8 yfile, sfile, ofile
      character*25 path
c
      data vvcal/3.30e-7/, hhcal/4.26e-7/, nspec/512/, sfreq/4./
      data fcut3/0.6/, istart/11/
      data karray/2, 1/, nsmth/2/, g/9.8/, nwidth/10/
      no2p1 = nspec / 2 + 1
      deltaf = sfreq / float(nspec)
      ncut3 = int( fcut3 / deltaf ) + 1
      fact = deltaf * deltaf * ( 8. * atan(1.) )**2 / g
c
      open (35, file = 'kshallow.dt2')
      read (35,*) (ksh(i), i = 1, no2p1)
```

```
c
c     READ IN NUMBER OF DATA FILES TO PROCESS
c
      open (15, file = 'sxbreak2.in')
      read(15,*) nfile
      read(15,*) npts
      read(15,*) fdcut
      read(15,*) gain
      read(15,'(a)') path
      do 10 i = 1, 25
      j = 26 - i
      if(path(j:j) .ne. ' ') go to 20
10    continue
20    npath = j
      gain = 10.**(gain / 10.)
c
c     LOOP FOR EACH HOUR - PROCESS SIX 10-MIN FILES AT A TIME
c
      nhrs = nfile / 6
      print *, 'nhrs = ', nhrs
      do 700 ihr = 1, nhrs
      print *, 'ihr = ', ihr
      nwave = 0
      fdavg = 0.
      vvsig0 = 0.
      hhsig0 = 0.
c
c     LOOP FOR EACH 10-MINUTE FILE
c
      do 500 ifile = 1, 6
      read (15,'(a8, 16x, 2(1x, f5.3))') yfile, ustar(ifile),
     1                                   u10(ifile)
c
c     ASSIGN spdfac AS REQUIRED:
c     - FIELD DATA: spdfac = 10
c     - TAPE DATA PLAYED AT 4 TIMES: spdfac = 40 (ALL EXCEPT RUN12)
c     - TAPE DATA PLAYED AT 2 TIMES: spdfac = 20 (RUN 12 ONLY)
c
      if (yfile(1:3) .eq. 'sax') then
      spdfac = 10.
      ioff = 12
      else
      num = ( ichar(yfile(8:8)) - 48 ) +
     1      ( ichar(yfile(7:7)) - 48 ) * 10 +
     2      ( ichar(yfile(6:6)) - 48 ) * 100
      ioff = 6
      if (num .le. 239) then
      spdfac = 40.
      else
```

```fortran
      spdfac = 20.
      endif
c
      if (ifile .eq. 3) afile = yfile
      if (ifile .eq. 4) ofile = yfile
c
c  NB: SPECTRA FOR EACH HOUR IS IN FILE NAMED AFTER 3RD 10-MIN FILE
c      IN EACH GROUP OF SIX MAKING UP THE HOUR
c
      open (25, file = path(1:npath) // '\' // yfile // '.dat',
     1    access = 'direct', recl = 8192, blocksize = 8192,
     2    form = 'binary', status = 'old')
c
c  READ IN DATA
c
      read(25) idata0
      iout = 1
c
      do 150 ipt = 1, npts
      sigvv(ipt) = gain * vvcal *
     1    expt float(idata0(iout + 1) ) / spdfac
      fd(ipt) = float(idata0(iout + 1) ) / spdfac
      bw(ipt) = float(idata0(iout + 2) ) / spdfac
      sight(ipt) = gain*hhcal *
     1    expt float( idata0(iout+3) )/ 2000.)
      pr(ipt) = sigvv(ipt) / sighh(ipt)
      iout = iout + ioff
150   continue
c
c  COMPUTE AND MEAN FROM fd
c
      call bar(fd, npts, fdbar)
      call bar(bw, npts, bwbar)
      call bar(sigvv, npts, svbar)
      call bar(sighh, npts, shbar)
      fdavg = fdavg + fdbar
      vvsig0 = vvsig0 + svbar
      hhsig0 = hhsig0 + shbar
c
c  FIND FIRST ZERO UPCROSSING IN DOPPLER FREQ RECORD fd
c
      do 100 i = 1, npts
      fd(i) = fd(i) - fdbar
      if (fd(i) .le. 0. .and. fd(i+1) .gt. 0.) go to 110
100   continue
110   ileft = i
      do 500 i = ileft+1, npts-1
      fd(i) = fd(i) - fdbar
      if (fd(i) .le. 0. .and. fd(i+1) .gt. 0.) then
      call iclmax(fd, ileft, i, fdchk, ifmax)
```

```fortran
      call iclmax(sigvv, ileft, i, svchk, ivmax)
      call iclmax(sighh, ileft, i, shchk, ihmax)
      call iclmax(bw, ileft, i, bwchk, ibmax)
      if (fdchk .lt. fdcut) go to 490
      if (svchk .lt. svbar) go to 490
      if (shchk .lt. shbar) go to 490
      if (bwchk .lt. bwbar) go to 490
      nwave = nwave + 1
      call sscon(sigvv, npts, nwidth, ivmax, svbar, ss1, ss2)
      vss1(nwave) = ss1
      vss2(nwave) = ss2
      call sscon(sighh, npts, nwidth, ihmax, shbar, ss1, ss2)
      hss1(nwave) = ss1
      hss2(nwave) = ss2
      fdmax(nwave) = fdchk
      fdpk(nwave) = fd(ifmax)
      svmax(nwave) = svchk
      shmax(nwave) = shchk
      bwmax(nwave) = bwchk
      prmin(nwave) = sigvv(ivmax) / sighh(ihmax)
      ileft = i
490   endif
500   continue
      call barvar(u10, 6, u10bar, u10var)
      call barvar(ustar, 6, usbar, usvar)
      open(35, file = sfile//'.psd', access = 'direct', recl = 1028,
     1    form = 'binary')
      read (35) wpsd
      call smooth(wpsd, junk, no2p1, karray, nsmth)
      rms = 0.
      srms3 = 0.
      vacc3 = 0.
      ymax = 0.
      do 550 i = istart, ncut3
      rms = rms + wpsd(i)
      srms3 = srms3 + ksh(i) * ksh(i) * wpsd(i)
      vacc3 = vacc3 + ( float(i-1) )**4 * wpsd(i)
      if (wpsd(i) .gt. ymax) then
      ymax = wpsd(i)
      ipk = i
      endif
550   continue
      do 580 i = ncut3+1, no2p1
      rms = rms + wpsd(i)
      if (wpsd(i) .gt. ymax) then
      ipk = i
      ymax = wpsd(i)
      endif
580   continue
      rms = sqrt ( rms * deltaf )
```

```
      srms3 = sqrt ( srms3 * deltaf)
      vacc3 = fact * sqrt( deltaf * vacc3)
      fpk = float(ipk-1) * deltaf
c
c     WRITE OUTPUT FOR THIS HOUR
c
      u10var = sqrt(u10var)
      usvar = sqrt(usvar)
      open (16, file = ofile // '.bk2')
      write (16,1000) ofile, u10bar, u10var, usbar, usvar, fdavg/6.,
     1      nwave, fpk, rms, srms3, vacc3, vvsig0/6., hhsig0/6.
      do 600 iwave = 1, nwave
      write(16, 2000) svmax(iwave), shmax(iwave), prmin(iwave),
     1      fdmax(iwave), fdpk(iwave), bumax(iwave), vas1(iwave),
     2                          vas2(iwave), hss1(iwave), hss2(iwave)
600   continue
1000  format(a8, 1x, f5.2, 1x, f4.3, 1x, f4.3, 1x, f5.4, 1x, f4.1,
     1      1x, i4, 2(1x, f4.3), 2(1x, f5.4), 2(1x, f5.4) )
2000  format(2(f6.4, 1x), 1x, f4.2, 3(1x, f5.1), 4(1x, e9.3) )
      stop
      end
c
c
c
      subroutine lclmax(x, il, ir, xmax, imax)
c
c     SUBROUTINE TO FIND LOCAL MAXIMUM xmax OF ARRAY x(i) FOR
c                         il <= i <= ir
c
      real x(1)
      real xmax
      integer i, il, ir, imax
c
      xmax = -1e20
      do 100 i = il, ir
        if (x(i) .gt. xmax) then
          xmax = x(i)
          imax = i
        endif
100   continue
      return
      end
c
c
      subroutine bar(x, n, xbar)
c
c     SUBROUTINE TO COMPUTE  xbar OF ARRAY x
c
```

```
      real x(1)
      real xbar
      integer i, n
c
      xbar = 0.
      do 100 i = 1, n
100   xbar = xbar + x(i)
      xbar = xbar / float(n)
      return
      end
c
c
      subroutine wavg(x, i, iwd, ravg)
c
c     SUBROUTINE TO COMPUTE WEIGHTED AVG OF HALF-WIDTH iwd ON x AT i
c     ALL POINTS WEIGHTED AS 1 EXCEPT END POINT ARE 0.5
c
      real x(1)
      integer i, iwd, j
      real ravg
c
      if ( i-iwd .le. 0 ) then
          ravg = x(i)
          return
      endif
      ravg = 0.5 * ( x(i-iwd) + x(i+iwd))
      do 100 j = -(iwd-1), iwd-1
100   ravg = ravg + x(i+j)
      ravg = ravg / float(2 * iwd)
      return
      end
```

```
36      nfile
4735    npts - number of points per file
0.      fdcut
6.      gain
h:\saxtape\run12
sxt00249 286:22:45 .480 .425 10.45
sxt00250 286:22:55 .435 .420 10.35
sxt00251 286:23:05 .381 .417 10.27
sxt00252 286:23:15 .383 .428 10.52
sxt00253 286:23:25 .455 .443 10.82
sxt00254 286:23:35 .507 .456 11.09
sxt00255 286:23:45 .414 .443 10.82
sxt00256 286:23:55 .469 .427 10.49
sxt00257 287:00:04 .439 .438 10.73
sxt00258 287:00:14 .449 .443 10.82
sxt00259 287:00:24 .560 .456 11.09
sxt00260 287:00:34 .479 .463 11.23
sxt00288 287:07:15 .444 .413 10.10
sxt00289 287:07:25 .517 .413 10.12
sxt00290 287:07:35 .665 .414 10.14
sxt00291 287:07:45 .443 .404 9.92
sxt00292 287:07:55 .393 .385 9.52
sxt00293 287:08:04 .409 .371 9.22
sxt00302 287:09:34 .383 .344 8.64
sxt00303 287:09:43 .396 .344 8.64
sxt00304 287:09:53 .408 .340 8.56
sxt00305 287:10:03 .330 .337 8.50
sxt00306 287:10:13 .367 .346 8.69
sxt00307 287:10:23 .466 .334 8.42
sxt00264 287:13:00 .339 .411 10.11
sxt00265 287:13:10 .371 .406 10.01
sxt00266 287:13:20 .420 .417 10.24
sxt00267 287:13:30 .453 .428 10.47
sxt00268 287:13:40 .551 .410 10.08
sxt00269 287:13:50 .532 .398 9.83
sxt00270 287:13:59 .596 .387 9.58
sxt00271 287:14:09 .599 .376 9.35
sxt00272 287:14:19 .381 .383 9.51
sxt00273 287:14:29 .422 .380 9.43
sxt00274 287:14:39 .591 .380 9.45
sxt00275 287:14:49 .602 .391 9.69
```

```fortran
      program sxbchar3
c
c     10-31-89: MDFY FRM sxbchar1 TO PROCESS MULTIPLE THRESHOLDS
c
c     10-29-89: PROGRAM TO COMPUTE AVERAGE SEA SPIKE PARAMETERS FROM
c     OUTPUT FILES *.bk2 GENERATED BY PROGRAM sxbreak2.for
c
c
      character*16 infile(50)
      character*12 ofile
      character*8 fname
      real ksh(257)
      real u10, uster, fpk, rms, vacc, ytfrat, ydelta, dx, slsqo2, pct
      real sigvv, sighh, fd, bw, pr, g, sfreq, deltaf, a2sqo2
      real pi, twopi, tamda, fnpts, fsec, uoc, fnbrk
      real vvcut, hhcut, prcut, bwcut, a4, funk
      real twopi4, fdrift, svbar, shbar, prbar, fdbar, bwbar, bwnor
      real vv0, hh0, vs1con, vs2con, hs1con, hs2con, vs1, vs2, hs1, hs2
      integer iylen, nwave, ifile, nfile, ipt, nmax, nspec, lpt, inc
      integer nplot, ioport, model, ilntyp, i, iplt, nbreak
      integer iablen, ndeca, l, isym
c
      data rmax/800/, g/9.8/
      data nspec/512/, sfreq/4./, inc/1/, fnpts/14208/, fsec/3352./
c
      pi = 4. * atan(1.)
      twopi = 2. * pi
      twopi4 = twopi**4
      deltaf = sfreq / float(nspec)
c
      open(15, file = 'sxbchar3.in')
      read(15,*) nfile
      do 10 ifile = 1, nfile
10    read(15,'(a)') infile(ifile)
c
c     READ IN SHALLOW WATER WAVE NUMBER ARRAY CORRESPONDING TO DISCRETE
c     FREQUENCY OF WAVE HEIGHT SPECTRUM:
c
      open(35, file = 'kshallow.d12')
      read(35,*) ksh
      read (15,*) nthrsh
      open(26, file = 'sxbchar3.out', status = 'new')
c
c     LOOP THROUGH EACH THRESHOLD COMBINATION
c
      print *, 'ENTER ID NUMBER TO START (THREE DIGITS):'
      read (5,*) iadd
      do 500 ithrsh = 1, nthrsh
      writeofile, '(5hsxb3-, i3.3, 4h.out)') ithrsh+iadd-1
```

```fortran
      read(15, *) vvcut, hhcut, prcut, bwcut
      print *, ofile, vvcut, hhcut, prcut, bwcut
      open (16, file = ofile, status = 'new')
      write(16, '( 3(f4.2, 1x), f3.0 )' ) vvcut, hhcut, prcut, bwcut
      write(26, '( 1x, a8, 3(f4.2, 1x), f3.0 )' )
     1    ofile, vvcut, hhcut, prcut, bwcut
      write(16,3000)
3000  format('No fname   brk   pct   u10 uster  uoc  fpk  m(4)  L  ',
     1'vv0  hh0  svb  shb  prb  fdb  bwb bwn  vss1  vss2 hss1  hss2')
      do 200 ifile = 1, nfile
      print *, infile(ifile)
c
c
c     FILE NAME FORMAT: runXY\ssx00000 - USE SYMBOL NUMBER XY IN PLOT
c                       1234567890l234
c
      isym = 10 * ( ichar( infile(ifile)(4:4) ) - 48) +
     1                ( ichar( infile(ifile)(5:5) ) - 48)
c
      open (25, file = infile(ifile) // '.bk2', blocksize = 8192)
      read(25, 1000) fname, u10, uster, fpk, rms, a4, vv0, hh0
1000  format(a8, 1x, f5.2, 6x, f4.3, 16x, 2(1x, f4.3), 6x, 3(1x, f5.4))
      nbreak = 0
      svbar = 0.
      shbar = 0.
      prbar = 0.
      fdbar = 0.
      bwbar = 0.
      bwnor = 0
      vs1con = 0.
      vs2con = 0.
      hs1con = 0.
      hs2con = 0.
      do 100 lpt = 1, nmax
      read(25, *, end = 101) sigvv, sighh, pr, fd, funk, bw, vs1,
     1                       vs2, hs1, hs2
      if (sigvv .lt. vvcut) go to 100
      if (sighh .lt. hhcut) go to 100
      if (pr    .gt. prcut) go to 100
      if (bw    .lt. bwcut) go to 100
      svbar = svbar + sigvv
      shbar = shbar + sighh
      prbar = prbar + pr
      fdbar = fdbar + fd
      bwbar = bwbar + bw
      bwnor = bwnor + bw / fd
      vs1con = vs1con + vs1
      vs2con = vs2con + vs2
      hs1con = hs1con + hs1
      hs2con = hs2con + hs2
      nbreak = nbreak + 1
100   continue
```

```
101     if (nbreak .eq. 0) go to 200
        fnbrk = float(nbreak)
        svbar = svbar / fnbrk
        shbar = shbar / fnbrk
        prbar = prbar / fnbrk
        fdbar = fdbar / fnbrk
        bdbar = bdbar / fnbrk
        benor = benor / fnbrk
        vs1con = 10. * alog10( vs1con / frpts )
        vs2con = 10. * alog10( vs2con / frpts )
        hs1con = 10. * alog10( hs1con / frpts )
        hs2con = 10. * alog10( hs2con / frpts )
c
c       COMPUTE X DATA
c
        ipk = int (fpk / deltaf) + 1
        lamda = twopi / kah(ipk)
        uoc = u10 / lamda / fpk
        pct = 100. * fnbrk / fpk / fsec
        write(16, 2000) isym, fname, nbreak, pct, u10, uster, uoc, fpk,
     1    m4, int(lamda), vv0, hh0, svbar, shbar, prbar, int(fdbar),
     2    int(bdbar), benor, vs1con, vs2con, hs1con, hs2con
        close(25)
200     continue
        close(16)
500     continue
2000 format(i2, 1x, a5, 1x, i3, 1x, f5.2, 1x, f4.1, 1x, f4.3, 1x, f5.2,
     1    1x, f4.3, 1x, f5.4, 1x, i3, 4(1x, f5.4), 1x, f4.2, 1x, i3, 1x,
     2    i2, 1x, f4.2, 4(1x, f5.1) )
C23456789012345678901234567890123456789012345678901234567890123456789012345678901234567890
co fname brk tot u10 uster fpk rms  slp lamba drft  svb shb prb fdb bdb
CIAAAAAxIIIxIIIxFF.Fx.FFFx.FFFx.FFFxFFF.FxFF.Fx.FFFx.FFFx.FFFxF.FxFF.FxFF.F
        stop
        end
```

```
                nfile
18
run04/sxt00147.bk2
run04/sxt00153.bk2
run04/sxt00159.bk2
run05/sxt00105.bk2
run05/sxt00111.bk2
run06/sxt00020.bk2
run06/sxt00038.bk2
run11/sxt00177.bk2
run11/sxt00201.bk2
run11/sxt00207.bk2
run11/sxt00225.bk2
run11/sxt00237.bk2
run12/sxt00252.bk2
run12/sxt00258.bk2
run12/sxt00267.bk2
run12/sxt00273.bk2
run12/sxt00291.bk2
run12/sxt00305.bk2
3
.30   0.  9.9   0.
.25   0.  9.9   0.
.15   0.  9.9  50.
```

```
c
c     PROGRAM TO COMPUTE USTAR BY ITERATION
c
      program calust

      real a, aprm, g, nuprm, ustar, ustprm, ustar2, zwind, gamma
      real ztemp, uz, ts, tz, czol, psi, dpsi, q1, f, fprime, dz0
      real ucheck, ferror, frh, z0, kappa, ustbar, c10ol, psi10
      real c5ol, psi5
      integer nmax, nguess, nfile, i, j, ifile, npts, nout
      integer itime
      real ws, wd, ta, tw, rh
      real error, ustcal, u10, c10, u5, c5, cdn10, el
      character*8 infile(25)
      dimension itime(144), idate(144)
      dimension ws(144), wd(144), ta(144), tw(144), rh(144)
      dimension error(144), ustcal(144), u10(144), c10(144)
      dimension u5(144), c5(144), cdn10(144), el(144)

      data g/9.8/, nuprm/1.54e-6/, kappa/0.4/, gamma/0.01/
c
      open (15, file = 'calust.in', status = 'old')
      read (15,*) zwind
      read (15,*) ztemp
      read (15,*) a
      read (15,*) nmax
      read (15,*) ferror
      read (15,*) nfile
      read (15,'(a)') (infile(i), i = 1, nfile)
      aprm = a / g
      do 500 ifile = 1, nfile
      open (25, file = infile(ifile)//'.env', status = 'old')
      read (25,*) npts
      i = 1
      do 400 j = 1, npts
      read(25, 2000) idate(i), itime(i), ws(i), wd(i), ta(i), tw(i),
     1      rh(i)
      if (ws(i) .le. 0.) ws(i) = 0.1
      print *, itime(i), ws(i), ta(i), tw(i), rh(i)
      if (ws(i) .eq. 99.9) go to 400
c
c     FIRST GUESS USING Cdn AND Uz IN FORMULA FROM
c     GEERNAERT, G. L, LARSEN, S. E., AND HANSEN, F. Measurements of
c     Wind Stress, Heat Flux, and Turbulence Intesity During Storm
c     Conditions Over the North Sea, J. Geopys. Res., 92(C12),
c     13127-13139, 1987.
c
      1000. * Cdn = (0.0847 * Uz + 0.577)

      tz = ta(i)
      ts = tw(i)
```

```
      uz = ws(i)
      frh = 0.01 * rh(i)
      ustprm = sqrt( (0.0847 * uz + 0.577) * 1.e-3 ) * uz
      nguess = 0
c
c     BEGIN ITERATION LOOP
c
      call cstab(zwind, ztemp, uz, ts, tz, frh, czol)
100   uster = ustprm
      nguess = nguess + 1
      ustar2 = ustar * ustar
      z0 = aprm * ustar2 + nuprm / ustar
c
c     COMPUTE psi and d(psi) / d(ustar)
c
      call cdpsi(czol, ustar, ustar2, psi, dpsi)
c
      q1 = (alog(zwind / z0) - psi) / kappa
c
c     COMPUTE FUNCTION f(ustar) = 0
c
      f = ustar * q1 - uz
c
c     COMPUTE DERIVATIVE OF f(ustar)
c
      dz0 = 2. * aprm * ustar - nuprm / ustar2
      fprime = -1. * ustar / kappa * (dz0 / z0 + dpsi) + q1
c
c     COMPUTE NEW GUESS ustprm
c
      ustprm = ustar - f/fprime
c
c     CHECK TO SEE IF CONVERGENCE UNLIKELY - ABORT THIS DATA IF SO
c
      if (ustprm .le. 0.) go to 400
c
c     CHECK TO SEE IF FRACTIONAL ERROR IS LESS THAN ferror
c     OR nguess > nmax
c
      ustbar = (ustprm + ustar) / 2.
      ucheck = abs(ustprm - ustar) / ustbar
      if (nguess .gt. nmax)  then
         print *, 'nguess > ', nmax, ' ferror = ', ferror
         go to 400
      endif
      if (ucheck .gt. ferror) go to 100
c
c     COMPUTE PARMETERS OF INTEREST: C10, CDN10, USTAR, Z/L, L
c
```

```
300  error(i) = ucheck
     ustcal(i) = ustbar
     ustar2 = ustbar*ustbar
     c10ol = czol * 10. / zwind
     call cpsi(c10ol, ustbar, ustar2, psi10)
     c5ol = c10ol / 2.
     call cpsi(c5ol, ustbar, ustar2, psi5)
     u10(i) = uz - ustbar/kappa * ( alog(zwind/10.) - psi + psi10 )
     c10(i) = ustar2 / u10(i) / u10(i)
     u5(i) = uz - ustbar/kappa * ( alog(zwind/5.) - psi + psi5 )
     c5(i) = ustar2 / u5(i) / u5(i)
     q1 = 1. + sqrt( c10(i) ) / kappa * psi10
     cdn10(i) = c10(i) / q1 / q1
     el(i) = zwind / czol * ustar2 * ustbar
     te(i) = te(i) + gamma * (ztemp - 5.)
     i = i + 1
400  continue
     nout = i - 1

c
c    OUTPUT RESULTS
c
     print *, 'FILE: ', infile(ifile), ' nin: ', npts, ' nout ', nout
     open (16, file = infile(ifile)//'.blk')
     write(16,*) nout
     write(16,*)
1'date time    u*    uz   wd   u10   c10   cdn   u5   c5      L    te'
2 t5'
     do 450 i = 1, nout
     if(error(i) .gt. ferror) go to 450
     write(16,3000) idate(i), itime(i), 100.*ustcal(i), ws(i), wd(i),
1              u10(i), 1000.*c10(i),
2              1000.*cdn10(i), u5(i), 1000.*c5(i), el(i),
3              te(i)
450  continue
c time  d*  uz   wd   u10   c10   cdn   u5    c5   L    te
c234x12345x12345x12345x12345x12345x12345x12345x123456x1234
500  continue
2000 format( i6, i4, 6x, f4.1, 1x, f4.0, 2(1x, f5.1), 1x, f5.0)
3000 format(i4.4, 1x, i4.4, 1x, f5.2, 1x, f5.2, 1x, f5.0, 1x, f5.2, 1x,
1        f5.3, 1x, f5.3, 1x, f5.2, 1x, f5.3, 1x, f8.0, 1x, f4.1)
999  stop
     end
```

```
42.       zwind
39.       ztemp          SAX09-19
0.0185    a              SAX09-22
1000      nmax           SAX09-23
1.e-3     ferror         SAX09-24
24        nfile          SAX09-25
                         SAX09-26
                         SAX09-27
                         SAX09-28
                         SAX09-29
                         SAX09-30
                         SAX10-01
                         SAX10-02
                         SAX10-03
                         SAX10-04
                         SAX10-05
                         SAX10-06
                         SAX10-07
                         SAX10-08
                         SAX10-09
                         SAX10-10
                         SAX10-11
                         SAX10-12
                         SAX10-13
                         SAX10-14
```

DOCUMENT LIBRARY

January 17, 1990

Distribution List for Technical Report Exchange

Attn: Stella Sanchez-Wade
Documents Section
Scripps Institution of Oceanography
Library, Mail Code C-075C
La Jolla, CA 92093

Hancock Library of Biology &
  Oceanography
Alan Hancock Laboratory
University of Southern California
University Park
Los Angeles, CA 90089-0371

Gifts & Exchanges
Library
Bedford Institute of Oceanography
P.O. Box 1006
Dartmouth, NS, B2Y 4A2, CANADA

Office of the International
  Ice Patrol
c/o Coast Guard R & D Center
Avery Point
Groton, CT 06340

NOAA/EDIS Miami Library Center
4301 Rickenbacker Causeway
Miami, FL 33149

Library
Skidaway Institute of Oceanography
P.O. Box 13687
Savannah, GA 31416

Institute of Geophysics
University of Hawaii
Library Room 252
2525 Correa Road
Honolulu, HI 96822

Marine Resources Information Center
Building E38-320
MIT
Cambridge, MA 02139

Library
Lamont-Doherty Geological
  Observatory
Columbia University
Palisades, NY 10964

Library
Serials Department
Oregon State University
Corvallis, OR 97331

Pell Marine Science Library
University of Rhode Island
Narragansett Bay Campus
Narragansett, RI 02882

Working Collection
Texas A&M University
Dept. of Oceanography
College Station, TX 77843

Library
Virginia Institute of Marine Science
Gloucester Point, VA 23062

Fisheries-Oceanography Library
151 Oceanography Teaching Bldg.
University of Washington
Seattle, WA 98195

Library
R.S.M.A.S.
University of Miami
4600 Rickenbacker Causeway
Miami, FL 33149

Maury Oceanographic Library
Naval Oceanographic Office
Stennis Space Center
NSTL, MS 39522-5001

Marine Sciences Collection
Mayaguez Campus Library
University of Puerto Rico
Mayagues, Puerto Rico 00708

Library
Institute of Oceanographic Sciences
Deacon Laboratory
Wormley, Godalming
Surrey GU8 5UB
UNITED KINGDOM

The Librarian
CSIRO Marine Laboratories
G.P.O. Box 1538
Hobart, Tasmania
AUSTRALIA 7001

Library
Proudman Oceanographic Laboratory
Bidston Observatory
Birkenhead
Merseyside L43 7 RA
UNITED KINGDOM

50272-101

REPORT DOCUMENTATION PAGE	1. REPORT NO. WHOI-90-27	2.	3. Recipient's Accession No.

4. Title and Subtitle

Detection nnd Characterization of Deep Water Wave Breaking Using Moderate Incidence Angle Microwave Backscatter from the Sea Surface

5. Report Date

August 1990

6.

7. Author(s)

Andrew Thomas Jessup

8. Performing Organization Rept. No.

WHOI-90-27

9. Performing Organization Name and Address

The Woods Hole Oceanographic Institution
Woods Hole, Massachusetts 02543

10. Project/Task/Work Unit No.

11. Contract(C) or Grant(G) No.

(C) N00014-87-K-0007

(G) N00014-89-J-111
NA86AA-D-SG090

12. Sponsoring Organization Name and Address

The Office of Naval Research, the National Science Foundation
and the National Aeronautics and Space Administration through
MIT and the MIT Sloan Basic Research Fund

13. Type of Report & Period Covered

PhD Thesis

14.

15. Supplementary Notes

This report should be cited as: Andrew Thomas Jessup, 1990.Detection and Characterization of Deep Water Wave Breaking Using Moderate Incidence Angle Microwave Backscatter from the Sea Surface. Ph.D. Thesis, MIT/WHOI, WHOI-90-27

16. Abstract (Limit: 200 words)

The importance of wave breaking in microwave remote sensing and air-sea interaction has motivated this investigation of a K_u-Band CW Doppler scatterometer to detect and characterize wave breaking in the open ocean. Field and laboratory measurements by previous authors of microwave backscatter from sharp-crested and breaking waves show that these events can exhibit characteristic signatures in the radar cross-section (RCS) and Doppler spectrum.

Simultaneous microwave, video, and environmental measurements were made during the SAXON experiment off Chesapeake Bay in fall 1988. The scatterometer was pointed upwind at 45 degree incidence with an illumination area small compared to the dominant surface wavelength. An autocovariance estimation technique produced time series of RCS mean Doppler frequency, and Doppler spectral bandwidth in real-time.

Joint statistics of microwave quantities indicative of breaking are used to investigate detection schemes for breaking events identified from the video recordings. Sea spike statistics are investigated as functions of wave field paramenters and friction velocity u*. Wind speed dependence of the percentage of crests producing sea spikes is comparable to that of the fraction of breaking crests reported by previous authors. Doppler frequency and bandwidth measurements are also used to inquire into the kinematics of the breaking process.

17. Document Analysis   a. Descriptors

1. wavebreaking
2. sea spikes
3. scatterometry

b. Identifiers/Open-Ended Terms

c. COSATI Field/Group

18. Availability Statement

Approved for publication; distribution unlimited.

19. Security Class (This Report) UNCLASSIFIED	21. No. of Pages 344
20. Security Class (This Page)	22. Price

(See ANSI-Z39.18)   *See Instructions on Reverse*   OPTIONAL FORM 272 (4-77)
(Formerly NTIS-35)
Department of Commerce